SYNTHESIS AND CHARACTERIZATION OF METAL OXIDE NANOCOMPOSITE FILMS AND THEIR APPLICATIONS AS OPTO-ELECTRONIC HUMIDITY SENSORS

THESIS SUBMITTED FOR THE AWARD OF THE DEGREE OF

Doctor of Philosophy

in

Applied Physics

by

Samiksha Sikarwar
Enrollment No. 599/11

Under the Supervision of

Prof. Bal Chandra Yadav

DEPARTMENT OF APPLIED PHYSICS
SCHOOL FOR PHYSICAL SCIENCES
BABASAHEB BHIMRAO AMBEDKAR UNIVERSITY, LUCKNOW, (U.P.)
INDIA – 226025

September, 2018

DECLARATION

I declare that the thesis entitled **"Synthesis and characterization of metal oxide nanocomposite films and their applications as opto-electronic humidity sensors"** has been prepared by me under the supervision of Prof. Bal Chandra Yadav, Department of Applied Physics, School for Physical Sciences, Babasaheb Bhimrao Ambedkar University, Lucknow. No part of this thesis has formed the basis for the award of any degree, diploma or fellowship previously. Further, I declare that the material embodied in the present work is based on original research work and the indebtedness to others has been duly acknowledged at relevant places. This is also declared that the thesis is essentially free from all kinds of plagiarism.

Samiksha Sikarwar

(**Samiksha Sikarwar**)

Department of Applied Physics, School for Physical Sciences,
Babasaheb Bhimrao Ambedkar University, Vidya Vihar,
Raebareli Road, Lucknow-226025, U.P., India.

Date: 25th September 2018
Place: Lucknow

Dedicated to My Parents

CERTIFICATE

This is to certify that the thesis titled **"Synthesis and characterization of metal oxide nanocomposite films and their applications as opto-electronic humidity sensors"** submitted by **Ms. Samiksha Sikarwar** is an original research work and has not been previously submitted in part or full for the award of any other degree or diploma to this or any other university or institutions.

The thesis submitted to the Babasaheb Bhimrao Ambedkar University, Lucknow satisfies all the requirements as stipulated in the *Doctor of Philosophy (Ph.D.) regulations -1999 as amended in 2010* and it is fit for submission and evaluation for the award of Doctor of Philosophy of the University.

B Yadav

Prof. B. C. Yadav
(Supervisor)

Prof. (Dr.) Bal Chandra Yadav
Professor & Ex-Head
Department of Physics
School for Physical & Decision Sciences
B.B. Ambedkar University, Lucknow-226025

D Kumar 25/9/18

Prof. Devesh Kumar
(Head of the Department)

Date: 25th September 2018
Place: Lucknow

ACKNOWLEDGEMENT

It is my firm belief that any major research work to result in a positive outcome including a worthy thesis requires the culmination of several factors such as a meaningful subject which can motivate a determined researcher to take up the challenge, a learned and sincere guide in the form of friend, relative and colleague who selflessly encourage and help the researcher throughout the research. I had the honour and privilege to have **Prof. Bal Chandra Yadav** as an excellent guide. I take this opportunity to place on record my heartfelt and sincere gratitude and deep indebtedness to him without whose guidance this work could not have been meaningfully concluded. I also owe my sincere thanks and sense of deep gratitude to **Prof. Devesh Kumar**, Head, Department of Applied Physics, School for Physical Sciences, Babasaheb Bhimrao Ambedkar University, for providing necessary facilities in the department in a very kind behaviour.

I am extremely thankful to my teachers **Dr. Ramesh Chandra**, **Dr. Anil K. Yadav**, **Dr. Khem B. Thapa**, **Dr. Devendra Singh** for their valuable suggestions and encouragements which have been a great asset to me during the entire course of study. I owe my deep gratitude towards them for their constant motivation and moral support. I feel myself blessed to have such teachers. Also, I am thankful to staff members at Babasaheb Bhimrao Ambedkar University especially **Mr. Ankit Kumar** (FO), **Mr. Mukesh Kumar** (USIC) and **Mr. Mukesh Tyagi** (DAP).

I wish to express my reverence and sense of deep gratitude to **Prof. (Dr.) Gulzhian I. Dzhardimalieva**, Head, Laboratory of Metallopolymers, Institute of Problems of Chemical Physics, Russian Academy of Sciences, Chernogolovka, Moscow, Russia for her priceless, insightful comments and suggestions to improve the quality of this work. Also, I wish to express my reverence and sense of thankfulness to **Prof. Nina D. Golubeva**, Senior Researcher, in the same laboratory for her constant guidance in the synthesis and exploration of the material.

I am highly grateful to **Dr. Rakesh K. Sonker**, NPDF, Department of Physics and Astrophysics, University of Delhi for his constant support and providing help at the hour of need. Without his support, the thesis cannot be in its present form. Also, I am thankful to **Dr. Ravikant Tripathi**, DSK Fellow, DAP, SPS, BBAU for his valuable suggestions and encouragements. Also, I express my gratitude towards **Dr. Satyendra Singh**, Assistant

Professor, Department of Physics, MPGPGC, Hardoi for his support in my academic upliftment.

I am obliged to **Prof. O.N. Srivastava**, Padam Shree, Emeritus Professor, Department of Physics, Banaras Hindu University, Varanasi, **Mr. Subodh Kumar**, Retired Scientist, Geological Survey of India, Lucknow, **Dr. L.K.S. Chauhan**, Retired Scientist, Indian Institute of Toxicological Research, Lucknow, **Prof. Rajeev Prakash**, IIT-BHU, Varanasi for providing characterization facilities.

I would like to acknowledge the contribution of my friends and colleagues, **Ms. Priyanka Chaudhary** and **Mr. Anwesh Pandey** at the hour of need and **Dr. Monika Singh**, **Mr. Shakti Singh**, **Mr. Utkarsh Kumar**, **Ms. Abhisikta Bhaduri**, **Ms. Rolly Yadav**, **Mr. Krishan Pal**, **Mr. Kuldeep Kumar**, **Mr. Ashish Kumar** and **Mr. Pawan Singh** for a joyful and healthy environment around me to work.

I gratefully acknowledge to **Department of Science and Technology, Govt. of India** for financial support in the form of **INSPIRE AORC fellowship grant no. DST/INSPIRE Fellowship/2014/IF140317**, India and **Indo-Russian project (Ref no. INT/RUS/RFBR/P-148)**.

Finally, I would like to pay my highest regard to my grandparents **Shri Virendra Singh Sikarwar** and **Smt. Vidya Devi**. I owe my indebtedness towards my parents **Shri Rakesh Kumar Singh** and **Smt. Neelam Singh** for their love, support and sacrifice from the very first day of my journey of life. Also, I express my sincere thanks to my uncle **Shri Ravindra Kumar Singh** and aunt **Smt. Annu Singh** for providing me with every kind of support. Also, I am highly thankful to my pride, my brother **Er. Mayank Sikarwar** for his unconditional love and support. I would like to acknowledge the sweet smile of my cousins **Harshit** and **Tanisha** which inspired and imparted happiness in my life and gave strength to overcome the failures and to start over again.

Last but not the least, my final words of thanks will be for Almighty God, for His countless blessings, mercy and companionship through all turmoil of my life.

Samiksha Sikarwar

Samiksha Sikarwar
(Ph.D. Scholar)

LIST OF PUBLICATIONS

Part of the thesis published and communicated in the refereed journals:

1. **Samiksha Sikarwar**, B.C. Yadav, Opto-electronic Humidity Sensor: A Review, Sens. Actuators A: Physical 233 (2015) 54–70.

2. **Samiksha Sikarwar**, B.C. Yadav, S. Singh, G.I. Dzhardimalieva, S.I. Pomogailo, N.D. Golubeva, A.D. Pomogailo, Fabrication of nanostructured yttria stabilized zirconia multilayered films and their optical humidity sensing capabilities based on transmission, Sens. Actuators B: Chemical (2016) 232 283–291.

3. **Samiksha Sikarwar**, B.C. Yadav, G.I. Dzhardimalieva, N.D. Golubeva, P. Srivastava, Synthesis and characterization of nanostructured MnO_2–CoO and its relevance as an opto-electronic humidity sensing device, RSC Advances 8(37) (2018) 20534-20542.

4. **Samiksha Sikarwar**, B.C. Yadav, R.K. Sonker, G.I. Dzhardimalieva, Synthesis and characterization of nanostructured CeO_2-Gd_2O_3-CoO and its application as opto-electronic humidity sensor, Sens. Actuators B: Chem. (Communicated).

5. **Samiksha Sikarwar**, B.C. Yadav, I.E. Uflyand, G.I. Dzhardimalieva, Synthesis of La_2O_3-Cr_2O_3-SrO by pyrolysis of metal carboxylates and its humidity sensing, Nano Research (Communicated).

Work not included in Thesis

1. **Samiksha Sikarwar**, A. Kumar, B.C. Yadav, G.I. Dzhardimalieva, N.D. Golubeva, Nanostructured spherical-shaped Sc(III) Polyacrylate for monitoring the moisture level, IEEE Sensors 18(11) (2018) 4384-4391.

2. **Samiksha Sikarwar**, R.K. Sonker, A. Shukla, B.C. Yadav, Synthesis and investigation of cubical shaped barium titanate and its application as opto-electronic humidity sensor, J. Mater. Sci.: Mater. in Electronics (2018).

3. **Samiksha Sikarwar**, S. Singh, Satyendra, R. Srivastava, B.C. Yadav and V.V. Tyagi, Design and development of lab model of piezo-optic sensor for Structural Health Monitoring, Smart Mater. Struct. 26 (2017) 105047 (7pp).

4. **Samiksha Sikarwar,** Satyendra, S. Singh, B.C. Yadav, A Review on Pressure Sensors for Structural Health Monitoring, Photonic Sensors: Springer (2017).

5. P. Chaudhary, **Samiksha Sikarwar**, B.C. Yadav, G.I. Dzhardimalieva, N.D. Golubeva, I.E. Uflyand, Synthesis and characterization of copper (II) nitrate polyacrylamide &its application as opto-electronic humidity sensor, Sens. Actuators A: Phy. 263 (2017).

6. V. Manikandan, **Samiksha Sikarwar**, B.C. Yadav, R.S. Mane, Fabrication of tin substituted nickel ferrite (Sn-$NiFe_2O_4$) thin film and its application as opto-electronic humidity sensor, Sens. Actuators A: Phy. 272 (2018) 267–273.

7. R.K. Sonker, **Samiksha Sikarwar**, S.R. Sabhajeet, Rahul, B.C. Yadav, Spherical growth of nanostructures ZnO based optical sensing and photovoltaic application, Optical Materials 83 (2018) 342-347.

8. B.C. Yadav, **Samiksha Sikarwar**, R. Yadav, P. Chaudhary, G.I. Dzhardimalieva, N.D. Golubeva, Preparation of zinc (II) nitrate poly acrylamide (PAAm) and its optoelectronic application for humidity sensing, J Mater Sci: Mater Electron 29 (2017) 7770–7777).

9. B.C. Yadav, K.S. Chauhan, S. Singh, R.K. Sonker, **Samiksha Sikarwar**, R. Kumar, Growth and characterization of sol–gel processed rectangular shaped nanostructured ferric oxide thin film followed by humidity and gas sensing, J Mater Sci: Mater Electron 28 (2017) 5270–5280.

10. U. Kumar, **S. Sikarwar**, R.K. Sonker, B.C. Yadav, Carbon Nanotube: Synthesis and Application in Solar Cell, J. Inorg. Organometallic Poly. Mater. 26 (2016) 1231-1242.

11. A. Gautam, S. Rawat, J. Singh, **S. Sikarwar**, B.C. Yadav, A.S. Kalamdhad, Green synthesis of iron nanoparticle from extract of waste tea: An application for phenol red removal from aqueous solution, Environmental Nanotechnology, Monitoring & Management (Published online).

12. B.C. Yadav, **S. Sikarwar**, A. Bhaduri and P. Kumar, Synthesis, Characterization and Development of Opto-Electronic Humidity Sensor using Copper Oxide Thin Film, Int. Adv. Res. J. Sci., Engg. Tech. 2(11) (2015) 105-109.

13. **S. Sikarwar**, S.B. Yadaw, A.K. Yadav, B.C. Yadav, Nanocomposite material for packaging of electronic goods, Int. J. of Scientific and Innovative Research 1(2) (2013) 93-108.

14. R. Dixit, S. Gupta, P. Kumar, **Samiksha Sikarwar**, B.C. Yadav, Preparation and Properties of Transparent Conducting Oxide (TCOs) Thin Films: A Review, Int. J. Innovative Res. Sci., Engg. Tech. 6(2) (2017) 1944-1959.

15. D.K. Maurya, **Samiksha Sikarwar**, S. Angiah, B.C. Yadav, Synthesis and characterization of nanostructured Copper Zinc Tin Sulphide (CZTS) for humidity sensing applications, IEEE Sensors (Minor Revision).

16. V. Manikandan **Samiksha Sikarwar**, B.C. Yadav, S. Vigneselvan, Enhanced humidity sensing properties of lithium substituted copper ferrite (Li-$CuFe_2O_4$) thin film, Mater. Res. Exp. (Communicated).

17. P. Chaudhary, D.K. Maurya, **Samiksha Sikarwar**, B.C. Yadav, G.I. Dzhardimalieva, Development of nickel reinforced Polyacrylamide via frontal polymerization for a reliable room temperature humidity sensor, Materials and Design (Communicated).

Papers presented in International Conferences/Proceedings

1. **Samiksha Sikarwar**, B.C. Yadav, Opto-electronic humidity sensor, International Conference on Nanoscience and Nanotechnology (ICNN-2013), 18^{th} – 20^{th} November 2013, BBAU, Lucknow.
2. **Samiksha Sikarwar**, B.C. Yadav, Opto-electronic humidity sensor: A Review, International Symposium on Advances in Materials Characterization (ISAMC-2014), 14^{th} July, 2014, BBAU, Lucknow.
3. **Samiksha Sikarwar**, B.C. Yadav, Synthesis and characterization of nanostructured Yttria stabilized Zirconia, International Symposium on Advances in Biological & Material

Sciences (ISABMS-2014), 15th July, 2014, Humboldt Academy Lucknow & University of Lucknow, Lucknow.

4. **Samiksha Sikarwar**, B.C. Yadav, S. Singh, G.I. Dzhardimalieva, S.I. Pomogailo, N.D. Golubeva, A.D. Pomogailo, Nanostructured Yttria stabilized Zirconia and its humidity sensing, International Pharmaceutical Conference - 2015 on "Nanoformulations and Translational Research: Small Getting Bigger", 2nd – 3rd February, 2015, BBAU, Lucknow.
5. Workshop on Nano Science and Life (under the auspices of UGC Networking Programme) 26th February – 2nd March, 2015, BHU, Varanasi.
6. **Samiksha Sikarwar**, S. Singh and B.C. Yadav, Design and development of lab model of piezo-optic sensor for crack detection, 3rd International Conference on Nanostructured Materials and Nanocomposites (ICNM-2015), 12th – 14th Dec. 2015, HCST, Mathura.
7. **Samiksha Sikarwar**, B.C. Yadav, G.I. Dzhardimalieva, A.D. Pomogailo, Nanocomposite MnO_2-CoO and its humidity sensing, International Conference on "Environmental Systems and Sustainable Development", 15th – 16th Jan, 2016, CTBC, Shirur and SPPU, Pune.
8. **Samiksha Sikarwar**, R. Yadav, B.C. Yadav, G.I. Dzhardimalieva, N.D. Golubeva, Synthesis and Characterization of Zinc (II) Nitrate Acryl Amide & its Application as Opto-electronic Humidity Sensor, International Conference on 'New Scintillations on Materials Horizon' (ICNSMH-2016) organized by Department of Applied Physics, Faculty of Engineering & Technology, M. J. P. Rohilkhand University, Bareilly (U. P.) during 21-23 Oct, 2016.
9. **Samiksha Sikarwar**, Arun Kumar, B.C. Yadav, G.I. Dzhardimalieva, N.D. Golubeva, Synthesis and characterization of Sc (III) Polyacrylate and its application as opto-electronic humidity sensor, 2nd International Conference on Recent Advances in Nanosciences and Nanotechnology-2016" ICRANN-2016 organized by School for Physical Sciences, Jawahar Lal University, Delhi during 18-20 Dec, 2016.
10. **Samiksha Sikarwar**, B.C. Yadav, G.I. Dzhardimalieva, N.D. Golubeva, Synthesis and characterization of nanostructured MnO_2-CoO using metal carboxylates as precursors and its opto-electronic humidity sensing, International Conference on Renewable Energy for Sustainable Environment: Challenges and Remedies, 20th – 21st March, 2017, SMVDU, Jammu.

11. **Samiksha Sikarwar**, B.C. Yadav, G.I. Dzhardimalieva, I.N. Shershneva, V.A. Shershnev, Multimetallic nanostructured component of La_2O_3-Cr_2O_3-Sr_2O_3: synthesis, characterization and application as moisture sensor, International Conference on Nanoscience and Nanotechnology (ICNN-2013), 24^{th} – 26^{th} September, 2017, BBAU, Lucknow.

Papers in National Conferences/Proceedings

1. **Samiksha Sikarwar**, B.C. Yadav, S. Singh, G.I. Dzhardimalieva, S.I. Pomogailo, N.D. Golubeva, A.D. Pomogailo, Design and development of lab model of humidity detection in unmanned stations using nanostructured yttria stabilized zirconia films 2^{nd} Lucknow Science Congress (LUSCON-2014), 27^{th} – 28^{th} March, BBAU, Lucknow.
2. **Samiksha Sikarwar**, B.C. Yadav, National Symposium on "Interfacing Chemical Biology & Drug Design" 2015, 24^{th} – 25^{th} February, 2015, Amity University, Lucknow.
3. **Samiksha Sikarwar**, B.C. Yadav, K.B. Thapa, G.I. Dzhardimalieva, S.I. Pomogailo, N.D. Golubeva, L.M. Bogdanova, Synthesis and characterization of nanostructured MnO_2-CoO using metal carboxylates as precursors and its opto-electronic humidity sensing, 3^{rd} Lucknow Science Congress (LUSCON-2014) and National Conference on "Science for Society: An Interdisciplinary Approach", 31^{st} Oct – 2^{nd} Nov, 2015, BBAU, Lucknow.
4. **Samiksha Sikarwar**, B.C. Yadav, G.I. Dzhardimalieva, N.D. Golubeva, Multimetallic nanostructured component of La_2O_3-Cr_2O_3-Sr_2O_3: synthesis, characterization and application as humidity sensor, National Seminar on Nano Science and Nano Biotechnology, 25^{th} – 26^{th} February, 2017, DAVC, Kanpur.

ABSTRACT

Humidity is the amount of water vapour in the air which indicates the probability of precipitation. Also, humid air being less dense is one of the fundamental biotic factors that decide the habitat of a particular plant or animal. There are three main measurements of humidity: absolute, relative and specific. Absolute humidity is the content of water vapour in the air, regardless of temperature; relative humidity (RH) is the ratio of the current absolute humidity to the maximum humidity at that temperature; and specific humidity is the ratio of the mass of water vapour content in the mixture to the total mass of the air. Humidity in terms of %RH is also measured on a global scale using remotely placed satellites for climate monitoring and weather forecasts which detect the concentration of water vapour in the troposphere using the inbuilt sensors.

Humidity sensors are classified mainly as four physical principles: electrical mechanical, optical and integrated sensors. Electrical sensors are limited by distance (capacitive type) and long-term stability (resistive type). Mechanical sensors are very selective. Integrated sensors contain a lot of circuit system. The humidity sensors based on optical methods are the best as they are highly sensitive, can work at remote places and are electromagnetic disturbance-free. There is, therefore, an ever increasing need to develop economical, robust, and highly sensitive opto-electronic humidity sensors.

Chapter 1 contains the introductory part of humidity sensors and the role of nanoscience and nanotechnology in this field. It also focuses on the detailed description of the humidity sensing mechanism and its attribute. Surface morphology with the large surface area and more active sites or interstitial site is an important aspect of humidity sensing. Adsorption and desorption are the two phenomena which are responsible for whole sensing mechanism. Semiconducting metal oxides are the best suited for the fabrication of humidity sensors. However, obtaining high sensitivity, good reproducibility, negligible ageing effect with fast response and recovery time at room temperature are the major concern which is not yet reported in the literature. The modulation of optical properties of the sensing layer with humidity is expected to improve the response characteristics to a great extent, which can be easily attained using thin film technology. Metal oxide nanomaterials symbolize an increasing asset in numerous productions, particularly due to their sharp chemical, physical, and electronic

properties and have versatile applications like environmental monitoring, health and personal care, energy, water treatment. Also, as the crystallite size of these materials reduces, great enhancement in their properties is observed. This diverted the research community towards the low dimensional metal oxides while ensuring that their properties remain stable even at high operating temperature. Specifically, transition and rare earth metal oxides are of great interest because of their vacant d- and f-orbitals respectively. They can be easily oxidized as well as reduced and hence has potential application in gas/humidity sensing. Their exclusive electronic configuration has conveyed them with excellent magnetic, electrical, optical, and catalytic properties.

In present investigations synthesis and characterization of nanocomposites of transition and rare earth metal oxides like Yttrium oxide-Zirconium dioxide (Y_2O_3-ZrO_2), Manganese dioxide-Cobalt oxide (MnO_2-CoO), Cerium oxide-Gadolinium oxide-Cobalt oxide (CeO_2-Gd_2O_3-CoO) and Lanthanum oxide-Chromium oxide-Strontium oxide (La_2O_3-Cr_2O_3-SrO) have been carried out. Thin films of various thicknesses and borosilicate glass substrates have been fabricated using a spin coating technique. Further, they were employed as opto-electronic humidity sensor.

Chapter 2 reports the study of modulation in light transmitted through the thin films of nanostructured yttria stabilized zirconia (YSZ) with the exposure of moisture at room temperature. For this purpose, the precursor of YSZ (Y_2O_3-ZrO_2) was prepared and used for the deposition of multilayered thin films on various substrates of borosilicate. The film was then investigated using SEM, XRD and UV-visible absorption techniques. Refractometer investigated the r.i. of the film as 1.448829. SEM showed the macroporous nature of the film and XRD revealed the minimum crystallite size as 5 nm which was further confirmed using TEM and Particle Size Analyser. Energy band-gaps of one-, two-, three- and four-layered films were estimated as 3.927, 3.919, 3.873 and 3.830 eV respectively by UV-vis spectrophotometer. These films were employed as transmission based opto-electronic humidity sensor. Maximum sensitivity was found as ~ 1.937, 1.642, 1.393 and 1.143 μW/%RH for one layered, two-layered, three-layered and four layered films. Response and recovery times were found as 28 s and 30 s respectively. Experiments were repeated from time to time and found that the sensor gave ~94%

reproducible results. Thus the investigated opto-electronic sensor has excellent potential to replace its electrical counterpart.

Chapter 3 describes the synthesis and fabrication of CeO_2-Gd_2O_3-CoO nanocomposite films using metal carboxylates as precursors. The refractive index of the material was found as 1.445538. The crystallinity was confirmed from XRD and the minimum crystallite size calculated was 9 nm. TEM analysis showed the hexagonal crystals where the minimum dimension was obtained as 6 nm. The dimensionality was further confirmed by Particle Size Analyser. The film was then investigated using SEM which revealed highly porous morphology. By UV-Vis spectrophotometer, it was found that the absorption of the film takes place in UV-region and optical band-gap was observed as 3.987 eV from the Tauc plot. The film was employed as transmission based opto-electronic humidity sensor. Maximum sensitivity was found as ~2.006 µW/%RH. Response and recovery times were found as 71 s and 86 s respectively. Experiments were repeated from time to time and the results were found ~ 90% reproducible.

In Chapter 4 the synthesis of MnO_2-CoO using metal carboxylates as precursors and effect of humidity on the transmitted power through its thin film at room temperature is reported. The material was investigated through various characterization techniques. The refractive index of the material was found as 1.445930. TEM reported the minimum grain size of ~5.7 nm and SAED confirmed the crystalline nature of the material which was confirmed by XRD. The particle size was further confirmed from Particle Size Analyser. The film was then investigated using SEM which exhibited macroporous morphology. By UV-Vis spectrophotometer, it was found that the absorption of the film takes place in UV-region and optical band-gap was observed as 3.849 eV from the Tauc plot. The film was employed as transmission based opto-electronic humidity sensor. Average sensitivity was found as ~2.225 µW/%RH with the response and recovery times of 47 s and 59 s respectively. Experiments were repeated from time to time and found that reproducibility of the result is ~ 89%. Also in this chapter, an effort has been made to theoretically verify the experimental results from the computational method. The graphical abstract for this chapter is shown in Fig.3.

Chapter 5 reports the synthesis of nanocomposite La_2O_3-Cr_2O_3-SrO by pyrolysis of metal carboxylates and the effect of humidity on the transmitted power through its thin films at room

temperature. The refractive index of the material was found as 1.442302. The film was investigated using SEM, XRD and UV-Vis spectrophotometer. SEM revealed the uniform mesoporous nature and XRD showed the crystalline nature of the material with a minimum crystallite size of 9 nm. TEM gave the minimum grain diameter of ~ 2.7 nm. Particle Size Analyzer reported that all the particles in the solution are in the range ~2-50 nm. From UV-Vis spectrum, it was found that the absorption through the material takes place in UV-region and the energy band-gaps of the one-, two-, three- and four-layered films were found to be 3.842, 3.837, 3.802 and 3.789 eV respectively. The dilute solution of the material was investigated through TEM and it was found that the minimum grain diameter was ~2.71 nm. The film was then employed as electrical humidity sensor from which the sensitivities were observed as 9.369, 6.006, 3.699 and 1.995 MΩ/%RH respectively for one-, two-, three- and four-layered film. Electrical sensors have certain drawbacks, therefore, the films were further employed as transmission based opto-electronic humidity sensor. In this case, the sensitivity for one-, two-, three- and four- layered films were found to be 3.604, 3.444, 3.250 and 3.063 μW/%RH respectively. Response and recovery times for one-layered sensing element were found as 15 s and 56 s whereas the reproducibility of the results was ~95.71%. Experiments were repeated from time to time and found that ageing effect on the sensor is very less. The investigated sensor being optical in nature has the capability of multiplexing the information with the signal.

Chapter 6 summarizes the entire work of the thesis with concluding remarks and future scope of bimetallic and multimetallic oxide nanocomposites based humidity sensors.

PREFACE

Over the past few decades, humidity has acquired much importance owing to its frequent measurement in different fields from nuclear power reactors to residential air-conditioners. Humidity refers to the water in gaseous form, therefore, obeys gas laws. Humidity is one of the fundamental biotic factors that decide the habitat of a particular plant or animal. Humidity monitoring is important for weather forecasts also as it is not only itself a climate variable but also interacts with other climate variables sturdily. Also, at high humidity if the surrounding is warmer than the body temperature, the condition of hyperthermia, fatigue and loss of concentration may occur; whereas some respiratory disorders may be tracked through humidity concentration in breath. Also, the early detection of moisture can prevent man-made structures from severe damage and would allow the proper action to be taken. Also, monitoring of moisture level in agriculture and during the food processing is necessary. Moisture content in a fuel decides the uncertainty in its energy content hence moisture sensing of the fuel is important. Also, the humidity sensors have an important role to play to determine the possibility of habitat in other planets by observing the water content of soil there which significantly influences the biological processes. Also, humidity monitoring is important for human comfort and achieving hygienic conditions. Due to the above described manifold significance of humidity for the mankind, researchers are keenly interested to work in the field of humidity sensors.

Semiconducting metal oxides, specifically, based on transition and rare earth metals (owing to their vacant d- and f-orbitals respectively) are the best suited for the fabrication of humidity sensors. Metal oxide nanomaterials symbolize an increasing asset in numerous productions, particularly due to their sharp chemical, physical, and electronic properties and have versatile applications like environmental monitoring, health and personal care, energy, water treatment. Also, as the crystallite size of these materials reduces, great enhancement in their properties is observed. This diverted the research community towards the low dimensional metal oxides, while ensuring that their properties remain stable even at high operating temperature. Optical humidity sensors have tremendous advantages over their other counterparts are highly sensitive, can work at remote places and are electromagnetic disturbance-free. Therefore, there is

an ever-increasing need to develop economical, robust, and highly sensitive opto-electronic humidity sensors.

The present thesis is divided into six chapters. Chapter 1 contains the introductory part of humidity sensors and the role of nanoscience and nanotechnology in this field. It also focuses on the detailed description of the humidity sensing mechanism and its attribute. A detailed investigation including synthesis, characterization and application as opto-electronic humidity sensor on nanostructured Y_2O_3-ZrO_2 multilayered films is depicted in Chapter 2. In chapter 3, the synthesis, characterization and humidity sensing properties of CeO_2-Gd_2O_3-CoO nanocomposite are reported. Chapter 4 describes the fabrication of MnO_2-CoO thin film using metal carboxylates as precursors and its application as humidity sensor at room temperature. Chapter 5 reports the synthesis of a nanostructured composite of La_2O_3-Cr_2O_3-SrO by pyrolysis of metal carboxylates and the effect of humidity on the transmitted power through its thin films at room temperature. A study of synthesis, characterization and humidity sensing properties of Y_2O_3-ZrO_2, CeO_2-Gd_2O_3-CoO, MnO_2-CoO and La_2O_3-Cr_2O_3-SrO is summarized in chapter 6. This chapter also gives the guidelines for further research work in the field of bimetallic and multimetallic oxide nanocomposite films.

The investigated opto-electronic humidity sensors in the thesis being optical in nature have the capability of multiplexing the information with the signal and may be used to monitor the moisture level at remote places or unmanned stations.

LIST OF ABBREVIATIONS

S. No.	Name Compound	Full Name
1.	YSZ	Yttria Stabilized Zirconia
2.	r.i.	Refractive index
3.	XRD	X-ray diffraction
4.	SEM	Scanning Electron Microscope
5.	UV-vis	Ultra Violet-Visible spectroscopy
6.	TEM	Transmission Electron Microscope
7.	IPA	Isopropyl alcohol
8.	NIST	National Institute of Standards and Technology

LIST OF TABLES

LIST OF FIGURES

Appendix: Experimental Methods and Characterization Technique

LIST OF APPENDICES

TABLE OF CONTENTS

CHAPTER 1

Introduction and Aim of Present Work

The present chapter reports the detailed study of the recent achievements in the field of various metal oxide nanomaterials as opto-electronic humidity sensor. The sensor elements were fabricated and characterized as thin or thick film of the semi-conducting metal oxides. As semi-conducting metal oxides are known for their n-type conduction because of the presence of oxygen vacancies and change in refractive indices with the exposure of moisture therefore, they were proven to be very good sensors for humidity. Depending upon the need, the sensing materials were deposited either on the base of the prism or on the U-shaped borosilicate glass rods or on some other transparent substrates for opto-electronic humidity sensing. Light from LED or He-Ne laser was launched into the sensing element from one side and collected into the other side by optical power meter. The mode of propagation of light was transmission, reflection or partial refraction. Modulations in the intensity of light with changes in humidity were recorded. Being optical in nature, such types of sensors are very useful for detection of moisture level at remote places or unmanned stations. The primary purpose of this article is to focus on the techniques used in these sensors.

1.1 Introduction

A sensor is an electronic component or module that detects the changes in its environment and sends the information to another device. A humidity sensor senses, measures and reports the amount of water (H_2O) vapour in the air and converts into a measurable parameter. The warmer the air temperature is, the more moisture it can hold. Humidity is one of the most frequently measured quantities in measurement sciences [1]. Measurement of humidity is not only complex but also an old problem. Recent achievements in sensor technology have resulted today in humidity sensors for a wide range of applications ranging from nuclear power reactors to residential air-conditioners [2-5]. Literature shows that humidity sensors for various temperatures [6-7], robotics application [8] and water condensation prevention [9] have been reported. In recent decades, various sensing modalities have been developed, which sense relative humidity (RH) in terms of resistance [10-14], capacitance [15], or refractive index (RI) [16-17]. A desirable humidity sensor should have high sensitivity, long-term durability, fast response, low cost and operable over a wide range of humidity and temperature [18].

The humidity control is becoming much important for improving quality of life and enhancing the industrial process. Humidity sensors based on different working principles have been utilized in various applications [13-14].

1.1.1 Humidity

Water (H_2O) can exist in three different phases (ice, liquid and vapour) depending on the temperature and pressure of the surrounding. Fig.1.1 shows the schematic of a water molecule whereas Table 1.1 shows some of its properties. The air around us always has some content of water vapour in it. The presence of water vapour in the air gives rise to what is commonly known as humidity. Humidity refers to the water in gaseous form whereas moisture refers to the water in liquid form. Therefore, humidity obeys gas laws and the amount of pressure it exerts is equal to the water vapour components in the gas mixture [15]. Humid air being less dense is one of the fundamental biotic factors that decide the habitat of a particular plant or animal [16]. The saturation point of humidity depends upon temperature, due to which in summers, %RH increases which decrease the

rate of evaporation or perspiration from the skin leading to increase in the apparent temperature to the body [18].

Humidity is also measured on a global scale using remotely placed satellites for climate monitoring and weather forecasts which detect the concentration of water vapour in the troposphere using the inbuilt sensors [19]. The humidity is not only itself a climate variable but also interacts with other climate variables sturdily. On one hand, humidity is affected by winds and rainfall, whereas on the other hand, it affects the energy budget and so impacts on temperature. Water vapour containing highly reactive dipolar molecules gets condensed on or evaporates from the surface even with the small change in temperature and has a lot of "latent" energy [20]. At the time of evaporation, this latent heat is removed from the surface, cooling the earth's surface resulting in the biggest non-radiative cooling effect and compensates for ~70% of the average net radiative warming at the surface [21]. Also, water vapour is the most abundant of all greenhouse gases and acts like a double-edged sword. It transmits most of the solar energy while absorbs red light and infrared energy radiated upward by the earth's surface whereas blocks the harmful UV rays and thus makes life possible on Earth. Also due to this selective nature of water vapours, humid areas experience very little nocturnal cooling than dry desert areas [22].

Also, at high humidity if the surrounding is warmer than the body temperature, the blood brought to the skin cannot dissipate heat by conduction to the air, and results to the condition of hyperthermia [23]. Therefore, a lot of blood goes to the external surface of the body, inspite of going to the active muscles, brain, and other internal organs and hence causes fatigue and loss of concentration [24]. Because humans perceive the rate of heat transfer from the body rather than temperature itself, we feel warmer when the relative humidity is high than when it is low [25]. Due to the above described manifold significance of humidity for the mankind, researchers are keenly interested to work in the field of humidity sensors.

Also, humidity has acquired such tremendous importance because of the fact that these vapours consist of highly reactive dipolar molecules which get condensed on or evaporate from the surface even with slight variations in temperature of the environment

(this high polarity is due to the differences in electro-negativity of the hydrogen and oxygen atoms). It, therefore, becomes necessary to measure and control the humidity [16, 17].

1.1.2 Measurement of Humidity

Humidity measurement can be done in diverse ways based on the measurement technique used. The most commonly used terms are — Absolute Humidity (AH) and Relative Humidity (RH). Absolute humidity can be measured by two modes: Parts Per Million by weight or volume and Dew/Frost Point. Absolute Humidity (vapour density) is defined as the ratio of the mass of water vapour in the air to the volume of air. Its unit is grams per cubic meter or grains per cubic foot (1 grain = 1/7000 pound lb.) and expressed as Eqn. 1.1:

$$\text{Absolute Humidity (AH)} = \frac{m}{V} \quad \ldots. (1.1)$$

where m is the mass of water vapour and V is the volume of air.

Relative humidity is defined as the ratio of the amount of moisture content in the air to the maximum (saturated) moisture level that the air can hold at same temperature and pressure. The RH measurement is stated as a percentage and obtained by the following expression given in Eqn. 1.2:

$$\text{Relative Humidity}(\%\text{RH}) = \frac{Q_1}{Q_2} \times 100\ \% \quad ..... (1.2)$$

where Q_1 is the amount of water vapour present in a given volume of air at a given temperature and Q_2 is the amount of water vapour required to saturate the same volume of air at the same temperature.

RH being temperature dependent quantity hence called the relative measurement. Also, it can be expressed in terms of partial pressure as the ratio of the actual partial pressure of moisture content in air (P_a) to the saturated pressure of moist air (P_s) at the same temperature (both in Bar or KPa), given in Eqn. 1.3:

$$\text{Relative Humidity}\ (\%\text{RH}) = \frac{P_a}{P_s} \times 100\ \% \quad ..... (1.3)$$

Also, RH can be defined as the ratio of absolute humidity (AH) to saturation humidity (SH) as shown in Eqn. 1.4:

$$\text{Relative Humidity (\%RH)} = \frac{\text{AH}}{\text{SH}} \times 100\ \% \qquad \text{..... (1.4)}$$

Parts Per Million by volume (PPMv) is defined as the volume of water vapour content per volume of dry gas, and Parts Per Million by weight (PPMw) is obtained by multiplying PPMv by the molar weight of water per molar weight of that gas or air. Dew point is defined as the temperature (above 0°C) at which the water vapour content of the gas begins to condense into liquid form, and Frost point is the temperature (below 0°C) at which the water vapour in a gas solidifies into ice. D/F point parameters are functions of the pressure of the gas, but independent of temperature and are amongst the absolute humidity measurements. In other words, the dew point is the temperature at which the saturation water vapour pressure is equal to the partial pressure of the water vapour (in an air atmosphere). The difference between the ambient temperature and the dew point temperature is a measure of the ambient relative humidity.

Fig.1.2 shows the relation among RH, PPMv and D/F Point. RH measurement covers higher humidity range, PPMv covers lower humidity range and D/F Point covers all the humidity range. Therefore, for daily life, RH is mostly preferred. For trace moisture measurement, it would be better to use PPMv or D/F Point, because it tells us the absolute amount of water vapour in a gas or air.

Humidity can be measured by various techniques. In the classical Sling Psychrometer (wet and dry bulb Hygrometer) [18-21] evaporation cools the wet bulb more than the dry bulb, and the humidity is obtained as a function of the change in temperature. In Dew Point Temperature Hygrometers [22-24], the temperature corresponding to condensation at a cooled surface varies with humidity whereas, in a Gravimetric Hygrometer [25], the increase in weight of a powerful desiccant caused by absorption of water from humid air directly gives the amount of humidity present in it. In a Piezoelectric Hygrometer [26], the hygroscopic coating changes the crystal frequency with change in humidity. Some inexpensive hygroscopic hygrometers [27-29], use the

extension of a natural or synthetic fibre, the length of which is proportional to the surrounding water vapour concentration. Fig.1.3 shows various types of humidity sensors/hygrometers available in the market.

The most commonly used sensors are those that measure the variation in capacitance of a dielectric material [30] or the variation in resistance [31-34] of a conductive material as a function of RH. The principal sensor groups for humidity sensing thus include many resistive ceramics [35-38], organic polymers [39, 40] and resistive polyelectrolytes [41]. Although polymer sensors [27, 29, 39, 40] are of simple structure and low cost, however, they can measure only a limited range of moisture content and show hysteresis and drift at high humidity and they are relatively sensitive to chemical interference and dust deposition. Electrolytic sensors [41] require a constant flow rate for measurement. Also, the cell in which measurements are to be carried out requires regular-regeneration. This cell may be easily damaged by accidental water immersion. Infrared spectroscopy can also be used to measure RH. In infrared hygrometer [42, 43] absorption due to water vapour takes place at 2.6 μm and the split beam is used to compare sample cell and reference. Some other methods for humidity measurement are based on the surface acoustic wave (SAW) [44-47] and on microwave attenuation.

Also, there are certain parameters which decide the efficiency of a particular sensor at a particular place. These parameters depend upon the type of sensing element. Some material that is efficient for a particular place may not be as good for some other place. The parameters of the humidity sensing are defined as below:

Sensitivity: It is the ratio of the change in the output signal to that of the input signal.

Accuracy: It is the conformity to a standardized reference signal.

Response time: It is the time required to reach 10% of the final sensor output after stepwise increasing the humidity.

Recovery time: It is the time required to reach 10% of the final sensor output after stepwise decreasing the humidity.

Drift: It is the change of the sensor output signal with time at a constant input signal.

Repeatability: It is the distribution of sensor outputs after when performing consecutive readings under similar conditions.

Reproducibility: It is the distribution of sensor outputs when measuring the same under different conditions.

Hysteresis: It is the difference in the output signal when measured for an up-trace and down-trace of the input signal.

Temperature dependence: It is the variation of sensor output with the temperature at constant humidity.

1.1.3 Types of Humidity Sensors

Humidity sensors are classified in following groups:

- Electrical sensors
- Mechanical sensors
- Optical sensors
- Integrated sensors

The first group consists of sensors based on capacitive or impedance-type and measures the variation in capacitance or resistance of a dielectric material or conductive material respectively as a function of RH. The second group i.e. mechanical sensors consist of sensors based on strain-effects and mass-loading effects. The third and the most important group i.e. optical sensors, variation of the optical signal in terms of transmission, reflection and quenching of electromagnetic waves is considered. The last group contains miscellaneous integrated humidity sensors that contain on-chip passive or electronic components for linearization, calibration, transmission etc. [48]. A flow chart regarding the classification of humidity sensors based on techniques and design is shown in Fig.1.4.

1.1.4 Drawbacks of Electrical and Mechanical Sensors

- Capacitive type sensors are limited by distance.
- Resistive sensors are limited by long-term stability when exposed to chemical vapours and other contaminants such as oil mist which may lead to premature failure.

- They have a tendency to shift values when exposed to condensation if a water-soluble coating is used.
- Thermal conductivity humidity sensors are very durable and operable at high temperatures but they respond to any gas that has thermal properties different from those of dry air (mainly nitrogen). This will affect the selectivity of the sensor [49].

1.1.5 Need of Optical Sensor over Other Sensors

There are a large number of techniques used for humidity measurements depending upon the purpose of measurement and the environment in which these measurements are to be made. The humidity sensors based on optical methods play a very important role. They not only have high sensitivity but also remote analysis capability and electromagnetic disturbance-free monitoring. There is, therefore, an ever-increasing requirement to develop cheap, robust and highly sensitive opto-electronic humidity sensors [50].

In most of the opto-electronic sensors, the optical channel is comprised of optical fibre which makes this technology attractive. Optical fibre acts like a waveguide for the transmission of light. The advantages include:

- Optical fibres exhibit low attenuation and large wide-band which makes it adorable for a large distance.
- Optical fibres are made of dielectric materials that are chemically inert. Therefore, these sensors are immune to electromagnetic interferences.
- Their small size, simple geometries and nature of optical fibre make them light-weight systems.
- Optical fibre being biocompatible can be used to develop biomedical instrumentation.
- Having a high fusion point, optical fibres can be used at high temperatures, e.g. in blackbody based sensors.
- The sensitivity, dynamic range and resolution of optical fibre sensor are much higher than that of conventional electrical-based sensors [51].

1.1.6 Opto-Electronic Sensors

Opto-electronic sensors are the systems that use optical fibre technology to transport a light input signal that is modulated according to a measured object magnitude and then collected by a detector, conditioned and processed [52]. Fig.1.5 shows the block diagram of opto-electronic sensor. The origin of opto-electronic humidity sensor lies with the invention of the laser in 1960. Further, in 1963, it was observed that optical signals could be transmitted along glass with less loss than that of copper cables. This laid the foundation stone of low-transparency fibres and the first patent of fibre optic sensing appeared soon [53-55].

1.1.7 Choice of Material

There are a large number of humidity sensitive materials; therefore, selection of a suitable material is rather a tough task. The material to be carried out for investigation should possess good sensitivity over an entire range of %RH with properties that are stable over time and thermal cycling after exposure to the various chemical species likely to be present in the ambient.

Among different sensing elements, metal oxide based sensors are promising in terms of their response speed, stability and repeatability [56, 57]. Therefore the present work shows the study of fabrication and characterization of bimetallic and multimetallic oxide nanocomposite films and their structural, morphological and optical properties with the change in humidity.

1.2 Adsorption and Desorption Mechanism of Water Molecule

Since water is a polar molecule, the negatively charged oxygen of the water molecule is electrostatically attracted to the positively charged cationic side of the metal oxide surface. If the charge density of the cationic side is low, water remains physically adsorbed at the surface by a weak electrostatic field. When the cationic charge density is high, as in the case of alkali salts, the electrostatic force is high enough to form a chemical bond between hydrogen and oxygen of a water molecule, which in turn may break the bond between oxygen and one of the hydrogen atoms [60-62]. Mostly the force

is high enough to break the bond in the initially adsorbed water vapour layer. Therefore, the initial monolayer is chemisorbed. This chemisorbed layer can be thermally removed by increasing the ambient temperature. The irreversible reaction for the first layer can be given by Eqn. 1.5:

$$M^{+} + H_2O \rightarrow M{-}OH + H^{+} \quad \text{..... (1.5)}$$

The complete water adsorption process is schematically depicted in Fig.1.6. The subsequent water layers are physically adsorbed on the first chemisorbed layer. This physisorbed water layer is built by a weak electrostatic force (known as hydrogen bonding) on the underlying chemisorbed layer and can be reversibly removed by decreasing humidity. Therefore this layer is mostly contributed by the humidity sensitive conduction of ceramic materials. The chemisorbed water molecule exerts an electrostatic field which not only attracts the water molecules but also weakens the oxygen to hydrogen bonds of the physisorbed water molecules [63-64]. It has been concluded that weakening action of the surface electrostatic fields promotes the dissociation of a physisorbed water molecule in the following manner given in Eqn. 1.6:

$$2H_2O \leftrightarrow H_3O^{+} + OH^{-} \quad \text{.....(1.6)}$$

In pure water, the fraction of dissociated water molecules is approximately 1×10^{-8} [60].

1.3 Sensor Fabrication

The thin film sensors are synthesized by various methods preferably sol-gel spin coating technique. To increase the effectivity of the sensor, doping of various materials can be done with different concentrations. Now depending upon the need and technique, the film of the required material is deposited on various transparent substrates. After deposition, this film is dried and then annealed for different duration and temperature to make it porous and sensitive to humidity.

1.3.1 Sol-Gel Spin Coating Process

A sol is a dispersion of the solid particles (~0.1-1 μm) in a liquid phase where the Brownian motions suspend the particles and a gel is a state where both liquid and solid

are dispersed in each other and presents a solid network containing liquid components. The sol-gel spin-coating technique usually consists of the following 4 steps:

- Initially, two or more chemicals in the required proportion are mixed thoroughly using a magnetic stirrer so that the desired colloidal particles are made to disperse in a liquid for the formation of a sol. The solution is then filtered.
- A drop of this filtrate is put on the substrate for coating and spreads uniformly. The substrate itself is held by a vacuum chuck. When a proper vacuum condition is achieved at the substrate, the vacuum sensor starts the spinning at the desired speed from 1 to 6 KRPM. When the preset time (0 to 60 seconds) elapses, the spinner stops. The multi-layer film can be deposited using this method.
- A gel in a state of a continuous network is formed when the particles in sol are polymerized through the removal of the stabilizing components.
- The final heat treatments pyrolyze the other organic or inorganic components and finally, an amorphous or crystalline coating is obtained [65-68].

1.4 Humidity Sensing Set-Up, Working and Discussion

There are different methods based on different principles for opto-electronic humidity sensing. These methods include the deposition of a film on various transparent substrates. The basic principle for sensing requires that increase in humidity increases adsorption of water vapour and their condensation in pores of the sensing surface causing a corresponding change in the refractive index of the film which further leads to the change in the output power obtained through the sensing element. Researchers have performed experiments in the different range of %RH using various techniques for humidification and dehumidification. Initially, the humidity controlled chamber is humidified and %RH is measured by some standard hygrometer. The consequential changes in the intensity of light emerging out of the metal oxide coated substrateare recorded for each case. The chamber is then dehumidified and again corresponding light intensity is measured. The increase in %RH results in a decrease in the temperature of the chamber. For detailed discussion various cases are discussed below:

1.4.1 U-Shaped Glass rod based Opto-Electronic Humidity Sensor

The optical humidity sensors investigated in this study consists of a thin U-shaped glass rod of 1 mm diameter having different curvatures on which film of metal oxide is deposited [69]. The experimental set-up U-shaped glass rod based humidity sensor is shown in Fig.1.7. The glass rod is fixed on the wall of a steel chamber with the help of two holes drilled in it such that the material coated bend of the U-shaped rod remains inside the chamber and the two arms protrude outside. The two ends of these arms are then coupled to plastic optical fibres. Light from an unpolarized 2 mW He-Ne laser source or a LED is launched from one of these fibres and after being travelled in the entire rod, it is collected from the fibre coupled to the other end of the rod. This fibre is then fed into an optical power meter for measurement of its intensity. This U-shaped glass rod has been used here as a substitute for the film cladded U-shaped optical fibre.

Observations are taken for variation in optical intensity with respect to the variation in %RH for the different U-shaped geometries. This sensor can be used with a high degree of sensitivity to measure %RH in the broad range of 5-95 %RH. Only the drawback is that it is quite fragile, therefore,smooth handling is necessary. The humidity sensing mechanism for this experiment is described as under:

Initially, the film is free from water molecules having only dry air in its pores. On exposure to lower humidity, rapid surface adsorption of water vapours into the porous film takes place. This causes rapid attenuation of the light propagating through the film cladded thin glass rod. This attenuation is due to the increased leakage of light into the cladding of the rod, the refractive index of which increases as %RH increases. Therefore, the sensitivity is higher in this region. In the higher range of %RH, the capillary condensation occurs and forms a meniscus in the capillaries of the cladding. This causes attenuation of light and hence the sensitivity starts decreasing in this range of %RH. As the %RH increases further, the porous film starts becoming saturated resulting in a still smaller sensitivity for this region. Experimental results indicate that above 90%RH, changes in the output intensity of light become negligibly small. Also, a larger thickness of films results in larger sensitivities.

Here the fast response of the sensors can be attributed to the fast penetration of water molecules into the cladding and the slow recovery in the response is caused by a slow desorption process and capillary forces [69].

In one of the works, nanocrystalline [70] coated glass rods were used as optical fibre humidity sensor. Here, MgO was prepared by a sol-gel method which contained fine particles possibly with enhanced surface activities very useful for absorbing polar gaseous molecules including water vapours. The MgO offers an advantage of attracting polar organic species possibly because of having coordinatively unsaturated sites with dangling bonds over its surface and thus can be utilized as a sensor for water vapour monitoring the humidity content. The monitoring of humidity in ambient conditions can be done by the change in the refractive index of the material coated on the substrate [71]. Schematic of the propagation of the optical wave inside the used optical fibre is shown in Fig.1.8.

In the conventional modulated sensor, the magnitude of the emergent light is related to environmental refractive index in terms of variation of total internal reflection inside the light guide. To measure the change in refractive index two methods can be employed (a) sensitive refractometer, the instrument required to measure refractive index and (b) the optical fibre method. In this report, the later method has been employed to measure the change in refractive index with moisture adsorption as optical fibre is very sensitive to any change. The numerical aperture (NA) of the optical fibre is defined as light gathering power and is an important propertyof the fibre. A meridional ray is shown entering the fibre and reflecting from the innermost interface at the critical angle. This angle represents the smallest angle at which the ray can be totally reflected from this interface and thus, determines the maximum angle α at which a ray can be accepted for transmission along the fibre. If the incident ray is in a medium of refractive index n_o then there exists a relation between α and n_o given in Eqn. 1.7:

$$n_o \sin\alpha = (n_1^2 - n_2^2) \qquad \text{..... (1.7)}$$

The term $n_o \sin\alpha$ is called the numerical aperture (NA) of the fibre and n_1 is the refractive index of fibre and n_2 is the refractive index of the cladding. The NA changes on

the bending and also on removing the cladding. This is a sensitive property of optical fibre. Here the use of optical fibre in the shape of U-shaped glass rod without conventional cladding but coated with MgO as a cladded film, is coupled properly with the optical fibre for the input and output of light wave. The transmission of the fibre optic component is determined by the following four factors (a) NA (b) packing fraction ratio of core area to total area (PF) (c) Fresnel reflectional losses (T_f) (d) internal transmittance of the core (T_i). The transmission can be expressed as given in Eqn. 1.8:

$$T = (NA)^2 \times PF \times T_f \times T_i \;\&\; T_i = e^{-\mu l} \qquad \text{..... (1.8)}$$

where l is the length of the component and μ is the absorption coefficient of the core. Thus, the power of light intensity transmitted from a source to power meter will depend upon the various factors including a square of numerical aperture.

1.4.2 Prism based Sensor with light travelling through Optical Fibre

Fig.1.9 describes the ray diagram of the propagation or reflection of light through the film at the base of the prism. The prism is fixed on a rectangular cut on the wall of a specially designed humidity controlled steel chamber with the support of a metallic plate such that only base of the prism on which film is deposited remains inside the chamber. Light from an unpolarized 2 mW He-Ne laser of wavelength 630 nm enters the prism from one of its isosceles faces and gets reflected from glass-film interface at its base. Reflected light emerging out from another isosceles face of the prism is collected through an optical fibre and fed into an optical power meter for measurement. The change in %RH inside the chamber leads to the corresponding change in the intensity of reflected light I_r from the glass-film interface [72, 73]. Fig.1.9(b) shows a continuous decrease in output power throughout humidity range before saturation. Results obtained above are reproducible and no ageing effect is observed [73].

1.4.3 Prism Based Sensor with Incident Light in the Form of a Conical Beam

Fig.1.10 shows the experimental set up in which parallel light beam from a monochromatic unpolarized 2 mW He-Ne Laser of wavelength 630 nm passes through a combination of two microscope objectives producing a divergent beam of some semi-cone angle. In a symmetrical situation, when a central ray PG of this beam cone falls at a

right angle on the isosceles face AC of the prism, the light spot FH on this surface is circular and that given by F'H' on the μ_g - μ_{film} interface is elliptical in shape. The angle of incidence θ_i on the major axis F'H' of this ellipse increases continuously with the smallest angle lying on the point F' on the largest on H'. The spot formed from the emergent light beam is again circular in shape. The light beam is reflected from the glass-film interface. For a given divergence of the incident conical beam, the diameter of the emergent spot at a particular distance is fixed. A sheet of diameter equal to that of the spot is taken in which several holes at equal distances are made along the horizontal diameter of the emergent spot where each hole approximately corresponds to a particular angle of incidence at the glass-film interface. At a particular time, only a single hole is opened keeping other holes covered. Thus the reflected rays corresponding to approximately a single angle of incidence are isolated which are collected through a lens combination and focused on to a power meter.

The intensity of the reflected light I_r from the glass-film interface is recorded as %RH inside the chamber slowly changes [74]. Experimental results are explained on the basis of Fresnel reflection & proved by representative curves. For the single-layered film, normalized output power decreases as %RH increases at a particular angle of incidence whereas it increases for some other particular angle of incidence. It is noteworthy that the conical beam used as an incident light in the experiment can also be produced with the help of an optical fiber. This lead to a small sized compact humidity sensing device.

1.4.4 High-Sensitivity Optical Humidity Sensor Based on a Thin Dielectric Waveguide

Here a low-cost, high-sensitivity humidity sensor based on low-loss dielectric thin film waveguide (WG) [75] is shown in Fig.1.11. The guided mode was produced by coupling laser light into the film by optical tunnelling. This optical tunnelling was done by depositing a solid gap on the base of a semi-cylindrical lens. The light reflected from this optical system was the function of the refractive index of the medium neighbouring the WG. This reflected light was detected by a low-cost CCD linear sensor and analyzed with a microcontroller or personal computer. The technique presented a good sensitivity

to relative humidity (RH) changes, especially below 10 %RH. The linear behaviour was observed between 20 and 80 %RH with a response time of a few seconds.

1.4.5 High-Speed Optical Humidity Sensors Based on Chiral Sculptured Thin Films

The fabrication and characterization of an optical humidity sensor based on a chiral sculptured thin film (CSTF) should have identical arrays of helical nanowires (aligned parallel). It provides the CSTF with a distinguished axis of chirality aligned normal to the substrate. This helical morphology gives rise to a resonance for either left or right circularly polarized (LCP or RCP) light. Here CSTF acts as circular polarization filter [76-79].

CSTFs were deposited with electron beam evaporation system consisting of the serial bideposition (SBD) technique in which the substrate is tilted at an angle χ_v (the angle between the directions of the impinging vapour flux and the substrate plane). During the deposition of CSTF, the substrate was periodically rotated normal (the z-axis in Fig.1.12) to obtain adesired helical morphology. The distance between the evaporation source and the centre of the substrate was kept fixed. The deposition rate was controlled by a resonating quartz crystal sensor (kept at normal incidence located near the substrate). A well-controlled deposition rate at low vacuum leads to a uniform pitch. The pitch of the helical nanowires in the CSTF was defined as the width of one complete turn along the axis.

The experimental set-up is shown in Fig.1.12. A structurally right-handed CSTF was attached to a Teflon substrate. The CSTF was normally illuminated with the help of a halogen lamp which was made either LCP or RCP through a combination of a linear polarizer and a quarter wave plate. The total transmittance through the CSTF was measured with a spectrometer for a certain wavelength range. Inside the humidity chamber, a water tank and a fan system were made to control the operating temperature and %RH between 40 and 95. Here to characterize the sensor's response time, a separate small transparent chamber (4cm × 4cm × 4cm) was used to quickly oscillate the %RH between 20 and 100. RCP light from an external He-Ne laser was incident normally

through the structurally right-handed CSTF and the transmitted light was collected by the photo-detector. The response time was then extracted from the recorded data [80].

A well-defined circular Bragg regime was presented as a deep trough in the total transmittance spectrum for incident RCP light, with a minimum 10% of light transmitted; whereas there is the uniformly high transmission of incident LCP light over the same spectral regime. The central wavelength of the circular Bragg regime and the FWHM bandwidth was calculated.

The ratio 'υ' of the central wavelength to the pitch was calculated as the function of three principal refractive indices of the CSTF and of the angle of rising of the helical nanowires. This ratio was considered as an equivalent refractive index. Fig.1.13 shows that as RH increases/decreases, the trough in the total transmittance spectrum for RCP incidence red-shifted/ blue-shifted and the total transmittance in the trough increases/ decreases. When the water vapour diffuses through the pores, the dielectric properties of the CSTF get changed. The three principal refractive indices of the CSTF and therefore υ increases to cause the red shift of the circular Bragg regime to decrease; for a fixed pitch and thickness. The total transmittance in the trough would then increase. Both features are evident in Fig.1.13 (a) and are more pronounced at higher humidity because more water molecules are adsorbed in the void regions. As the water molecules desorbed with a decrease in the RH, the total transmittance spectrum returned to the initial state, as shown in Fig.1.13 (b) [80].

1.4.6 Evanescent Wave Optical Fibre Humidity Sensor

Khijwania et al. reported a fibre optic relative humidity (RH) sensor based on the evanescent wave absorption spectroscopy using a single U-bend plastic-clad silica fibre as shown in Fig. 1.14(a) [81]. The sensor was fabricated on the bare fiber core with a thin coating of $CoCl_2$ doped polymer. The sensor mechanism was based on the knowledge of the penetration depth (*d*) of the evanescent wave fibre. In the case of straight fibre, *d* was calculated from Eqn. 1.9:

$$d = \frac{\lambda}{2\pi n_1 (cos^2\theta_{cs} - cos^2\theta)^{1/2}} \quad \text{..... (1.9)}$$

where, λ = free space wavelength of light launched into the fibre, n_1 = core refractive index of fibre, θ = angle of the ray with respect to the normal at the core-clad interface in the fibre, θ_{cs} = critical angle of the fiber in the sensing region.

Here θ varies from 75º to 90º. However, as a ray enters the U-bend sensing region, θ changes from ϕ_1 to ϕ_2 (given in Eqn. 1.10) at the outer surface and from δ_1 to δ_2 (given in Eqn. 1.11) at the inner surface with respect to the normal at the interface.

$$\phi_1 = \sin^{-1}\left[\left(\frac{R+h}{R+2\rho}\right)\frac{n_{cl}}{n_1}\right] \text{and}, \phi_2 = \sin^{-1}\left[\frac{R+h}{R+2\rho}\right] \quad \text{..... (1.10)}$$

whereas,

$$\delta_1 = \sin^{-1}\left[\left(\frac{R+h}{R}\right)\frac{n_{cl}}{n_1}\right] \text{and}, \delta_2 = 90^o \quad \text{..... (1.11)}$$

Here,

ρ = fiber core radius, R = bending radius, h = entrance height of ray, n_{cl} = refractive index of cladding. Thus it was calculated that θ is a function of h and ρ and hence d.

The prepared sensor probe with multiple coating was kept in a specially designed humidity chamber as shown in Fig. 1.14(b). The ratio of the compressed air and moist air was changed from the time to time to study variations in humidity. One end of the optical fiber was coupled to a He-Ne laser while the other end was coupled to a photodiode. The output from the photodiode was observed in a computer-based data acquisition system. It was observed that the absorption of light in $CoCl_2$ increased with a decrease in humidity and vice versa. Thus the modulated light at the receiving end was the function of humidity.

Thus it can be concluded that bending of fiber in the sensing region increased the sensor interaction with evanescent light and the total response range. Also, the reagent mediated film characteristic and the fiber core diameter played a crucial role in sensitivity. A fiber with a smaller core diameter and the optimum film thickness was better for sensor design. This sensor had a dynamic range of 10-90 %RH with sensitivity. It had a good response time of less than 1 s with great reliability and repeatability [81].

1.5 Applications of Humidity Sensors

Humidity sensors have revealed noteworthy significance in a broad range of applications [82]. Some of them are shown in Fig.1.15. Various techniques of humidity sensing have been employed to perform humidity measurements depending upon the need and type of application. Some of them are discussed below:

1.5.1 Building and Construction

The deterioration in the reinforced steel bars affects the potency of the concrete structure in roads and bridges. Therefore, the early detection of moisture can save the reinforced concrete structure by the delivery of the chloride ions through the cracks or porous concrete. Thus, moisture monitoring can prevent the roads from severe damage and would allow the proper action to be taken and hence proved cost saving.

Also in mountainous regions, check dams are made of timber woods for regulating the speed of water. Biotic agents like fungi grow and spread when wood moisture is between 20% and 40% by weight. This decreases the strength of the wood. Therefore, wood water detection can predict the degree of wood degradation and prevent dams from severe damage.

Fig.1.16 shows a set-up used for moisture ingress rate measurement using FBG humidity sensors. It measures the moisture ingress characteristics of various concrete specimens using a sensor positioned at 25 mm away from the cube face [83].

1.5.2 Food Processing

Monitoring of moisture level during the food processing is quite necessary. The recession of moisture due to transportation and storage often limits the life of fruits and vegetables and too humid condition provides a suitable environment for the growth of fungus. Fruits such as capsicum are stored below 90 %RH to provide precocious desiccation of the peel whereas currants, avocado, pears etc dry out very easily in less humidity. Also, humid conditions provide a suitable environment for the growth of fungal disease as for example, moulds rapidly grow above 75 %RH. Regarding the food storage potential, the measurement of RH is more important than the measurement of moisture content as it gives an indication of the biological activity of the product [84].

1.5.3 Agriculture

Growing of the root and its capacity to absorb the water has been a subject of interest in agriculture and ecology. Each crop has its specific moisture level of maximum growth. Therefore, soil moisture content sensors are useful tools for farmers to achieve optimum condition for the satisfactory growth of crop while saving their time and money.

Fig.1.17 shows the soil moisture sensor set-up for detecting the humidity levels in the soil. It consists of a polymer coated Fibre Bragg Grating sensor for moisture sensing in soil [83].

1.5.4 Medical and Health Monitoring

Prediction and detection of respiratory disorders and the health of a person are based on the breathing air flow technique. For example, Magnetic resonance imaging (MRI) or during oncological treatment, optical humidity sensors are strictly recommended over their electrical counterparts as the administration of radiation or high electric/magnetic field can fail them. Also, it may causea burning hazard to the patient [83].

Also, Morisawa et al. developed a language recognition system for persons with speaking difficulties in which moisture included devoiced breaths act as a method of communication [85]. Fig.1.18 shows the tapered optical fibre sensor with ISAMC overlay for determining the change in humidity in human breathes.

1.5.5 Fuel

Biomass is widely used for heat and power production as renewable alternatives to fossil fuels. Moisture content is an important parameter for biomass, the variation of which gives rise to an uncertainty in its energy content while delivering to a plant. Hence moisture sensing of the fuel is important. It can be done either by direct entering the fuel or by measuring the release of the moisture and oxygen content of the fuel gases [84].

1.5.6 Aerospace

Recently there has been a rapidly growing interest in humidity sensors to measure water content in space and specifically in the near-surface atmosphere of Mars. Detailed atmospheric conditions including RH data will provide an improved data of the water

vapour dynamics and the stability of water near the surface. The water content of soils significantly influences the chemical and physical properties of the environment and is also needful for biological processes to proceed. Thus moisture sensing technology would aid Martian explorations for habitability and other related research. Optical fibre sensors are more reliable than the conventional electrical sensors for aerospace application as these sensors can be used for remote planets or unmanned stations [84].

1.5.7 Human Comfort

Apart from the above-mentioned applications, humidity measurement is important for human comfort as in air condition monitoring and for achieving hygienic conditions. Hydrothermal analysis has become much important in building design as moisture can cause structural damage, reduce thermal resistance, change the physical properties and deform the building materials. It also helps to construct healthy buildings with good indoor air quality. RH in operating theatres is maintained at 40 to 60 %RH [84].

1.6 Literature survey

A year-wise thorough literature survey, regarding the design, fabrication and application of opto-electronic humidity sensor has been summarized in Table 1.2. Advances in nanotechnology have lifted this field to a very high level, leading to a broad spectrum of designs with great opportunities. The field is mature in many respects and emerging in others and a great progress has been made in a short span of time. From a technological point of view, there hardly seem harsh limitations in future. Applications range from aerospace physical measurements to biochemical sampling, along with extreme environments in the nuclear industry or innovative measurements and technological processes.

1.7 Objective of the Work

The main objective of the present work is to synthesise bimetallic and multimetallic oxide nanocomposites using sol-gel extraction route. Further, their thin films were fabricated on flat borosilicate glass substrates using a spin coating technique. The films were then investigated through various characterization techniques. Digital

refractometer gave the refractive index of the film. X-Ray Diffraction (XRD) analysis was done to check the crystallinity of the fabricated film. The further crystallite size was calculated using the Debye Scherrer formula. The Particle Size Analyzer gave the average particle size of the dilute solution. Scanning Electron Microscope (SEM) was used to obtain the image of surface morphology at various scales and magnifications whereas Transmission Electron Microscope (SEM) images gave the information about the internal structure including the shape and size of the crystals. Optical properties were studied through UV-vis absorption techniques and the optical energy band gap was calculated from the Tauc plot. Further, the films were employed as opto-electronic humidity sensor. A humidity-controlled chamber was used in which film was fixed in such a way that laser beam may pass through the film and collect at the output. The modulation in the output power with the increase/decrease in humidity is recorded at room temperature. The corresponding sensing characteristic curves have been plotted for each sample showing the sensitivity, reproducibility, ageing effect and response and recovery times.

1.8 Outline of the Thesis

There are six chapters in the thesis and a brief outline of the content of the thesis is as follows:

Chapter 1: This chapter contains basic introduction of humidity sensors and their role in the environment. Different types of humidity sensors have also been discussed, and the advantage of opto-electronic sensors over their counterparts is described. The chapter also provides information regarding the applications of humidity sensors in various fields from agriculture to industry. The chapter also provides the detailed information about the ongoing research during the past decade in the field of opto-electronic humidity sensors.

Chapter 2: This chapter reports the study of modulation in light transmitted through the thin films of nanostructured yttria stabilized zirconia (YSZ) with the exposure of moisture at room temperature. For this purpose, YSZ was prepared using metal carboxylates as precursors and used for the deposition of multilayered thin films on flat

substrates of borosilicate. The film was then investigated using SEM, XRD and UV-visible absorption techniques and the dilute solution of the material was analyzed using TEM and Particle Size Analyzer. These films were employed as transmission based opto-electronic humidity sensor to observe the humidity sensing potential of the film. Sensitivity along with response and recovery times was calculated. Experiments were repeated from time to time to check the repeatability and response and recovery times.

Chapter 3: In this chapter, the synthesis of CeO_2-Gd_2O_3-CoO using metal carboxylates as precursors and effect of humidity on the transmitted power through its thin film at room temperature is reported. The film was then investigated using SEM, XRD and UV-visible absorption techniques and the dilute solution of the material was analyzed using TEM and Particle Size Analyzer. These films were employed as transmission based opto-electronic humidity sensor to observe the humidity sensing potential of the film. Sensitivity along with response and recovery times was calculated. Experiments were repeated from time to time to check the repeatability and response and recovery times.

Chapter 4: This chapter describes the synthesis of MnO_2-CoO using metal carboxylates as precursors and effect of humidity on the transmitted power through its thin film at room temperature is reported. The film was then investigated using SEM, XRD and UV-visible absorption techniques and the dilute solution of the material was analyzed using TEM and Particle Size Analyser. These films were employed as transmission based opto-electronic humidity sensor to observe the humidity sensing potential the film. Sensitivity along with response and recovery times was calculated. Experiments were repeated from time to time to check the repeatability and response and recovery times.

Chapter 5: This chapter includes the synthesis of nanocomposite La_2O_3-Cr_2O_3-SrO by pyrolysis of metal carboxylates and the effect of humidity on the transmitted power through its thin films at room temperature. The refractive index of the material was found as 1.442302. The film was then investigated using SEM, XRD and UV-visible absorption techniques and the dilute solution of the material was analyzed using TEM and Particle Size Analyzer. These films were employed as transmission based opto-electronic humidity sensor to observe the humidity sensing potential of the film. Sensitivity,

response and recovery times were calculated. Experiments were performed after three months in order to see the repeatability of the sensor. Since this nanocomposite showed the highest potential towards humidity, therefore, they were also checked for the electrical mode of humidity sensing and the effect of humidity on the impedance, capacitance, inductance and phase angle were investigated.

Chapter 6: This chapter summarizes the entire work of the thesis with concluding remarks and future scope of bimetallic and multimetallic oxide nanocomposites based humidity sensors.

References

[1] Z.M. Rittersma, Humidity Sensor. Encyclopedia of Sens. 4(2006)481-509.

[2] C.Y. Lee, G.B.Lee, Humidity sensors: A review. Sens. Lett. 3 (2005) 1-15.

[3] N. Yamazoe, Y. Shimizu, Humidity sensors: principles and applications. Sens. Actuators 10 (1986) 397-398.

[4] J.R. Huang, M.Q. Li, Z.Y. Huang, J.H. Liu, A novel conductivity humidity sensor based on field ionization from carbon nanotubes. Sens. Actuators A: Phy. 133 (2007) 467-471.

[5] R. Fenner, E. Zdankiewicz, Micro-machined vapour sensors: a review of sensing technologies. IEEE Sens.14 (2001)309-317.

[6] K.V. Heber, Humidity sensing at high temperatures. Sens. Actuators 12 (1987) 145-157.

[7] R. Murria, N. Pintoa, C. Ercolia, Technical Digest 8th Int. Conf. on Solid-State, Sens. Actuators 2 (1995) 829. Int. Conf. on Robotics and Automation (1988) 1302.

[8] J.S. Kim, P.J. Reucroft, Solid state water vapour sensor for robotics applications. Proc. of the 1988 IEEE Inter. Conf. on Robotics and Automation 2 (1988) 1302-1303.

[9] O. Vancauwenberghe, J. Short, E. Geihler, P. Bildstein, P. Ancey, M. Gschwind, Design of the interface electronics for an integrated microsensor for the preventive detection of water condensation. Solid-State Sens. Actuators, 1995 and Eurosensors. 835 (1995) 28-29.

[10] R. Singh, S. Singh, R. Srivastava, A. Mishra, B.C. Yadav, Humidity sensing investigations on nanostructured antimony-substituted tin oxide nanoparticles. Adv. Sci. Lett. 20 (2014)887-894.

[11] B.C. Yadav, R. Srivastava, C.D. Dwivedi, P. Pramanik, Moisture sensor based ZnO nanomaterial synthesized through oxalate route. Sens. Actuators B: Chem. 131 (2008) 216-222.

[12] B.C. Yadav, R. Srivastava, C.D. Dwivedi, Synthesis and characterization of ZnO-TiO_2 nano-composite and its application as a humidity sensor. Philosophical Magazine 88 (2008) 1113–1124.

[13] B.C. Yadav, R. Srivastava, C.D. Dwivedi, Synthesis of ZnO nanomaterials through hydroxide route and their application as a humidity sensor. Synth. React. Inorg. Met. Org Nano-Met. Chem. 37 (2007) 1–7.

[14] R. Srivastava, B.C. Yadav, Nanostructured ZnO, ZnO-TiO_2 and ZnO-Nb_2O_5 as solid state humidity sensor. Adv. Mater. Letters 3(3) (2012) 197-203.

[15] Z. Chen, C. Lu, Humidity sensors: a review of materials and mechanism. Sens. Lett. (2005) 274–295.

[16] S. Muto, O. Suzuki, O. Amano, M. Morisawa, A plastic optical fibre sensor for real-time humidity monitoring. Meas. Sci. Technol. 14 (2003) 746-740.

[17] R. Srivastava, N. Verma, B.C. Yadav, Nanostructured zinc ferrite as electrical and optoelectronic humidity sensors. Adv. Sci. Lett. 20 (2014)917-922.

[18] S. Kamekichi, T. Tatsumi, Wet and dry plate dew point Hygrometer, Humidity and Moisture1, Ed. by R. E. Ruskin (1965) 64-69.

[19] M. Yoshitake, I. Shimizu, Experimental results of the psychrometer constant, humidity and moisture 1, Ed. by R. E. Ruskin (1965) 70-75.

[20] R.J. Taylor, The response of psychrometer fluctuations in vapour pressure, Humidity and Moisture 1, Ed. by R. E. Ruskin (1965) 76-82.

[21] W.W. Robert, Psychrometer Determination of relative humidities in the air with dry-bulb temperatures exceeding 212˚F, Humidity and Moisture1, Ed. by R. E. Ruskin (1965) 105-109.

[22] R.G. Wylie, D.K. Davies, W.A. Caw, The basic process of the dew-point hygrometer, Humidity and Moisture 1, Ed. by R. E. Ruskin (1965) 125-135.

[23] A.W. Brewer, The dew-or frost-point hygrometer, Humidity and Moisture 1, Ed. by R. E. Ruskin (1965) 136-143.

[24] C.Y. Lee, G.B. Lee, Micro-machine based humidity sensors with integrated temperature sensors for signal drift compensation. J. Micromech. Microeng.13 (2003) 620-625.

[25] P. Pascal-Delannoy, B. Sorli, A. Boyer, Quartz Crystal Microbalance (QCM) used as a humidity sensor. Sens. Actuators B: Chem. 84 (2000) 285-291.

[26] W.H. King Jr., The piezoelectric sorption hygrometer, Humidity and Moisture 1, Ed. by R. E. Ruskin (1965) 570-583.

[27] M. Jose, M. Perez, C. Freyre, A poly(ethyleneterephthalate)-based humidity sensor. Sens. Actuators B: Chem. 42 (1977) 27-30.

[28] I. Hayakawa, Y. Iwamoto, K. Kikuta, S. Hirano, Gas sensing properties of metal organics derived Pt dispersed-TiO_2 thin film fired in NH_3. Sens. Actuators B: Chem. 67 (2000) 270-274.

[29] Y. Sakai, M. Matsuguchi, T. Hurukawa, Humidity sensor using cross-linked poly (chloromethyl styrene). Sens. Actuators B: Chem. 66 (2000) 135-138.

[30] J. Das, S.M. Hossain, S. Chakraborty, U. Gangopadhyay, H. Saha, Capacitive type Humidity Sensor based on Porous Silicon. Proceedings of the Tenth International Workshop on the Physics of Semiconductor Devices 1 (1999) 707-710.

[31] B.C. Yadav, A.K. Srivastava, P. Sharma, Resistance based humidity sensing properties of TiO_2. Sens. & Trans. J. 81(7) (2007)1348-1353.

[32] W. Qu, W. Wlodarski, U. Jorg, Comparative study on micromorphology and humidity sensitive properties of thin-film and thick-film humidity sensors based on semiconducting $MnWO_4$.Sens. Actuators B: Chem. 64 (2000) 76-82.

[33] B.C. Yadav, R. Srivastava, C.D. Dwivedi, Synthesis of ZnO nanorods and their application as humidity sensors. Synthesis and Reactivity in Inorganic, Metal-Organic and Nano-Metal Chemistry 37 (2007)1-7.

[34] B.C. Yadav, P. Sharma, A.K. Srivastava, A.K. Yadav, Synthesis of antimony doped tin oxide and it's use as an electrical humidity sensor. Sens. & Trans. J. 92(5) (2008) 99-107.

[35] B.C. Yadav, P. Sharma, P.K. Khanna, Morphological and Humidity Sensing Characteristics of SnO_2-CuO, SnO_2-Fe_2O_3 and SnO_2-SbO_2 nano co-oxides. Bull.of Mater. Sci. 34(1) (2011) 1-10.

[36] W. Qu, M. Jorg-Uwe, A novel thick film ceramic humidity sensor, Sens. Actuators B: Chem. 40 (1997) 175-182.

[37] B.C. Yadav, R. Srivastava, C.D. Dwivedi, Synthesis and characterization of ZnO-TiO_2 nano-composite and its application as a humidity sensor. Philosophical Magazine 88 (2008) 7.

[38] A.K. Srivastava, B.C. Yadav, Humidity sensing properties of TiO_2-Sb_2O_5 nanocomposite. Materials Science 28(2) (2010) 493-504.

[39] Y. Sakai, Y. Sadaoka, Y. Matsuguchi, Humidity sensors based on polymer thin films. Sens. Actuators B: Chem. 35 (1-3) (1996) 85-90.

[40] B. Yang, B. Aksas, Q. Lin, M. Sitti, Compliant and low-cost Humidity Sensors using Nano-porous polymer membranes. Sens. Actuators B: Chem. 114 (2006) 254-262.

[41] Y. Mu-Roug, C. Ko-Shao, Humidity Sensors using polyvinyl alcohol mixed with electrolytes, Sens. Actuators B: Chem. 49 (1998) 240-247.

[42] F.S. Wayne, W.F. Laurence, P.J. Hans, Infrared Absorption Hygrometer, Humidity and Moisture 1, Ed. by R. E. Ruskin (1965) 465-480.

[43] R.C. Wood, The Infrared Hygrometer-Its application to Difficult humidity measurement Problems, Humidity and Moisture 1, Ed. by R.E. Ruskin (1965) 492-506.

[44] N.M. Tashtoush, J.D.N. Cheeke, N. Eddy, Surface Acoustic Wave Humidity Sensor based on a thin poly XIO film. Sens. Actuators B: Chem. 49 (1998) 218-225.

[45] R.H. Huang, Sensor Calibration of a SAW Resonator for absolute humidity measurements in microelectronic packages.Sens. Actuators B: Chem.25 (1-3) (1995) 686-688.

[46] D.W. Galipean, J.D. Stroschine, K.A. Snow, K.A. Vetelino, K.R. Hines, A study of condensation and dew point using a SAW. Sens. Actuators B: Chem. 25(1-3) (1995) 696-700.

[47] C. Caliendo, E. Verona, A. D'Amico, A. Furlani, G. Iucci, M.V. Russo, Surface acoustic wave humidity sensor. Sens. Actuators B: Chem. 16(1-3) (1993) 288-292.

[48] B.M. Kulwicki, Humidity Sensors. J. Am. Ceram. Soc. 74 (1991) 697-708.

[49] B.C. Yadav, M. Singh, C.D. Dwivedi, Optical Characterization and Humidity Sensing Properties of Praseodymium Oxide. Sens. & Trans. J. 125 (2011) 68-75.

[50] B.C. Yadav, N. Verma, S. Singh, Nanocrystalline SnO_2-TiO_2 thin film deposited on the base of equilateral prism as an opto-electronic humidity sensor. Optics & Laser Technology 44 (2012) 1681-1688.

[51] I.R. Matias, F.J. Arregui, R.O. Claus, Optical Fibre Sensors. Encyclopedia of Sensors 7 (2006) 163-181.

[52] K. Brain, Fiber optics in Sensing and Measurements. IEEE J of Selected Topics in Quantum Elect. 6(6) (2000) 1014-1021.

[53] J.C. Simon, E. Spitz, Communications a la Societe Francaise de Physique 24 (1963) 1449.

[54] C.K. Kao, G. Hockman, Proceedings of IEEE113 (1966) 1151.

[55] C. Menaider, C. Kissinger, H. Adkins, Instruments and Control Systems 40(1967) 114.

[56] B.C. Yadav, R.C. Yadav, P.K. Dwivedi, Sol-gel processed (Mg-Zn-Ti) oxide nanocomposite film deposited on prism base as an opto-electronic humidity sensor. Sens. Actuators B: Chem. 148 (2010) 413-419.

[57] B.C. Yadav, N.K. Pandey, Study of Optical Humidity Sensing Properties of TiO_2 and MgO Films. Sens. & Trans. J. 78 (2007) 1127-1133.

[58] Y. Shimizu, H. Arai, T. Seiyama, Theoretical studies on the impedance-humidity characteristics of ceramic humidity sensors. Sens. Actuators 7 (1985) 11-22.

[59] H.C. Verma, Concepts of Physics, Part-2, Bharti Bhawan Publishers and Distributors, India (1999).

[60] G.W. Bundrett, Criteria of Moisture Control (London: Butterworths) (1990) 19.

[61] T. Morimoto, M. Nagao, F. Tokuda, The relation between the amounts of chemisorbed and physisorbed water on metal oxides. J. Phys. Chem.73 (1969) 243-248.

[62] T. King, Water, Miracle of Nature (New York: Macmillan) (1953).

[63] J.J. Fripiat, A. Jelli, G. Poncelet, J. Andre, Thermodynamic properties of adsorbed water molecules and electrical conduction in montmorillonites and silicas. J. Phys. Chem. 69 (1965) 2185-97.

[64] J.H. Anderson, G.A. Parks, Electrical properties of silica-gel in the presence of adsorbed water, J. Phys. Chem. 72 (1968) 3662–8.

[65] C.J. Brinker, G.W. Sherer, Sol-gel Science. Academic Press. San Diego.(1990).

[66] C.J. Brinker, A.J. Hurd, P.R. Schunk, C.S. Ashley, R. Caircross, J. Samuel, K.S. Chen, C. Scotto, R.A. Schwartz, Sol-gel derived Ceramic Films - Fundamentals and Applications, in: K.Stern (Ed.), Metallurgical and Ceramic Protective Coatings, Chapman & Hall, London (1996) 112-151.

[67] T. Troczynski, Q. Yang, Process for Making Chemically Bonded Sol-Gel Ceramics, U.S. Pat. 6(284) (2001) 682.

[68] T. Oldings, M. Sayer, D. Barrow, Ceramic Sol-Gel Composite Coatings for Electrical Insulation. Thin Solid Films 398-399 (2001) 581-586.

[69] B.C. Yadav, R.K. Shukla, L.M. Bali, Sol-gel Processed TiO_2 films on U-shaped glass-rods as Optical Humidity Sensor. Ind. J of Pure and Applied Physics 43 (2005) 51-55.

[70] S.K. Shukla, G.K. Parashar, P. Misra, B.C. Yadav, R.K. Shukla, L.M. Bali, G.C. Dubey, Nano like magnesium oxide films and its significance in optical fiber humidity sensor, Sens. Actuators B: Chem. 98(1) (2004) 5-11.

[71] A. Kumar, M.R. Shenoy, B.P. Pal, I.C. Goyal, A novel temperature sensor using mercury cladded optical fibers. J. Inst. Telecommunication Eng. 32 (1986) 347-348.

[72] B.C. Yadav, Sol-gel processed titaniafilms on prism substrates as an Optical Moisture Sensors. Sens. & Trans. J. 79(5) (2007) 1217-1224.

[73] B.C. Yadav, N.K. Pandey, R. Srivastava, P. Sharma, Study of optical humidity sensor based on titania films fabricated by sol-gel and thermal evaporation methods. Meas. Sci. & Techno. 18 (2007) 1-5.

[74] B.C. Yadav, A. Srivastava, R.K. Shukla, G.C. Dubey, Opto-electronic humidity sensor with incident light in the form of a conical beam. Ind. J. Pure App. Phys. 44 (2006) 694-699.

[75] R.A.S. Ribeiro, J.F.M. Domenegueti, S.C. Zilio, High-sensitivity optical humidity sensor based on a thin dielectric waveguide. Applied Optics 52 (2013) 4287-4293.

[76] Q. Wu, I.J. Hodgkinson, A. Lakhtakia, Circular polarization filters made of chiral sculptured thin films: experimental and simulation results. Opt. Eng. 39 (2000) 1863-1868.

[77] A. Lakhtakia, R. Messier, Sculptured Thin Films: Nanoengineered Morphology and Optics. Bellingham. SPIE Press, WA, USA (2005).

[78] A. Lakhtakia, M.W. McCall, J.A. Sherwin, Q.H. Wu, I.J. Hodgkinson, Sculptured-thin-film spectral holes for optical sensing of fluids. Opt. Commun. 194 (2001) 33-46.

[79] I.J. Hodgkinson, Q.H. Wu, B. Knight, A. Lakhtakia, K. Robbie, Vacuum deposition of chiral sculptured thin films with high optical activity. Appl. Opt. 39 (2000) 642-649.

[80] L.Y. Jun, J. Shi, F. Zhang, H. Liang, J. Xu, A. Lakhtakia, S.J. Fonash, J.H. Tony, High-Speed Optical Humidity Sensors based on chiral sculptured thin films.Sens. Actuators B: Chem.156 (2011) 593-598.

[81] S.K. Khijwania, K.L. Srinivasan, J.P. Singh, An evanescent-wave optical fiber relative humidity sensor with enhanced sensitivity. Sens. Actuators B: Chem. 104 (2005) 217-222.

[82] B.C. Yadav, R.C. Yadav, S. Singh, P.K. Dwivedi, H. Ryu, S. Kang, Nanostructured cobalt oxide and cobalt titanate thin films as optical humidity sensor: A new approach. Opt. & Laser Techno. 49 (2013) 68-74.

[83] T.L. Yeo, T. Sun, K.T.V. Grattan, Fibre-optic sensor technologies for humidity and moisture measurement. Sens. Actuators A: Phy. 144 (2008) 280-295.

[84] L. Alwis, T. Sun, K.T.V. Grattan, Optical fibre-based sensor technology for humidity and moisture measurement: Review of recent progress. Measurement. 46 (2013) 4052-4074.

[85] S. Sikarwar, A. Kumar, B.C. Yadav, G.I. Dzhardimalieva, N.D. Golubeva, Nanostructured spherical-shaped Sc(III) Polyacrylate for monitoring the moisture level, IEEE Sensors 18(11) (2018) 4384-4391.

[86] B.C. Yadav, S. Sikarwar, R. Yadav, P. Chaudhary, G.I. Dzhardimalieva, N.D. Golubeva, Preparation of zinc (II) nitrate polyacrylamide (PAAm) and its optoelectronic application for humidity sensing, J Mater Sci: Mater Electron 29 (2017) 7770–7777.

[87] N. Irawati, T.N.R. Abdullah, H.A. Rahman, H. Ahmad, S.W. Harun, PMMA microfiber loop resonator for humidity sensor, Sens. Actuators A: Phy. 260 (2017) 112–116.

[88] P. Chaudhary, S. Sikarwar, B.C. Yadav, G.I. Dzhardimalieva, N.D. Golubeva, I.E. Uflyand, Synthesis and characterization of copper (II) nitrate polyacrylamide & its application as opto-electronic humidity sensor, Sens. Actuators A: Phy. 263 (2017) 415–422.

[89] Y. Wang, C. Shen, Fiber optic humidity sensor based on the graphene oxide/PVA composite film, Optic Commun. 372 (2016) 229–234.

[90] B.C. Yadav, K.S. Chauhan, S. Singh, R.K. Sonker, S. Sikarwar, R. Kumar, Growth and characterization of sol-gel processed rectangular shaped nanostructured ferric oxide thin film followed by humidity and gas sensing, J Mater Sci: Mater Electron 28 (2017) 5270–5280.

[91] B.C. Yadav, S. Sikarwar, A. Bhaduri, P. Kumar, Synthesis, characterization and development of opto-electronic humidity sensor using copper oxide thin film, Int. Adv. Res. J. in Sci., Engg. and Tech. 2(11) (2015) 105-109.

[92] W. Xie, M. Yang, Y. Chen, D. Li, Y. Zhang, Z. Zhuang, Optical fibre relative-humidity sensor with evaporated dielectric coatings on fibre end-face. Optic Fibre Techno. 30 (2014).

[93] P. Hu, X. Dong, K. Ni, L.H. Chen, W.C. Wong, C.C. Chan, Sensitivity-enhanced Michelson interferometric humidity sensor with waist-enlarged fibre bitaper. Sens. Actuators B: Chem. 194 (2014) 180-184.

[94] H. Chen, Z. Gu, K. Gao, Humidity sensor based on cascaded chirped long-period fibre gratings coated with TiO_2/SnO_2 composite films. Sens. Actuators B: Chem. 196 (2014) 18-22.

[95] J.S. Santos, I.M.R. Jr, C.M.B. Cordeiro, C.R. Biazoli, C.A.J. Gouveia, P.A.S. Jorge, Characterisation of a nafion film by optical fibre Fabry-Perot interferometry for humidity sensing. Sens. Actuators B: Chem. 196 (2014) 99-105.

[96] D. Zhang, J. Tong, B. Xia, Humidity-sensing properties of chemically reduced graphene oxide/polymer nanocomposite film sensor based on layer-by-layer nano self-assembly. Sens. Actuators B: Chem. 197 (2014) 66-72.

[97] N. Verma, S. Singh, R. Srivastava, B.C. Yadav, Fabrication of iron titanium oxide thin film and its application as opto-electronic humidity and liquefied petroleum gas sensors. Opt. & Laser Techno. 57 (2014) 181-188.

[98] L. Xia, L. Li, W. Li, T. Kou, D. Lie, Novel optical fibre humidity sensor based on a no-core fibre structure. Sens. Actuators A: Phy. 190 (2013) 1-5.

[99] J. An, Y. Zhao, Y. Jin, C. Shen, Relative humidity sensor based on SMS fibrestructure with polyvinyl alcohol coating. Optik.124 (2013) 6178-6181.

[100] J. Hu, P. Wu, D. Deng, X. Jiang, X. Hou, Y. Lv, An optical humidity sensor based on CdTe nanocrystals modified porous silicon. Microchemical J. 108 (2013) 100-105.

[101] S.S. Voznesenskiy, A.A. Sergeev, A.Y. Mironenko, S.Y. Bratskaya, Y.N. Kulchin, Integrated-optical sensor based on chitosan waveguide films for relative humidity measurements. Sens. Actuators B: Chem. 188 (2013) 482-487.

[102] G. Rajan, Y.M. Noor, B. Liu, E. Ambikairaja, D.J. Webb, G.D. Peng, A fast response intrinsic humidity sensor based on an etched single mode polymer fibre Bragg grating. Sens. Actuators A: Phy. 203 (2013) 107-111.

[103] J. Mathew, Y. Semenova, G. Farrell, Fibre optic hybrid device for simultaneous measurement of humidity and temperature. IEEE Sensors (2013).

[104] L. Alwis, T. Sun, A.P. Zhang, J. Qian, S. He, Optical fibre relative humidity sensor based on FBG incorporated thin-film fibre modal interferometer. Optics Express 19 (2011) 4140-4146.

[105] S. Zheng, Y. Zhu, S. Krishnaswamy, Fibre humidity sensors with high sensitivity and selectivity based on interior nanofilm coated photonic crystal fibre long period gratings. Sens. Actuators B: Chem. 176 (2013)264-274.

[106] A. Urrutia, J. Goicoechea, P.J. Rivero, I.R. Matias, F.J. Arregui, Electro spun nano fibre mats for evanescent optical fibre sensors.Sens. Actuators B: Chem. 176 (2013) 569-576.

[107] P.J. Rivero, A. Urrutia, J. Goicoechea, F.J. Arregui, Optical fibre humidity sensors based on Localized Surface Plasmon Resonance (LSPR) and Lossy-mode resonance (LMR) in overlays loaded with silver nanoparticles.Sens. Actuators B: Chem. 173 (2012) 244-249.

[108] S.F.H. Correia, P. Antunes, E. Pecoraro, P.P. Lima, H. Varum, L.D. Carlos, R.A.S. Ferreira, P.S. Andre, Optical fibre relative humidity sensor based on a FBG with a di-ureasil coating. Sensors12 (2012)8847-8860.

[109] W. Zhang, D.J. Webb, G.D. Peng, Investigation into time response of polymer fibre Bragg grating based humidity sensors. J. of Light wave Techno.30 (2012) 1090-1096.

[110] Y. Liu, Y. Zhang, H. Lei, J. Song, H. Chen, B. Li, Growth of well-arrayed ZnO nanorods on thin silica fibre and application for humidity sensing. Optics Express 20 (2012) 19404-19411.

[111] R. Aneesh, S.K. Khijwania, Titanium dioxide nanoparticle based optical fibre humidity sensor with linear response and enhanced sensitivity. Appl. Optics. 51 (2012) 2164-2171.

[112] T. Li, X. Dong, C.C. Chan, C. Zhao, P. Zu, Humidity sensor based on a multimode-fibre taper coated with polyvinyl alcohol interacting with a fibre Bragg grating. IEEE Sensors 12 (2012) 2205-2208.

[113] J. Mathew, Y. Semenova, G. Rajan, P. Wang, G. Farrell, Improving the sensitivity of a humidity sensor based on fibre bend coated with a hygroscopic coating. Optics & Laser Techno. 43 (2011) 1301-1305.

[114] H. Liang, Y. Jin, J. Wang, X. Dong, Relative humidity sensor based on polarization maintaining fibre loop mirror with a polymer coating. Microwave Optic. Techno. Lett. 54 (2012) 2364-2366.

[115] L.H. Chen, C.C. Chan, T. Li, M. Shaillender, B. Neu, P. Balamurali, R. Menon, P. Zu, W.C. Wong, C.L. Poh, K.C. Leong, Chitosan coated polymerization maintaining fibre-based sagnac interferometer for relative humidity measurement. IEEE J of Selected Topics in Quantum electronics 8 (2012) 1597-1604.

[116] W.C. Wong, C.C. Chan, L.H. Chen, T. Li, K.X. Lee, K.C. Leong, Polyvinyl alcohol coated photonic crystal optical fibre sensor for humidity measurement, Sens. Actuators B: Chem. 174 (2012) 563-569.

[117] L. Alwis, T. Sun, K.T.V. Grattan, Fibre optic long period grating-based humidity sensor probe using a Michelson interferometric arrangement, Sens. Actuators B: Chem. 178 (2013) 694-699.

[118] M.Y. Noor, N. Khalili, I. Skinner, G.D. Peng, Optical relativity humidity sensor based on a hollow core-photonic band gap fiber. Measurement Sci. & Techno.23 (2012) 85103-85110.

[119] P. Mohan, R. Shinta, J. Fujiwara, H. Takahashi, D. Mott, Y. Matsumura, G. Mizutani, K. Iwami, N. Umeda, S. Maenosono, Boehmide nanorod/gold nanoparticle nanocomposite film for an easy-to-use optical humidity sensor. Sens. Actuators B: Chem. 168 (2012) 429-435.

[120] J. Mathew, Y. Semenova, G. Farrell, A fibre bend based humidity sensor with a wide linear range and fast measurement speed.Sens. Actuators A: Phy. 174 (2012) 47-51.

[121] W.C. Wong, C.C. Chan, L.H. Chen, T. Li,K.X. Lee, K.C. Leong, Polyvinyl alcohol coated photonic crystal optical fibre sensor for humidity measurement.Sens. Actuators B: Chem. 174 (2012) 563-569.

[122] S. Singh, N. Verma, B.C. Yadav, R. Prakash, A comparative study on surface morphological investigations of ferric oxide for LPG and opto-electronic humidity sensors. Appl. Surf. Sci. 258 (2012) 8780-8789.

[123] Z. Zhao, Y. Duan, A low-cost fibre optic humidity sensor based on silica sol-gel film. Sens. Actuators B: Chem. 160 (2011) 1340-1345.

[124] G. Berruti, M. Consales, A. Cutolo, A. Cusano, G. Breglio, S. Buontempo, P. Petagno, Glordano, Radiation hard humidity sensors for high energy physics applications using polymide coated fibre Bragg grating sensors. Conference Proceedings. IEEE Sensors (2011) 1484-1487.

[125] D. Viegas, M. Hernaez, J. Goicoechea, J.L. Santos, F.M. Araujo, F.J. Arregui, I.R. Matias, Simultaneous measurement of humidity and temperature based on

SiO_2-nanospheres film deposited on a long-period grating in-line with a fibre Bragg grating. IEEE Sensors 11 (2011) 162-166.

[126] M.Y. Fu, G.R. Lin, W.F. Liu, C.W. Wu, Fibre-optic humidity sensor based on an air-gap long-period fibre grating, Opt. Rev. 18(1) (2011) 93-95.

[127] Y. Zhao, Y. Jin, H. Liang, X. Dong, J. Wang, All-fibre-optic sensor for relative humidity measurement, Int. Conf. on Electronics and Opto-electronics (2011).

[128] Z. Zhao, Y. Duan, A low-cost fibre-optic humidity sensor based on silica sol-gel film.Sens. Actuators B: Chem. 160 (2011) 1340-1345.

[129] Y. Wu, T.H. Zhang, Y.J. Rao, Y. Gong, Miniature interferometric humidity sensors based on silica/polymer microfiber knot resonators.Sens. Actuators B: Chem. 155 (2011) 258-263.

[130] M. Consales, A. Buosciolo, A. Cutolo, G. Breglio, A. Irace, S. Buontempo, P. Petagna, M. Giordano, A. Cusano, Fibre optic humidity sensors for high energy physics applications at CERN. Sens. Actuators B: Chem. 159 (2011) 66-74.

[131] B. Gu, M. Yin, A.P. Zhang, J. Qian, S. He, Optical fibre relative humidity sensor based on FBG incorporated thin-core fiber modal interferometer. Opt. Express 19 (2011) 4140-4146.

[132] P. Sanchez, C.R. Zamarreno, M. Hernaez, I.D. Villar, C.F. Valdivielso, I.R. Matias, F.J. Arregui, Lossy mode resonances toward the fabrication of optical fiber humidity sensors. Meas. Sci. Techno. 23 (2012) 14002-14008.

[133] B. Wang, F. Zhang, F. Pang, T. Wang, An optical fiber humidity sensor based on optical absorption.in: Proc. of SPIE-OSA-IEEE Asia Communications and Photonics 8311 (2011)83112A.

[134] C.R. Zamarreno, M. Hernaez, P. Sanchez, I.D. Villar, I.R. Matias, F.J. Arregui, Optical fiber humidity sensor based on lossy mode resonances supported by TiO_2/PSS coatings.Procedia Engineering 25 (2011) 1385-1388.

[135] S. Akita, H. Sasaki, K. Watanabe, A. Seki, A humidity sensor based on a hetero core optical fiber. Sens. Actuators B: Chem. 147 (2010) 385-391.

[136] B.C. Yadav, R.C. Yadav, P.K. Dwivedi, Sol-gel processed (Mg-Zn-Ti) oxide nanocomposite film deposited on prism base as an opto-electronic humidity sensor. Sens. Actuators B: Chem. 148 (2010) 413-419.

[137] J.M. Corres, F.J. Arregui, I.R. Matias, Sensitivity optimization of tapered optical fiber humidity sensors by means of tuning the thickness of nanostructured sensitive coatings. Sens. Actuators B: Chem.122 (2007) 442-449.

[138] M.A. Zanjanchi, S. Sohrabnezhad, Evaluation of methylene blue incorporated in zeolite for construction of an optical humidity sensor. Sens. Actuators B.105 (2005) 502-507.

[139] F.J. Arregui, Y. Liu, I.R. Matias, R.O. Claus, Optical fiber humidity sensor using a nano Fabry-Perot cavity formed by the ionic self-assembly method. Sens. Actuators B: Chem. 59 (1999) 54-59.

Tables

Table 1.1: Some properties of the H_2O molecule.

Property	**Value**
H-O-H Angle	104.5˚
OH-bond length	0.957Å
Molar Weight	18.01528
Molecule Radius	1.45 Å
OH-dissociation energy	498 kJ/mol (5.18 eV)
Dipole-moment	6.1×10^{-30}A-s-m (1.83-D)

Table 1.2: Literature survey regarding technique and application of opto-electronic humidity sensor.

S. No	**Ref**	**Year**	**Authors**	**Sensing method**	**Sensing material**	**Range (%RH)**	**Sensitivity & response time**
1.	85	2018	S. Sikarwar et al.	Transmission based	$Sc(CH_2=CH-COO)_3$	10-90	2.1 μW/%RH
2.	86	2018	B.C. Yadav et al.	Transmission-based	$Zn(NO_3)_2{\cdot}(AAm)_4{\cdot}2H_2O$	10-90	1.831 μW/%RH
3.	87	2017	N. Irawati et al.	PMMA microfiber loop resonator (PMLR) coated with ZnO	PMMA/ PMLR/ ZnO	20-80	0.1746 dBm/%RH
4.	88	2017	P. Chaudhary et al.	Transmission based	$Cu(NO_3)_2{\cdot}(AAm)_4$	10-90	0.838 μW/%RH
5.	89	2016	Y. Wang et al.	in-fiber Mach–Zehnder interferometer	Graphene oxide/PVA	25-80	0.193 dB%RH
6.	90	2016	B.C. Yadav et al.	Transmission based	Fe_2O_3	10-90	1.172 μW/%RH
7.	91	2015	B.C. Yadav et al.	Transmission based	CuO	10-90	0.85 μW/%RH
8.	92	2014	W. Xie et al	Evaporated dielectric coatings on fibre end-face	Ti_3O_5 and SiO_2	1.8-74.7	0.43 nm/%RH

9.	93	2014	P. Hu et al.	Sensitivity-enhanced Michelson interferometer with waist-enlarged fibre bitaper	Chitosan film	25-90	135 pm/%RH ~ 5 s
10.	94	2014	H. Chen et al.	Cascaded chirped long-period fibre gratings	TiO_2/SnO_2 composite films	40-95	0.221 nm/% (15˚C) 0.281 nm/% (20˚C) 0.214 nm/% (30˚C) 0.211 nm/% (40˚C)-
11.	95	2014	J.S. Santos et al.	Optical fibre Fabry-Perot interferometer	Nafion film	22-80	3.5 nm/%RH 242 ms
12.	96	2014	D. Zhang et al.	Layer-by-layer nanoself assembly	Reduced graphene oxide (RGO)/ poly (diallylimethyam monia chloride) (PDDA)	11-97	- -
13.	97	2014	N. Verma et al.	Total Internal Reflection based	Iron-Titanium Oxide thin film	5-95	4.5 µW/%RH -
14.	98	2013	L. Xia et al.	No-core fibre structure	HEC/PVDF	40-90	0.196 dB/%RH -
15.	99	2013	J. An et al.	SMS fibre structure	Polyvinyl alcohol coating (PVA)	30-80	0.09 nm/%RH -
16.	100	2013	J. Hu et al.	CdTe nanocrystals modified porous silicon	Psi/CdTe NCs composite	12-93	- -
17.	101	2013	S.S. Voznesens kiy et al.	Chitosan waveguide films	Chitosan films	15-95	- -
18.	102	2013	G. Rajan et al.	Etched singlemode polymer fibre Bragg grating	POFBG	10-90	0.23 mV/%RH -
19.	82	2013	B.C. Yadav	Transmission loss	Nanostructured	10-99	0.76 µW/%RH

			et al.	measurement	cobalt oxide and cobalt titanate thin films		1.48 µW/%RH -
20.	103	2013	Mathew et al.	Transmission loss measurement in the hybrid FBG-PCF interferometer (FBG for temperature reference)	Agarose	20-60	0.026 dB/%RH
21.	104	2013	Alwis et al.	LPG resonance band shift measurement of a LPG in a Michelson configuration	PI	20-80	0.10 nm/%RH
22.	105	2013	Zheng et al.	Intensity and wavelength measurement of a LPG written in a PCF	$Al_2O_3^+$/PSS^-nano-film	22-29 38-39	0.0007%/pm 0.00022%/ 10^{-3} dBm
23.	106	2013	Urrutia et al.	Absorbance measurement of a PCF MMF where cladding is chemically removed	PAA electrospun nanowires	30-95	<0.5 s
24.	107	2012	P.J. Rivero et al.	Based on Localized Surface Plasmon Resonance (LSPR) and Lossy-mode Resonance (LMR) in overlays loaded with silver nanoparticles	LbL polymeric coating loaded with Ag NPs	20-80	0.943 nm/%RH (LMR1) 0.126 nm/%RH (LMR2) -
25.	108	2012	Correia et al.	Straininduced Bragg wavelength measurement	Silica/di-ureasil	5-95	22.2 pm/%RH
26.	109	2012	Zhang et al.	Straininduced Bragg wavelength measurement of etched POF	No coating (PMMA polymer cladding)	30-90	33.6 pm/%RH
27.	110	2012	Liu et al.	Transmission loss measurement in straight hydrothermally thinned	ZnOnanorodsgrown on fibre	10-95	0.014 RH^{-1}

				silica fibre			
28.	111	2012	Aneesh et al.	Output power measurement of a de-clad MMF	TiO_2	24-95	27.1 mV/%RH <0.5 s
29.	112	2012	Li et al.	Reflected power loss measurement of a hybrid SMF-polymer coated MFT-FBG probe configuration	PVA	30-95	1.994 µW/%RH ~2s
30.	113	2012	Mathew et al.	Ratiometric power measurement of a cladding removed u-bend MMF	PEO	85-90	High sensitivity
31.	114	2012	Liang et al.	Etched PMF loop mirror	PVA	20-80	0.98 nm/%RH <6s
32.	115	2012	Chen et al.	Straininduced on chemically etched PM fibre in a Sagnac configuration	Chitosan	20-95	0.13 nm/%RH
33.	116	2012	Wong et al.	Wavelength measurement following a merge of PCF at the tip forming a Michelson interferometer	PVA	90	0.60 nm/%RH
34.	117	2012	Alwis et al.	LPG resonance band shift measurement of a LPG in a Michelson configuration	PVA	20-85	~0.6 nm/%RH (for 40-85%RH) -
35.	118	2012	Noor et al.	Absorption power measurement of a hollow core photonic band-gap filter	(No coating)	0-90	3.02 mV/%RH 78-118 s
36.	119	2012	Mohan et al.	Absorption spectra measurement using SPR	Au-NP/boehmite	-	- <20 s
37.	120	2012	J. Mathew et al.	Based on a single mode optical fibre	Agarose coated fibre	25-90	- 50 ms

38.	121	2012	W.C. Wong et al.	Based on miniature photonic crystal fibre (PCF) modal interferometer formed by the excitation of the cladding mode at the tip	PVA coated PCF	30-90	0.60 nm/%RH Rise/fall time 300/500 ms
39.	122	2012	S. Singh et al.	Based on total internal reflection	Nanostructured ferric oxide coated prism	10-90	2.4 µW/%RH
40.	50	2012	B.C. Yadav et al.	Based on total internal reflection	Nanocrystalline SnO_2-TiO_2 thin film coated prism	10-90	4014 µW/%RH
41.	123	2011	Z. Zhao, Y. Duan	Based on wave scattering and evanescent wave absorption	Silica sol-gel film	1.1-70	0.087 dB/%RH
42.	124	2011	Berruti et al.	Strain-induced Bragg wavelength measurement	PI	0-75	2.1 pm/%RH -
43.	125	2011	Viegas et al.	Wavelength measurement of LPG and FBG configured in series (FBG for temperature calibration)	SiO_2 nano-sphere film	20-50 50-80	-63.33 pm/%RH -451.78 pm/%RH <1 s
44.	126	2011	Fu et al.	Resonance-band wavelength measurement of an Air-Gap LPG (AG-LPG)	$CaCl_2$	55-95	1.36 nm/%RH -
45.	127	2011	Zhao et al.	Wavelength measurement in a SMF-MMF-SMF sensor structure	PVA	50-89	0.18 nm/%RH -
46.	128	2011	Zhao et al.	Absorbance measurement of U-bend fibre	Silica/Methylene blue	1.1-4.1	0.0087 RH^{-1} 20 s^{-3} min
47.	129	2011	Wu et al.	Wavelength measurement of	(No coating)	17-98	~8.8 pm/%RH <0.5 s

				silica/polymer microfiber knot resonator			
48.	130	2011	Consales et al.	Output power measurement following a FPI configuration at the coated distal end of MMF	TiO_2	2-5 5-40	$6.9\times10^{-3}\%^{-1}$ $5\times10^{-3}\%^{-1}$
49.	131	2011	Gu et al.	Wavelength shift of a thin-core fibre modal interferometer (TCFMI) and FBG hybrid structure	TiO_2	20-90	84.3 pm/%RH
50.	132	2011	Sanchez et al.	Wavelength measurement using LMR for two different coating materials	ITO In_2O_3	20-80	0.283 nm/%RH 0.935 nm/%RH
51.	133	2011	Wang et al.	Intensity measurement of MMF coated with sensing material at distal end	$PVA/SiO_2/CoCl_2$	25-65	- <2min
52.	134	2011	Zamarreno et al.	Cladding removed MMF using LMR	ITO	20-60	2.7%RH/nm -
53.	135	2011	S. Akita et al.	Based on a hetero-core optical fibre	Poly-glutamic acid/poly-lysine nanostructured overlay	50-92.2	- 400ms
54.	136	2010	B.C. Yadav et al.	Based on total internal reflection	Nanocrystalline (Mg-Zn-Ti) oxide films	10-95	~2 18
55.	137	2007	J.M. Corres et al.	Sensitivity optimization of tapered optical fiber by means of turning the thickness of nanostructured sensitive coatings	PDDA/Poly R-478	75-100	- 300 ms

56.	138	2005	M.A. Zanjanchi, S. Sohrabnezhad et al.	Evaluation of methylene blue	Zeolite	9-98	- 2 min for adsorption 4 min for desorption
57.	139	1999	F.J. Arregui et al.	Based on nanofabry-Perot cavity formed by the ionic self-assembly method	[Au: $PDDA^{+}/PSS^{-}$]n bilayers	11.3-100	- <1.5 s

Figures

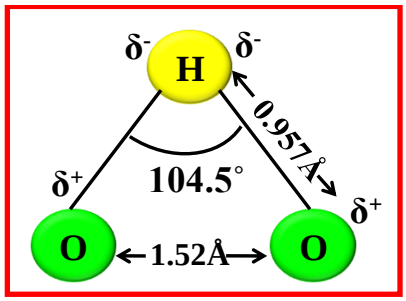

Figure 1.1: Schematic of the H_2O molecule.

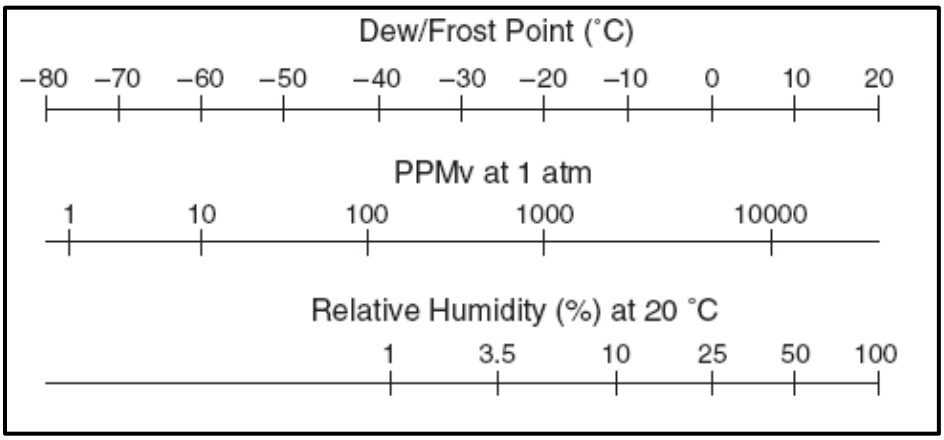

Figure 1.2: Correlation among various humidity measurement units.

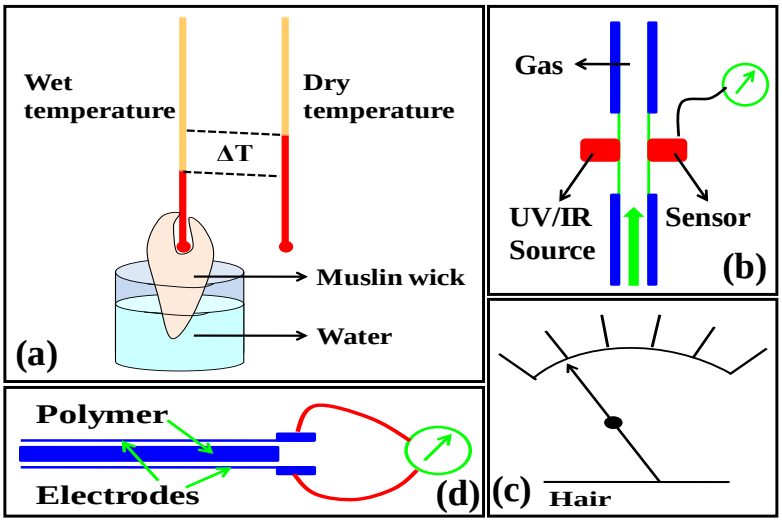

Figure 1.3: Some commonly used methods of measuring humidity which shows (a) Sling Psychrometer, (b) Hygroscopic Hygrometer, (c) Polymer Sensor and (d) Infrared Hygrometer.

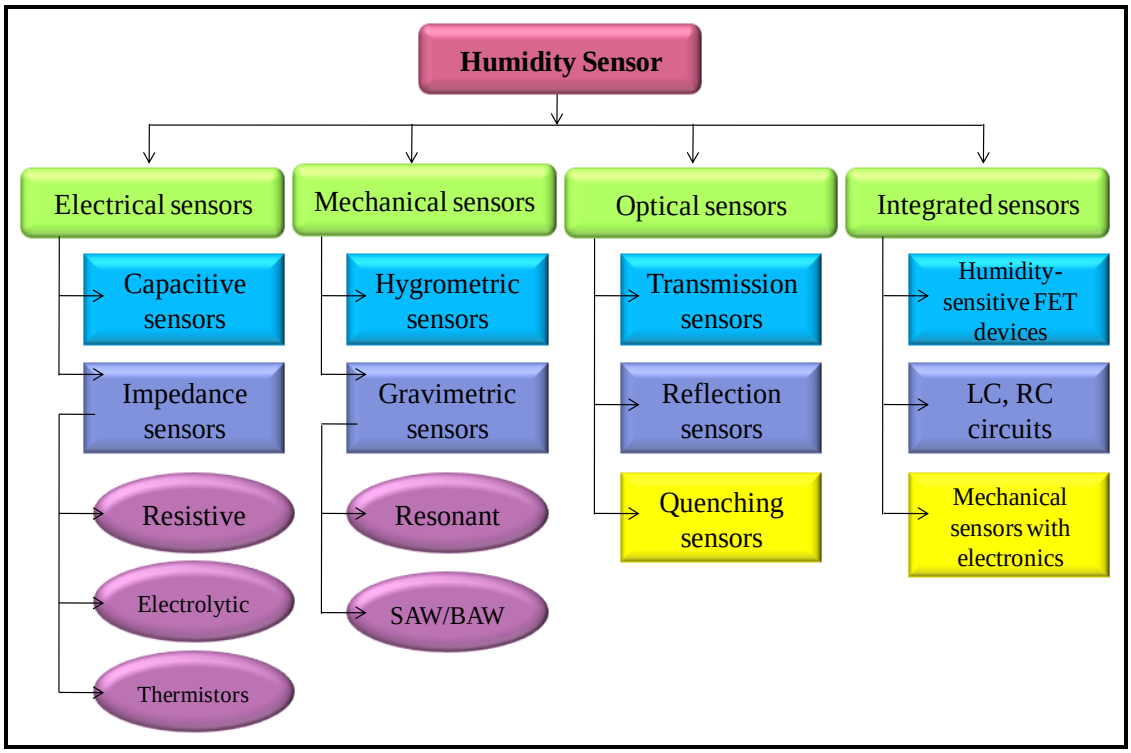

Figure 1.4: Classification of humidity sensors on the basis of techniques and design.

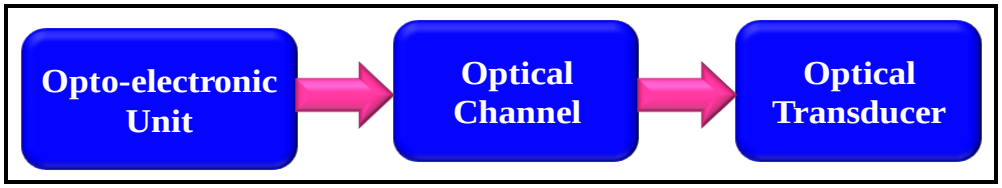

Figure 1.5 Block diagram of a generic Opto-electronic sensor system.

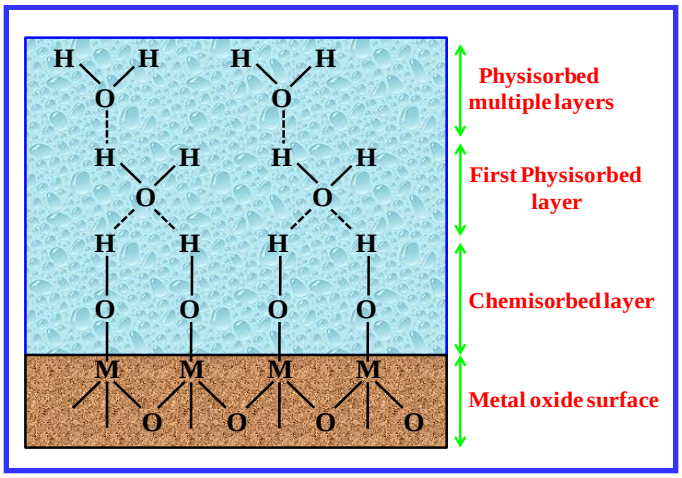

Figure 1.6: Simplified physical model of water adsorption proton charge conduction on the surface of a solid state humidity sensor.

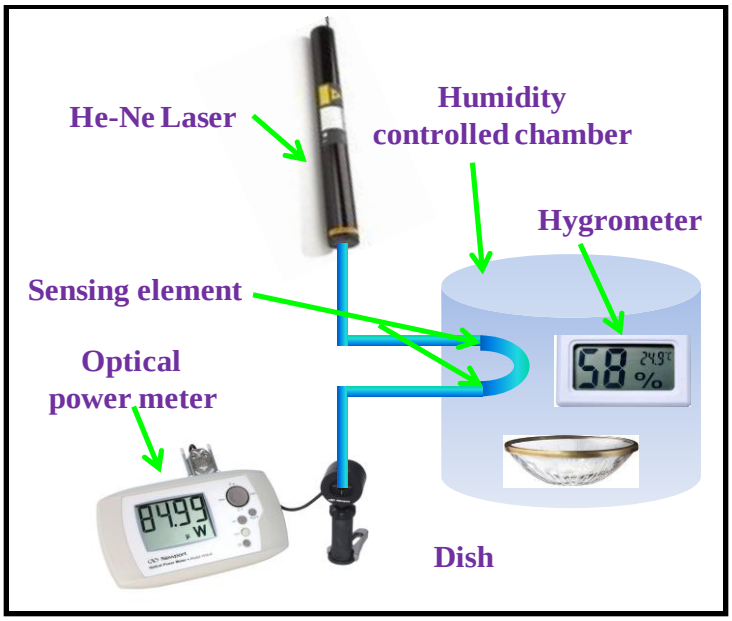

Figure 1.7: Experimental set-up for U-shaped glass rod based humidity sensor.

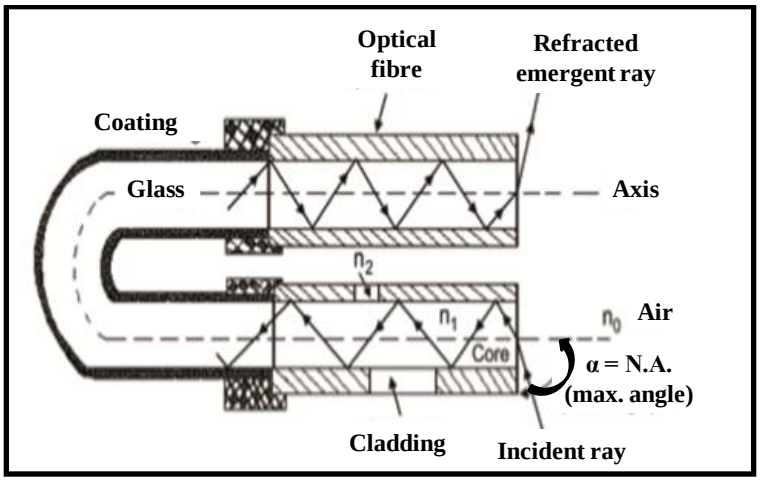

Figure 1.8: Schematic diagram of reflection and refraction in an optical fiber attached to U-shaped borosilicate rod coated with a film.

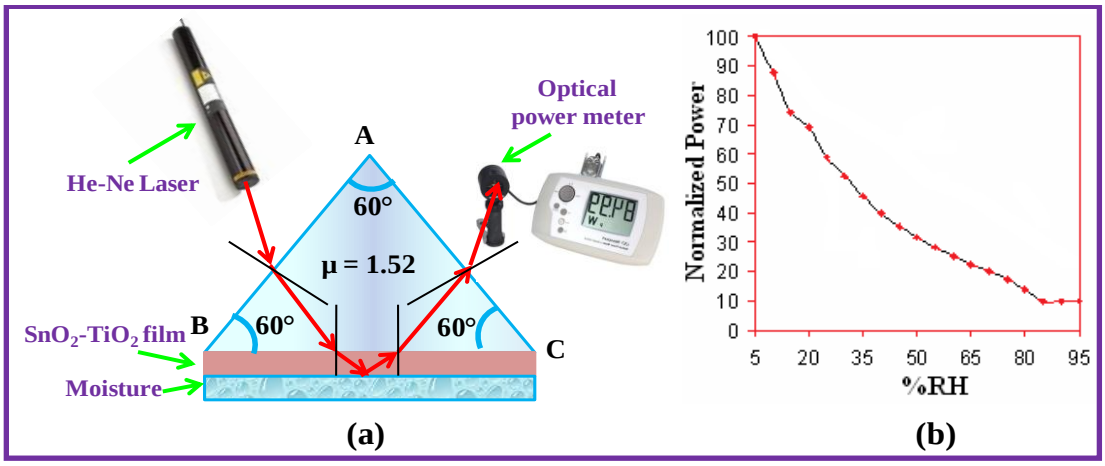

Figure 1.9: (a) Ray diagram of reflection through the film on the base of a prism (b) Variations in the reflected intensity of light I_r against %RH deposited on the base of the prism.

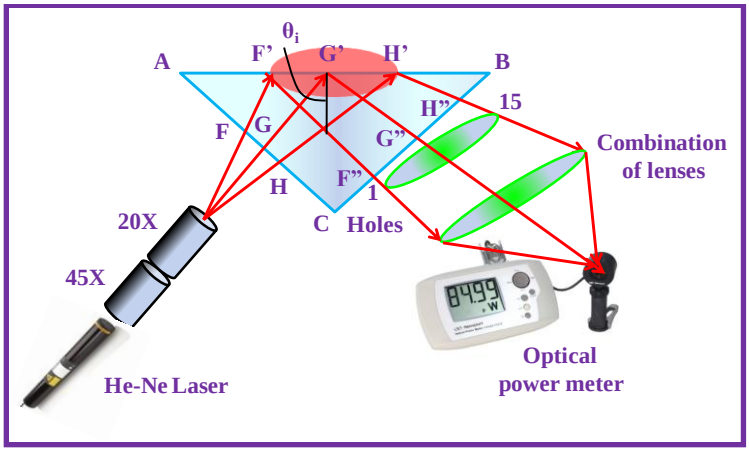

Figure 1.10: Experimental set-up for Prism-based sensor with incident light in the form of a conical beam.

Figure 1.11: Proto type optical humidity sensor. Reprinted with permission from [75].

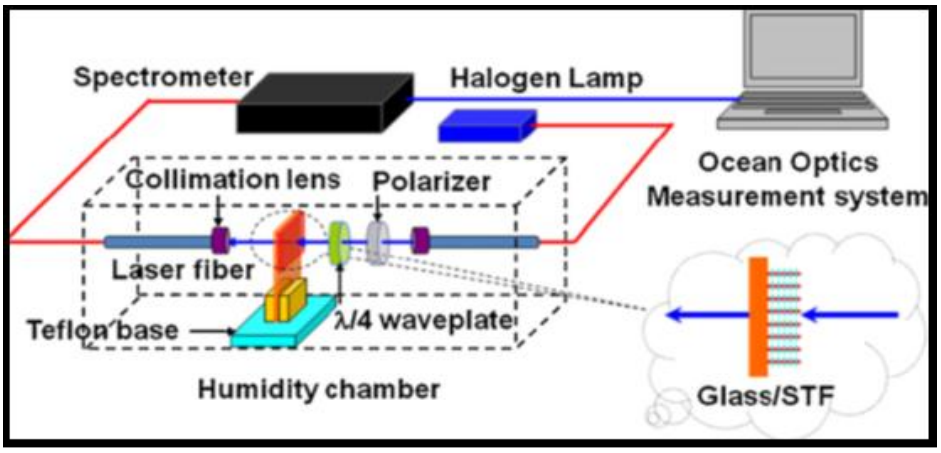

Figure 1.12: Experimental set-up for chiral sculptured thin film based humidity sensor. Reprinted with the permission from [80].

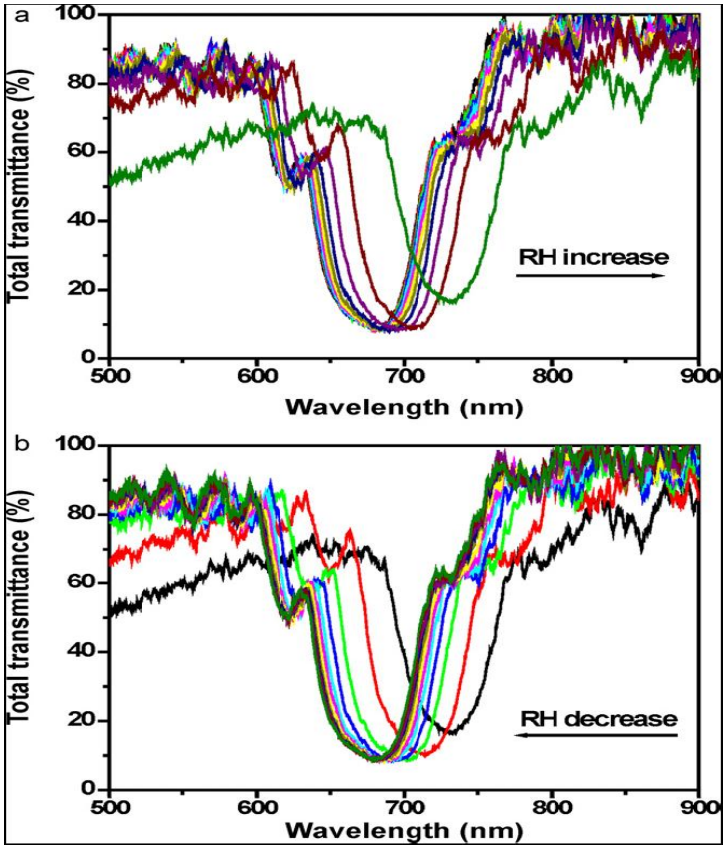

Figure 1.13: Total-transmittance spectra of a CSTF with (a) increasing and (b) decreasing RH.Reprinted with the permission from [80].

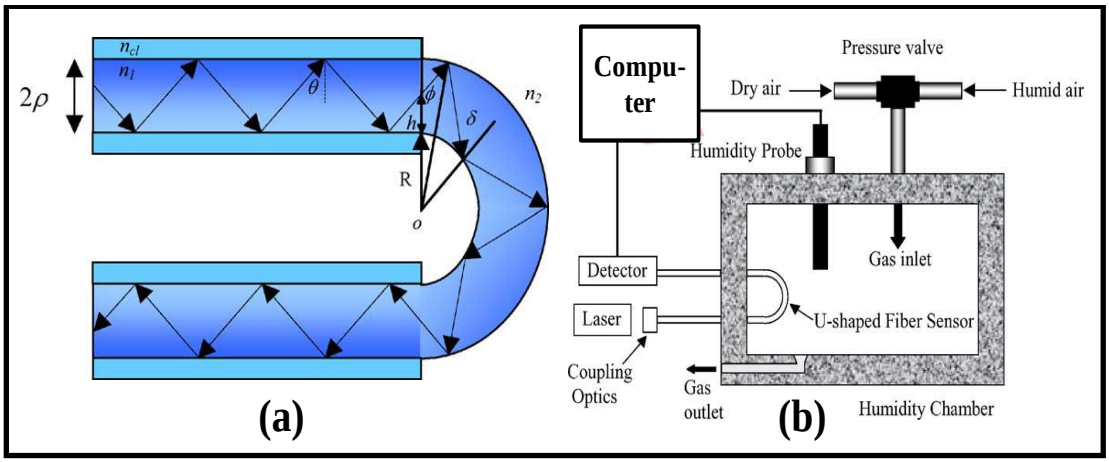

Figure 1.14: (a) Path of the light ray followed in U-shaped optical fiber sensing probe (b) Experimental set-up for the evanescent wave optical fiber relative humidity sensor. Reprinted with the permission from [81].

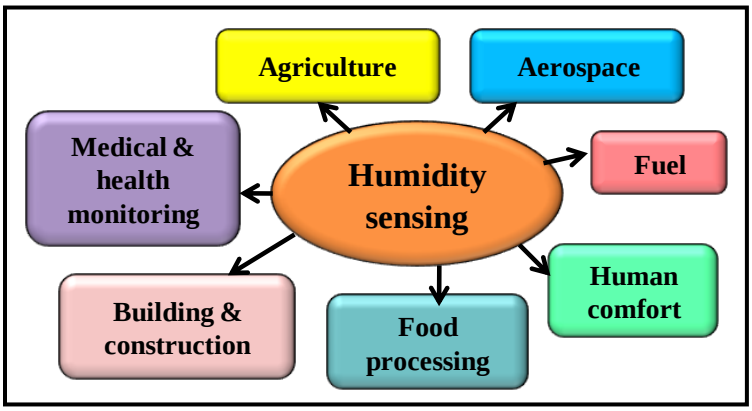

Figure 1.15: Application of humidity sensor in various fields.

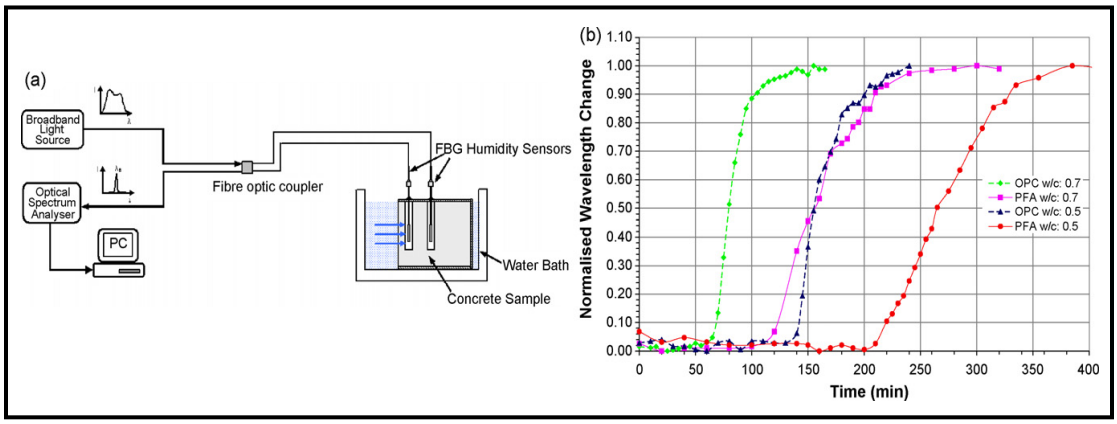

Figure 1.16: (a) Schematic of Moisture ingress rate measurement of various concrete specimens (b) Sensor response. Reprinted with permission from [83].

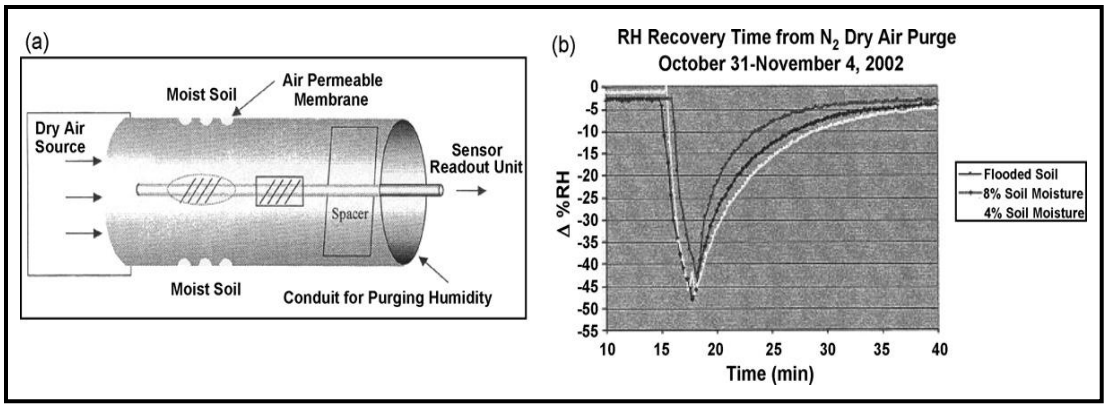

Figure 1.17: (a) Schematic of a soil moisture sensor (b) Data showing evaporation rate of soil samples with various moisture content. Reprinted with the permission from [83].

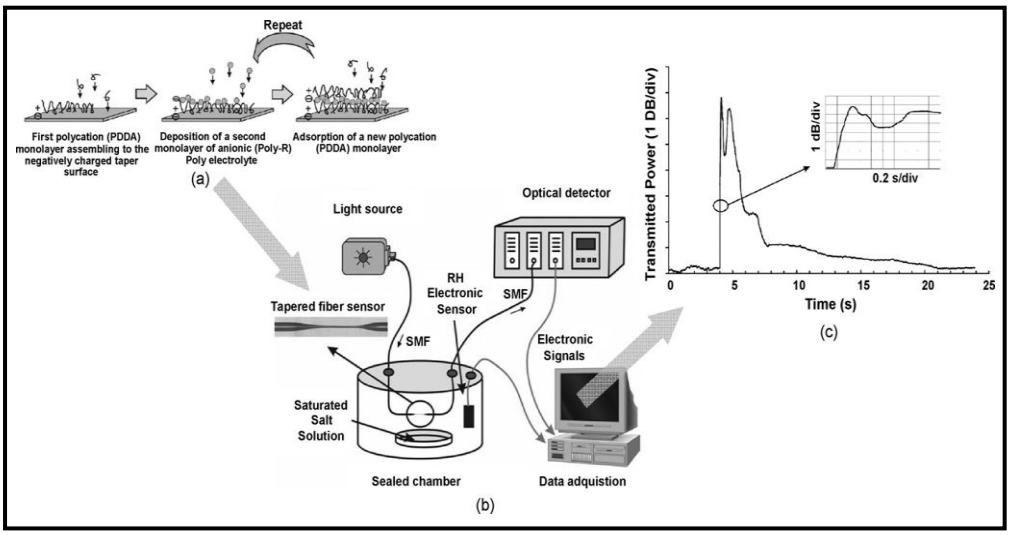

Figure 1.18: Humidity sensing set-up with ISAM overlay, (a) Schematic of the ISAM deposition process, (b) Experimental set-up for sensor characterization (c) Sensor response. Reprinted with the permission from [83].

CHAPTER 2

Fabrication of Nanostructured Y_2O_3-ZrO_2 Multilayered Films and their Optical Humidity Sensing Capabilities based on Transmission

The present chapter reports the study of modulation in light transmitted through the thin films of nanostructured yttria stabilized zirconia (YSZ) with the exposure of moisture at room temperature. For this purpose the precursor of YSZ was prepared and used for the deposition of multilayered thin films on various substrates of borosilicate. The film was then investigated using SEM, XRD and UV-visible absorption techniques. Refractometer investigated the refractive index of the film as 1.448829. SEM showed the macroporous nature of the film and XRD revealed the minimum crystallite size as 5 nm which was further confirmed using TEM and Particle Size Analyzer. Energy band-gaps of one-, two-, three- and four-layered films were estimated as 3.927, 3.919, 3.873 and 3.830 eV respectively by UV-vis spectrophotometer. These films were employed as transmission based opto-electronic humidity sensor. Maximum sensitivity was found as ~ 1.937, 1.642, 1.393 and 1.143 μW/%RH for one layered, two layered, three layered and four layered films. Response and recovery times were found as 28 s and 30 s respectively. Experiments were repeated time to time and found that the sensor gave ~94% reproducible results. Thus the investigated opto-electronic sensor has excellent potential to replace its electrical counterpart.

2.1 Introduction

In recent years, humidity/gas sensing is becoming more important, mainly in control systems for industrial processes and human comfort [1]. An extensive diversity of metal oxides and their nano-composites, ceramics and polymers have been investigated as humidity sensors. These sensors are mainly based on the modulation in electrical signals such as impedance, resistance and capacitance [2-6]. Moreover, another category of the sensors is also available whose principle is based on modulation in optical parameters such as refractive index, intensity modulation, frequency shift and wavelength modulation; these are frequently called optical/opto-electronic sensors [7]. With the growth of industrialization, there is an urgent need of electrical-circuit-free sensor system. Optical sensors have tremendous advantages over their electrical counterpart as they can operate without any interference from nearby electric or magnetic fields and hence, optical humidity sensing is more effective compared to electrical humidity sensing [8].

Different types of metal oxides such as ZnO [9], TiO_2 [10], CuO [11], MoO_3 [12], SnO_2 [13], Fe_2O_3 [14] etc. were considered to be the promising candidate for the investigation because of their inherent chemical and physical stability as gas sensors. Nanostructured zirconia is an important functional material known for its advanced applications such as biomaterial and orthopedic ceramic [15, 16]. Nano zirconia ceramics are of more importance for their high improvement in strength and toughness which play an important role for its excellent mechanical, electrical, thermal, magnetic and optical properties [17, 18]. Pure zirconia has three polymorphic phases (stable at various temperatures): cubic, tetragonal and monoclinic. The zirconia material commonly used by most manufactures is a tetragonal polycrystalline zirconia, partially stabilized with yttrium oxide [19-21] as shown in Fig. 2.1 [22]. Yttria stabilized zirconia is very attractive material for orthopedic application [20]. The addition of yttria to pure zirconia replaces some of the Zr^{4+} ions in the zirconia lattice with Y^{3+} ions. This produces oxygen vacancies, as three O^{2-} ions replace four O^{2-} ions. It also permits yttria stabilized zirconia to conduct O^{2-} ions provided that there is sufficient vacancy site mobility. This ability to conduct O^{2-} ions makes yttria stabilized zirconia well suited to be used in solid oxide fuel cells [23]. It is also used as air-fuel ratio sensors for automotive application. YSZ is a high k-transparent dielectric ceramic which can be used for capacitors in dynamic RAM, as FET for

oxygen sensors and as buffer layer for growing oxide films [24, 25]. Also plasma sprayed and electron beam deposited YSZ coatings are used as thermal barrier coatings for material's low thermal conductivity and exceptional mechanical properties [26, 27]. It can be used for functional as well as structural applications.

In 1999 C.M. Mari and G. Rabotti together studied the behaviour of a pinhole type 8 mol.% yttria stabilized zirconia pellet based sensor for the determination of humidity in the range 3.5-90 RH% in N_2 and in N_2/O gas mixtures at an operating temperature of 500°C [28]. In another work done by M. Su et al. in 2011 Y^{3+} and Mg^{2+}-doped zirconia thick film humidity sensors were investigated in the range of 11–98 %RH at 20°C. The sensor exhibited high sensitivity with low response and recovery time [29]. Currently Zouaoui et al. measured the effect of humidity on the dielectric constant and electrical impedance of porous 8 mol% yttria stabilized zirconia ceramic samples of pore volume fractions in the range 33% to 55% in different relative humidity from 3% to 100%. The sensor showed a strong increase of dielectric constant with water content [30]. Hence we can find that some electrical humidity sensors have been designed using YSZ but upto our knowledge no such optical sensor has been yet designed. Here our motto is to design a cheap and efficient YSZ based opto-electronic humidity sensor for the full %RH range.

Here in the present chapter, the opto-electronic humidity sensing characteristics of YSZ based multilayered films deposited on a plane transparent borosilicate glass substrate were investigated. Humidity sensing is basically a surface phenomenon which depends on the adsorption of water vapor on the surface of the sensing films and its condensation inside the pores [8]. The modulation in the light intensity transmitted out from the sensing film was mainly due to the variation in refractive index and thickness of the film with the variation in %RH.

2.2 Experimental Details

2.2.1 Synthesis

Ethylhexanoic acid (95%), Belgium, ACROS; $Y(NO_3)_3{\cdot}6H_2O$, $ZrO(NO_3)_2{\cdot}6H_2O$ (100%) were used as received. For the synthesis of Y_2O_3 stabilized ZrO_2 the mixture of ethyl hexanoates of Zr(IV) and Y(III) was prepared. Meta hexanoates were synthesized by the extraction method in two-phase system of metal nitrate solution-organic acid by the following reaction given in Eqn. 2.1:

$$(M^{n+})_{aqua} + CH_3(CH_2)_3CH(C_2H_5)COOH \rightarrow M[CH_3(CH_2)_3CH(C_2H_5)COO]_n + nH^+ \quad \ldots. (2.1)$$

(M^{n+} - metal ion, n = 2, 3, 4).

Extraction was carried out in the acidic medium for 0.5 h; pH was controlled by using the NH_4OH solution. Water phase was isolated in a separation funnel. The contents of zirconium and yttrium in the extracts were 100 and 84.6 g/Kg, respectively obtained after elemental analysis of the products on the atomic absorption spectrometer AAS-3. Then metal hexanoates of Y(III) and Zr(IV) were mixed in the ratio of 81:19 (wt.%) and stirred at 105-108ºC followed by vacuum distillation at 150ºC for 10 h. The Y:Zr:O atomic ratio in the product obtained was equal to 7:27.5:65.5 determined by quantitative chemical analysis. Schematic representation of the synthesis of yttria stabilized zirconia is shown in Fig. 2.1.

2.2.2 Fabrication of Sensing Element

Microstructure and uniformity of the deposited film can be controlled by regulating the preparation conditions like solution concentration, fluid density/ viscosity, speed of the spinner and annealing temperature. Therefore, spin coating technique [7] was used to deposit the uniform thin films on borosilicate substrates having dimensions 1.5 × 1.5 cm^2. These substrates were cleaned in an ultrasonic cleaner (WUC-AO2H) by dipping in de-ionized water followed by IPA and then acetone for 10 min each. The cleaned substrates were dried in an electric oven (METREX) at 100°C for 15 min. A thin film of YSZ was deposited on the glass substrate using a photo resist spinner (METREX RC100, India) at a speed of 3000 rpm and dried for 15 min at 60°C on a hot plate (AMBASSADOR, India). Similarly 2, 3 and 4 layered films were deposited on the glass substrates and were then kept for annealing at 400°C for 3 h in a tubular electric furnace (METREX) in the presence of 20% oxygen. Further, these films were used as sensing elements for the study of optical humidity sensing. Schematic representation of the fabrication of yttria stabilized zirconia multi layered films is shown in Fig. 2.3.

2.2.3 Description of Sensing Set-Up

The experimental set-up used for optical humidity sensing is shown in schematic Fig. 2.4. It consists of 2 mW He-Ne LASER (Research Electro Optics Inc. 30989) with 633 nm wavelength as input light source. A diverging lens of ×10

magnification is used as beam expander for splitting the laser light beam so that it may incident and cover the whole surface of the sensing element. A glass chamber with humidity controlled system consisting of a hygrometer (HTC-1) of range of 10-90 %RH along with a dish kept inside was used. Here the dish was used to carry the humidifier/dehumidifier solution. The saturated solution of K_2SO_4/KOH (Fisher Scientific) in distilled water was used as humidifier/dehumidifier. The sensing element was fixed on one wall of the chamber such that it was perpendicular to the incident beam and also the beam covers the maximum surface area of the film. A beam condenser for converging the laser light beam to obtain the maximum intensity at a particular point was used. An optical power meter (Newport 1916-R) for detecting the modulated power of the transmitted beam by the sensing element was used. The detector part was kept perpendicular to beam for obtaining the maximum output power and the whole experimental was performed on the Vibration free table (M-RS2000-48-8). The whole experiment was performed at room temperature of 300K.

2.2.4 Characterization Techniques Used

The material was investigated through a digital refractometer (Anton Paar Abbemat 550) at room temperature with an accuracy of 0.000001. This refractometer allows fast and non-destructive refractive index measurements and is calibrated with official standards. The formation and the phase of the one layered sensing film were investigated with X-ray diffractometer X'Pert Pro recording system (PANalytical, Netherlands) using Cu K_α (λ = 1.5406Å) radiation. The instrument was operated using power: 45 kV, 40 mA and scanning parameters: from 20° to 80°; typical 2θ step size: 0.008°. TEM analysis of the material was carried out using FEI-G2 SPRIT, Netherland. YSZ was loaded over carbon coated copper grid at scale of 50 nm. The particle size of YSZ dissolved in distilled water was analyzed by Particle Size Analyzer (Nano-ZS90). The SEM analysis of one layered YSZ film has been carried out at various scales and resolutions using Scanning electron microscope (JEOL, JSEM-6490LV). UV–vis absorption spectra of each film were recorded in the wavelength range 190–1100 nm using UV–vis Spectrophotometer (Evolution 201).

2.3 Results and Discussion

2.3.1 Refractometer Analysis

The digital refractometer investigated the refractive index of the material as 1.448829 with an accuracy of 0.000001 at room temperature 300 K.

2.3.2 X-ray Diffraction Analysis

The diffraction pattern shows good agreement with the diffraction data from JCPDS 01-077-0743 and 00-032-1500. The XRD pattern shown in Fig.2.5 reveals the formation of Y_2O_3 stabilized ZrO_2. The asterisk (*) peaks denote the zirconia crystals whereas hatch (#) peaks represent yttria crystals whereas dots (.) show the YSZ structure. The minimum crystallite size of the material was estimated as 5 nm using Debye Scherrer Formula from (111) peak which is the least value of crystallite size reported in open literature. The average crystallite size was estimated as 28 nm. As crystallite size decreases, the specific surface to volume ratio increases, that is the active centres for the adsorption of water molecules increases. Also the data shows that yittria is occupied as guest in zirconia lattice forming a rhombohedral shape.

2.3.3 Transmission Electron Microscopy Analysis

Fig.2.6 (a) shows the transmission electron microscopy (TEM) image of YSZ at 50 nm scale. It reveals the crystalline structure with uniform distribution of clusters of oval shape made of yttrium and zirconium oxides and shows homogeneous porous composite structure. The minimum observed size of the crystal in the clusters is 5 nm which confirms the result obtained by XRD analysis.

2.3.4 Particle Size Analysis

The particle size of YSZ dissolved in distilled water was analyzed by Particle Size Analyser and the corresponding data is plotted in Fig. 2.6(b). It is a dynamic light scattering system for nano particle and molecular size measurement. From the particle size distribution curve, the minimum size of the particles is ~2 nm which is quite comparable to the results obtained from XRD and TEM. Around 59% of the total particles are of 2 nm.

2.3.5 Scanning Electron Microscopy Analysis

The scanning electron microscopy (SEM) analysis of one layered YSZ film has been carried out at various scales and resolutions are shown in Fig. 2.7(a–e).

Surface morphology of YSZ thin films exhibits the porous structure with few cracks which is quite favorable for the adsorption process. These pores/active centres serve as humidity adsorption sites and the sensitivity of the sensor depends on the size of these pores. Accordingly, macroporous YSZ [31] with a higher surface area provides more surface adsorption sites, which is advantageous to the sensors operating at room temperature. The sensing property is based on the moisture adsorption/desorption at the surface of the material, which causes a change in the output power due to the change in refractive index of the material. The surfaces of such morphologies have many dangling bonds on account of which the sensing surface is optically very reactive. Owing to this reactivity, the sensing surface easily adsorbs the moisture that comes into the contact.

2.3.6 UV-visible Absorption Analysis

The optical absorbance spectra of one, two, three and four layered YSZ thin films with their corresponding Tauc plot is shown in Fig.2.8 (a–d) respectively. It is observed from the figure that one, two, three and four layered YSZ thin films exhibit absorption in the ultra-voilet range (370 nm). The variation of optical absorption coefficient (α) with photon energy hν was obtained using the absorption data of different films and is given in inset of Fig. 2.8(a–d). The optical energy band-gap E_g of the films can be estimated from the following relation given in Eqn. 2.2:

$$\alpha h\nu = A(h\nu - E_g)^n \qquad \ldots\ldots (2.2)$$

where A is a constant, ν is the transition frequency and the exponent 'n' characterizes the nature of band transition (n = 1/2 and 3/2 corresponds to direct allowed and direct forbidden transitions while n = 2 and 3 corresponds to indirect allowed and indirect forbidden transitions, respectively). Here the transition is direct allowed type, therefore n = 1/2 is taken in the above formula. The optical band-gap E_g was observed by extrapolating the straight line portion of $(\alpha h\nu)^2$ vs. hν curves to $\alpha = 0$. The values of band-gaps for the representative films are shown by the respective curves of Fig.2.8 (a–d). The estimated band-gap of the multilayered YSZ thin films was found to be 3.927, 3.919, 3.873 and 3.830 eV for one, two, three and four layered films respectively. With increase in the thickness of the film, absorption decreases which leads to decrease in the band-gap [32]. The results obtained are found very close to the reported values by various methods [33].

2.3.7 Humidity Sensing

The humidity sensing characteristics at room ambient of one, two, three and four layered films of YSZ annealed at 400°C have been plotted in Fig. 2.9 (a-d) showing the linear decrement in transmitted intensity with corresponding increase in %RH. Also the corresponding readings are depicted in Table 2.1.

Curves show decrease in intensity in lower and higher region of %RH i.e. 10-90 %RH; however in higher region decrease becomes slower. All the curves show nearly linear variation in the transmitted intensity through the entire region i.e. 10-90 %RH. As the number of layers increases the transmitted output intensity shifts downwards at 10 %RH showing the absorption of light due to increase in thickness of the sensing films. Sensitivity is the most important parameter of the sensor. In general, it is the ratio of the change in output signal to that of input signal. Here, it is defined as given by Eqn. 2.3:

$$\text{Sensitivity} = \frac{\Delta I_t}{\Delta \%RH}\ \mu W/\%RH \qquad \ldots\ldots (2.3)$$

where ΔI_t is the change in transmitted intensity of light and Δ%RH is the corresponding change in %RH. Average sensitivity is calculated by taking the average of all measured sensitivities ranging from 10 to 90 %RH. Single layered film was found most sensitive among the other multilayered films and the sensitivity goes on decreasing with increase in thickness of the sensing films. Average sensitivities of sensing elements made of one, two, three and four layered films are found as ~ 1.937, 1.642, 1.393 and 1.143 μW/%RH respectively and are shown graphically in Fig. 2.10. It may be noted here that thinner the YSZ film, the more encouraging sensitivity it posses due to rapid adsorption and desorption rate. The material YSZ being translucent and having high refractive index 1.448829 [34], has very less transmittance. The transmitted light from the film was collected on a photo detector through a lens combination. It was observed that as the humidity inside the chamber increases, the transmitted light at the output decreases. This characteristic is responsible for its potential as a humidity sensor.

The modulation in the transmitted intensity w.r.t. variation of %RH can be explained on the basis of adsorption and desorption mechanism of water molecule in the capillaries formed on the surface of metal oxide film. The sensing mechanism, devoted to the surface morphology is based on the adsorption of water vapour and capillary condensation. Initially the nanocomposite film was free from water

molecules, having only dry air in its pores. When exposed to low humidity environment as shown in Fig. 2.11 (a), adsorption of water vapour takes place rapidly on the surface of film. Due to high cationic charge density of metal oxide surface, the electrostatic force is high enough to break one of the O–H bonds of H_2O and form a strong chemical bond between M^+ (metal ion) and OH^-. Thus, initial layer is chemisorbed. As the %RH increases, adsorption on surface of the film increases. However, in 40–70 %RH range, adsorption takes place on the surface as well as on the walls of capillaries. This is the mid-humidity region and is shown in Fig. 2.11 (b). In higher humid region i.e. from 70-90 %RH, the condensation of water vapour takes place through the capillaries and forms a meniscus in the capillaries of the film. In this region maximum bending of light may occur as shown in Fig. 2.11 (c) and transmitted power is highly reduced.

With the exposure of humidity, output power decreases due to the following reasons:

- In high humidity region, the water molecule starts condensing inside the pores; therefore, a large amount of light intensity is absorbed by them resulting in a decrease in the output power.
- Also with increasing humidity, the charge carriers in the form of hydronium ion (H_3O^+) also increase. This increase in charge concentration leads to decrease in refractive index of the sensing element which further results in bending of light. This is why continuous decrease in output power is observed with increase in humidity [35].

Reproducibility is one of the most important factors for a sensor. It is the distribution of output when measurements are taken under same environmental conditions as before. The reproducibility of the one layered film is shown in Fig. 2.12(a) and it was found that the sensing element was 93.63% reproducible. The sensitivity observed in this case was 1.8142 μW/%RH. The standard deviation of the output power as obtained from the principle experiment is plotted in Fig. 2.12(b).

Ageing effect is also an important sensor parameter. It is the distribution of sensor outputs when performing consecutive readings under similar conditions after a long time. Here the consecutive measurements were taken after one week, three weeks, one month and three months. Therefore, the aging effect was observed after one week, three weeks, one month and three months, the results of which are plotted

and shown as square, circle, triangle, and star-shaped in Fig. 2.12(c). Here it can be concluded that YSZ is quite stable material having very less effect of aging and the sensor is quite stable. The corresponding data of the reproducibility and ageing effect have been presented in Table 2.2.

The time required to reach 10% of the final sensor output after stepwise ramping the humidity is called the response time of the sensor whereas recovery time is the time taken by the sensor signal to return to its initial value after a step concentration change from a certain value to zero. The response and recovery time calculated here for one-layered sensing film were 28 s and 30 s respectively as shown in Fig. 2.12(d). The corresponding readings are given in Table 2.3. All the sensor parameters calculated here for one-layered sensing element have been presented in Table 2.4.

2.4 Conclusion

We have successfully synthesized YSZ using sol gel extraction route and fabricated an opto-electronic humidity sensor which is based on the modulation in output power of light transmitted through the sensing element. Single and multilayered sensing films were fabricated using spin coating technique. XRD of the film shows the crystallinity, phase formation and minimum crystallite size as 5 nm. A study of the optical energy band gaps of the sensing films demonstrate that as the number of layers or film thickness increase, their optical energy band gaps are found to be decreased. These results show that particle size increases with film thickness and hence absorption or band-gap decreases. Also the sensitivity of the sensor decreases which is confirmed by the experimental results. Single layered sensing element of YSZ was found most sensitive among the multilayered sensing elements annealed at 400°C. The maximum average sensitivity of opto-electronic humidity sensor for one layered YSZ film was found 1.937 μW/%RH.

References

[1] S. Sikarwar, B.C. Yadav, Opto-electronic humidity sensor: a review, Sens. Actuators A: Phy. 233 (2015) 54-70.

[2] B.C. Yadav, S. Singh, A. Yadav, Nanonails structured ferric oxide thick film as room temperature liquefied petroleum gas (LPG) sensor, App. Surf. Sci. 257 (2011) 1960-1966.

[3] B.C. Yadav, A.K. Yadav, A. Kumar, Effect of nanostructured zinc oxide additives on the humidity and temperature sensing properties of cuprous oxide, Int. J. Green Nanotechnology 4 (2012) 345-353.

[4] K.K. Dey, D. Bhatnagar, A.K. Srivastava, M. Wan, S. Singh, R.R. Yadav, B.C. Yadav, M. Deepa, VO_2 nanorods for efficient performance in thermal fluids and sensors, Nanoscale 7 (2015) 6159-6172.

[5] R.K. Sonker, S.R. Sabhajeet, S. Singh, B.C. Yadav, Synthesis of ZnO nanopetals and its application as NO_2 gas sensor, Mat. Lett. 152 (2015) 189-191.

[6] B.C. Yadav, R.K. Shukla, An Opto-Electronic Sensor to monitor Glucose concentration in water, J. of Optics, 32 (2003) 13-17.

[7] B.C. Yadav, R.C. Yadav, P.K. Dwivedi, Sol-gel processed (Mg-Zn-Ti) oxide nanocomposite film deposited on prism base as an opto-electronic humidity sensor, Sens. Actuators B: Chem. 148 (2010) 413-419.

[8] B.C. Yadav, R.C. Yadav, S. Singh, P.K. Dwivedi, H. Ryu, S. Kang, Nanostructured cobalt oxide and cobalt titanate thin films as optical humidity sensor: a new approach, Optics Laser Tech. 49 (2013) 68-74.

[9] Y.K. Mishra, G. Modi, V. Cretu, V. Postica, O. Lupan, T. Reimer, I. Paulowicz, V. Hrkac, W. Benecke, L. Kienle, R. Adelung, Direct growth of freestanding ZnO tetrapod networks for mutifunctionl applications in photocatalysis, UV Photodetection, and gas sensing, ACS Appl. Mater. Interfaces 7 (2015) 14303-14316.

[10] M. Enachi, O. Lupan, T. Braniste, A. Sarua, L. Chow, Y.K. Mishra, D. Gedamu, R. Adelung, I. Tiginyanu, Integration of individual TiO_2 nanotube on the chip: Nanodevice for hydrogen sensing, Phys. Status Solidi RRL 9(3) (2015) 171-174.

[11] O. Lupan, V. Cretu, V. Postica, N. Ababii, O. Polonskyi, V. Kaidas, F. Schutt, Y.K. Mishra, E. Monaico, I. Tiginyanu, V. Sontea, T. Strunskus, F. Faupel, R. Adelung, Enhanced ethanol vapour sensing performances of copper oxide nanocrystals with mixed phases, Sens. Actuators B: 224 (2016) 434-448.

[12] O. Lupan, V. Cretu, M. Deng, D. Gedamu, I. Paulowicz, S. Kaps, Y.K. Mishra, O. Polonskyi, C. Zamponi, L. Kienle, V. Trofim, I. Tiginyanu, R. Adelung, Versatile growth of freestanding orthorhombic α-Molybdenum Trioxide nano- and microstructures by rapid thermal processing for gas nanosensors, J. Phys. Chem. C 118 (2014) 15068-15078.

[13] R.K. Sonker, B.C. Yadav, Chemical route deposited SnO_2-Pt-SnO_2-Pd thin films for LPG detection, Adv. Sci. Lett. 20 (2014) 1374-1377.

[14] R. Srivastava, S. Singh, B.C. Yadav, Humidity sensor based on nanostructured ferric oxide thick film, Int. J. of Green Nanotechnology 4(3) (2012) 215-218.

[15] D.W. Stolberg, W.B. Carter, J.M. Hampikian, Nanohardness and fracture toughness of combustion chemical vapor deposition deposited yttria stabilized zirconia-alumina films, Thin Solid Films 483 (2005) 211-217.

[16] A.M. Limarga, S. Shian, M. Baram, D.R. Clarke, Effect of high-temperature aging on the thermal conductivity of nanocrystalline tetragonal yttria-stabilized zirconia, Acta Materialia 60 (2012) 5417- 5424

[17] J.S. Kim, D.H. Lee, S. Kang, D.S. Bae, H.Y. Park, M.K. Na, Synthesis and microstructure of zirconia nanopowders by glycothermal processing, Trans. Nonferrous Met. Soc. China 19 (2009) 88-91.

[18] V. Thakare, Progress in synthesis and applications of zirconia, Int. J. Eng. Res. Dev. 5 (2012) 25-28.

[19] L.J. Tomar, B.S. Chakrabarty, Synthesis, structural and optical properties of TiO_2-ZrO_2 nanocomposite by hydrothermal method, Adv. Mat. Lett. 4 (2013) 64-67.

[20] I.O. Usov, S. Rubanov, J. Won, A.A. Suvorova, Transformation of YSZ under high fluence argon ion implantation, Nuclear Ins. Met. in Phys. Res. B 326 (2014) 283-288.

[21] K.M. Jasim, Characterization of laser sealed coatings of yttria partially stabilized zirconia, Optics Lasers in Eng. 49 (2011) 785-792.

[22] https://en.wikipedia.org/wiki/Yttria-stabilized_zirconia

[23] S. Saridag, O. Tak, G. Alniacik, Basic properties and types of zirconia: An overview, World J. of Stomatology 2 (2013) 40-47.

[24] M.B. Ponnuchamy, A.S. Gandhi, Lattice expansion and contraction in nanocrystalline yttria-stabilized zirconia powders, Scri. Mat. 83 (2014) 21-24.

[25] V. Vonk, N. Khorshidi, A. Stierle, H. Dosch, Atomic structure and composition of the yttria-stabilized zirconia (111) surface, Surf. Sci. 612 (2013) 69-76.

[26] R. Pascu, S. Somacescu, G. Epurescu, M. Filipescu, C. Luculescu, D. Colceag, P. Osiceanu, Pulsed laser deposition of yttria stabilized zirconia based hetero structure, Thin Solid Films 553 (2014) 98-103.

[27] C.H. Lei, G.V. Tendeloo, M. Siegert, J. Schubert, C. Buchal, Structural investigation of the epitaxial yttria-stabilized zirconia films deposited on (001) silicon by laser ablation, J. Crys. Growth 222 (2001) 558-564.

[28] C.M. Mari, G. Rabotti, Humidity determination by solid state limiting current sensor, Solid State Ionics 124 (1999) 309–315.

[29] M. Su, J. Wang, Y. Hao, Development of Y^{3+} and Mg^{2+}-doped zirconia thick film humidity sensors, Mater. Chem. Phy. 126 (2011) 31–35.

[30] M.J. Zouaouia, B.N. Alia, N. Glandutb, D.S. Smitha, Effect of humidity on the dielectric constant and electrical impedance of mesoporous zirconia ceramics, J. European Ceramic Society 36(1) (2016) 163–169.

[31] J. Rouquerol, D. Avnir, C.W. Fairbridge, D.H. Everett, J.M. Haynes, N. Pernicone, J.D.F. Ramsay, K.S.W. Sing, K.K. Unger, Recommendations for the characterization of porous solids, Pure Appd. Chem. 66(8) (1994).

[32] C. Das, J. Begum, T. Begum, S. Choudhury, Effect of thickness on the optical properties of GaAs thin films, J. Bangladesh Acad. Sci. 37 (2013) 83-91.

[33] S. Heiroth, R. Ghisleni, T. Lippert, J. Michler, A. Wokaun, Optical and mechanical properties of amorphous and crystalline yttria-stabilized zirconia thin films prepared by pulsed laser deposition, Acta Materialia 59 (2011) 2330-2340.

[34] S.R. Casolco, J. Xu, J.E. Garay, Transparent /translucent polycrystalline nanostructured yttria stabilized zirconia with varying colors, Scripta Materialia 58(6) (2008) 516–519.

[35] F. Xu, L. Zhang, X. Yin, L. Tong, Polymer Single-Nanowire Optical Sensors, Nano Letters 8 (2008) 2757-2761.

Tables

Table 2.1: Variations in the output power obtained for both the adsorption and desorption phenomenon corresponding to one-, two-, three- and four-layered films of nanostructured YSZ with %RH for opto-electronic mode of humidity sensing.

%RH	Output power (μW)							
	One layered film		Two layered film		Three layered film		Four layered film	
	Increasing mode	Decreasing mode	Increasing mode	Decreasing mode	Increasing mode	Decreasing mode	Increasing mode	Decreasing mode
10	245.5	243.5	222.8	217.1	209.9	204.2	175.6	169.9
15	225.1	230.5	208.5	205.6	198.5	195.6	167.1	161.4
20	205.3	215.1	197.1	194.2	187.1	187.1	158.5	155.6
25	190.1	201.3	185.6	182.8	175.6	178.5	149.9	149.9
30	175.2	186.3	177.1	171.4	167.1	169.9	141.4	144.2
35	160.6	174.2	168.5	162.8	158.5	161.4	132.8	138.5
40	150.4	162.4	159.9	154.2	149.9	155.6	127.1	132.8
45	140.2	150.6	151.4	145.6	144.2	149.9	121.4	127.1
50	130.3	140.2	142.8	137.1	138.5	144.2	115.7	121.4
55	122.4	133.1	134.2	128.5	132.8	138.5	109.9	115.7
60	116.2	125.3	125.7	119.9	127.1	132.8	104.2	109.9
65	110.6	118.2	117.1	114.2	121.4	127.1	98.5	104.3
70	105.2	110.4	111.4	108.8	115.7	121.4	95.7	98.5
75	100.3	105.1	105.7	105.1	109.9	115.7	92.8	95.7
80	95.1	100.3	99.9	102.4	104.2	109.9	89.9	92.8
85	92.3	95.1	94.2	99.9	101.4	107.1	87.1	89.9
90	90.1	92.2	91.4	97.1	98.5	104.2	84.2	89.9

Table 2.2: Variations in the output power obtained for both the adsorption and desorption phenomenon corresponding to one-layered film of nanostructured YSZ with %RH for observing reproducibility and ageing effect.

%RH	Output power (μW)					
	Reproducibility		Ageing effect			
	Increasing mode	Decreasing mode	One week	Three weeks	One month	Three months
10	244.6	240.9	243.9	242.7	240.9	235.8
15	234.2	230.6	233.2	230.4	228.1	227.5
20	217.1	214.2	223.8	221.5	220.9	216.1
25	205.6	202.8	211.8	214.7	212.1	208.1
30	188.5	194.2	203.8	204.9	203.8	200.9
35	179.9	185.6	195.8	198.1	194.1	190.1
40	171.4	177.1	188.4	188.4	186.7	182.7
45	162.8	168.5	178.9	178.9	176.1	173.2
50	154.2	159.9	172.4	172.4	169.5	166.7
55	145.6	151.4	162.7	163.5	162.7	159.8
60	137.1	145.6	152.9	152.9	155.8	152.9
65	128.5	139.9	144.5	147.4	150.4	147.8
70	123.8	131.2	136.9	140.8	142.7	139.7
75	116.1	122.5	128.4	133.2	134.9	131.5
80	111.2	115.8	120.7	125.5	126.7	123.8
85	105.4	109.1	114.2	119.5	120.5	117.7
90	99.5	104.2	109.8	114.1	115.5	112.7

Table 2.3: Variations in the output power obtained for both the adsorption and desorption phenomenon corresponding to one-layered film of nanostructured YSZ with time for observing response and recovery times.

Time (s)	Increasing mode (μW)	Decreasing mode (μW)
0	245.5	92.2
50	200.2	105.1
100	180.3	115.2
200	170.4	118.1
290	160.2	121.3
390	148.4	123.4
500	140.1	126.5
630	135.5	128.6
800	130.2	130.4

Table 2.4: Sensors parameters of the one-layered nanostructured YSZ film as opto-electronic humidity sensor

Sensor parameters	Sensitivity	Reproducibility	Ageing effect	Response time	Recovery time
Values	1.937 μW/%RH	93.63%	Very less	28 s	30 s

Figures

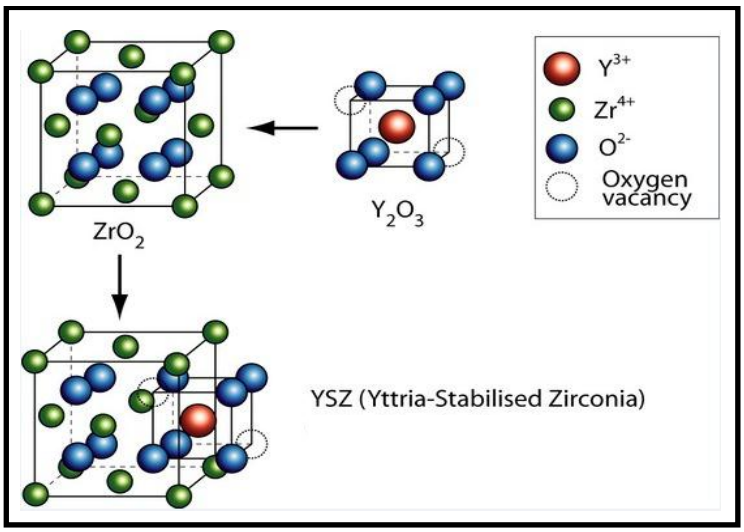

Figure 2.1: Crystalline lattice structure of yttria stabilized zirconia (YSZ) [22].

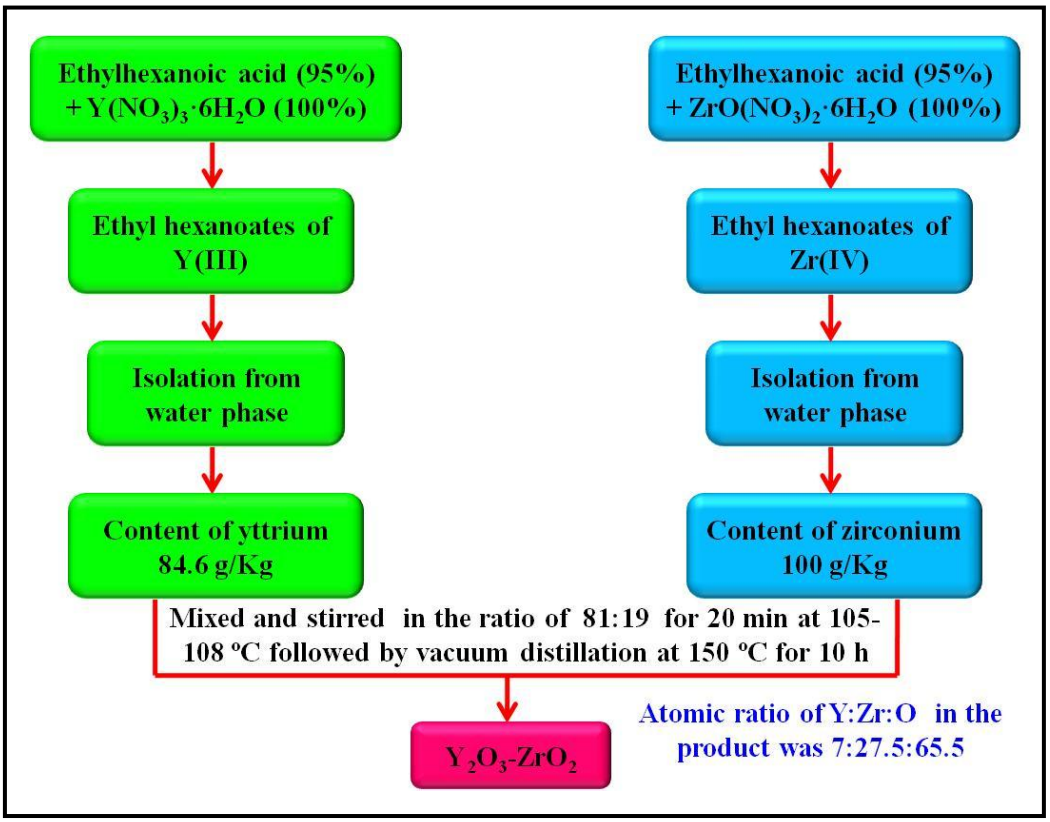

Figure 2.2: Schematic representation of the preparation of yttria stabilized zirconia.

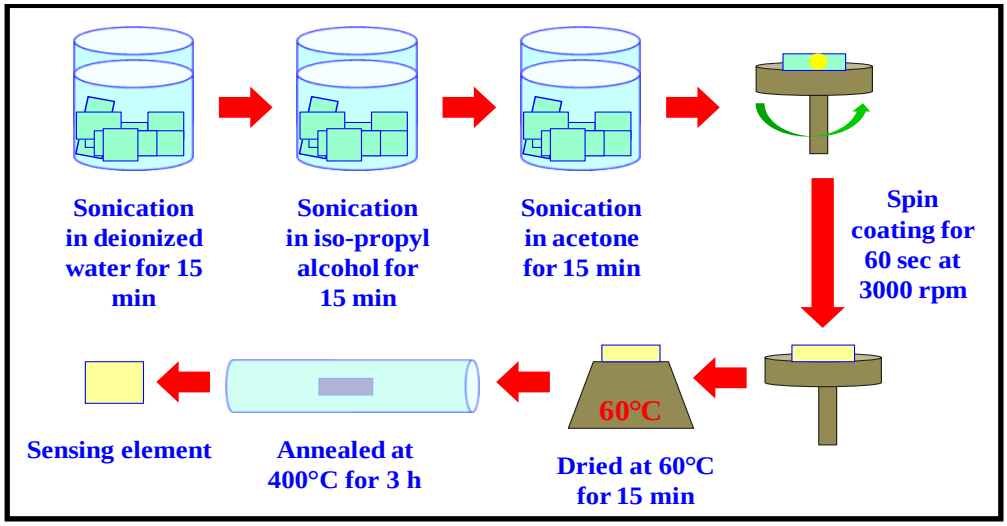

Figure 2.3: Schematic representation of the fabrication of sensing element.

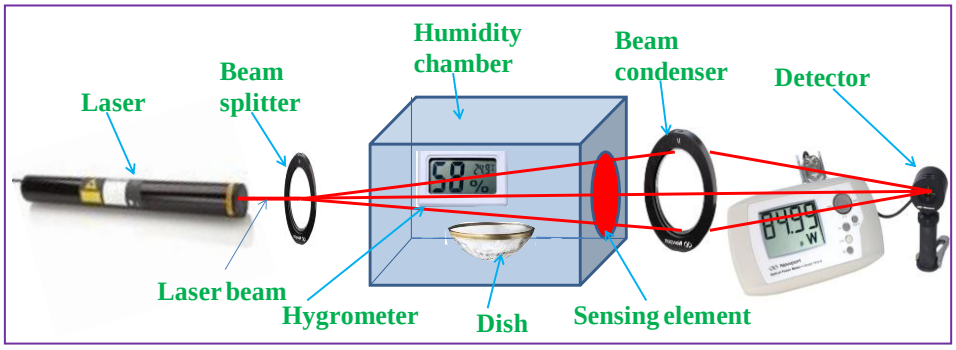

Figure 2.4: Schematic of experimental set-up for transmission based optical humidity measurements.

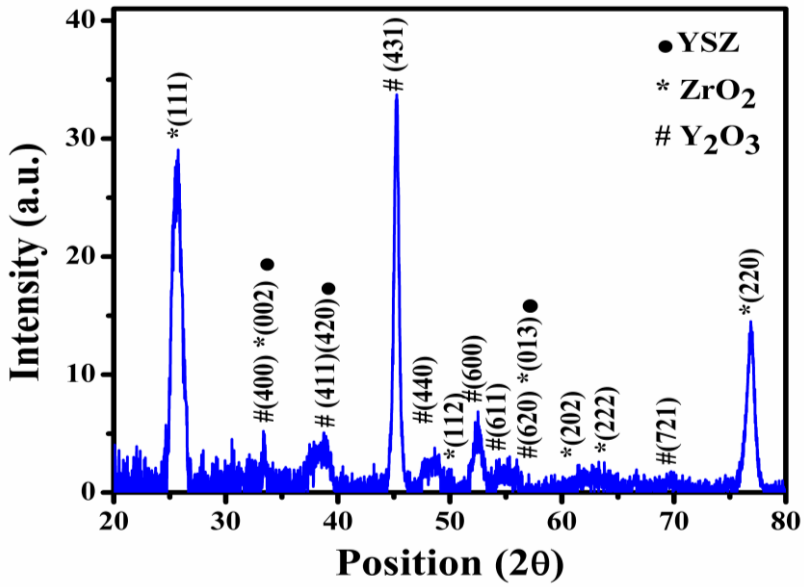

Figure 2.5: XRD pattern of YSZ single layered film annealed at 400°C showing the crystalline nature of the material. Here the minimum crystallite size observed is 5 nm whereas the average crystallite size is 28 nm.

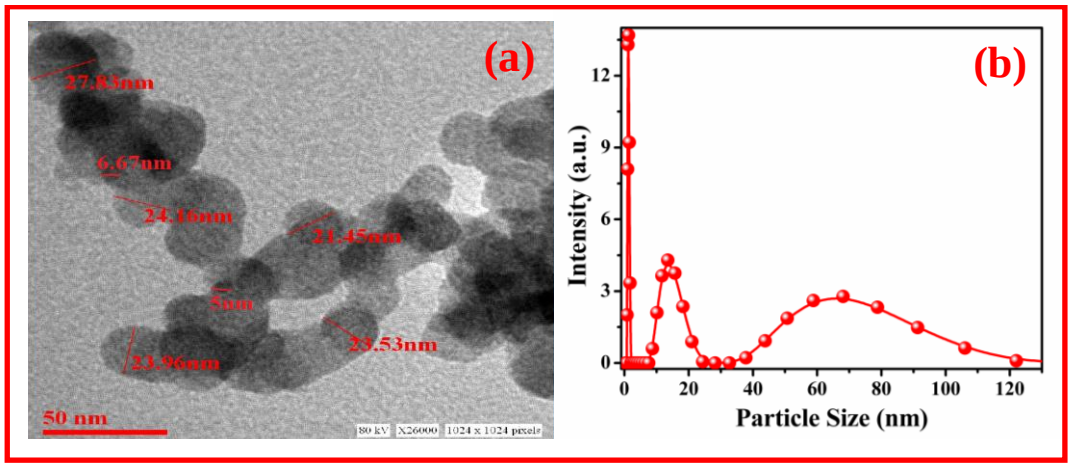

Figure 2.6: (a) TEM image of YSZ at 50 nm scale confirming the result of XRD (b) Particle size distribution by Nano-ZS90 showing about 50% of the particles is of 2 nm.

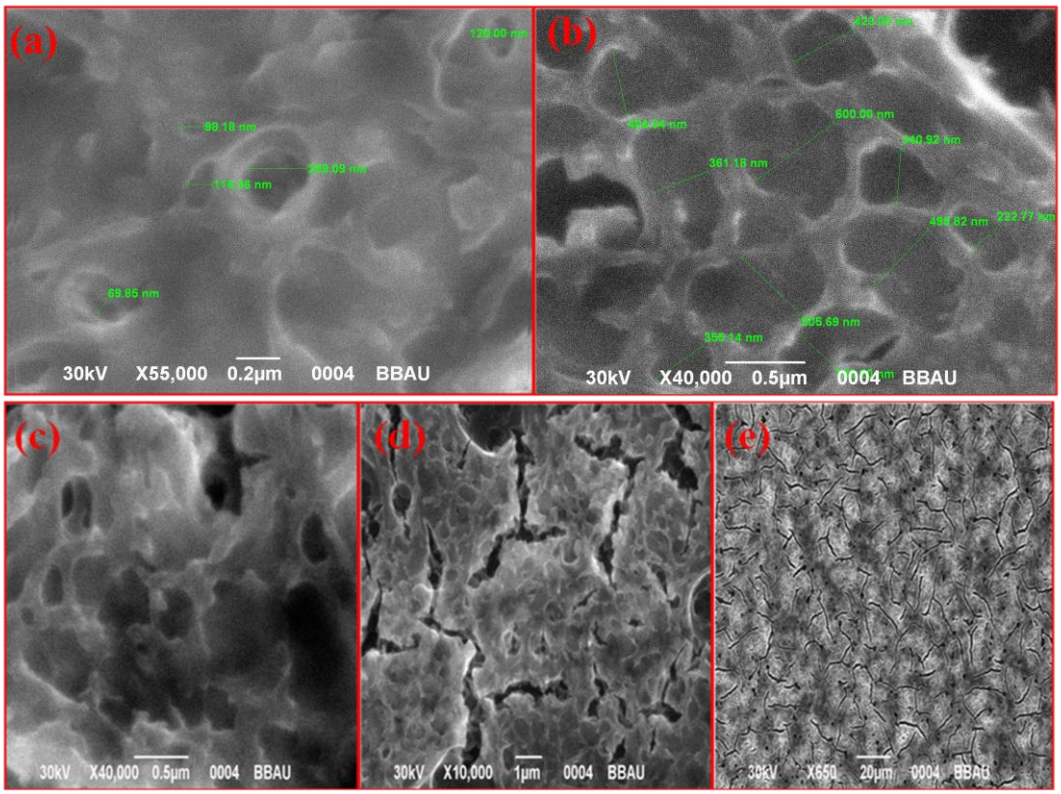

Figure 2.7: SEM micrographs of YSZ one layered film at various scales and resolution showing the macroporous nature of the film.

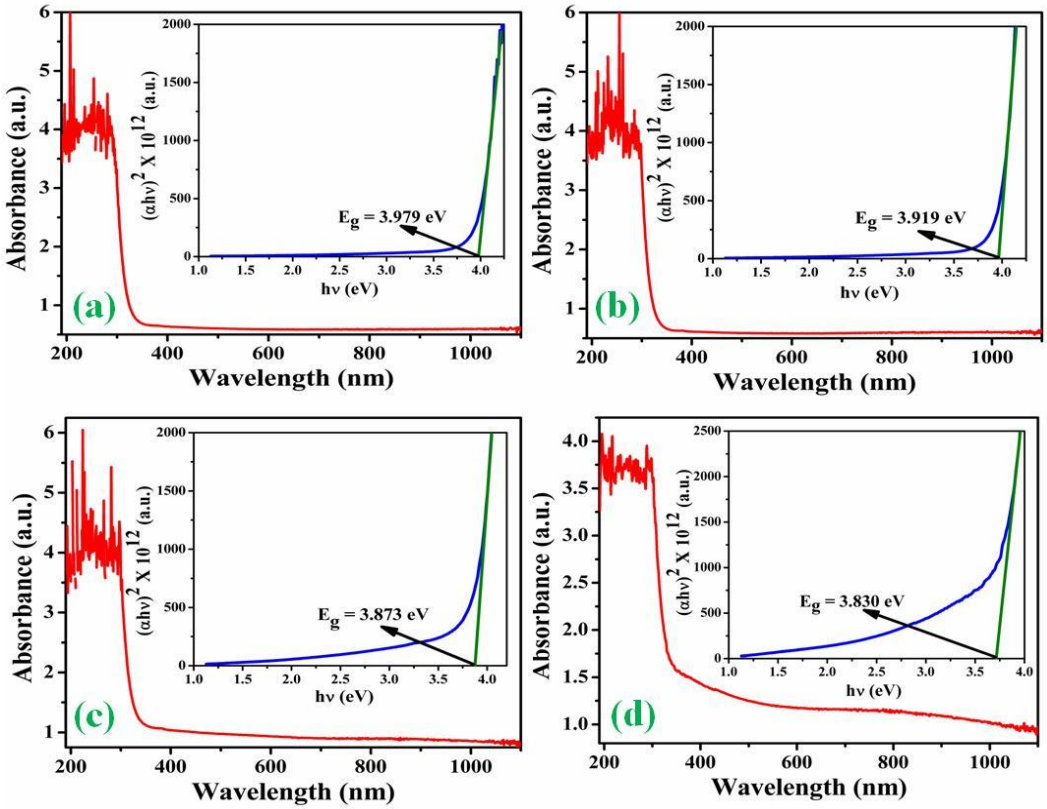

Figure 2.8: Absorption spectra of the YSZ for (a) one, (b) two, (c) three and (d) four layered thin films and inset display the Tauc plot of the respective layered film for band-gap calculation showing the widest band-gap for one-layered film.

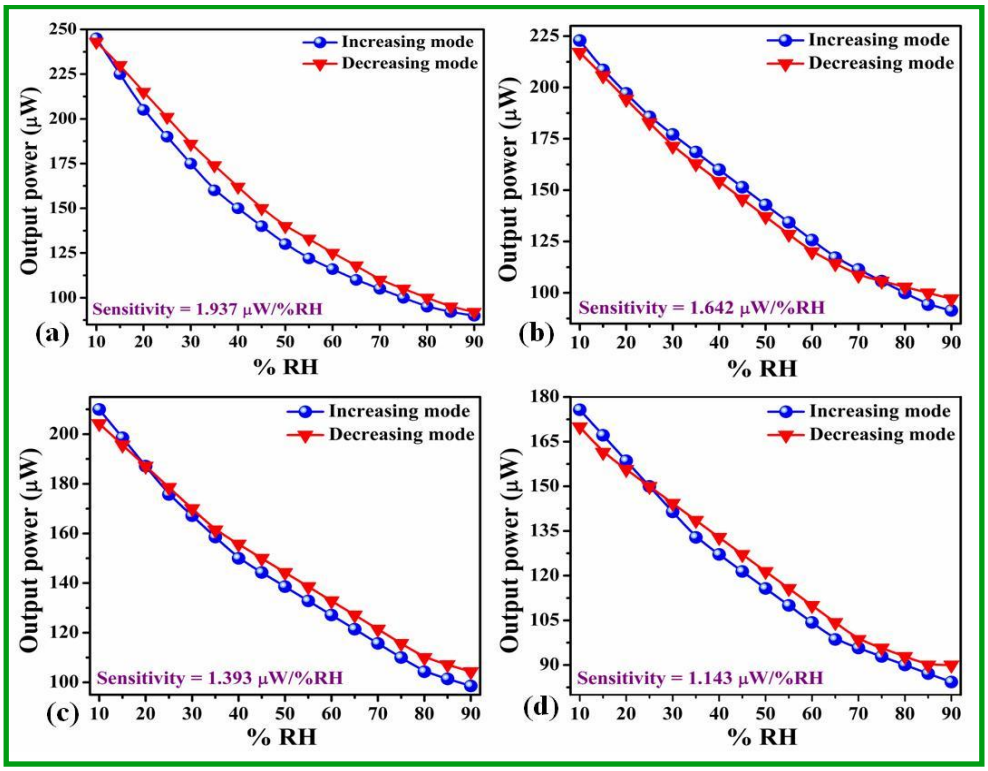

Figure 2.9: Variation of output power with %RH for (a) one layered film, (b) two layered, (c) three layered and (d) four layered film.

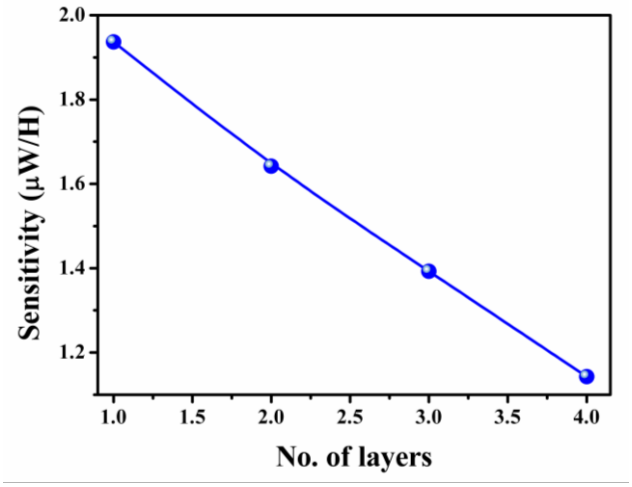

Figure 2.10: Graph showing decrease in sensitivity with increase in layers of the film

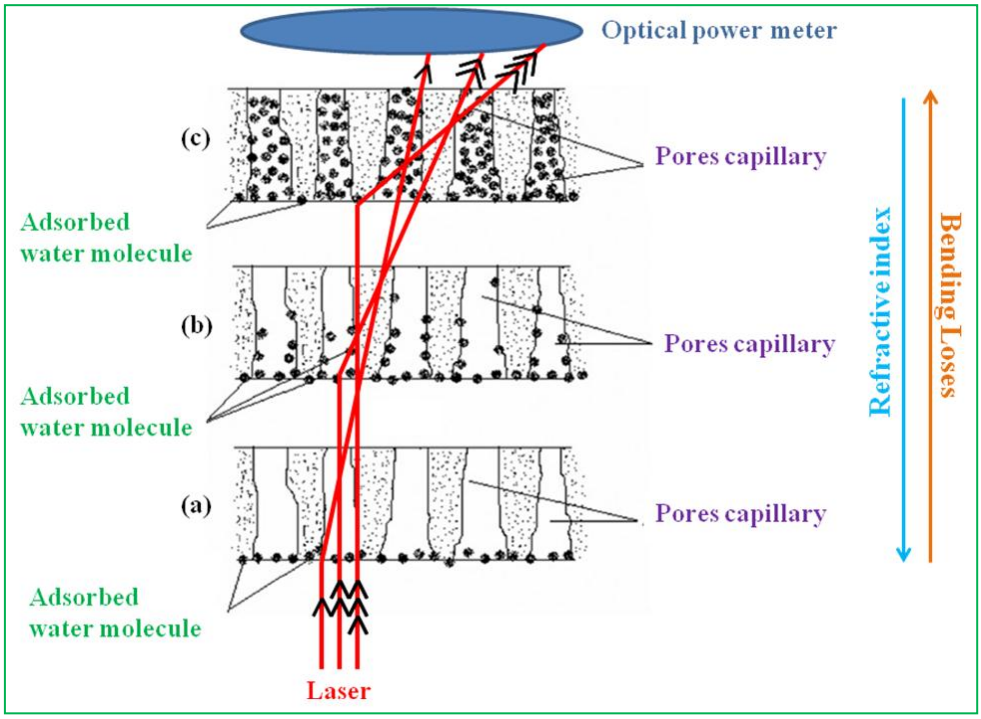

Figure 2.11: Mechanism of change in output power with exposure of humidity (a) at lower humidity (surface adsorption), (b) at intermediate humidity (adsorption on capillary walls) and (c) at higher humidity (full capillary condensation).

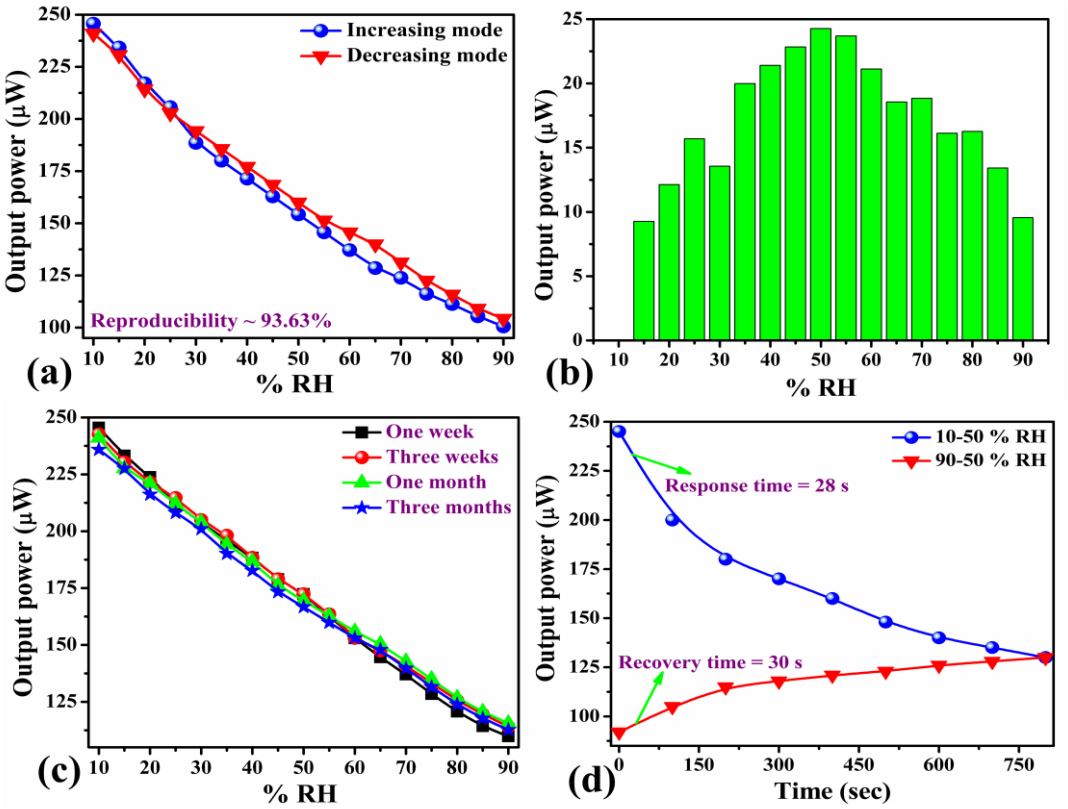

Figure 2.12: Variation of output power with %RH for one layered film to observe the (a) reproducibility (b) standard deviation (c) aging effect after one week, three weeks, one month and three months showing the stability of the material and (d) response and recovery time.

CHAPTER 3

Synthesis and Characterization of CeO_2-Gd_2O_3-CoO Nanocomposite and its Application as Opto-electronic Humidity Sensor

The present chapter reports the synthesis and fabrication of CeO_2-Gd_2O_3-CoO nanocomposite films using metal carboxylates as precursors. The refractive index of the material was found as 1.445538. The crystallinity was confirmed from XRD and the minimum crystallite size calculated was 9 nm. TEM analysis showed the hexagonal crystals where the minimum dimension was obtained as 6 nm. The dimensionality was further confirmed by Particle Size Analyzer. The film was then investigated using SEM which revealed highly porous nature of the material. By UV-Vis spectrophotometer, it was found that the absorption of the film takes place in UV-region and optical band-gap was observed as 3.987 eV from the Tauc plot. The film was employed as transmission based opto-electronic humidity sensor. Maximum sensitivity was found as ~2.006 µW/%RH. Response and recovery times were found as 71 s and 86 s respectively. Experiments were repeated time to time and the results were found ~ 90% reproducible.

3.1 Introduction

Humidity is one of the elementary biotic factors that fix the habitat of a particular living being. The saturation point of humidity is solely related to temperature, therefore in summers, %RH increases and hence the rate of perspiration from the skin tending to an increase in the apparent temperature to the body. Also, humidity measurement is useful in climate monitoring and weather forecasts as it is not only itself a climate variable but also affects other climate variables. Also, water vapour acts as a green house gas by transmitting the solar energy while absorbing red and infrared radiations from the earth's surface whereas blocking the harmful UV rays thereby making the possibility of life on Earth. This is the reason why humid areas experience negligible nocturnal cooling than dry deserts [1]. In structural health monitoring (SHM) also humidity plays a vital role as moisture monitoring can avert the buildings and structures from harsh deterioration and thus saving the life and cost [2]. Moreover, not only the growth rate of a particular crop but its transportation and storage also depends on the humidity. Various instruments and machines in industries also require an optimum humidity level for their efficient working [3]. Thus humidity has manifold significance for mankind; therefore, researchers across the globe are intensely fascinated towards humidity sensors.

A lot of research has been done in this field [4-10] and few of the latest are shown in Table 3.1. It can be seen that metal oxides have proven themselves to be potential in this field. Therefore, in the present chapter, an effort has been made to synthesize the nanocomposite CeO_2-Gd_2O_3-CoO using chemical extraction route and the sensing element was fabricated using spin coating technique. Further, the relationship between humidity and transmitted optical power was obtained and hence the potential of synthesized material as humidity sensor was determined.

Metal oxide nanomaterials symbolize an increasing asset in numerous productions, particularly due to their sharp chemical, physical, and electronic properties and have versatile applications like environmental monitoring, health and personal care, energy, water treatment [11-12]. Also, as the crystallite size of these materials reduces, great enhancement in their properties is observed. This diverted the research community towards the low dimensional metal oxides while ensuring that their properties remain stable even at high operating temperature. Specifically, transition metal oxides are of

great interest because of their vacant d-orbital. They can be easily oxidized as well as reduced and hence has potential application in gas/humidity sensing. One among them is cobalt oxide, a significant functional material, has versatile applications in energy storage, sensors, catalysis and magnetism [13-14]. A more interesting group of elements called rare earth metals have attracted the scientists more due to their vacant f-orbitals. Their exclusive 4f electron configuration has conveyed them with excellent magnetic, electrical, optical, and catalytic properties [15]. Nanostructured rare-earth compounds are of much importance due to the occurrence of quantum confinement effects. Cerium, most copious rare earth elements and its oxide has applications ranging from catalysis, polishing agents, fuel cells, UV blockers, pharmacological treatment, gas sensors, cosmetic products etc. [16-20]. Another rare earth element, Gadolinium, has high dielectric constant, large band-gap and superior thermal stability. It is broadly considered for its potential usage in optoelectronics, data storage, and display devices [21].

3.2 Experimental Details

3.2.1 Synthesis

Reagents: Ethylhexanoic acid (95%), Belgium, ACROS; $Gd(NO_3)_3.6H_2O$ (ACROS), $Co(NO_3)_2.H_2O$ (PANREAC), $Ce(NO_3)_3.6H_2O$ (HimReakt) -"chemical purity" are used as received.

For the synthesis of CeO_2-Gd_2O_3-CoO, the mixture of ethyl hexanoate of Ce (III), Gd(III) and Co(II) was prepared. Metal hexanoates were synthesized by the extraction method in the two-phase system of metal nitrate solution-organic acid by the following reaction given in Eqn. 3.1:

$$(M^{n+})_{aqua} + CH_3(CH_2)_3CH(C_2H_5)COOH \rightarrow M[CH_3(CH_2)_3CH(C_2H_5)COO]_n + nH^+ ...(3.1)$$

(M^{n+} - metal ion, n = 2, 3, 4).

Extraction was carried out for half an hour in acidic medium by maintaining the pH at 5-7 by adding the NH_4OH solution. The water phase was isolated in a separation funnel. The contents of ceria, gadolinium and cobalt in the extracts were 90.1, 137.0 and 136.1 g/Kg, respectively obtained after elemental analysis of the products on the atomic

absorption spectrometer AAS-3. Then the mixture of metal hexanoates in the required ratio (CeO_2:Gd_2O_3:CoO = 90.3:7.7:2.0 mol.%) was stirred at 105-108ºC followed by vacuum distillation at 150ºC for 10 h. The synthesis process has been shown schematically in Fig.3.1.

3.2.2 Fabrication of Sensing Element

For the characterization and application purpose, films of a nanostructured composite of CeO_2-Gd_2O_3-CoO were fabricated. For this, flat borosilicate pieces of dimensions 1.5 × 1.5 × 0.5 cm^3 were used as substrates and the technique used was spin coating [22]. The characteristic feature of the films depends on fabrication conditions (density and viscosity of the solution, spinning speed and heating/annealing temperature). Before film deposition, the substrates were properly rinsed by plunging them in an ultrasonicator (WUC-AO2H) for 15 min each in lab detergent (Extran), de-ionized water, isopropyl alcohol and acetone. For the removal of organic impurities, heat treatment (100°C for 15 min) was given to the substrates to evaporate these impurities. Further, these rinsed substrates were used for the film deposition at a spinning speed of 3000 rpm using spin coater and dried for 15 min at 60°C on a hotplate. Finally, the films were annealed at 400°C for 3 h and used as sensing elements for humidity detection. Schematic representation for film fabrication is shown in Fig.3.2.

3.2.3 Description of Sensing Set-up

The experimental set-up for the humidity sensing based on opto-electronic mode is previously shown in section 2.2.3 of Chapter 2. The set-up is comprised of an input as 2 mW He-Ne Laser, the optical channel contains a transparent humidity controlled chamber having sensing element fixed on one of its walls from which the laser beam is transmitted. At the end part, the output part contains a photodetector to obtain the transmitted power from the sensing element.

3.2.4 Characterization Techniques Used

The nanostructured composite of CeO_2-Gd_2O_3-CoO was investigated under various characterization techniques for the determination of their properties. The refractive index was obtained from the digital refractometer (Anton Par Abbemat 550)

having an accuracy of 0.000001 at room temperature. The information about crystallinity was obtained through X-ray diffractometer X'Pert Pro recording system (PANalytical, Netherlands) using Cu K_α (λ = 1.5406 Å) radiation, operated at 45 kV and 40 mA from 20° to 80°; typical 2θ step size: 0.008°. The morphological investigation at various scales and resolutions was done using Scanning electron microscope (JEOL, JSEM-6490LV). TEM analysis of the dilute solution of the nanocomposite loaded over carbon-coated copper grid (mesh size 200) was performed using FEI-G2 SPRIT, Netherland at the scales 100 and 200 nm. The particle size of the nanocomposite dissolved in acetone was analyzed by Particle Size Analyzer (Nano-ZS90). For the determination of optical properties, UV–Vis Spectrophotometer (Evolution 201) was used to record the UV–Vis absorption spectra of films in the wavelength range 190–1100 nm.

3.3 Results and Discussion

3.3.1 Refractometer Analysis

The nanocomposite film was kept on the prism of the digital refractometer (Anton Paar Abbemat 550) and the piston was pressed at room temperature with an accuracy of 0.00001 and it was found that refractive index of the material is 1.445538. The technique involves fast and non-destructive measurements, calibrated with official standards.

3.3.2 X-ray Diffraction Analysis

The formation and the phase of the sensing film were investigated with X-ray diffractometer X'Pert Pro recording system (PANalytical, Netherlands) using Cu K_α (λ = 1.5406 Å) radiation. The instrument was operated using power: 45 kV, 40 mA and scanning parameters: from 20° to 80°; typical 2θ step size: 0.008°. The XRD pattern is shown in Fig. 3.3(a). The hatch peaks corresponding to (111), (200), (220), (222) and (400) lattice planes denote CeO_2 (confirmed from JCPDS file no. 81-0792), the star peaks corresponding to (222), (400), (411), (431), (440) and (662) lattice planes denote Gd_2O_3 (confirmed from JCPDS file no. 43-1014) whereas plus peaks corresponding to (100), (102), (110) and (400) lattice planes denote CoO (confirmed from JCPDS file no. 80-0075) in the nanostructured composite. The minimum crystallite size as obtained from Debye Scherrer Formula from the (111)/(222) peak is 4.67 nm.

3.3.3 Particle Size Analysis

The particle size of the nanostructured composite of CeO_2-Gd_2O_3-CoO dissolved in acetone was analyzed by Particle Size Analyzer and the corresponding data is plotted in Fig. 3.3(b). It is a dynamic light scattering system for nanoparticle and molecular size measurement. From the size distribution curve, it was obtained that there are two ranges of particles size. The first range lies between ~5-110 nm whereas the other range lies between 200-700 nm.

3.3.4 Scanning Electron Microscopy Analysis

The SEM analysis of nanocomposite CeO_2-Gd_2O_3-CoO film was done at various scales and resolutions using Scanning Electron Microscope. The SEM images at 5, 0.5 and 0.2 μm scales are shown in Fig. 3.4(a-c). It can be observed from Fig. 3.4(a), that the particles on the surface of the film are agglomerated in such a way that wide cracks are left in between the clusters which seems to be the colonies and roads like morphology. On further magnifying the image and focusing on one of the colonies, it can be seen from Fig. 3.4(b) that there are pores on them. On further magnifying and focusing on one of the pore as shown in Fig. 3.4(c), there are in situ many pores within a single pore. This highly porous structure is rather encouraging for the excellent adsorption/desorption of humidity thus serving as active centers by providing many dangling bonds for water molecules.

3.3.5 Transmission Electron Microscopy Analysis

TEM analysis has been carried out at various scales and resolutions using FEI-G2 SPRIT, Netherland. Fig. 3.5(a & b) depicts the TEM image of dilute solution of nanocomposite CeO_2-Gd_2O_3-CoO at 200 and 100 nm scales. TEM image shows the uniform distribution of hexagonal crystals with diffused edges. This is the exquisiteness of the synthesis efforts and monitor over physical parameters that almost all the crystals are hexagonal in shape. The dimensionality of the particles can be more precisely checked by the Fig. 3.5(b) which is at 100 nm scale. From image, the minimum dimension of the particle is ~6 nm.

3.3.6 UV-visible Absorption Analysis

The optical absorbance spectrum of CeO_2-Gd_2O_3-CoO film in the wavelength regime 190-1100 nm is shown in Fig. 3.6. It determines the attenuation of the beam after passing through the film [23]. Here it can be observed that the film reveals absorption (~320 nm) in the ultra-violet range. The change of optical absorption coefficient (α) with photon energy hν was achieved using the absorbance data shown in the inset of Fig.3.6. The optical band-gap E_g of the film can be estimated from the Eqn. 3.2:

$$\alpha h\nu = A(h\nu - E_g)^n \quad \ldots\ldots (3.2)$$

where 'A' is a constant, 'ν' is the transition frequency and the exponent 'n' defines the characteristic of band transition. Here 'n' assigns different values and each value corresponds to specific transition. For n = 1/2, 3/2, 2 and 3 corresponds to direct allowed, direct forbidden, indirect allowed and indirect forbidden transitions, respectively. Here the transition being direct allowed type, therefore, n is taken as ½. The optical band-gap E_g was calculated by extending the linear portion of $(\alpha h\nu)^2$ vs. hν curves to α = 0. The optical band-gap of the film was estimated to be 3.941 eV.

3.3.7 Humidity Sensing

The humidity detection nature of CeO_2-Gd_2O_3-CoO film covering different sensor parameters at room ambient has been shown in Fig. 3.7(a-e). The sensing response curve shows an almost linear decrease in transmitted output power relative to the continuous increase in %RH.

The curve plotted by the spherical dots is for adsorption process while that from triangular dots represent the desorption process. It can be observed from Fig. 3.7(a) that the sensing element is sensitive towards humidity in the entire range of %RH, although the slope is less, both in lower and higher range of %RH, whereas maximum slope can be observed in the mid-range of humidity. This implies that the sensing element is maximum sensitive in the mid-range of humidity whereas less sensitive in the lower and higher range of %RH. The average sensitivity of sensing element for the entire range of %RH (i.e. from 10-90 %RH) is found to be 2.006 μW/%RH. This shows the quite potent nature of CeO_2-Gd_2O_3-CoO nanocomposite film towards entire range of humidity. The readings

obtained during the experiment for different sensing parameters are shown in Table 3.2(a & b).

The other important sensor parameter is reproducibility which involves the repetition of the same output while repeating the experiment. Here reproducibility of the experiment is shown in Fig. 3.7(b) and it shows almost the same curve as obtained in the principal experiment. The deviation of the readings from the principal experiment is shown in Fig. 3.7(c). The sensing element gave ~90% reproducible results. Also, the ageing effect is an important parameter. It determines the effect of time of the performance of the sensor. Here the experiment was repeated several times. The corresponding sensing characteristic curves after one, two and three months are shown in Fig. 3.7(d) and it was found that the reported sensor is very less affected by ageing. Further, the sensor is determined by its quickness towards its response. Response time and recovery times are the major parameters which define the efficiency of the sensor. Response time is the time which the sensor takes while completing the 90% of the experiment during adsorption of humidity whereas recovery time is that taken while desorption [24]. Here response and recovery times were measured from Fig. 3.7(e) and were found as 71 and 86 s respectively. All the sensor parameters have been shown in Table 3.3.

It can be observed from Table 3.2 that the reported sensing element possess encouraging sensor parameters. The efficiency towards humidity sensing may be basically due to the presence of transition and inner transition metals in the sample, as they provide vacant d- and f-orbital respectively. The low dimensionality adds more potency to their properties. Less crystallite size (as observed from XRD and TEM analysis) enhances the aspect ratio and hence provides more surface area for the water molecule to adsorb/desorb. Also, high optical band-gap provides more probability for the adsorption of a water molecule. Further, it can be observed from the SEM image that the surface of the material is porous in nature which further provides more active centers for the adsorption and desorption of water molecule.

The sensing film was fixed on the wall of the controlled humidity chamber and laser beam was made to incident on it whereas the transmitted beam from the film was collected on a photodetector through lens combination. It was observed that with the

increase in humidity inside the chamber, the intensity of the transmitted beam at the output decreases. This nature of the film shows its potency towards humidity sensing. The variation in the transmitted laser beam relative to increase/decrease in humidity can be explained on the basis of adsorption and desorption phenomena of water molecule on the surface of metal oxide film. Initially the sensing film was dry having vacant pores. With the exposure of humidity, adsorption of water molecule starts taking place on the surface of film. The metal parts of the metal oxide nanocomposite film have such a high cationic charge density that it is sufficient to attract $O–H^-$ ion from H_2O molecule through Coloumbic force. It thus forms a strong chemical bond M-OH ($Ce(OH)_4$, $Gd(OH)_3$, $Co(OH)_2$) between M^+ (Ce^{4+}, Gd^{3+} and Co^{2+}) and OH^- (hydroxyl ion). Thus initially chemisorbed layer of water molecule is formed on the metal oxide surface with the exposure of humidity. Meanwhile H^+ ion from the water molecule is released which travels on the entire surface and is responsible for the conductivity of the material. This charged ion (H^+) is also responsible for the change in the refractive index of the metal oxide. It is well known that when a material is ionized, its refractive index decreases. The same phenomenon is happening here. Also with the adsorption of water molecule in the less humid range (10-25 %RH), the density of the material decreases which further leads to the decrease in the refractive index of the material. Thus these two phenomena are leading to the decrease in refractive index of the sensing material with the exposure of humidity [25]. Further the decrease in refractive index causes the bending of the laser beam transmitted from the sensing element. As the %RH increases, adsorption of water molecule on the sensing surface increases and in the mid humid range (25-75 %RH) adsorption not only takes place on the porous surface but also on the walls of capillaries. Also physisorbed layers of water molecules start forming in this range. Due to distance factor, the chemical bond between metal ion and hydroxyl ion cannot form therefore water molecule just physically adsorb on the surface with weak Van der Waal's force. This tends to a greater bending of light and hence less power is obtained at the output. In high humid region (75-90 %RH), next layers of physisorbed water molecules are observed. Here the condensation of water vapour thus formation of meniscus in the capillaries of the film takes place. In this region maximum decrease in refractive index and hence greatest bending of light occurs. The transmitted power obtained at the output

is least in this range of humidity. The schematic diagram explaining the sensing mechanism is shown in Fig. 3.8.

3.4 Conclusion

We have successfully synthesized CeO_2-Gd_2O_3-CoO nanocomposite using sol-gel extraction route and fabricated its films on glass substrates. The films were further annealed at 400°C. Refractive index of the film was found as 1.445538. XRD of the film shows the crystalline nature of the material. Minimum crystallite size as calculated from the Debye Scherrer formula was 9 nm. Morphological investigation as obtained from SEM shows the porous morphology. TEM analysis shows the formation of regular hexagonal crystals with diffused edges distributed uniformly. The minimum grain diameter as obtained from TEM image is ~6 nm. A study of the UV-Vis spectra of the nanocomposite film demonstrates that absorption of the material occurred in the UV-region (~320 nm). The optical energy band-gap as estimated from the Tauc plot is 3.987 eV. Further, the film was checked for humidity detection capability using opto-electronic mode. The sensitivity obtained here is ~2.006 µW/%RH. The experiment was repeated and the sensor gave ~98% reproducible results. The effect of ageing was also checked and it was found negligible after a long run. The response and recovery times were found as 71 s and 86 s respectively.

References

[1] S. Sikarwar, A. Kumar, B.C. Yadav, G.I. Dzhardimalieva, N.D. Golubeva, Nanostructured spherical-shaped Sc(III) Polyacrylate for monitoring the moisture level, IEEE Sensors 18(11) (2018) 4384-4391.

[2] S. Sikarwar, Satyendra, S. Singh, B.C. Yadav, A review on pressure sensors for structural health monitoring, Photonic Sensors: Springer (2017).

[3] S. Sikarwar, B.C. Yadav, Opto-electronic humidity sensor: A review, Sens. Actuators A: Physical 233 (2015) 54–70.

[4] A.L. Aldaba, D.L. Torres, C. Elosua, J.L. Auguste, R. Jamier, P. Roy, F.J. Arregui, M. Lopez-Amo, SnO_2-MOF-Fabry-Perot optical sensor for relative humidity measurements with high sensitivity enhanced by UV photoexcitation, Sens. Actuators B: Chem. 257 (2018) 189-199.

[5] N. Irawati, T.N.R. Abdullah, H.A. Rahman, H. Ahmad and S.W. Harun, PMMA microfiber loop resonator for humidity sensor, Sens. Actuators A: Phy. 260 (2017) 112–116.

[6] B.C. Yadav, S. Sikarwar, A. Bhaduri, P. Kumar, Synthesis, characterization and development of opto-electronic humidity sensor using copper oxide thin film, Int. Adv. Research J. in Sci., Engg. and Tech.2(11) (2015) 105-109.

[7] S.F.A.Z. Yusoff, C.S. Lim, S.R. Azzuhri, H. Ahmad, R. Zakaria, Studies of Ag/TiO_2 plasmonics structures integrated in side-polished optical fiber used as humidity sensor, Results in Physics 10 (2018) 308-316.

[8] B.C. Yadav, K.S. Chauhan, S. Singh, R.K. Sonker, S. Sikarwar, R. Kumar, Growth and characterization of sol-gel processed rectangular shaped nanostructured ferric oxide thin film followed by humidity and gas sensing, J Mater Sci: Mater Electron 28 (2017) 5270–5280.

[9] P. Murkute, H. Ghadi, S. Patil, H. Rawool, S. Pandey, S. Chakrabarti, Emerging material zinc magnesium oxide-based nanorods: Growth process optimization and sensor application towards humidity detection, Sens. Actuators B: Chem. 256 (2018) 204-216.

[10] S. Sikarwar, B.C. Yadav, S. Singh, G.I. Dzhardimalieva, S.I. Pomogailo, N.D. Golubeva, A.D. Pomogailo, Fabrication of nanostructured yttria stabilized zirconia multilayered films and their optical humidity sensing capabilities based on transmission, Sens. Actuators B: Chem. 232 (2016) 283–291.

[11] C. Kelba, M. Körner, O. Prucker, J. Rühe, E. Reithmeier, B. Roth, A planar low-cost full-polymer optical humidity sensor, Procedia Technology 26 (2016) 530–536.

[12] J.R. Mann, R.N. Bhattacharya, Thin film growth of epitaxial gadolinium oxide, gadolinium yttrium oxide, and gadolinium cerium oxide by electrodeposition, Thin Solid Films 519 (2010) 210–213

[13] S. Sriram, V. Nagarajan, R. Chandiramouli, H_2S and NH_3 adsorption characteristics on CoO nanowire molecular device – A first-principles study, Chem. Phy. Letters 636 (2015) 51–57.

[14] S. Sikarwar, B.C. Yadav, G.I. Dzhardimalieva, N.D. Golubeva, P. Srivastava, Synthesis and characterization of nanostructured MnO_2–CoO and its relevance as an opto-electronic humidity sensing device, RSC Advances 8(37) (2018) 20534-20542.

[15] F. Chen, X.H. Zhang, X.D. Hu, W. Zhang, R. Zeng, P.D. Liu, H.Q. Zhang, Synthesis and characteristics of nanorods of gadolinium hydroxide and gadolinium oxide, J. Alloys Comp. 664 (2016) 311-316.

[16] T. Montini, M. Melchionna, M. Monai, P. Fornasiero, Fundamentals and Catalytic Applications of CeO_2 based Materials, Chem. Rev. 116 (2016) 5987−604

[17] V.R. Khadse, S. Thakur, K.R. Patil, P. Patil, Humidity-sensing studies of cerium oxide nanoparticles synthesized by non-isothermal precipitation, Sens. Actuators B: Chem. 203 (2014) 229-238.

[18] R.P. Senthilkumar, V. Bhuvaneshwari, R. Ranjithkumar, S. Sathiyavimal, V. Malayaman, B. Chandarshekar, Synthesis, characterization and antibacterial activity of hybrid chitosan-cerium oxide nanoparticles- as a bionanomaterials, Int. J. Biological Macromolecules 104(B) (2017) 1746-1752

[19] S. Rajeshkumar, P. Naik, Synthesis and biomedical applications of Cerium oxide nanoparticles – A Review, Biotechnology Reports 17 (2018) 1–5.

[20] S. Thakur, P. Patil, Rapid synthesis of cerium oxide nanoparticles with superior humidity-sensing performance, Sens. Actuators B: Chem. 194 (2014) 260– 268.

[21] M.R.S. Huang, C.P Liu, J.C. Wang, Y.K. Chen, C.S. Lai, Y.C. Fang, L. Shu, Microstructural effect of gadolinium oxide nanocrystals upon annealing on electrical properties of memory devices, Thin Solid Films 520 (2012) 5579–5583.

[22] J.K. Rajput, T.K. Pathak, V. Kumar, H.C. Swart, L.P. Purohit, Tailoring and optimization of optical properties of CdO thin films for gas sensing applications, Physica B: Condensed Matter 535 (2018) 314-318

[23] J.K. Rajput, T.K. Pathak, V. Kumar, M. Kumar, L.P. Purohit, Annealing temperature dependent investigations on nano-cauliflower like structure of CdO thin film grown by sol-gel method, Surfaces and Interfaces 6 (2017) 11-17.

[25] F. Xu, L. Zhang, X. Yin, L. Tong, Polymer single-Nanowire optical sensors, Nano Lett. 8 (2008) 2757–2761.

Tables

Table 3.1: A recent literature review of the reported opto-electronic humidity sensors

S. No.	Material	Sensitivity	Year	Ref.
1.	SnO_2-MOF	0.14 rad/%RH	2018	[4]
2.	PMMA microfiber loop resonator (PMLR) coated with ZnO	0.1746 dBm/%RH	2017	[5]
3.	CuO	0.85 μW/%RH	2015	[6]
4.	Ag/TiO_2	0.9201%	2018	[7]
5.	Fe_2O_3	1.172 μW/%RH	2016	[8]
6.	$Zn_{0.85}Mg_{0.15}O$	1.503/%RH	2018	[9]
7.	Y_2O_3-ZrO_2	1.937 μW/%RH	2016	[10]
8.	CeO_2-Gd_2O_3-CoO	2.006 μW/%RH	2018	Present work

Table 3.2(a): Variations in the transmitted intensity of light through the film of CeO_2-Gd_2O_3-CoO as RH increases from 10-90%.

%RH	Sensing Response (μW)		Reproducibility (μW)		Ageing effect (μW)		
	During Adsorption Cycle	During Desorption Cycle	During Adsorption Cycle	During Desorption Cycle	One Month	Two Months	Three Months
10	389.2	381.7	380.2	375.5	378.1	376.1	373.4
15	385.5	378.2	376.5	371.6	375.4	370.3	368.3
20	381.5	373.7	372.9	365.7	370.6	367.2	362.1
25	375.1	368.1	367.6	360.5	368.2	361.4	355.2
30	364.2	359.2	362.5	355.2	363.3	358.6	353.2
35	355.5	348.7	352.2	347.7	355.7	352.4	348.5
40	343.7	338.7	343.1	336.7	347.9	345.5	338.3
45	331.5	325.6	331.5	326.1	333.1	330.2	322.8
50	314.7	308.3	314.7	309.5	315.2	309.2	304.5
55	300.3	294.9.	300.1	294.3	302.4	294.1	289.2
60	282.7	274.7	286.4	281.2	283.1	280.9	274.6
65	275.5	267.1	275.5	269.7	273.7	262.3	259.1
70	258.7	255.2	263.7	262.1	258.1	254.5	247.4
75	246.5	247.3	251.2	255.6	249.3	246.3	242.2
80	235.5	240.8	243.4	247.5	242.8	239.2	238.5
85	232.2	238.5	237.1	245.2	239.1	237.1	235.4
90	228.5	234.4	235.4	241.3	237.3	235.4	234.1

Table 3.2(b): Variations of time in seconds with output in µW for observing response and recovery times.

Time (s)	Output Power During Adsorption (µW)	Output Power During Desorption (µW)
0	389.2	228.5
50	383.5	232.2
110	379.5	239.5
180	371.3	246.5
260	364.2	258.5
350	355.5	275.5
450	343.7	282.7
560	331.5	300.3
680	314.7	314.7

Table 3.3: Sensors parameters for CeO_2-Gd_2O_3-CoO nanocomposite film as opto-electronic humidity sensor.

Sensor Parameters	Sensitivity	Reproducibility	Ageing Effect	Response Time	Recovery Time
Values	2.006 µW/%RH	91%	Negligible	71 s	86 s

Figures

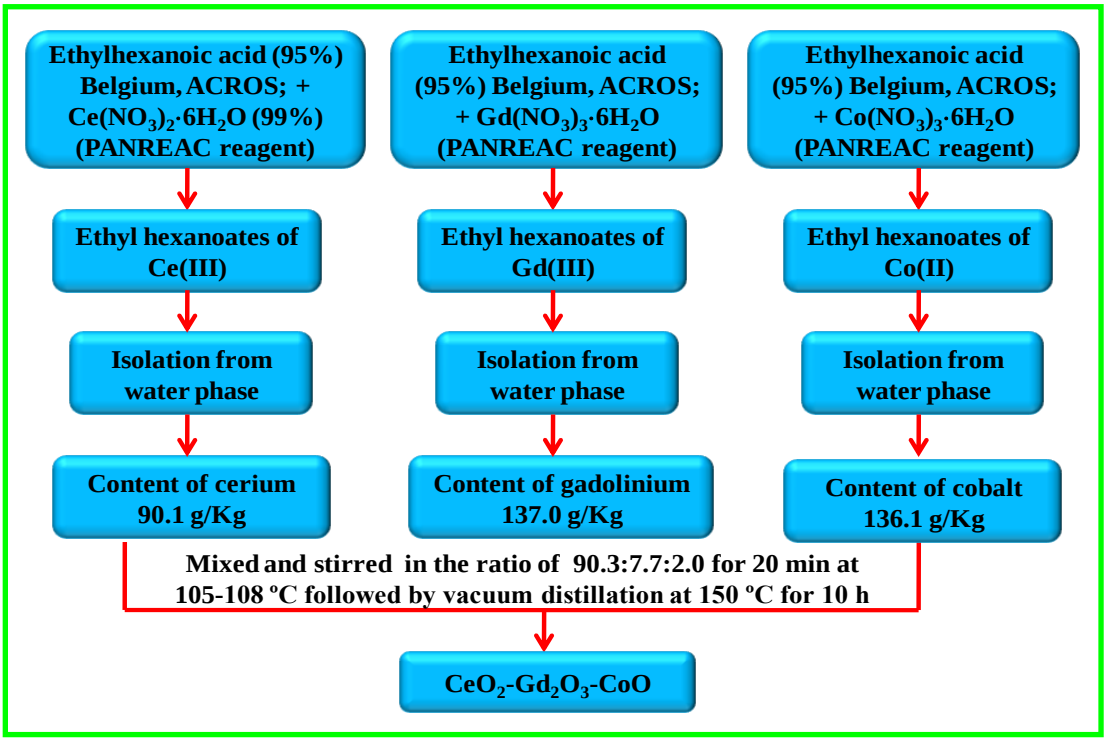

Figure 3.1: Flowchart for the synthesis of nanostructured composite of CeO_2-Gd_2O_3-CoO.

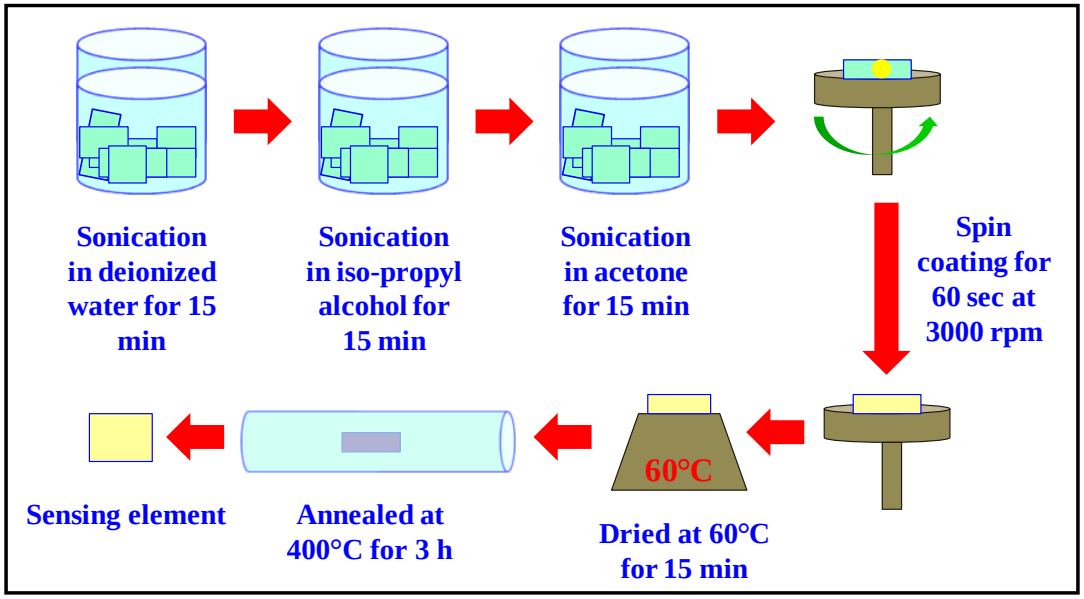

Figure 3.2: Schematic representation of film fabrication.

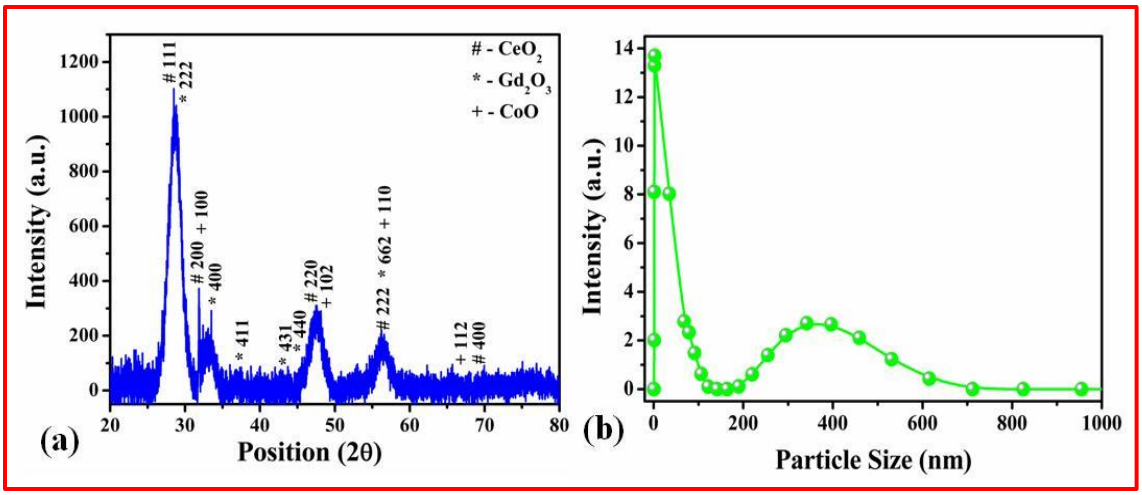

Figure 3.3: (a) XRD pattern of the nanostructured composite of CeO_2-Gd_2O_3-CoO film showing its crystalline nature. The minimum crystallite size was observed as ~4.7 nm (b) Particle size distribution curve showing the minimum range of particles is ~5-110 nm.

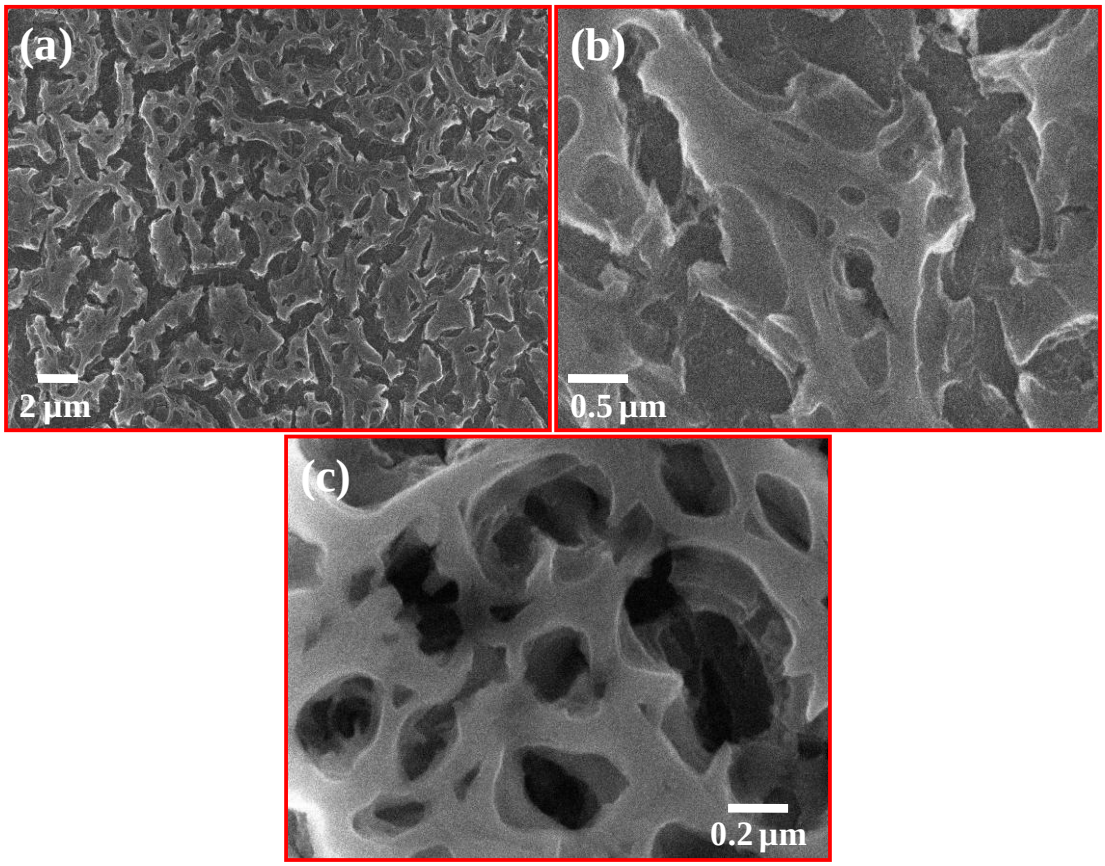

Figure 3.4: Morphological image as obtained by SEM at (a) 2 µm, (b) 0.5 µm and (c) 0.2 µm scales showing the presence of pores and cracks on the surface of the film

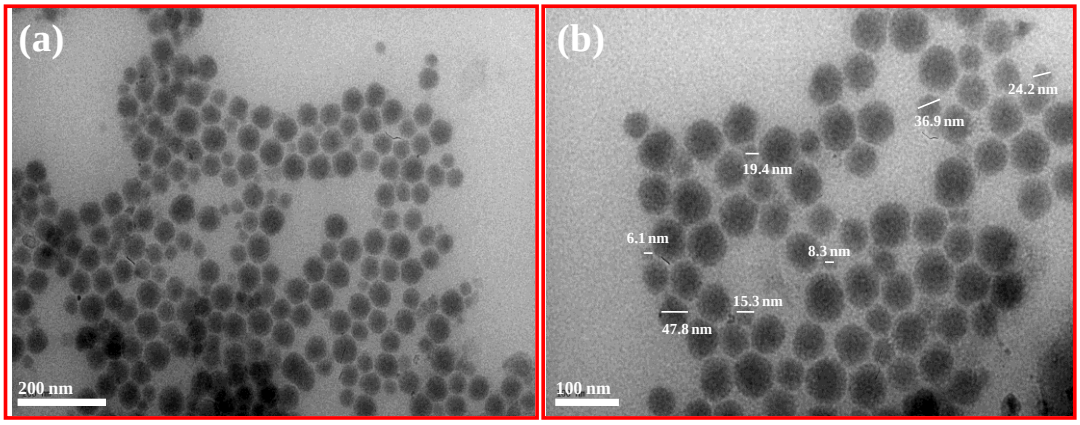

Figure 3.5: TEM image of dilute solution of nanocomposite CeO_2-Gd_2O_3-CoO at (a) 200 and (b) 100 nm scales depicting the minimum particle size as ~ 6 nm.

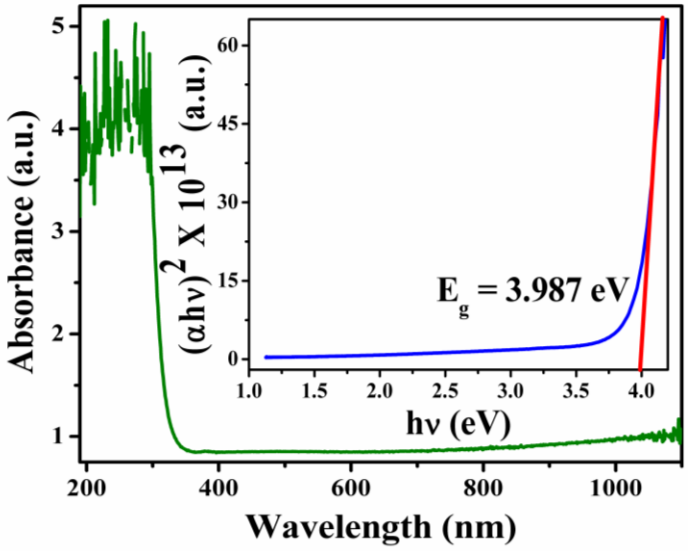

Figure 3.6: Optical absorbance spectra of CeO_2-Gd_2O_3-CoO film in the wavelength regime of 190-1100 nm where inset displays the Tauc plot from which optical energy band-gap was estimated as 3.987 eV.

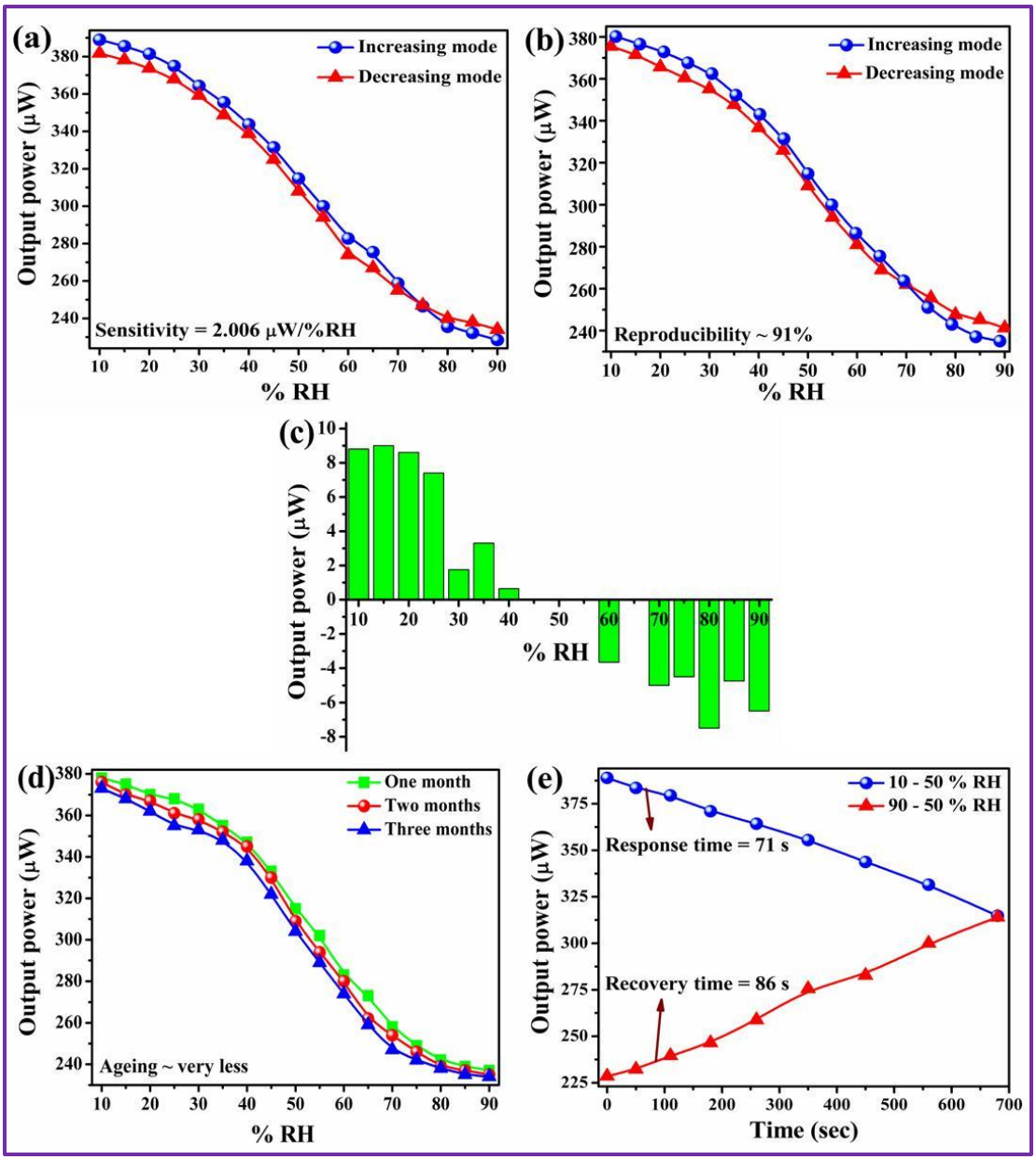

Figure 3.7: Humidity sensing characteristic curves for (a) sensing response, (b) reproducibility, (c) standard deviation, (d) ageing effect and (e) response and recovery times.

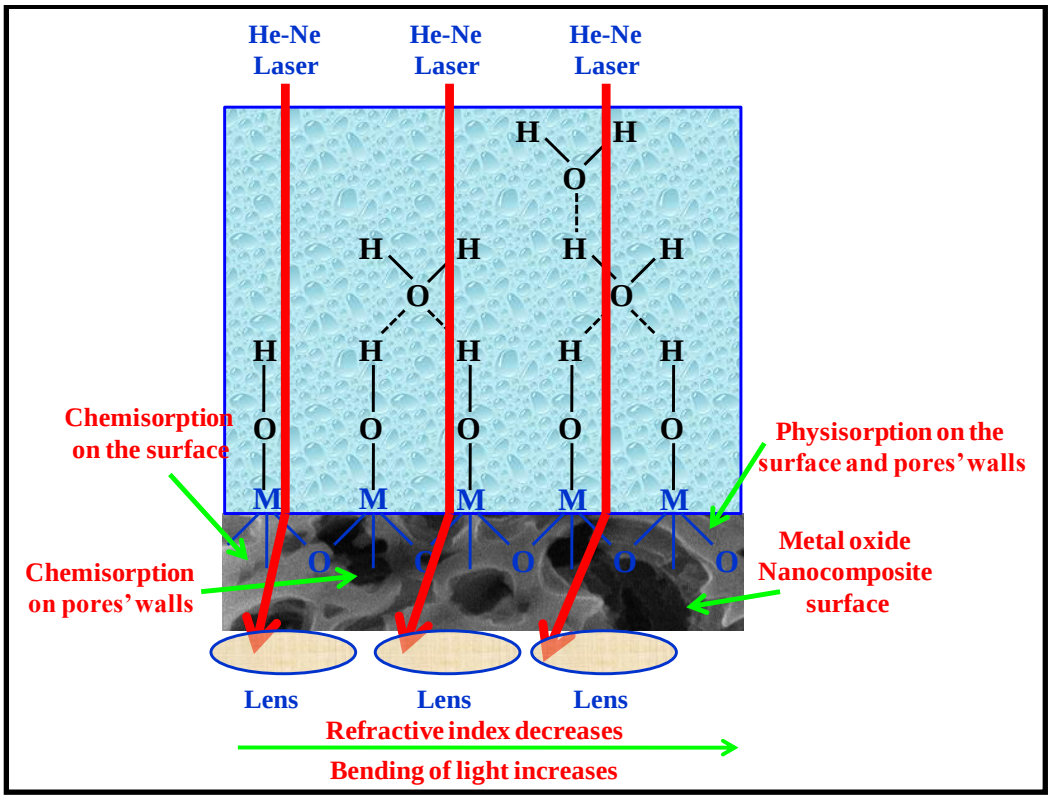

Figure 3.8: Schematic representation of the sensing mechanism showing a decrease in refractive index and hence in output power with an increase in %RH.

CHAPTER 4

Synthesis and Characterization of Nanostructured MnO_2-CoO and its Relevance as Opto-electronic Humidity Sensing Device

Metal carboxylates are widely used in science and technology and have been the subject of intense studies due to the practical importance of their products. The present chapter reports the synthesis of MnO_2-CoO using metal carboxylates as precursors and effect of humidity on the transmitted power through its thin film at room temperature. The refractive index of the material was found as 1.445930. TEM reported the minimum grain size of ~5.7 nm and SAED confirmed the crystalline nature of the material which was confirmed by XRD. The particle size was further confirmed from Particle Size Analyzer. The film was then investigated using SEM which exhibited the porous morphology. By UV-Vis spectrophotometer, it was found that the absorption of the film takes place in UV-region and optical band-gap was observed as 3.849 eV from the Tauc plot. The film was employed as transmission based opto-electronic humidity sensor. Average sensitivity was found as ~2.225 µW/%RH with response and recovery times of 47 s and 59 s respectively. Experiments were repeated time to time and found that reproducibility of result is ~ 89%.

4.1 Introduction

Unique surface properties and high catalytic activity of metal oxides make them very attractive for various sensor applications [1, 2]. Titanium, cerium, copper, iron, and manganese oxides have been widely used as catalysts, photocatalysts and electrocatalysts in a variety of reactions of organic synthesis [3-6]. Transition metal oxides such as Mn_2O_3, Co_3O_4, NiO etc. are of interest for optical waveguide gas sensors [7]. The V_2O_5 nanobelts ($V_2O_5 \cdot xH_2O$, V_2O_5·CTAB and V_2O_5 nanorods annealed at 400 °C) revealed the properties of ethanol sensor with high selectivity and stability [8]. The Cu-CuO nanocomposite was successfully used to modify glass carbon electrode to detect H_2O_2 and glucose [9].

Metal carboxylates are widely used in science and technology. They have been the subject of intense studies due to the practical importance of their products [10]. In particular, the controlled thermolysis of metal carboxylates can be considered as an effective way for the synthesis of nanocomposite materials [11]. Owing to the formation of ferromagnetic Fe_3O_4 and $CoFe_2O_4$ nanoparticles, the thermolysis products of metal acrylates and their co-crystallizates behave as solid magnets with a coercive force of 0.18 T and the residual magnetization of 15.5 mT at room temperature [12]. The spinel ferrites $Zn_{0.5}Mn_{0.5}Fe_2O_4$ [13], $CoFe_2O_4$ [14], and $MnFe_2O_4$ [15] synthesized by pyrolysis of the corresponding polyacrylate salts exhibit superparamagnetic properties at room temperature.

Humidity measurement is one of the most required parameters for various applications not only for improving the quality of life but also for enhancing the industrial process [16-17]. Advancements in sensor manufacturing technologies lead the researchers to know the degree of efficiency with predictions based on simulation techniques and design aids to improve sensitivity and sensor quality along with time-saving [18]. The humidity plays a very important role and has acquired such incredible significance due to the fact that these vapours consist of highly reactive dipolar molecules which get condensed on or evaporate from the surface even with small variations in temperature of the environment. Optical humidity sensors are better than their electronic counterparts due to their small size, low weight, immune towards electromagnetic disturbances, the possibility of multiplexing information and

working on high pressure and flammable environments [19]. Complex oxides containing cobalt and manganese show different oxidation states (Co^{2+}, Co^{3+}, Mn^{2+}, Mn^{3+}, and Mn^{4+}) [20] and hence attractive distinct properties like enhanced tunable surface, specific desirable pseudo capacitance, energy density. Also, they are easy to fabricate, have low cost, efficient structural properties, abundant in nature and environment-friendly [21] and hence can be proved as an excellent material for humidity sensing. Also recently their multicomponent electrocatalysts have been fabricated, like Mn_3O_4-CoO/CNT, Co_3O_4/Co_2MnO_4 and graphene/CNT/Co_3O_4 which showed excellent performance towards ORR (Oxidation Reduction Reaction) catalysis. [22]. A few works have been done on manganese oxide and cobalt oxide based humidity sensor. Kato et al. in 1997 investigated the sol-gel processed electrolytic manganese dioxide (EMD) as humidity sensor which showed good sensitivity between 50-80 %RH [23]. In another work, K. Miyazaki et al. in the same year developed a potential-type humidity sensor based on $M_1/MnO_x/M_2$ galvanic cell system, where MnO_x is an EMD-clay mineral mixture, M_1 is Pt, and M_2 is Cu or Al. Clay mineral samples included kaolinite, bentonite, activated clay, zeolite, and muscovite. Silica sand was used as a reference material. The EMD-kaolinite mixture responded in a wider humidity region of 20-90 %RH [24]. Similarly, Yang et al. in 2011 studied a micro humidity sensor which consisted of interdigitated electrodes and cobalt oxide nanosheet sensing film (prepared by precipitation–oxidation method). The capacitance of the sensor changes with the adsorption/desorption of water vapour [25]. In another work, Yadav et al. in 2013 investigated the multilayered sensing films prepared by sol-gel spin coating process using cobalt oxide precursor annealed at 450 °C which showed linear behaviour towards entire range of %RH with an average sensitivity of 0.76 μW/%RH [26].

Previously our group has worked on several metal oxide nanocomposite systems and their opto-electronic humidity sensing [27] but sensitivity was found lesser. As MnO_2-CoO is a hygroscopic material and synthesized first time in our laboratory at low dimension with high aspect ratio, therefore in order to improve the sensitivity, nanostructured MnO_2-CoO has been investigated as an opto-electronic humidity sensor.

4.2 Experimental Details

4.2.1 Synthesis

Reagents: Ethylhexanoic acid (95%), Belgium, ACROS; $Co(NO_3)_2.6H_2O$(98%) (PANREAC reagent), $Mn(NO_3)_2{\cdot}4H_2O$ (PANREAC reagent**)** are used as received. Metal hexanoates were synthesized by the extraction method in the two-phase system of metal nitrate solution-organic acid by the following reaction given in Eqn. 4.1:

$$(M^{n+})_{aqua} + CH_3(CH_2)_3CH(C_2H_5)COOH \rightarrow M[CH_3(CH_2)_3CH(C_2H_5)COO]_n + nH^+ \quad \ldots. (4.1)$$

(M^{n+} - metal ion, n = 2, 3, 4).

For the synthesis of cobalt (II) ethylhexanoate, 45.5 g of cobalt (II) nitrate hydrate was dissolved in 160 ml of H_2O, and then the solution of metal nitrate was mixed with 80 ml of ethyl hexanoic acid at pH 5 by adding NH_4OH. The resulting mixture was stirred for 1 h at room temperature, then after 12 h water phase was isolated in a separation funnel. For the synthesis of manganese ethyl hexanoate, 46.5 g of manganese (II) nitrate hydrate was dissolved in 400 ml of H_2O, and then the solution of metal nitrate was mixed with 205 ml of ethyl hexanoic acid at pH 5.6 by adding NH_4OH. The mixture was stirred for 1 h at room temperature, then after 12 h water phase was isolated in a separation funnel. The contents of cobalt and manganese in the extracts were 64 and 47.2 g/Kg, respectively obtained after elemental analysis of the products on the atomic absorption spectrometer AAS-3. Then the mixture of metal hexanoate's extracts in the required ratio (1:2 by weight) was stirred for 20 min at 105-108°C followed by vacuum distillation at 150°C for 10 h. The Co:Mn:O atomic ratio in the product obtained was equal to 1.5:1.5:4 determined by quantitative chemical analysis. Schematic representation for the synthesis of nanostructured MnO_2-CoO composite is shown in Fig. 4.1.

4.2.2 Fabrication of Sensing Element

Porosity and regularity of the deposited film can be restricted by monitoring the sample preparation environment like gel density/viscosity, speed of the spinner and heating/annealing temperature. Spin coating technique was used to deposit uniform sol-gel precursor MnO_2-CoO thin film with nanoscale on flat borosilicate

substrates [28] having dimensions 1.5 × 1.5 cm^2 using a photoresist spinner (METREX RC 100, India). Prior to spin coating, the flat borosilicate substrates were rinsed thoroughly with deionized water and isopropyl alcohol followed by acetone ultrasonically for 15 min each in order to remove microscopic contaminations [29]. The cleaned substrates were dried in an electric oven (METREX) at 100°C for half an hour to remove the organic precursors and moisture completely from them. A small amount of gel was dropped on the centre of the substrate and then rotated at high speed in order to extend the gel by centrifugal force on the whole substrate. The rotation was sustained for 60 s at 3000 rpm so that fluid spins off the edges of the substrate and the desired thickness of the film could be achieved [30]. After thin film formation, they were kept for drying on a hot plate at 60°C for 15 min and then annealed at 650°C for 3 h in a tubular electric furnace (METREX) in 78% nitrogen. Further, these films were used as sensing elements to investigate them as opto-electronic humidity sensing based on transmission. Schematic representation of the fabrication of MnO_2-CoO nanocomposite films is shown in Fig. 4.2.

4.2.3 Description of Sensing Set-up

The experimental set-up used for opto-electronic humidity sensing is shown in Fig. 4.3. It consists of 2 mW He-Ne LASER (Research Electro Optics Inc. 30989) with 633 nm wavelength as an input light source. A diverging lens of 10× magnification is used as a beam expander for splitting the laser light beam so that it may incident and cover the whole surface of the sensing film. A glass chamber with humidity controlled system consisting of a hygrometer (HTC-1) of the range 10-90 %RH along with a dish is kept inside for holding the humidifier/dehumidifier solution. The saturated solution of K_2SO_4/KOH (Fisher Scientific) in distilled water is used as a humidifier/dehumidifier. The sensing element is fixed on one wall of the chamber such that it is perpendicular to the incident beam and also the beam covers the maximum surface area of the film. A beam condenser is used for converging the laser light beam to obtain the maximum intensity at a fixed point. An optical power meter (Newport 1916-R) is employed for detecting the modulated power of the transmitted beam by the sensing element. The detector part is kept perpendicular to the beam for obtaining the maximum output power and the whole experiment was

performed on the Vibration Free Table (M-RS2000-48-8) at room temperature of 300K.

4.2.4 Characterization Techniques Used

The prepared film was investigated through a digital Refractometer (Anton Par Abbemat 550) in its original state at room temperature (300 K). The instrument is fast and non-destructive with a high accuracy of 0.000001. It is widely used for calibrating the official standards. TEM analysis of the material was carried out using Transmission Electron Microscope, JEOL JEM 200 CX. MnO_2-CoO precursor in dilute form, loaded over carbon-coated copper grid with mesh size 200 at the scale of 50 nm. The morphological study of the film has been carried out at various scales and resolutions using Scanning Electron Microscope, JEOL JSM 840 A. The structural information of the film was studied by X-ray diffractometer X'Pert Pro recording system (PANalytical, Netherlands) using Cu K_α (λ = 1.5406 Å) radiation. The instrument was operated at 45 kV, 40 mA with scanning parameters of 0° to 70°; typical 2θ step size: 0.008°. The particle size distribution of a dilute solution of the material was analyzed by Particle Size Analyzer (Nano-ZS90). UV–vis absorption spectrum of the film was recorded in the wavelength regime of 190–1100 nm using UV–vis Spectrophotometer (Evolution 201) with Hg lamp as the excitation source.

4.3 Results and Discussion

4.3.1 Refractometer Analysis

For the investigation of the refractive index of the film, the film was kept on the prism of the digital refractometer (Anton Par Abbemat 550) at room temperature and the piston of the instrument was pressed. Then screen showed the refractive index of the material as 1.445930.

4.3.2 Scanning Electron Microscopy Analysis

The SEM images of the film at 10 µm, 5 µm and 1 µm scales are shown in Fig. 4.4(a-c) respectively. Surface morphology of the MnO_2-CoO thin films exhibits highly porous nature. The dimension of these pores is of micron order (as depicted in Fig.4.4(c)); hence the film is macroporous in nature. This porosity enhances the

surface area of the material and hence provides many dangling bonds suitable for adsorption/desorption of water molecule. These active centres serve as humidity adsorption sites and the sensitivity of the sensor depends on the availability of these dangling bonds.

4.3.3 Transmission Electron Microscopy Analysis

Fig. 4.5 shows the TEM-SAED image of nanostructured MnO_2-CoO dilute precursor solution. Fig.4.5 (a) shows the SAED pattern of the material at 10 nm^{-1} scale. Here the concentric rings confirm the polycrystalline structure of nanocomposite. The indexing has been done for the observed rings of MnO_2 (tetragonal) and CoO (simple cubic) separately. Fig. 4.5(b) corresponds to the TEM image at 50 nm scale. It can be observed from the figure that there is a uniform distribution of spherical particles of nano dimension. The minimum grain diameter as obtained from the micrograph is ~5.7 nm which is not yet reported in open literature.

4.3.4 X-ray Diffraction Analysis

Fig. 4.6(a) shows the XRD pattern of the film of a nanostructured composite of MnO_2-CoO annealed at 650°C. The asterisk (*) peaks denote the MnO_2 crystals whereas hatch (#) peaks represent CoO crystals. The diffraction pattern shows good agreement with the diffraction data from JCPDS 240735 and 750419 for MnO_2 crystals and CoO crystals respectively. The minimum crystallite size of the material was estimated ~4 nm using Debye Scherrer Formula from (110) peak which is the least value of crystallite size reported in open literature. The crystallite size plays an important parameter in sensing as it increases the aspect ratio and hence provides more active centres for the adsorption/desorption of water molecules.

4.3.5 Particle Size Analysis

The particle size of the nanostructured composite of MnO_2-CoO dissolved in acetone was analyzed by Particle Size Analyzer and the corresponding data is plotted in Fig. 4.6(b). It is a dynamic light scattering system for nanoparticle and molecular size measurement. From the size distribution curve, it was obtained that there are two ranges of particles size. The majority of the particles range lies between ~5-100 nm whereas some particles have a dimension in the range between ~200-400 nm.

4.3.6 UV-visible Absorption Analysis

The optical absorbance spectrum of the MnO_2-CoO thin film deposited on the flat borosilicate substrate was recorded in the wavelength range 190-1100 nm and is shown in Fig. 4.6(c). It is observed from data that film exhibits absorption in the ultraviolet range of the electromagnetic spectrum. Tauc curve (inset of Fig.4.6 (c)) was plotted to show the variation of the square of the optical absorption coefficient (α^2) with photon energy hν from the absorption data. The optical energy band-gap E_g of the film can be estimated from the Eqn. 4.2:

$$\alpha h\nu = A(h\nu - E_g)^n \quad \text{…. (4.2)}$$

where 'h' is Planck's constant, 'ν' is the transition frequency and the exponent 'n' characterizes the nature of band transition (n = 1/2 and 3/2, 2 and 3 correspond to direct allowed and directly forbidden, indirect allowed and indirect forbidden transitions, respectively). Here the transition being the directly allowed type, therefore n is taken as 1/2 in the above equation. The optical energy band-gap E_g was obtained by extrapolating the straight line portion of the Tauc curve to $\alpha = 0$. The estimated band-gap of the thin film was found to be 3.849 eV, which is quite high and hence it can also be used in various optical devices.

4.3.7 Humidity Sensing

The optical humidity sensing characteristics for MnO_2-CoO thin film annealed at 650°C has been investigated and plotted in Fig.4.7 (a). The curve shows an almost linear decrement in transmitted power with a corresponding increase in %RH in all the lower (10-30 %RH), intermediate (30-70 %RH) and higher regions of %RH (70-90 %RH), maintaining a constant slope in the entire range of %RH. In our case, sensitivity is the most concerned parameter, calculated by taking the slope of the sensing response curve. Also, the sensitivity is defined as the ratio of the change in the output signal to that of the input signal, as shown by Eqn. 4.3:

$$\text{Sensitivity} = \Delta I_t/\Delta\%RH \ \mu W/\%RH \quad \text{…. (4.3)}$$

where ΔI_t is the change in the transmitted power of Laser light obtained at the detector and Δ%RH is the relative change in %RH, measured from hygrometer. So,

sensitivity has been calculated by taking the ratio of the difference in the initial and final readings of transmitted power to the corresponding difference in %RH. The sensitivity in the range 10-30 %RH is 2.85 µW/%RH, 30-70 %RH is 1.825µW/%RH and 70-90 %RH is 2 µW/%RH. The average sensitivity of the sensing element is taken as the average of all the values and is found ~ 2.225 µW/%RH as calculated from the blue-lined curve of Fig.4.7 (a). The red line in the curve of Fig.4.7 (a) shows the hysteresis while dehumidifying the environment inside the chamber. The average sensitivity, in this case, is found as ~1.875 µW/%RH showing 15.73% hysteresis.

Reproducibility is another most concerned parameter for an efficient sensor. It is the distribution of output when measurements are taken under a similar environmental state of affairs as earlier [34]. Here the experiment for observing the reproducibility of the sensor was performed and plotted in Fig.4.7 (b). The inset displays the error bars of the experiment. From the error bars, it can be observed that at 20 %RH, there is maximum error whereas it is minimum at 55 and 65 %RH. The sensitivity observed over the entire range of %RH, while observing the reproducibility, was 1.969 µW/%RH and results were found ~89% reproducible. This high reproducibility depicts the quite stable nature of the sensing element. Ageing effect is also an important sensor parameter. It is the distribution of sensor outputs when performing consecutive readings under similar conditions after a long time. The consecutive measurements were taken after one week, two weeks, one month and two months showing as green, red, blue and brown coloured curves respectively in Fig.4.7(c). The almost perfect overlapping among the curves indicates that nanostructured MnO_2-CoO is a quite stable material having the insignificant effect of ageing and the sensor is quite stable in the entire range of %RH. Response and recovery times were also measured for the reported sensor. The readings obtained during the experiment for calculating sensitivity, reproducibility and ageing effect are depicted in Table 4.1.

Response time is the time required to attain 10% of the final sensor output following stepwise ramping of %RH and recovery time is the time taken by the sensor signal to come back to its original value after a step concentration variation from a definite value to zero [35]. Here both the response and recovery times were calculated from Fig.4.7 (d) and it was observed that for sensing film, the response

time was 47 s and the recovery time was 59 s. The variations in output power relative to time are depicted in Table 4.2. Also, all the sensor parameters have been shown in Table 4.3.

It may be noted here that the film shows encouraging sensitivity due to rapid adsorption and desorption rate. A brief literature review has been shown in Table 4.4. Nanostructured MnO_2-CoO gel having high refractive index 1.448829, has a greater angle of transmittance. The laser light intensity after being transmitted from the film was collected on a photodetector through a lens combination. Besides the beautiful spherical shaped clusters and the flakes formation with enhanced surface morphology; wide optical energy band-gap is also an important factor responsible for high sensitivity of the sensing element. The low dimension of the material is also a very important factor responsible for good sensing property. As the grain size decreases, the aspect (surface to volume) ratio increases. By increasing aspect ratio more active sites for adsorption/desorption can be generated. It was observed that as the humidity inside the chamber increases, the transmitted power observed at the detector decreases. This decrease in output power with the corresponding increase in %RH is the responsible characteristic for its application as an opto-electronic humidity sensor.

The change in the transmitted power with respect to the variation of %RH can be explained on the basis of adsorption and desorption mechanism of the water molecule in the capillaries formed on the surface of nanostructured bimetallic oxide thin film. The sensing mechanism, dependent on the surface morphology is based on the chemisorption and physisorption of a water molecule. In the beginning, the nanostructured bimetallic oxide thin film was free from water molecules with only dehydrated air in its pores. When humidity was created inside the chamber using a humidifier, then at the low humid environment, adsorption of water vapour takes place rapidly on the surface of the film. The metal oxide surface being highly electrovalent has sufficient electrostatic force to break one of the O–H bonds of H_2O and form a strong chemical bond between M^+ (metal ion) and OH^- and forms the chemisorbed layer. With the increase in %RH inside the chamber, adsorption on the surface of the film increases and the refractive index of the material decreases and tends to the bending of transmitted laser light beam. In the mid humidity range (30-70

%RH), adsorption of water vapour in the form of OH^- ion not only takes place on the surface but also on the walls of capillaries of the film. This leads to the increase in the thickness of moisture layer which tends to a lateral shift of the transmitted light from the sensing element. So the number of light rays reaching the detector gradually decreases and therefore less power is obtained at the output. In high humid region (70-90 %RH), the condensation of water vapour takes place through the capillaries and forms a meniscus in the capillaries of the film in the form of a physisorbed layer. In this range, the moisture layer acquires the maximum thickness and thus the lateral shift of transmitted light takes place to its maximum level. Hence the highest reduction in transmitted power is obtained, as most of the power could not reach the detector and is scattered in the surroundings [41-43]. The whole sensing mechanism has been explained by the ray diagram in Fig. 4.8(a). The number of rays reaching the detector has been calculated on the above mentioned theoretical concept and the results well matched with the observed values as shown in Fig. 4.8(b).

4.4 Conclusion

Nanostructured MnO_2-CoO was successfully synthesized using metal carboxylates as precursors and thin films were fabricated via spin coating technique and annealed at 650°C. TEM investigated the minimum grain diameter of ~5.7 nm and SAED confirmed the polycrystalline nature. The minimum crystallite size as obtained from XRD was ~4 nm. Particle Size Analyzer also investigated the minimum range of particles between ~5-100 nm. SEM micrographs showed the enhanced surface area of the film by the formation of pores on the surface of the film. The Tauc plot obtained from the UV-Vis absorption spectrum estimated the optical energy band gap of 3.849 eV. The film was then employed efficaciously as opto-electronic humidity sensor and the average sensitivity was found as 2.225 µW/%RH along with the response and recovery times as 47 s and 59 s.

References

[1] G. Korotcenkov, Metal oxides for solid-state gas sensors: What determines our choice?, Materials Science and Engineering B 139 (2007) 1–23.

[2] E. Kanazawa, G. Sakai, K.Shimanoe, Y. Kanmura, Y. Teraoka, N. Miura, N. Yamazoe, Metal oxide semiconductor N_2O sensor for medical use, Sens. Actuators B: Chem. 77 (2001) 72–77.

[3] X.W. Xie, Y. Li, Z.Q. Liu, M. Haruta, W.J. Shen, Low-temperature oxidation of CO catalysed by Co_3O_4 nanorods, Nature 458 (2009)746–749.

[4] C.S. Pan, D.S. Zhang, L.Y. Shi, J.H. Fang, Template-free synthesis, controlled conversion, and CO oxidation properties of CeO_2 nanorods, nanotubes, nanowires, and nanocubes, Eur. J. Inorg. Chem. 15 (2008) 2429–2436.

[5] S.L. Brock, N. Duan, Z.R. Tian, O. Giraldo, H. Zhou, S.L. Suib, A review of porous manganese oxide materials, Chem. Mater. 10 (1998) 2619–2628.

[6] Y. Li, X.Y. Yang, Y. Feng, Z.Y. Yuan, B.L. Su, One-dimensional metal oxide nanotubes, nanowires, nanoribbons, and nanorods: synthesis, characterizations, properties and applications, Critical Reviews in Solid State and Materials Sciences 37(1) (1998) 1-74.

[7] J. Dakin, B. Culshaw, Vanadium pentoxide nanobelts: highly selective and stable ethanol sensor materials, Optical Fiber Sensors: Principles and Components, first ed., Artech House, Boston, 1988.

[8] J.F. Liu, X. Wang, Q. Peng, Y.D. Li, Vanadium pentoxide nanobelts: highly selective and stable ethanol sensor materials, Adv. Mater. 17 (2005) 764–767.

[9] X. Zhang, G. Wang, W. Zhang, N. Hu, H. Wu, B. Fang, Seed-mediated growth method for an epitaxial array of CuO nanowires on the surface of Cu nanostructures and its application as a glucose sensor, J. Phys. Chem. C 112 (2008) 8856–8862.

[10] G.I. Dzhardimalieva, A.D. Pomogailo, Macromolecular metal carboxylates as precursors of metallopolymer nanocomposites. Chapter in book: Nanocomposites: In situ Synthesis of Polymer-Embedded Nanostrutures (ed. By L. Nicolais, G. Carotenuto). John Wiley &Sons Inc., Hoboken, New Jersey (2014) 97-114.

[11] A.D. Pomogailo, G.I. Dzhardimalieva, Nanostructured Materials Preparation via Condensation Ways. Springer (2014) 460.

[12] M. Lawecka, A. Slawska-Wanievska, K. Racka, M. Leonowicz, G.I. Dzhardimalieva, A.S. Rozenberg, A.D. Pomogailo, Structure and magnetic properties of polymer matrix nanocomposite processed by pyrolysis of cobalt(II) acrylate, J. Alloys Comp. 369 (2004) 244-246.

[13] X.M. Liu, S.Y. Fu, Synthesis of nanocrystalline $Zn_{0.5}Mn_{0.5}Fe_2O_4$ via in situ polymerization technique, J. magnetism and magnetic materials 308(1) (2007) 61-64.

[14] X.M. Liu, S.Y. Fu, H.M. Xiaoa, C.J. Huang, Synthesis of nanocrystalline spinel $CoFe_2O_4$ via a polymer-pyrolysis route, Physica B 370 (2005) 14-21.

[15] H.M. Xiao, X.M. Liu, S.Y. Fu, Synthesis, magnetic and microwave absorbing properties of core-shell structured $MnFe_2O_4/TiO_2$ nanocomposites, Compos. Sci. Technol. 66 (2006) 2003-2008.

[16] S. Sikarwar, B.C. Yadav, Opto-electronic Humidity Sensor: A Review, Sens. Actuators A: Phy. 233 (2015) 54–70.

[17] Y. Zhou, H. Wang, M. Sheng, Q. Zhang, Z. Zhao, Y. Lin, H. Liu, G.R. Patzke, Environmentally friendly room temperature synthesis and humidity sensing applications of nanostructured $Bi_2O_2CO_3$, Sens. Actuators B: Chem. 188 (2013) 1312–1318.

[18] P. Chaudhary, S. Sikarwar, B.C. Yadav, G.I. Dzhardimalieva, N.D. Golubeva, I.E. Uflyand, Synthesis and characterization of copper (II) nitrate polyacrylamide & its application as opto-electronic humidity sensor, Sens. Actuators A: Phy. 263 (2017) 415–422.

[19] J. Ascorbe, J.M. Corres, I.R. Matias, F.J. Arregui, High sensitivity humidity sensorbased on cladding-etched optical fiber and lossy mode resonances, Sens. Actuators B: Chem. 233 (2016) 7–16.

[20] B.V. Golovkin, G.V. Bazuev, Phase equilibria in the system CaO-CoO-Co_2O_3-MnO-MnO_2, Russ. J. Gen. Chem. 80(2) (2010) 213–218.

[21] C. Li, J. Balamurugan, T.D. Thanh, N.H. Kim, J.H. Lee, 3D hierarchical CoO@MnO_2 core–shell nanohybrid for high-energy solid state asymmetric supercapacitors, J. Mater. Chem. A5 (2017) 397-408.

[22] W. Huang, H. Zhong, D. Li, P. Tang and Y. Feng, Reduced Graphene Oxide Supported CoO/MnO_2 Electrocatalysts from Layered Double Hydroxides for Oxygen Reduction Reaction, Electrochimica Acta 173 (2015) 575–580.

[23] T. Kato, Y. Tanaka, T. Hirata, S. Kumamoto, K. Miyazaki, Humidity sensing characteristics of manganese oxide prepared by sol-gel method, J. Mat. Sci. Letters 16 (1997) 1771-1773.

[24] K. Miyazaki, M. Hieda, T. Kato, Development of a Novel Manganese Oxide-Clay Humidity Sensor, Ind. Eng. Chem. Res. 36 (1997) 88-91.

[25] M.Z. Yang, C.L. Dai, P.J. Shih, Y.C. Chen, Cobalt oxide nanosheet humidity sensor integrated with circuit on chip, Microelectronic Engineering 88 (2011) 1742-1744.

[26] B.C. Yadav, R.C. Yadav, S. Singh, P.K. Dwivedi, H. Ryu, S. Kang, Nanostructured cobalt oxide and cobalt titanate thin films as optical humidity sensor: A new approach, Optics & Laser Technology 490 (2013) 68-74.

[27] S. Sikarwar, B.C. Yadav, S. Singh, G.I. Dzhardimalieva, S.I. Pomogailo, N.D. Golubeva, A.D. Pomogailo, Fabrication of nanostructured yttria stabilized zirconia multilayered films and their optical humidity sensing capabilities based on transmission, Sens. Actuators B: Chem. 232 (2016) 283–291.

[28] L.E. Scriven, Physics and applications of dip coating and spin coating, MRS proceedings, 1988, 121.

[29] T.K. Pathak, J.K. Rajput, V. Kumar, L.P. Purohit, H.C. Swart, R.E. Kroon, Transparent conducting ZnO-CdO mixed oxide thin films grown by the sol-gel method, J. Colloid and Interface Sci. 487 (2017) 378–387.

[30] D.A.H. Hanaor, G. Triani, C.C. Sorrell, Morphology and photocatalytic activity of highly oriented mixed-phase titanium dioxide thin films, Surface and coatings technology 205(12) (2011) 3658–3664.

[31] K.S. Prasad, A. Patra, Green synthesis of MnO_2 nanorods using Phyllanthusamarus plant extract and their fluorescence studies, Green Processing and Synthesis 6(6) (2017).

[32] B.K. Pandey, A.K. Shahi, R. Gopal, Magnetic colloid by PLA: Optical, magnetic and thermal transport properties, App. Surf. Sci. 347 (2015) 461–470.

[33] D.P. Singh, S. Pandey, S.K. Gupta, R. Manohar, A. Daoudi, A.H. Sahraoui, C. Phadnis, S. Mahamuni, Quenching of photoluminescence and enhanced contrast offerroelectric liquid crystal dispersed with $Cd_{1-X}Zn_XS$/ZnS core/shell nanocrystals, J. Luminescence 173 (2016) 250–256.

[34] B.C. Yadav, R.C. Yadav, P.K. Dwivedi, Sol-gel processed (Mg-Zn-Ti) oxide nanocomposite film deposited on Prism base as an Opto-Electronic Humidity Sensor, Sens. Actuators B: Chem. 148 (2010) 413-419.

[35] S. Kozhukharov, Z. Nenova, T. Nenov, N. Nedev, M. Machkova, Humidity sensing elements based on cerium doped titania-silica thin films prepared via a sol-gel method, Sens. Actuators B: Chem. 210 (2015) 676–684.

[36] N. Irawati, T.N.R. Abdullah, H.A. Rahman, H. Ahmad, S.W. Harun, PMMA microfiber loop resonator for humidity sensor, Sens. Actuators A: Phy. 260 (2017) 112–116.

[37] Y. Wang, C. Shen, Fiber optic humidity sensor based on the graphene oxide/PVA composite film, Opt. Commun. 372 (2016) 229–234.

[38] B.C. Yadav, R.C. Yadav, G.C. Dubey, Optical humidity sensing behaviour of sol-gel processed nanostructured ZnO films, OpticaApplicata39(3) (2009) 617–627

[39] B.C. Yadav, S. Sikarwar, R. Yadav, P. Chaudhary, G.I. Dzhardimalieva, N.D. Golubeva, Preparation of zinc (II) nitrate polyacrylamide (PAAm) and its opto-electronic application for humidity sensing, J Mater Sci: Mater Electron(2018) 1-8.

[40] S. Sikarwar, A. Kumar, B.C. Yadav, G.I. Dzhardimalieva, N.D. Golubeva, Nanostructured spherical-shaped Sc(III) Polyacrylate for monitoring the moisture level, IEEE sensors (2018).

[41] F. Xu, L. Zhang, X. Yin and L. Tong, Polymer single-Nanowire optical sensors, Nano Lett.8 (2008) 2757–2761.

[42] B.C. Yadav, K.S. Chauhan, S. Singh, R.K. Sonker, S. Sikarwar, R. Kumar, Growth and characterization of sol-gel processed rectangular shaped nanostructured ferric oxide thin film followed by humidity and gas sensing, J. Mater. Sci.: Mater. Electron 28 (2017) 5270–5280.

[43] Z. Nenova, S. Kozhukharov, T. Nenov, N. Nedev, M. Machkova, Combined influence of titania and silica precursors on the properties of thin film humidity sensing elements prepared via a sol-gel method, Sens. Actuators B: Chem. 224 (2016) 143–152.

Tables

Table 4.1: Variations in the transmitted intensity of light through the film of MnO_2-CoO as RH increases from 10-90%.

%RH	Sensing response (µW)		Reproducibility (µW)		Ageing effect (µW)			
	Increasing mode	Decreasing mode	Increasing mode	Decreasing mode	One week	Two weeks	One month	Two months
10	440.5	430.1	437.5	427.2	436.2	430.2	428.2	425.2
15	428.2	424.2	425.1	424.2	427.3	428.3	420.3	418.2
20	419.1	415.4	410.3	421.3	420.1	422.4	412.4	410.1
25	412.3	408.5	410.5	418.5	414.2	417.5	410.5	405.2
30	403.4	402.6	401.2	412.4	406.4	410.2	400.1	398.5
35	392.2	399.2	389.1	405.2	398.6	403.3	395.2	392.6
40	382.4	392.4	379.5	396.1	390.5	395.1	388.3	385.4
45	374.6	388.3	373.3	387.6	380.4	389.4	381.4	375.3
50	367.2	375.1	365.4	380.5	370.2	375.2	368.2	370.2
55	356.1	362.3	356.1	371.4	360.1	362.3	359.2	360.1
60	345.3	352.2	342.2	355.3	350.3	351.1	345.2	355.5
65	332.2	345.6	333.3	343.2	337.1	340.1	338.3	348.6
70	320.6	327.5	318.1	330.1	324.2	330.2	327.3	325.1
75	305.5	315.4	303.4	315.5	311.3	318.3	315.1	310.4
80	294.2	300.3	291.2	300.1	290.1	305.3	300.2	290.3
85	284.3	290.1	281.5	290.3	287.3	291.1	288.3	282.2
90	273.5	280.2	273.5	285.2	282.2	280.2	276.1	276.2

Table 4.2: Variations of time in seconds with output in μW for observing response and recovery times.

Time (s)	Output power during adsorption (μW)	Output power during desorption (μW)
0	440.5	280.2
100	423.3	290.1
200	410.2	300.3
300	395.3	312.4
400	383.1	330.6
500	378.5	339.2
600	371.4	348.5
700	362.6	352.4
800	350.4	350.4

Table 4.3: Sensing parameters for nanostructured MnO_2-CoO thin film based sensor.

Sensor parameter	Average sensitivity	Reproducibility	Ageing effect	Response time	Recovery time
Values	2.225 μW/%RH	~ 89%	Insignificant	47 s	59 s

Table 4.4: A brief literature review showing the humidity sensing capability of recently reported materials.

S. No.	Material	Sensitivity	Ref
1.	PMMA microfiber loop resonator (PMLR) coated with ZnO	0.1746 dBm/%RH	[36]
2.	Graphene oxide/PVA	0.193 dB/%RH	[37]
3.	$Cu(NO_3)_2{\cdot}(AAm)_4{\cdot}2H_2O$	0.838 μW/%RH	[18]
4.	Zinc oxide	0.88 μW/%RH	[38]
5.	$Zn(NO_3)_2{\cdot}(AAm)_4{\cdot}2H_2O$	1.831 μW/%RH	[39]
6.	Cobalt titanate	1.84 μW/%RH	[26]
7.	$MgTiO_2$	1.86 μW/%RH	[34]
8.	Y_2O_3-ZrO_2	1.937 μW/%RH	[27]
9.	$Sc(CH_2{=}CH\text{-}COO)_3$	2.1 μW/%RH	[40]
10.	MnO_2-CoO	2.225 μW/%RH	Present work

Figures

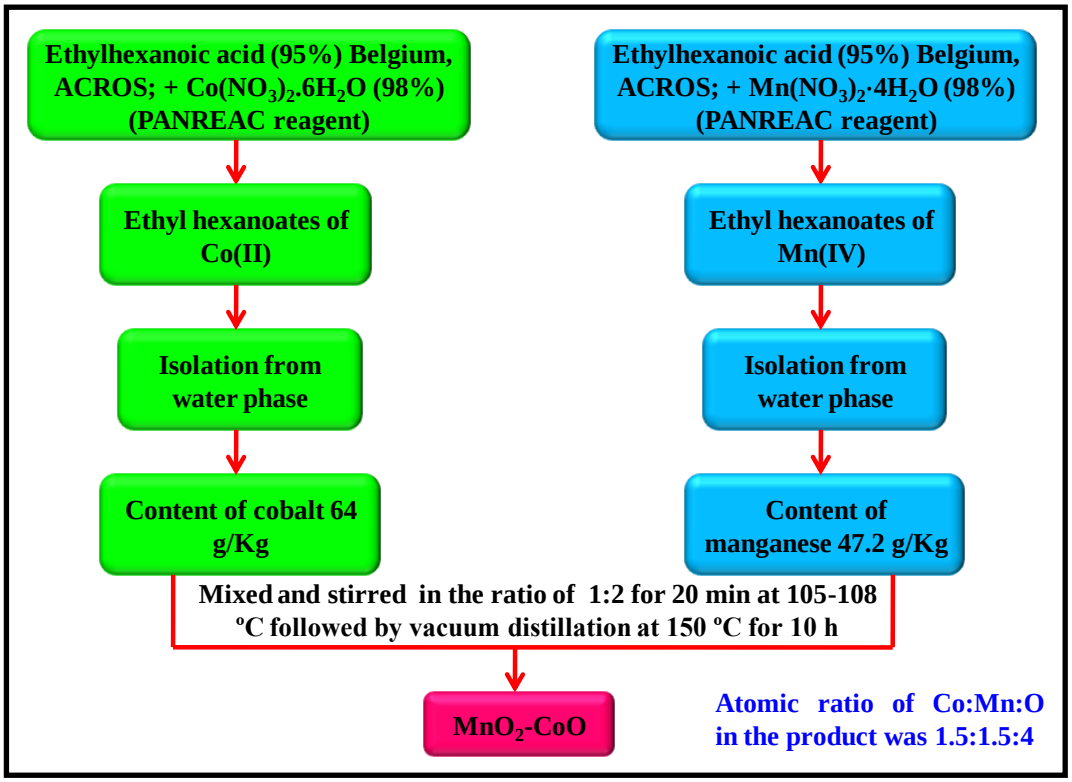

Figure 4.1: Schematic representation of the preparation of nanostructured MnO_2-CoO composite.

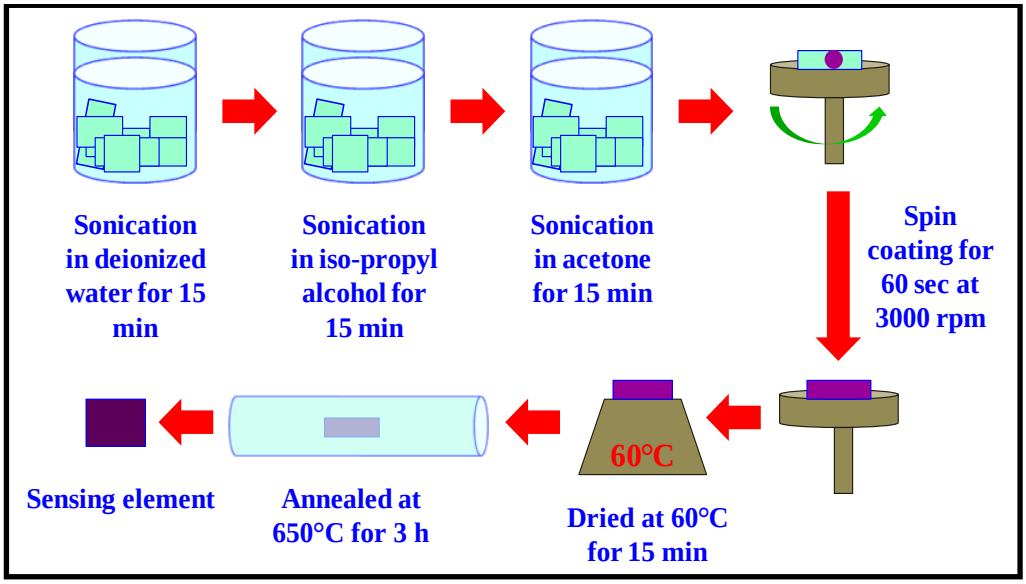

Figure 4.2: Schematic representation of the fabrication of sensing element.

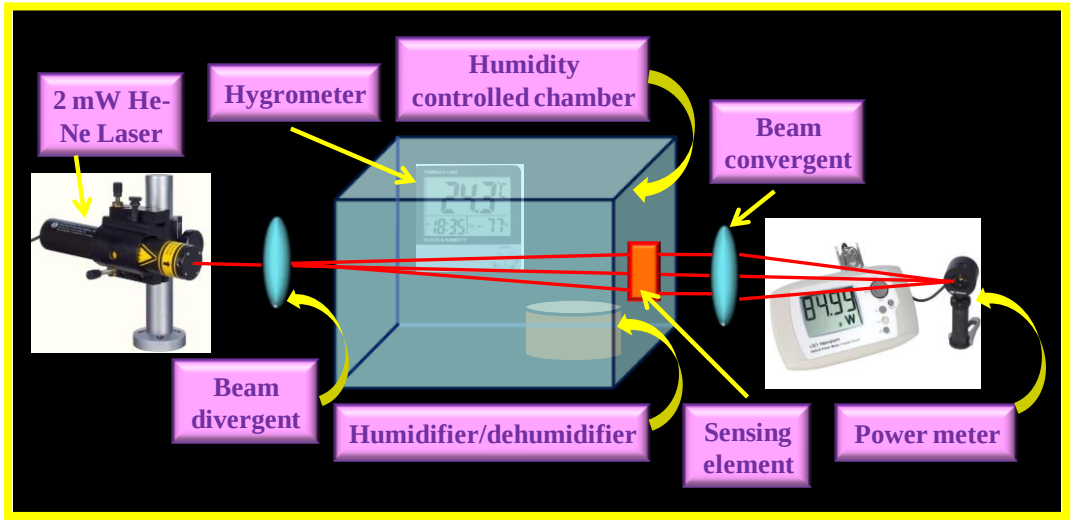

Figure 4.3: Schematic of transmission based opto-electronic humidity sensing set-up.

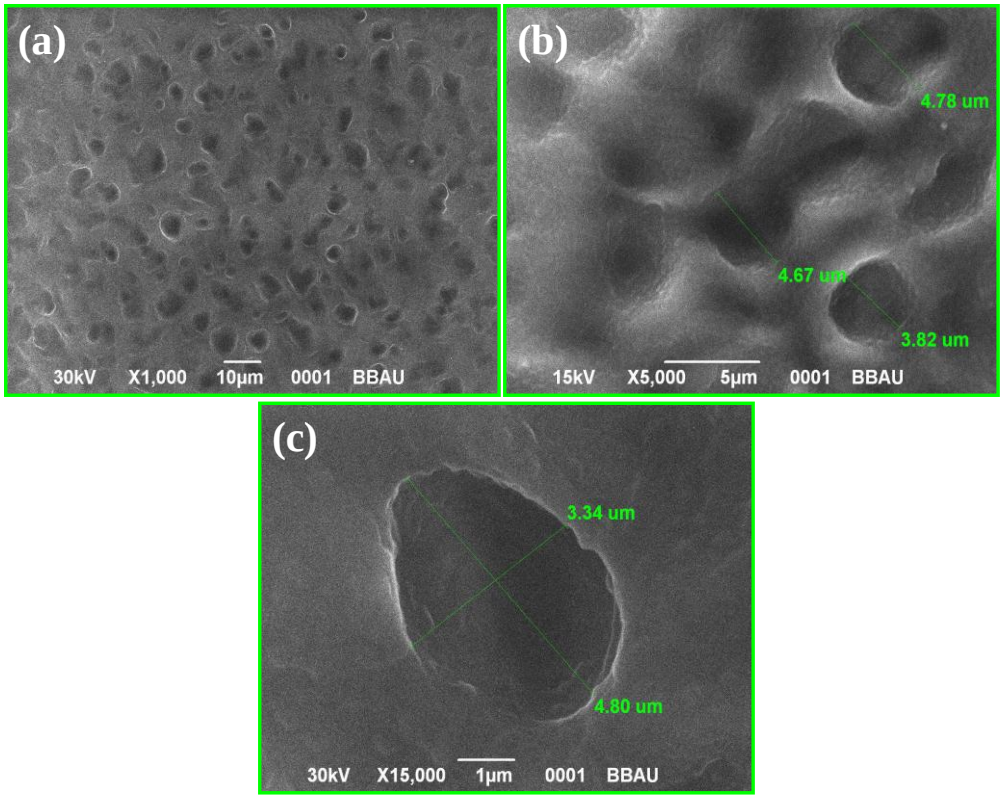

Figure 4.4:SEM micrographs of nanostructured MnO_2-CoO thin film at (a) 10 µm, (b) 5 µm and (c) 1 µm, showing the porous nature and hence enhanced surface area and availability of more active sites suitable for adsorption/desorption of moisture.

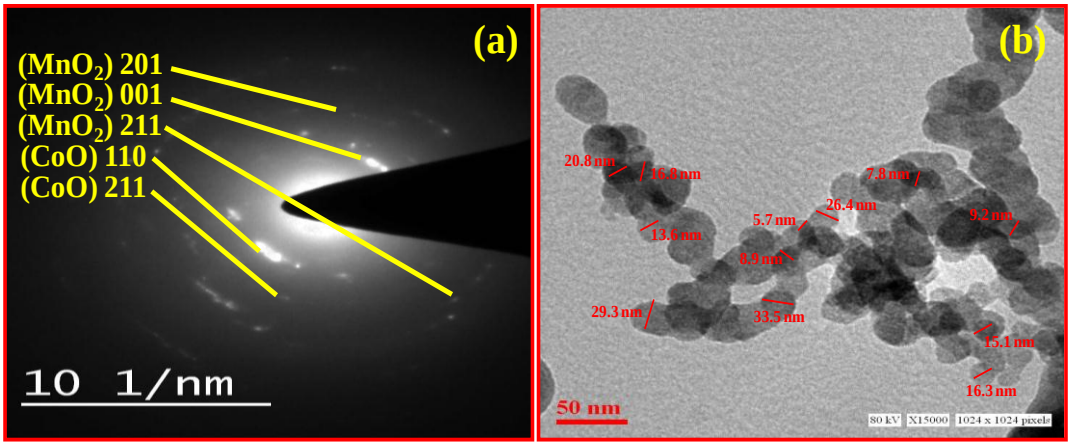

Figure 4.5: Images showing (a) SAED pattern where the concentric rings show the polycrystalline nature of MnO_2-CoO nanocomposite and (b) TEM image at 50 nm scale showing all the particles of nano dimension with a minimum grain diameter of ~5.7 nm.

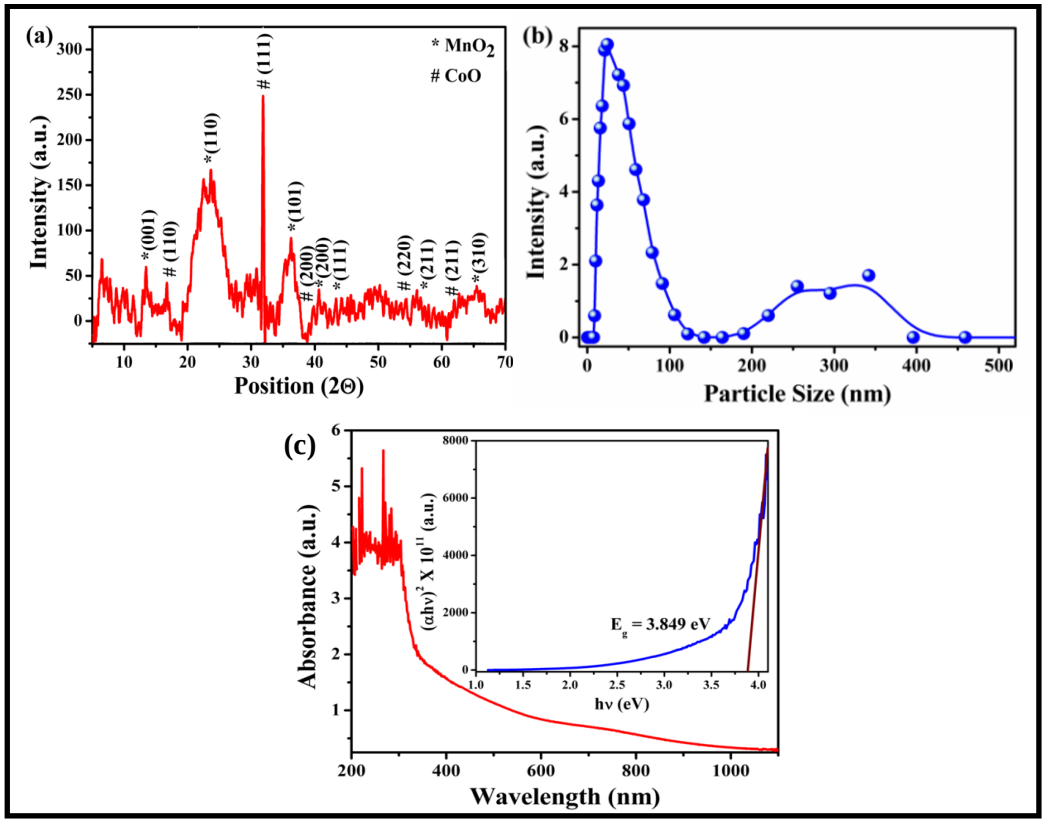

Figure 4.6 Curves showing (a) XRD pattern of nanostructured MnO_2-CoO composite from which minimum crystallite size was estimated ~4 nm (b) Particle size distribution in the dilute solution depicting majority of the particles in the range ~5-100 nm (c) Absorption spectrum of thin film and inset display the Tauc

plot for optical energy band-gap calculation showing the optical band-gap of 3.849 eV.

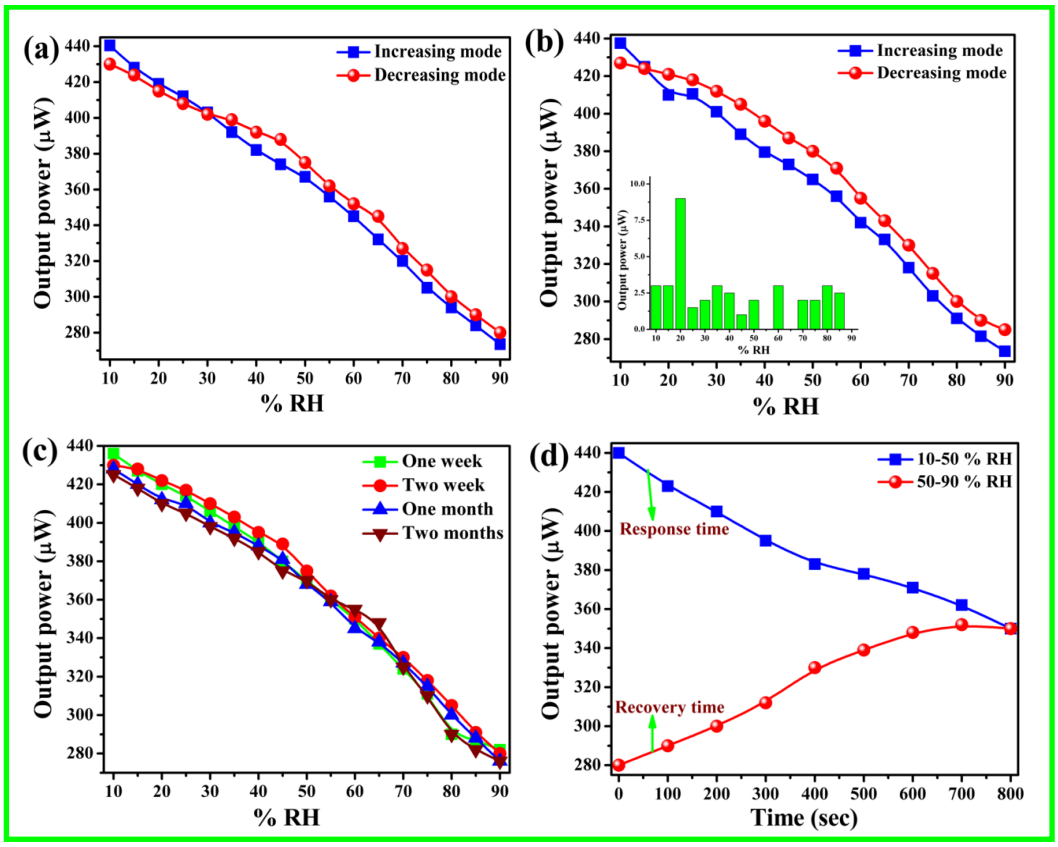

Figure 4.7 Variation of transmitted power with %RH for nanostructured MnO_2-CoO thin film to investigate the [a] sensing response (sensitivity observed was 2.225 μW/%RH) [b] reproducibility characteristics (~ 89% reproducible with 1.969 μW/%RH in this case) where inset figure displays the error bars [c] ageing effect (after one week, two weeks, one month and three months), and [d] response (47 s) and recovery (59 s) times.

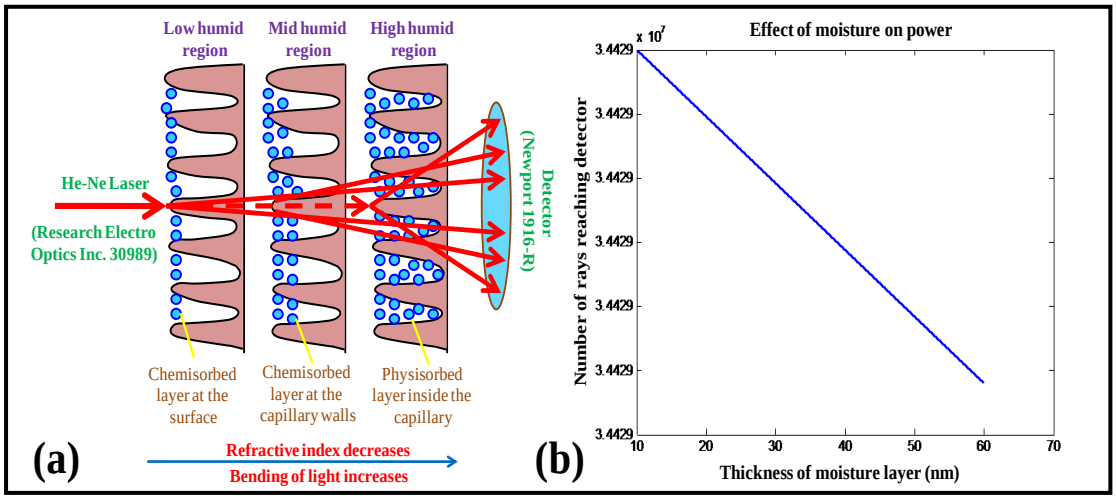

Figure 4.8 Ray diagram of sensing mechanism showing the decrease in output power with exposure of %RH showing (a) surface chemisorption at lower humidity (10-30 %RH), (b) chemisorption on capillary walls at intermediate humidity (30-70 %RH) and (c) physisorption with full capillary condensation at higher humidity (70-90 %RH).

CHAPTER 5

Synthesis of La_2O_3-Cr_2O_3-SrO Nanocomposite by Pyrolysis of Metal Carboxylates; its Characterization and Humidity Sensing

The present chapter reports the synthesis of nanocomposite La_2O_3-Cr_2O_3-SrO by pyrolysis of metal carboxylates and effect of humidity on the transmitted power through its thin films at room temperature. The refractive index of the material was found as 1.442302. The film was investigated using SEM, XRD and UV-Vis spectrophotometer. SEM revealed the uniform mesoporous nature and XRD showed the crystalline nature of the material with minimum crystallite size of 9 nm. TEM gave the minimum grain diameter of ~ 2.7 nm. Particle Size Analyzer reported that all the particles in the solution are in the range ~2-50 nm. From UV-Vis spectrum, it was found that the absorption through the material takes place in UV-region and the energy band-gaps of the one-, two-, three- and four-layered films were found to be 3.842, 3.837, 3.802 and 3.789 eV respectively. The dilute solution of the material was investigated through TEM and it was found that the minimum grain diameter was ~2.71 nm. The film was then employed as electrical humidity sensor from which the sensitivities were observed as 9.369, 6.006, 3.699 and 1.995 MΩ/%RH respectively for one-, two-, three- and four-layered films. Electrical sensors have certain drawbacks, therefore, the films were further employed as transmission based opto-electronic humidity sensor. In this case, the sensitivity for one-, two-, three- and four- layered films were found to be 3.604, 3.444, 3.250 and 3.063 µW/%RH respectively. Response and recovery times for one-layered sensing element were found as 15 s and 56 s whereas the reproducibility of the results was ~95.71%. Experiments were repeated time to time and found that ageing effect on sensor is very less. The investigated sensor being optical in nature has the capability of multiplexing the information with the signal.

5.1 Introduction

Solid electrolytes are perspective materials for sensors, fuel elements and other electrochemical devices. Sensors based on solid oxide electrolytes possess unique properties such as precision, low response limit, and stability in the gas detection. The $La_{1-x}Sr_xCrO_3$ perovskite oxides are of interest due to high chemical stability in oxidizing and reducing atmosphere [1-2]. The gas sensing properties of nanocrystalline $La_{1-x}Sr_xCrO_3$ (x = 0.0, 0.1, 0.2, 0.3 & 0.4) are reported and the gas sensor based on the nanocrystalline $La_{0.7}Sr_{0.3}CrO_3$ material shows good sensitivity and selectivity with the H_2S gas [3].

Numerous methods for the preparation of metal-containing composites are known. The key method is thermolysis of metal compounds that are readily decomposed both in the pure state and in the polymer matrix (carbonyls, nitrosyls, thiolates, saturated carboxylic acid salts, organometallic and complex compounds) where the destruction of organic part affords the polymeric shell [4]. By combining the synthesis and pyrolysis processes, heterometallic ceramics of various types have been obtained, for example, perovskites ABO_3. The natural perovskite $CaTiO_3$ mineral has a pseudo-cubic crystal lattice in which large cations (A) are located at cell vertices, small cations reside at the cell centers, and oxygen ions are at the midpoints of the faces. These materials are widely used in electronics owing to their specific ferro-, piezo- and pyroelectric properties; for example, $BaTiO_3$ is used in the capacitor industry [5]. Perovskite-type ferrites $M_3Fe_2O_{7x}$ (M = Sr, Ba) with a particle size of 50 ± 55 nm are formed upon thermal decomposition of molecular citrate precursors at a lower temperature (873 K) than that used in conventional ceramic production processes [6].

La_2O_3, a p-type semiconductor, has a high band gap with lowest lattice energy and very high dielectric constant. It is an odourless, white solid insoluble in water but soluble in dilute acid and depending on the pH, different crystal structures can be obtained [7]. Cr_2O_3 is one of the principal oxides of chromium and is used as a pigment. In nature, it occurs as the rare mineral eskolaite [8]. SrO is completely insoluble; has a high melting and boiling point and displays non-flammable characteristics [9]. All these compounds being hygroscopic, adsorb moisture and convert to their respective hydroxides.

Humidity is a sensible health parameter for the human. Also, it plays a vital role in industrial and environmental monitoring as water vapours consist of highly reactive dipolar molecules which get condensed on or evaporate from the surface even with slight variations in temperature [10]. Therefore, measurement of humidity is quite necessary in the current scenario. A lot of research has been done in this field and few of the latest are shown in Table 5.1. In the present work, an effort has been made to synthesize nanostructured composite of La_2O_3-Cr_2O_3-SrO using chemical extraction route and the sensing element was fabricated using spin coating technique. Initially, the relationship between humidity and electrical parameters were measured but electrical mode has certain drawbacks, therefore, its optical counterpart was employed which is more advantageous.

5.2 Experimental Details

5.2.1 Synthesis

Reagents: Ethylhexanoic acid (95%), Belgium, ACROS; $La(NO_3)_3{\cdot}6H_2O$ "chemical purity", $Cr(NO_3)_3{\cdot}6H_2O$ ("PANREAC"**)**, $Sr(NO_3)_2$ (ACS reagent, ≥99.0%) are used as received. Metal hexanoates were synthesized by the extraction method in the two-phase system of metal nitrate solution-organic acid by the following reaction given in Eqn 5.1:

$$(M^{n+})_{aqua} + CH_3(CH_2)_3CH(C_2H_5)COOH \rightarrow M[CH_3(CH_2)_3CH(C_2H_5)COO]_n + nH^+ \quad \ldots\ldots (5.1)$$

(M^{n+} - metal ion, n = 2, 3, 4).

Extraction was carried out in the acid medium for 0.5 h; pH was controlled by using the NH_4OH solution. The water phase was isolated in a separation funnel. The contents of lanthanum, chromium and strontium in the extracts were 68.4, 34 and 82 g/Kg, respectively. Then the mixture of metal hexanoate's extracts in the required weight ratio 4:5:1 was stirred for 20 min at 105-108ºC followed by vacuum distillation at 150ºC for 10 h. La:Cr:Sr atomic ratio in the products obtained was equal to 0.7:1:0.3. The schematic for the synthesis process is shown in Fig. 5.1.

5.2.2 Fabrication of Sensing Element

Quality of the coated films can be monitored by controlling the preparation conditions (solution concentration, spinning speed and temperature of heating/ annealing). Here spin coating technique [20] was used to deposit the uniform thin films on flat borosilicate substrates of dimensions 1.5 × 1.5 × 0.5 cm^3. Prior to this, the substrates were rinsed in an ultrasonic bath (WUC-AO2H) by immersing in lab detergent (Extran), followed by de-ionized water, isopropyl alcohol and acetone respectively for 10 min each. Further, heat treatment (100°C for 15 min) was given to the substrates to evaporate organic impurities. Then these substrates were used for the deposition of films. Initially, the single-layered thin film was deposited at a spinning speed of 3000 rpm and dried for 15 min at 60°C. Similarly, 2, 3 and 4 layered films were deposited one by one. Further, the films were annealed at 400°C for 3 h and then used as sensing elements towards humidity. Schematic diagram for film fabrication is shown in Fig. 5.2.

5.2.3 Description of Sensing Set-up

The electrical humidity sensing set-up is shown in Fig. 5.3 which consists of a humidity controlled chamber in which the sensing element was fixed using silver electrodes. The humidification and dehumidification inside the chamber was done using the saturated aqueous solutions of K_2SO_4 and KOH respectively. With increase in time these saturated solutions provide/absorb water vapours to/from the environment of the chamber and hence do humidification/dehumidification in a regular manner. Relative humidity of the chamber is measured using standard hygrometer (HTC-1). Variations in electrical impedance with respect to the variations in %RH of the sensing element have been observed using the Impedance Analyzer (Wayne Kerr Precision Component Analyzer, 6440B).

The experimental set-up used for opto-electronic humidity sensing is already described in previous chapters in Section 2.2.3 and Section 4.2.3 of Chapters 2 and 4 respectively. It consists of a He-Ne Laser as an input light source with humidity controlled chamber containing the sensing element on one of its walls and a photodetector to obtain the transmitted power from the film at the output. The whole sensing set-up was kept on a Vibration free table.

5.2.4 Characterization Techniques

Nanostructured La_2O_3-Cr_2O_3-SrO was investigated through digital refractometer (Anton Par Abbemat 550) at room temperature with an accuracy of 0.000001. The technique involves fast and non-destructive measurements, calibrated with official standards. The structural investigation was done through X-ray diffractometer X'Pert Pro recording system (PANalytical, Netherlands) using Cu K_α (λ = 1.5406 Å) radiation, operated at 45 kV and 40 mA from 20° to 80°; typical 2θ step size: 0.008°. TEM analysis of dilute material loaded over carbon-coated copper grid was carried out using FEI-G2 SPRIT, Netherland at the scale of 100 and 200 nm scales. Further, the particle size was confirmed from Particle Size Analyzer (Nano-ZS90). The morphological investigation was done using High-Resolution Scanning Electron Microscope (SUPRA 40, Zeiss). For the optical investigation, UV–Vis Spectrophotometer (Evolution 201) was used to record the UV–Vis absorption spectra of films in the wavelength range 190–1100 nm.

5.3 Results and Discussion

5.3.1 Refractometer Analysis

The film was investigated through a digital refractometer (Anton Paar Abbemat 550) at room temperature with an accuracy of 0.00001 and it was found that the refractive index of the film is 1.442302.

5.3.2 X-ray Diffraction Analysis

The formation and the phase of the one layered sensing film of nanostructured La_2O_3-Cr_2O_3-SrO were investigated with X-ray diffractometer, the pattern of which is shown in Fig. 5.4(a). The hatch peaks corresponding to (100), (101) and (110) lattice planes denote La_2O_3 (confirmed from JCPDS file no. 05-0602), the star peaks corresponding to (012), (104), (110), (113) and (202) lattice planes denote Cr_2O_3 (confirmed from JCPDS file no. 38-1479) whereas plus peaks corresponding to (220), (031), (131), (002) and (222) lattice planes denote SrO (confirmed from JCPDS file no. 34-0379) in the nanostructured composite. The average crystallite size as obtained from Debye Scherrer Formula is 32.72 nm whereas the minimum crystallite size as calculated from the plane (104) is 9.32 nm.

5.3.3 Particle Size Analysis

The particle size of nanostructured composite of La_2O_3-Cr_2O_3-SrO dissolved in ethyl alcohol was analyzed by Particle Size Analyzer and the corresponding data is plotted in Fig. 5.4(b). It is a dynamic light scattering system for nanoparticle and molecular size measurement. From the particle size distribution curve, it can be observed that all the particles are in the range ~2-50 nm which is quite comparable to the results obtained from XRD and TEM.

5.3.4 Scanning Electron Microscopy Analysis

The SEM analysis of one layered La_2O_3-Cr_2O_3-SrO film has been carried out at various scales and resolutions using High-Resolution Scanning Electron Microscope (SUPRA 40, Zeiss). The SEM images at 20 µm, 2 µm, 1 µm and 200 nm scales are shown in Fig. 5.5(a-d). Surface morphology of the film exhibits uniform pores throughout the surface of the film. It may be seen from Fig. 5.5(c & d) that particles are agglomerated to form clusters and thereby leaving pores. These pores are quite favourable for the adsorption/desorption process as they serve as active centers for humidity adsorption/desorption. Hence the sensitivity of the sensor depends on the number and size of these pores.

5.3.5 Transmission Electron Microscopy Analysis

Fig. 5.6 (a & b) shows the TEM image of nanostructured La_2O_3-Cr_2O_3-SrO dilute precursor solution at 200 and 100 nm scale. TEM image shows the uniform distribution of spherical particles of nano dimension. It can be seen from the image that most of the particles are less than 20 nm, which shows the beauty of the synthesis mechanism and monitor over physical parameters. The minimum grain diameter as obtained from the micrograph is ~ 2.71 nm which is not yet reported in the literature.

5.3.6 UV-visible Absorption Analysis

The optical absorbance spectra of La_2O_3-Cr_2O_3-SrO thin films deposited separately on the glass substrate is shown in Fig. 5.7(a-d). Spectra were recorded in the wavelength range 190-1100 nm using UV-Vis Spectrophotometer (Evolution 201). It is observed from the figure that film exhibit absorption (370 nm) in the UV-range. Also, it can be seen from all the curves, there is presence of a hump near UV-region and as the thickness of the film increases, the height of the hump also increases. This hump is actually the blue shift, which increases with the thickness of

the film. As the thickness increases, the electronic perturbation in the film increases. Using these spectra, Tauc plot was made where the variation of optical absorption coefficient (α) with photon energy hν was obtained using the absorption data of different films and is shown in the inset of Fig. 5.7(a-d). The optical band-gap E_g of the films, defined as the minimum threshold energy required for photons to be absorbed [12], can be obtained from the Eqn. 5.2:

$$\alpha h\nu = A(h\nu - E_g)^m \quad \text{..... (5.2)}$$

Here, 'C' is constant, 'ν' is the transition frequency and'm' defines the nature of band transition. The symbol 'm' can assign any of the values from 1/2, 3/2, 2 and 3 which corresponds to direct allowed, directly forbidden, indirect allowed and indirect forbidden transitions, respectively. Here the transition being direct allowed type; 'm' is taken as 1/2 in the above relation. E_g was observed by extrapolating the straight line portion of $(\alpha h\nu)^2$ vs. hν curves to α = 0. The estimated band-gap of the thin film was found to be 3.842, 3.837, 3.802 and 3.789 eV. It can be observed that with the increase in the thickness of the film, optical band-gap decreases. This is due to the decrease in the absorption which further leads to a decrease in E_g.

5.4 Humidity Sensing

5.4.1 Electrical Humidity Sensing

From Fig. 5.8(a-d), electrical sensing response of La_2O_3-Cr_2O_3-SrO multilayered films towards %RH can be observed. For a good sensor, sensitivity plays the most vital role in analyzing its capability. In the electrical mode of sensing, generally, sensitivity is defined as the change in impedance (ΔZ) corresponding to the change in %RH (Δ%RH), as given by the Eqn. 5.3

$$\text{Sensitivity} = \frac{\Delta Z}{\Delta \%RH} \ \text{MΩ/\%RH} \quad \text{.... (5.3)}$$

Fig. 5.8(a-d) shows that initially, the films were most responsive towards %RH but as the %RH increases, the sensing element becomes slightly responsive in the mid humid range and least in the high humid range. The sensitivity calculated at room ambient for one-, two-, three- and four-layered nanostructured La_2O_3-Cr_2O_3-SrO films from Fig. 5.8(a-d) is 9.369, 6.006, 3.699 and 1.995 MΩ/%RH respectively.

The readings from which sensing response curve plotted in Fig.5.8 is depicted in Table 5.2.

The decrease in impedance relative to increasing in %RH can be explained on the basis of chemisorption and physisorption of water molecules on the porous surface of the nanostructured La_2O_3-Cr_2O_3-SrO film. Initially, with the exposure of humidity, chemisorption of water vapour takes place on the surface of the film. Due to high cationic charge density of metal oxide surface, the electrostatic force is high enough to break one of the O–H bonds of H_2O and form a strong chemical bond between M^+ (metal ion) and OH^-. Thus, an initial layer formed in the less humidity (< 40%RH) is chemisorbed. The released H^+ from H_2O is responsible for the rapid increase in charge content and hence a sharp decrease in impedance of nanostructured La_2O_3-Cr_2O_3-SrO film [22] is taken place. This is the most sensitive range for humidity as a large amount of charge is created in this range due to the chemisorptions. In the mid-range of humidity (40–70 %RH), some chemisorption takes place on the walls of capillaries. Therefore less H^+ ions will be released in this range tending to a decrease in the impedance. In high humid region (70-90 %RH), multiple layers of physisorption occur where the water molecules in the form of hydronium ion (H_3O^+) will just physically adsorb causing the condensation of water vapour through the capillaries and formation of a meniscus in the capillaries. In this case, few ions shall be released, therefore, almost constant impedance is observed. The sensing mechanism is depicted schematically in Fig. 5.9.

Some other physical properties were also measured for the multi-layered films with a change in humidity level. The relationship between capacitance and %RH are plotted in Fig. 5.10, whereas that for inductance and phase angle is plotted in Fig. 5.11 and 5.12 respectively. The readings corresponding to these curves are given in Tables 5.4, 5.5 and 5.6. Then using the similar relation as given in Eqn. 5.2, sensitivities for capacitance, inductance and phase angle were calculated and shown in Table 5.3. The capacitive sensitivities for one-, two-, three- and four-layered films are 7.345, 5.081, 3.667 and 1.680 pF/%RH whereas that of inductive sensitivities and phase angle sensitivities are 7.734, 4.861, 2.767 and 1.755 KH/%RH and 2.429, 2.201, 2.039 and 1.878°/%RH respectively.

5.4.2 Opto-electronic Humidity Sensing

The humidity sensing characteristic curves as obtained from opto-electronic sensing set-up have been plotted in Fig. 5.13(a-d) and the corresponding readings are depicted in Table 5.7. Here, the sensitivity is calculated by taking the change in output power corresponding to the change in %RH. Mathematically, it is defined by Eqn. 5.4:

$$\text{Sensitivity} = \frac{\Delta I_t}{\Delta \%RH}\ \mu W/\%RH \qquad \ldots\ldots (5.4)$$

where ΔI_t is the change in the transmitted intensity of light and Δ%RH is the change in %RH. Fig. 5.13(a-d) shows a linear decrease in transmitted intensity of laser light with the increase in %RH at room ambient for one-, two-, three- and four-layered films of nanostructured La_2O_3-Cr_2O_3-SrO films annealed at 400°C.

Curves show a decrease in transmitted output power in the entire range of %RH i.e. 10-90 %RH; however, in a higher region, the decrease becomes slower. The sensitivity of sensing elements made of one-, two-, three- and four- layered films are found to be 3.604, 3.444, 3.250 and 3.063 μW/%RH respectively. It may be noted here that the film possesses encouraging sensitivity due to rapid adsorption/desorption rate. The material has a high refractive index of 1.442302 and therefore less transmitted power is obtained at the detector. It was observed that with the exposure of humidity, the refractive index of the material decreases causing the bending of light and hence a decrease in output power is observed. This phenomenon is solely responsible for its potential application as a humidity sensor.

The change in the transmitted power at the detector with %RH can be explained on the basis of adsorption/desorption of water molecules on the porous surface of the sensing element which further causes the change in refractive index of the film. The porous surface provides a large number of active sites for adsorption/desorption of water molecules and hence morphology plays a vital role in the sensing mechanism. Initially, the porous sensing element was free from water molecules, solely containing only dry air. When the exposure of humidity started, water molecules quickly adsorb by the porous cavity. Due to high cationic charge density of metal oxide surface especially Lanthanum here; the coulombic force becomes so prominent that it tends to break the O–H bond from H_2O thus forming a strong chemical bond with a metal ion. This bonding between hydroxyl and metal ion forms the initial chemisorbed layer. Thus in the less humid range, adsorption of water

molecules on the surface of the film takes place. This results in the decrease in refractive index of the sensing element and hence bending of light takes place tending to a decrease in the output power at the detector. With more exposure of humidity, in the mid humid range, adsorption takes place on porous walls of the film thereby tending to a greater decrease in refractive index and hence more bending of light, consequently less power at the detector. With the heavy exposure of humidity, in high humid region i.e. from 70-90 %RH, the water molecules form multiple physisorbed layers. In this case, due to distance factor, water molecules simply adsorb forming weak Vander wall's bond with the sensing surface. In this range, capillary condensation occurs in the form of hydronium ion (H_3O^+) thereby further decreasing the refractive index and hence more bending of light and furthermore decrease in output power [24]. The schematic representation of the sensing mechanism is shown in Fig. 5.14.

Reproducibility is one of the most important factors for a sensor. It is the distribution of output when measurements are taken under the same environmental conditions as before. The reproducibility curve for the film is shown in Fig. 5.15(a) which exhibits that the sensing characteristic of the film is 95.71% reproducible. The sensitivity observed, in this case, was 3.367 µW/%RH.

Ageing effect is also an important sensor parameter. It is the distribution of sensor outputs when performing consecutive readings under similar conditions after a long time. Here the consecutive measurements were taken after one month, three months and six months. Therefore, the ageing effect was observed after one month, three months and six months, the results of which are plotted and shown as a square, circle and triangle-shaped in Fig.5.15(b). Here it can be concluded that La_2O_3-Cr_2O_3-SrO is a quite stable material having very less effect of ageing and the sensor is quite stable. The corresponding data of the reproducibility and ageing effect have been presented in Table 5.8.

The time required to reach 10% of the final sensor output after stepwise ramping the humidity is called the response time of the sensor whereas recovery time is the time taken by the sensor signal to return to its initial value after a step concentration change from a certain value to zero. The response and recovery time as calculated here for one-layered sensing film from Fig.5.15(c) are 15 s and 56 s respectively. The corresponding readings are given in Table 5.9. All the sensor

parameters calculated here for one-layered sensing element have been presented in Table 5.10.

5.5 Conclusion

We have successfully prepared La_2O_3-Cr_2O_3-SrO composite using sol-gel extraction route and fabricated humidity sensing device based on the electrical and optical parameters. Single and multilayered sensing films were fabricated using spin coating technique. XRD of the film shows the crystallinity, phase formation and minimum crystallite size as 9 nm. A study of the UV-Vis spectrum of the sensing films demonstrates that as the number of layers or film thickness increase, their optical band gaps are found to be decreased whereas the height of the humps increases. The estimated band-gap of the thin film was found to be 3.842, 3.837, 3.802 and 3.789 eV for one-, two-, three- and four-layered film respectively. Therefore sensitivity of the sensor decreases which is confirmed by the experimental results. Single layered sensing element was found most sensitive towards humidity. The sensitivity of one-layered sensing element regarding electrical parameters of impedance, capacitance, inductance and phase angle were 9.369 MΩ/%RH,7.345 pF/%RH, 7.734 KH/%RH and 2.429°/%RH respectively; whereas for opto-electronic mode, it was ~3.367μW/%RH. The experiment was repeated and results were found ~98% reproducible. The effect of ageing was also checked and found the negligible variation of characteristic after a long run. The response and recovery times were found as 15 s and 56 s respectively.

References

[1] A.J. Jacobson, Materials for Solid Oxide Fuel Cells, Chem. Mater. 22 (2010) 660–674.

[2] X.F. Zhu, Q. Zhong, X.J. Zhao, H. Yan, Synthesis and Performance of Y-Doped $La_{0.7}Sr_{0.3}CrO_3$ as a Potential Anode Material for Solid Oxygen Fuel Cells, App. Surf. Sci. 57(6) (2011) 1967- 1971.

[3] A.V. Kadu, A.B. Bodade, A.B. Bodade, G.N. Chaudhari, Structural Characterization of Nanocrystalline$La_{1-x}Sr_xCrO_3$ Thick Films for H_2S Gas Sensors, J. Sens. Techno. 2 (2012) 13-18.

[4] A.D. Pomogailo, A.S. Rozenberg, G.I. Dzhardimalieva, Thermolysis of metallopolymers and their precursors as a method for the preparation of nanocomposites, Russ. Chem. Reviews 80(3) (2011) 257-292.

[5] A.D. Pomogailo, A.S. Rozenberg, I.E. Uflyand, Nanochastitsy Metallov v Polimerakh (Nanoparticles of Metals in Polymers) (Moscow: Khimiya, 2000).

[6] B.S. Randhawa, M. Kaur, Hyperfine Interact. 188 (2009) 95.

[7] G. Shang, P.W. Peacock, J. Robertson, Stability and band offsets of nitrogenated high-dielectric-constant gate oxides, App. Phy. Letters 84 (2004) 106–108.

[8] NIOSH Pocket Guide to Chemical Hazards #0141". National Institute for Occupational Safety and Health (NIOSH).

[9] Strontium Oxide American Elements. Access: April 29, 2016. https://www.americanelements.com/strontium-oxide-1314-11-0.

[10] S. Sikarwar, B.C. Yadav, Opto-electronic Humidity Sensor: A Review, Sens. Actuators A: Phy. 233 (2015) 54–70.

[11] N. Irawati, T.N.R. Abdullah, H.A. Rahman, H. Ahmad, S.W. Harun, PMMA microfiber loop resonator for the humidity sensor, Sens. Actuators A: Phy. 260 (2017) 112–116.

[12] Y. Wang, C. Shen, Fiber optic humidity sensor based on the graphene oxide/PVA composite film, Opt. Commun. 372 (2016) 229–234.

[13] P. Chaudhary, S. Sikarwar, B.C. Yadav,G.I. Dzhardimalieva, N.D. Golubeva, I.E. Uflyand, Synthesis and characterization of copper (II) nitrate polyacrylamide & its application as opto-electronic humidity sensor, Sens. Actuators A: Phy. 263 (2017) 415–422.

[14] B.C. Yadav, S. Sikarwar, A. Bhaduri, P. Kumar, Synthesis, characterization and development of opto-electronic humidity sensor using copper oxide thin film, Int. Adv. Research J. in Sci., Engg and Tech. 2(11) (2015) 105-109.

[15] B.C. Yadav, K.S. Chauhan, S. Singh, R.K. Sonker, S. Sikarwar, R. Kumar, Growth and characterization of sol-gel processed rectangular shaped nanostructured ferric oxide thin film followed by humidity and gas sensing, J. Mater Sci: Mater Electron 28 (2017) 5270–5280.

[16] B.C. Yadav, S. Sikarwar,R. Yadav, P. Chaudhary, G.I. Dzhardimalieva, N.D. Golubeva, Preparation of zinc (II) nitrate poly acrylamide (PAAm) and its optoelectronic application for humidity sensing, J Mater Sci: Mater Electron 29 (2017) 7770–7777.

[17] S. Sikarwar, B.C. Yadav, S. Singh, G.I. Dzhardimalieva, S.I. Pomogailo, N.D. Golubeva, A.D. Pomogailo, Fabrication of nanostructured yttria stabilized zirconia multilayered films and their optical humidity sensing capabilities based on transmission, Sens. Actuators B: Chem. 232 (2016) 283–291.

[18] S. Sikarwar, A. Kumar, B.C. Yadav, G.I. Dzhardimalieva, N.D. Golubeva, Nanostructured spherical-shaped Sc(III) Polyacrylate for monitoring the moisture level, IEEE Sensors 18(11) (2018) 4384-4391.

[19] S. Sikarwar, B.C. Yadav, G.I. Dzhardimalieva, N.D. Golubeva, P. Srivastava, Synthesis and Characterization of Nanostructured MnO_2-CoO and its relevance as opto-electronic humidity sensing device, RSC Advances 8(37) (2018) 20534-20542.

[20] J.K. Rajput, T.K. Pathak, V. Kumar, M. Kumar, L.P. Purohit, Annealing temperature dependent investigations on nano-cauliflower like structure of CdO thin film grown by sol-gel method, Surfaces and Interfaces 6 (2017) 11–17.

[21] V. Manikandan, S. Sikarwar, B.C. Yadav, R.S. Mane, Fabrication of tin substituted nickel ferrite (Sn-$NiFe_2O_4$) thin film and its application as opto-electronic humidity sensor, Sens. Actuators A: Phy. 272 (2018) 267–273.

[22] S. Kozhukharov, Z. Nenova, T. Nenov, N. Nedev, M. Machkov, Humidity sensing elements based on cerium doped titania-silica thin films prepared via a sol-gel method, Sens. Actuators B: Chem. 210 (2015) 676–684.

[23] Z. Nenova, S. Kozhukharov, T. Nenov, N. Nedev, M. Machkova, Combined influence of titania and silica precursors on the properties of thin film

humidity sensing elements prepared via a sol-gel method, Sens. Actuators B: Chem. 224 (2016) 143–152.

[24] F. Xu, L. Zhang, X. Yin, L. Tong, Polymer single-Nanowire optical sensors, Nano Lett. 8 (2008) 2757–2761.

Tables

Table 5.1: A recent literature review of the reported opto-electronic humidity sensors.

S. No.	Material	Sensitivity	Year	Ref.
1.	PMMA microfiber loop resonator (PMLR) coated with ZnO	0.1746 dBm/%RH	2017	11
2.	Graphene oxide/PVA	0.193 dB%RH	2016	12
3.	$Cu(NO_3)_2 \cdot (AAm)_4$	0.838 μW/%RH	2017	13
4.	CuO	0.85 μW/%RH	2015	14
5.	Fe_2O_3	1.172 μW/%RH	2016	15
6.	$Zn(NO_3)_2 \cdot (AAm)_4 \cdot 2H_2O$	1.831 μW/%RH	2018	16
7.	Y_2O_3-ZrO_2	1.937 μW/%RH	2016	17
8.	$Sc(CH_2=CH-COO)_3$	2.1 μW/%RH	2018	18
9.	MnO_2-CoO	2.225 μW/%RH	2018	19
10.	La_2O_3-Cr_2O_3-SrO	3.604 μW/%RH	2018	Present work

Table 5.2: Variations in the impedance obtained for both the adsorption and desorption phenomenon corresponding to one-, two-, three- and four-layered films of nanostructured La_2O_3-Cr_2O_3-SrO in the range of 10-90 %RH.

%RH	Impedance (MΩ)							
	One layered film		**Two layered film**		**Three layered film**		**Four layered film**	
	Increasing mode	Decreasing mode	Increasing mode	Decreasing mode	Increasing mode	Decreasing mode	Increasing mode	Decreasing mode
10	750.01	709.65	481.21	446.41	296.45	279.58	160.21	157.37
15	584.98	651.62	377.14	320.23	232.97	244.68	110.07	75.11
20	430.37	471.75	206.05	163.31	180.87	196.73	44.63	32.21
25	250.50	305.98	128.05	102.13	110.34	135.66	26.85	20.34
30	104.15	138.60	78.65	55.017	56.9	78.96	18.82	15.94
35	40.50	87.50	57.78	20.55	23.29	36.66	6.46	10.22
40	18.37	52.21	37.71	15.99	15.41	27.38	5.44	6.79
45	2.82	32.41	23.42	13.10	9.36	18.92	4.47	6.30
50	4.44	23.41	21.85	10.94	7.24	16.27	3.58	5.32
55	4.21	21.56	11.18	14.74	5.89	11.89	3.07	4.34
60	1.39	14.85	7.99	8.464	5.39	9.09	2.94	3.31
65	1.75	3.15	5.06	3.81	5.20	7.03	1.91	2.76
70	0.97	2.82	3.38	2.17	4.39	5.89	1.76	2.06
75	0.84	0.88	2.27	1.30	4.06	4.85	0.97	1.49
80	0.75	0.52	1.36	1.06	3.92	4.19	0.91	0.76
85	0.542	0.42	0.76	0.91	3.75	3.14	0.83	0.58
90	0.446	0.36	0.51	0.45	0.47	2.69	0.56	0.50

Table 5.3: The values of sensitivities as observed from the relationship between different electrical parameters and %RH.

Sensitivity	**Impedance-based**	**Capacitance-based**	**Inductance-based**	**Phase angle-based**
One-layered film	9.369 MΩ/%RH	7.345 pF/%RH	7.734 KH/%RH	2.429°/%RH
Two-layered film	6.006 MΩ/%RH	5.081 pF/%RH	4.861 KH/%RH	2.201°/%RH
Three-layered film	3.699 MΩ/%RH	3.667 pF/%RH	2.767 KH/%RH	2.039°/%RH
Four-layered film	1.995 MΩ/%RH	1.680 pF/%RH	1.755 KH/%RH	1.878°/%RH

Table 5.4: Variations of the capacitance obtained for both the adsorption and desorption phenomenon corresponding to one-, two-, three- and four-layered films of nanostructured La_2O_3-Cr_2O_3-SrO with %RH.

%RH	Capacitance (pF)							
	One layered film		Two layered film		Three layered film		Four layered film	
	Increasing mode	Decreasing mode	Increasing mode	Decreasing mode	Increasing mode	Decreasing mode	Increasing mode	Decreasing mode
10	-2.85	19.29	12.96	24.76	-47.72	-42.20	9.03	6.61
15	-1.47	21.56	15.17	23.26	-48.93	-40.81	11.73	8.12
20	2.31	30.76	22.05	27.81	-46.50	-31.40	13.80	13.28
25	5.06	37.81	25.36	36.81	-34.07	-25.62	17.88	13.28
30	10.62	47.11	34.61	50.49	-21.24	-4.73	22.01	15.82
35	18.74	54.46	54.17	70.84	-13.61	1.03	23.55	18.45
40	34.36	63.15	76.89	95.58	-3.17	15.45	27.64	20.98
45	37.83	72.85	102.11	124.28	7.63	24.84	31.25	24.59
50	54.14	84.79	123.25	141.18	17.72	45.58	34.35	27.63
55	67.86	95.74	147.98	169.32	38.72	55.65	38.47	31.77
60	79.35	104.43	172.71	194.13	59.63	74.38	47.80	39.98
65	120.87	127.32	197.93	213.76	84.12	105.61	60.41	51.33
70	199.44	165.11	259.38	235.81	111.89	138.68	69.61	64.72
75	266.67	218.33	287.46	267.47	138.68	159.05	91.43	85.88
80	354.43	315.79	325.11	294.39	164.25	179.85	106.60	106.31
85	479.67	437.73	361.64	332.19	192.18	206.73	128.93	122.42
90	584.82	541.73	418.44	404.48	245.85	231.53	143.45	131.31

Table 5.5: Variations in the inductance obtained for both the adsorption and desorption phenomenon corresponding to one-, two-, three- and four-layered films of nanostructured La_2O_3-Cr_2O_3-SrO with %RH.

%RH	Inductance (KH)							
	One layered film		Two layered film		Three layered film		Four layered film	
	Increasing mode	Decreasing mode	Increasing mode	Decreasing mode	Increasing mode	Decreasing mode	Increasing mode	Decreasing mode
10	-630.0	-598.42	-384.1	-358.39	-231.1	-224.24	-148.6	-141.65
15	-598.4	-441.21	-311.9	-283.91	-90.91	-63.54	-120.0	-111.15
20	-292.8	-179.98	-236.2	-167.89	-62.09	-39.28	-82.33	-71.79
25	-149.2	-120.14	-82.63	-61.44	-37.81	-23.12	-50.9	-42.89
30	-128.3	-83.23	-36.24	-58.41	-34.91	-18.82	-44.49	-31.38
35	-97.58	-65.17	-13.78	-44.62	-32.95	-15.87	-29.74	-22.21
40	-90.51	-40.68	-7.44	-33.05	-28.96	-14.28	-26.12	-19.97
45	-58.26	-26.57	-4.56	-25.41	-28.58	-14.42	-23.84	-17.96
50	-49.55	-24.25	-2.06	-21.05	-26.46	-13.28	-21.66	-15.84
55	-40.54	-22.36	-1.55	-18.31	-22.47	-12.53	-19.48	-13.48
60	-29.57	-18.92	-0.25	-16.99	-19.55	-11.62	-17.03	-11.96
65	-26.35	-16.07	-0.64	-15.37	-18.98	-10.93	-16.74	-11.95
70	-24.16	-14.03	0.36	-12.53	-16.31	-9.83	-14.74	-10.87
75	-15.37	-17.74	1.05	-12.57	-17.18	-8.55	-11.96	-9.85
80	-14.21	-17.13	2.43	-12.42	-13.25	-7.45	-10.87	-9.26
85	-12.11	-17.52	4.05	-11.11	-12.32	-4.59	-10.36	-7.75
90	-11.32	-11.32	4.70	-8.19	-9.72	-3.32	-8.258	-7.16

Table 5.6: Variations in the phase angle obtained for both the adsorption and desorption phenomenon corresponding to one-, two-, three- and four-layered films of nanostructured La_2O_3-Cr_2O_3-SrO with %RH.

%RH	Phase angle (°)							
	One layered film		Two layered film		Three layered film		Four layered film	
	Increasing mode	Decreasing mode	Increasing mode	Decreasing mode	Increasing mode	Decreasing mode	Increasing mode	Decreasing mode
10	-195.73	-189.12	-178.86	-166.12	-165.32	-151.67	-139.58	-130.99
15	-95.43	-119.25	-138.79	-100.95	-93.76	-79.53	-101.95	-68.53
20	-27.56	-46.93	-43.21	-63.27	-61.12	-51.53	-45.35	-27.24
25	-22.01	-12.35	-32.56	-50.03	-36.17	-23.65	-13.14	-23.08
30	-13.89	-8.48	-19.15	-31.95	-19.96	-11.14	-11.94	-19.82
35	-6.93	-6.32	-13.98	-27.11	-12.63	-2.19	-10.71	-17.55
40	-5.55	-7.25	-12.28	-23.08	-7.82	-2.76	-8.36	-12.84
45	-4.65	-6.29	-9.64	-19.77	-3.65	-2.49	-5.42	-10.51
50	-4.17	-5.95	-9.56	-18.43	-3.38	-2.48	-5.40	-10.44
55	-3.15	-5.02	-7.58	-17.18	-2.95	-2.59	-1.35	-8.08
60	-3.25	-5.05	-8.25	-13.62	-2.75	-2.48	1.29	-5.22
65	-3.58	-4.85	-7.23	-13.63	-2.77	-2.36	3.13	-4.16
70	-2.46	-4.25	-5.69	-10.94	-2.72	-2.30	2.92	-3.47
75	-2.38	-3.46	-3.63	-9.09	-2.51	-2.29	2.73	-2.31
80	-2.14	-2.425	-4.12	-8.21	-2.54	-2.27	4.71	-0.56
85	-2.03	-1.85	-3.11	-5.73	-2.33	-2.76	7.10	2.13
90	-1.75	-1.74	-2.84	-4.12	-2.19	-0.38	10.64	3.52

Table 5.7: Variations in the output power obtained for both the adsorption and desorption phenomenon corresponding to one-, two-, three- and four-layered films of nanostructured La_2O_3-Cr_2O_3-SrO with %RH for opto-electronic mode of humidity sensing.

%RH	Output power (μW)							
	One layered film		Two layered film		Three layered film		Four layered film	
	Increasing mode	Decreasing mode	Increasing mode	Decreasing mode	Increasing mode	Decreasing mode	Increasing mode	Decreasing mode
10	522.7	518.1	510.4	500.1	501.9	490.1	495.3	482.1
15	462.2	442.6	463.3	438.2	454.5	427.3	434.9	423.3
20	368.1	360.1	361.1	344.6	393.6	375.4	386.8	370.6
25	348.4	332.2	334.5	312.2	345.3	318.6	335.6	317.4
30	333.3	319.4	318.4	303.4	321.2	300.3	322.2	307.3
35	330.4	313.3	309.6	295.1	311.4	294.6	313.1	295.5
40	318.5	305.2	303.2	292.3	304.2	288.1	304.4	289.2
45	313.6	295.5	297.5	288.5	297.1	287.3	297.3	284.3
50	301.1	287.4	293.4	281.6	290.3	280.2	291.6	280.2
55	297.2	283.3	288.3	274.3	286.4	271.4	286.3	276.4
60	286.3	277.1	277.1	270.2	278.6	271.6	282.4	274.1
65	276.1	271.6	272.2	266.3	270.5	266.4	276.5	271.3
70	262.4	267.2	267.4	260.6	266.2	262.2	270.2	268.5
75	259.3	259.4	260.3	255.1	256.1	252.3	262.4	264.4
80	252.5	255.4	250.1	251.2	251.6	249.6	255.3	260.6
85	238.7	251.2	237.7	245.5	245.1	241.4	252.5	254.2
90	234.4	242.1	233.9	240.3	240.3	240.2	245.4	251.9

Table 5.8: Variations of the output power obtained for both the adsorption and desorption phenomenon corresponding to one-layered film of nanostructured La_2O_3-Cr_2O_3-SrO with %RH for observing reproducibility and ageing effect.

%RH	Output power (µW)				
	Reproducibility		Ageing effect		
	Increasing mode	Decreasing mode	One month	Two months	Three months
10	518.1	515.4	516.4	512.9	510.4
15	452.3	438.2	458.2	435.1	427.2
20	375.4	341.4	363.3	345.3	319.4
25	353.2	339.2	339.1	318.6	304.3
30	342.2	321.3	331.6	310.4	298.6
35	335.1	315.5	320.4	302.2	291.9
40	322.3	304.4	317.5	299.4	287.2
45	318.4	303.6	311.2	292.2	283.5
50	309.6	294.8	300.1	285.3	277.2
55	300.1	287.2	295.2	280.4	273.4
60	291.9	280.1	289.6	275.1	268.3
65	287.6	278.3	281.1	272.4	264.2
70	281.4	272.4	272.4	267.6	259.7
75	268.2	270.6	265.6	255.3	257.4
80	260.4	265.3	254.1	249.1	255.2
85	245.3	253.7	243.4	245.3	254.1
90	240.4	245.9	239.4	241.9	251.3

Table 5.9: Variations in the output power obtained for both the adsorption and desorption phenomenon corresponding to one-layered film of nanostructured La_2O_3-Cr_2O_3-SrO with %RH for observing response and recovery times.

Time (s)	Increasing mode (µW)	Decreasing mode (µW)
0	522.7	234.5
50	462.3	238.7
100	368.3	250.9
200	348.8	260.2
290	340.7	271.4
390	329.4	281.3
500	324.6	286.6
630	313.4	297.1
800	307.3	307.2

Table 5.10: Sensors parameters of the one-layered nanostructured La_2O_3-Cr_2O_3-SrO film as opto-electronic humidity sensor.

Sensor parameters	Sensitivity	Reproducibility	Ageing effect	Response time	Recovery time
Values	3.604 µW/%RH	95.71%	Negligible	15 s	56 s

Figures

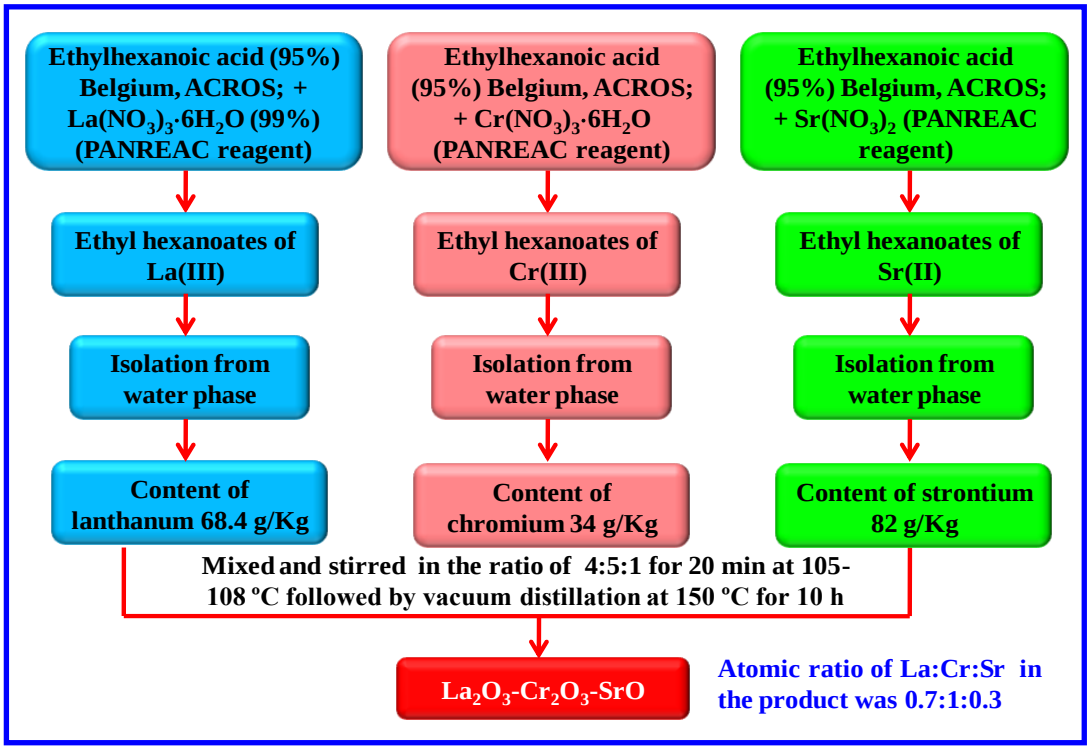

Figure 5.1: Schematic representation for the synthesis of nanostructured La_2O_3-Cr_2O_3-SrO composite.

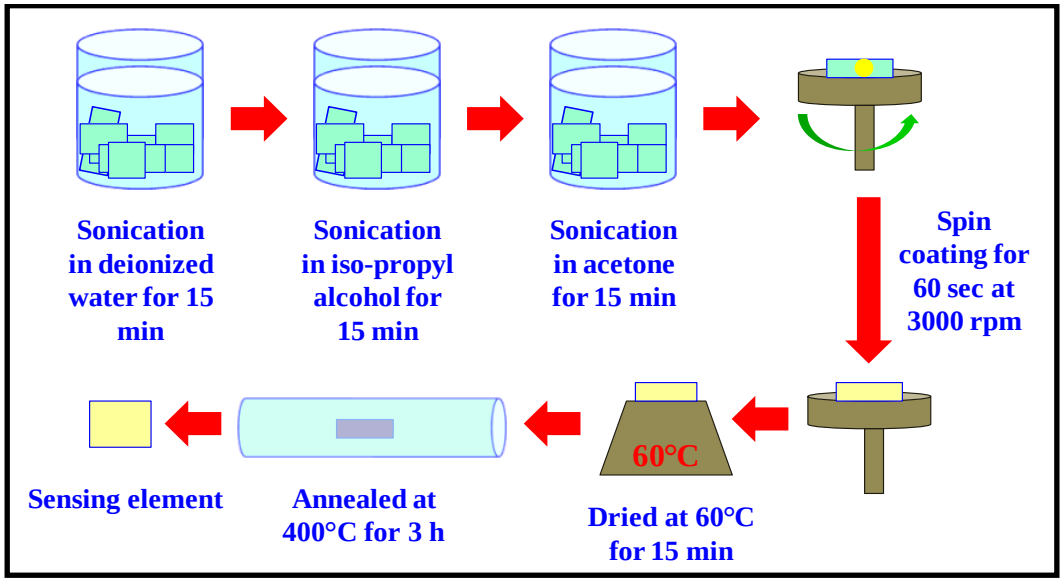

Figure 5.2: Schematic representation showing different steps for the fabrication of La_2O_3-Cr_2O_3-SrO nanocomposite films.

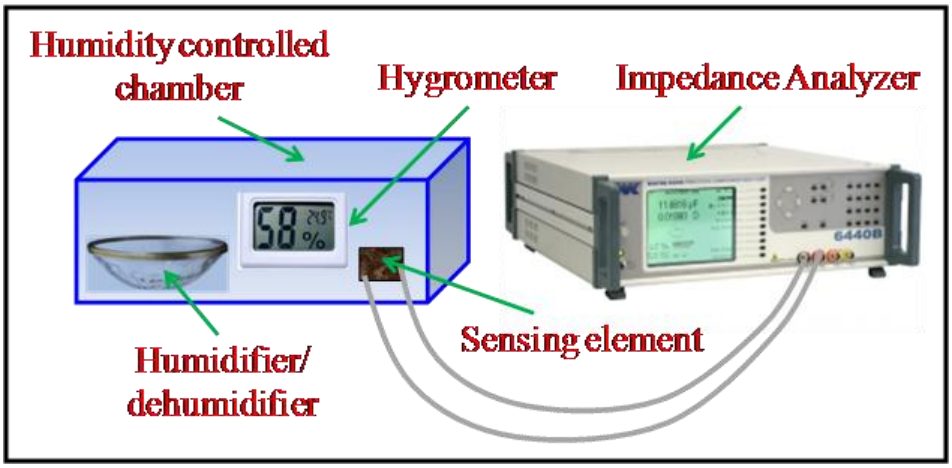

Figure 5.3: Experimental set-up for impedance based electrical humidity sensing.

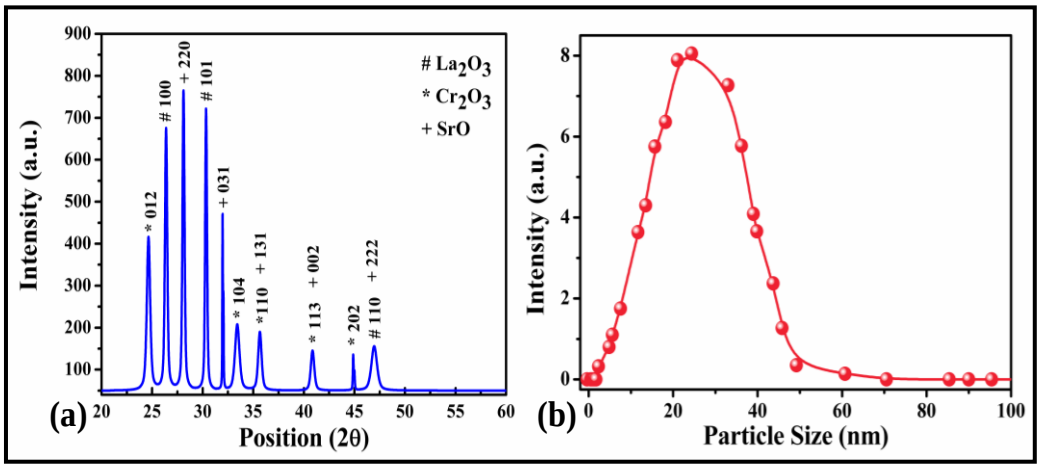

Figure 5.4: (a) XRD pattern of nanostructured La_2O_3-Cr_2O_3-SrO one-layered film where the hatch peaks denotes La_2O_3, star peaks denote Cr_2O_3 and plus peaks denote SrO. The average crystallite size as obtained from Debye Scherrer formula is ~32 nm and minimum crystallite size is ~9 nm. (b) Particle size distribution by Particle Size Analyzer showing all the particles in the range ~2-50 nm.

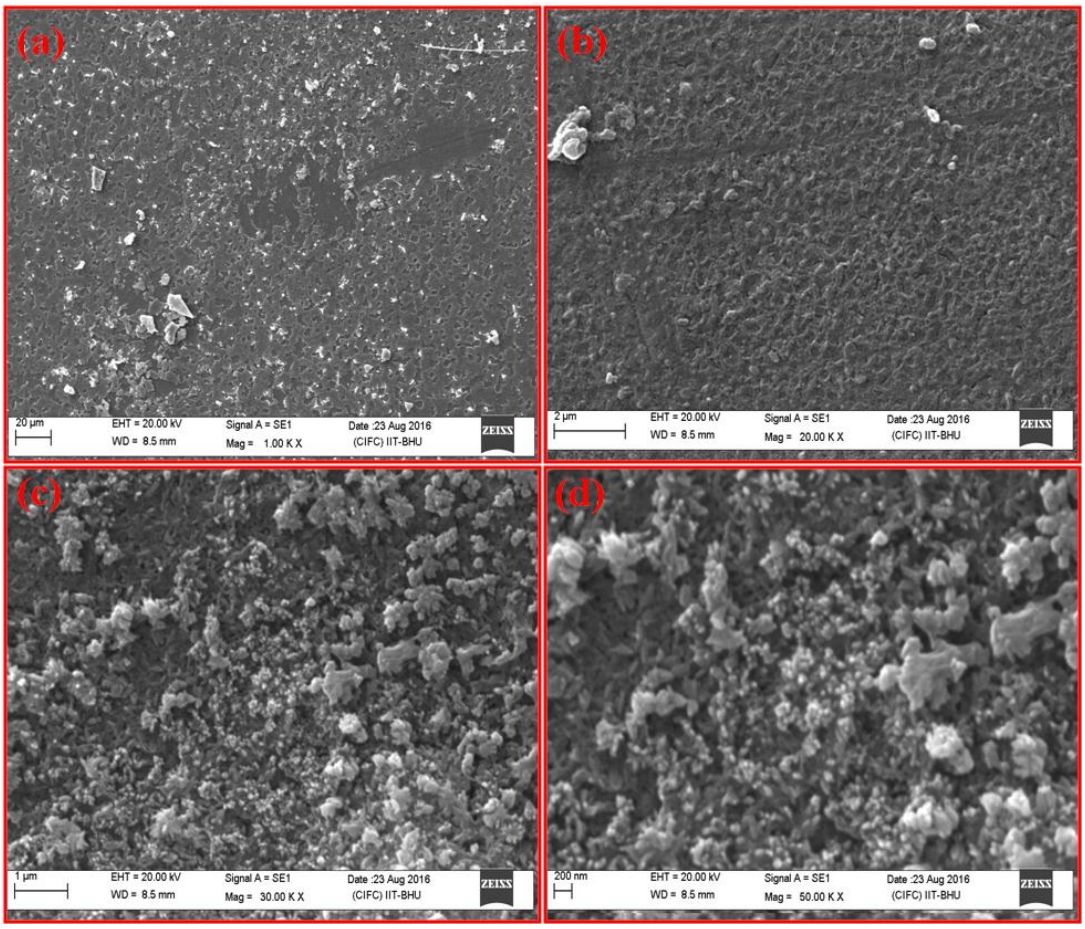

Figure 5.5: SEM micrograph of nanostructured La_2O_3-Cr_2O_3-SrO one layered film at (a) 20 µm, (b) 2 µm, (c) 1 µm and (d) 200 nm scales, showing porous nature which works as active centers for adsorption/desorption of humidity

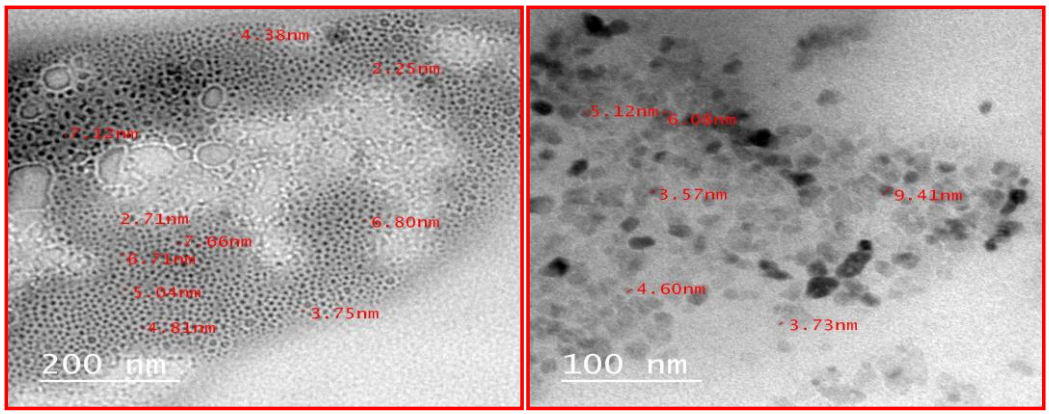

Figure 5.6: TEM image of nanostructured La_2O_3-Cr_2O_3-SrO dilute precursor solution at (a) 200 nm and (b) 100 nm scale.

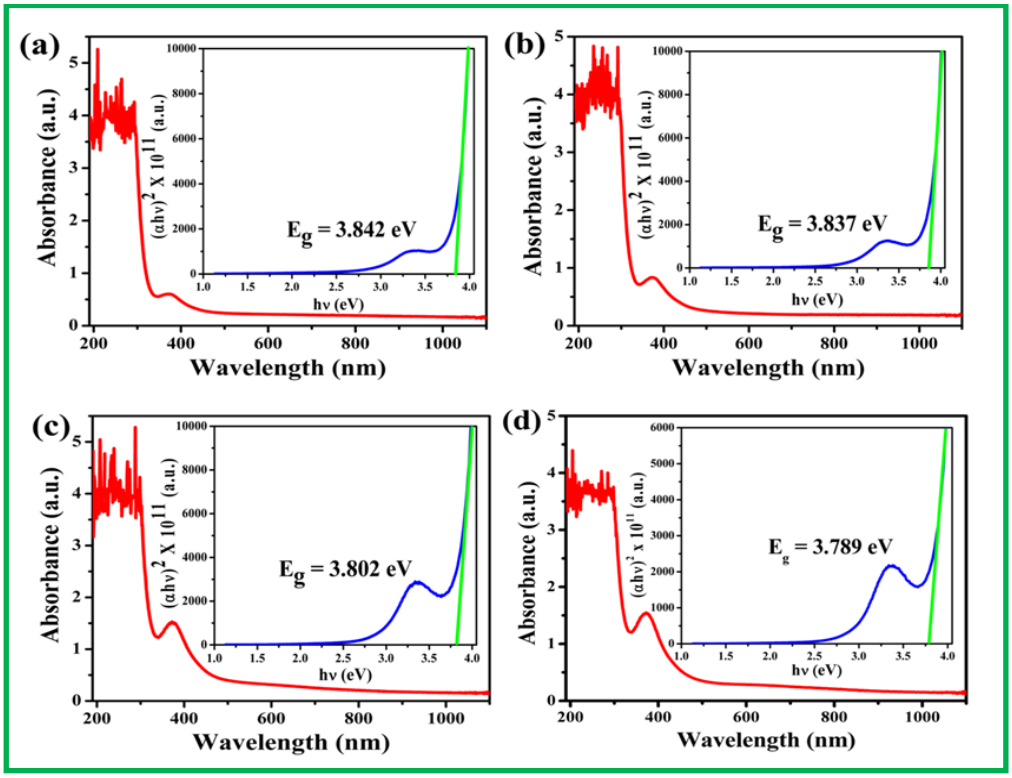

Figure 5.7: Curve showing optical absorbance spectra of nanostructured La_2O_3-Cr_2O_3-SrO thin films in the wavelength range 190-1100 nm. The estimated band-gap of (a) one-layered film is 3.842, (b) two-layered film is 3.837, (c) three-layered film is 3.802 and (d) four-layered film is 3.789 eV. Also, there is an increase in the height of the hump with the increase in the thickness of the film.

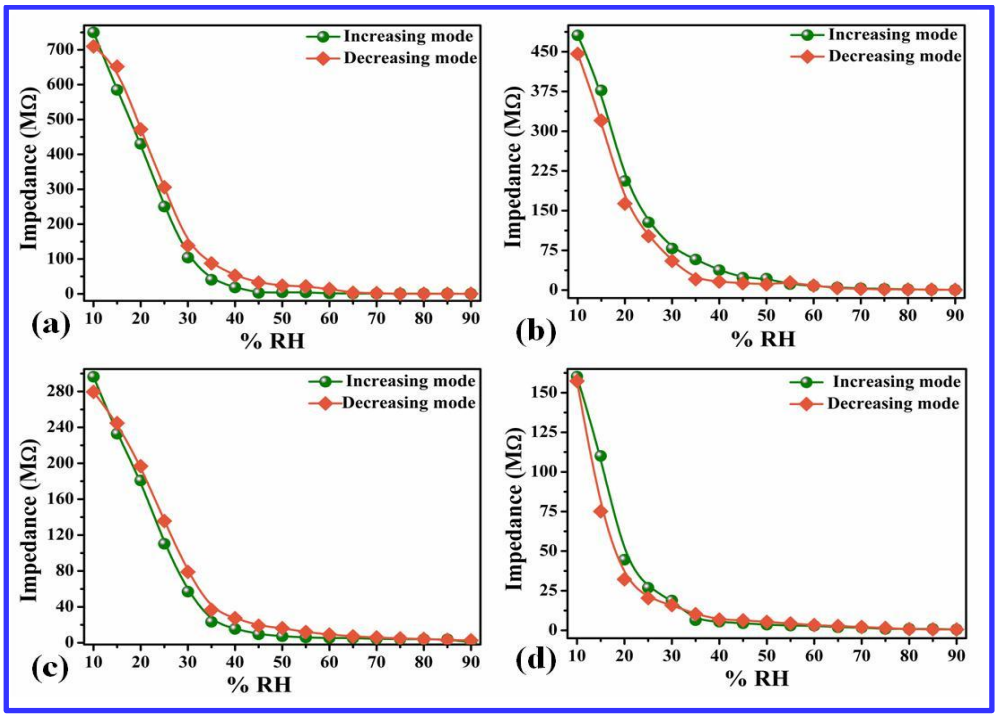

Figure 5.8: Humidity sensing characteristics of (a) one-, (b) two-, (c) three- and (d) four-layered films of nanostructured La_2O_3-Cr_2O_3-SrO in the range of 10-90 %RH showing the sensitivity of 9.369, 6.006, 3.699 and 1.995 MΩ/%RH respectively.

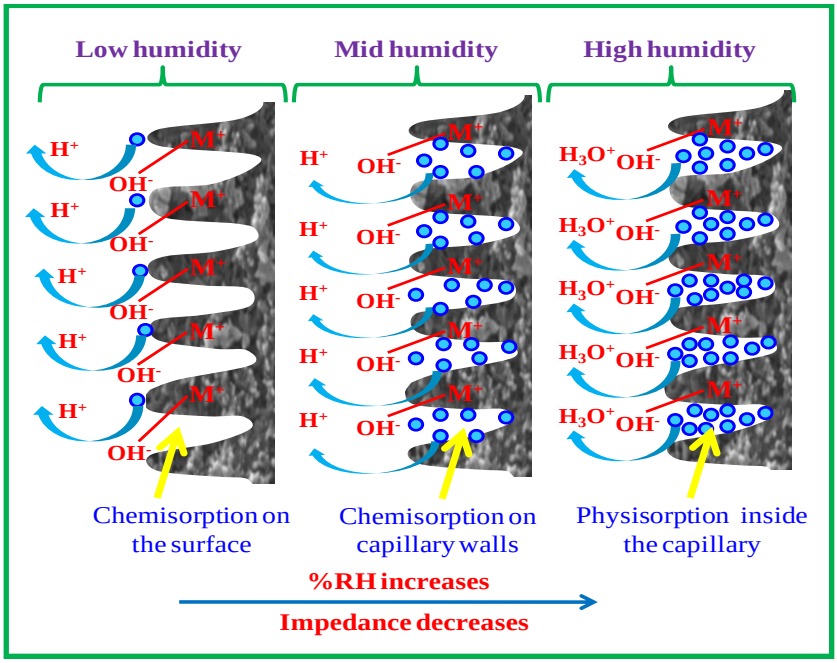

Figure 5.9: Schematic representation for the electrical mode of humidity sensing showing the phenomena of chemisorptions on the surface and capillary walls and physisorption and hence condensation inside the pores' capillary.

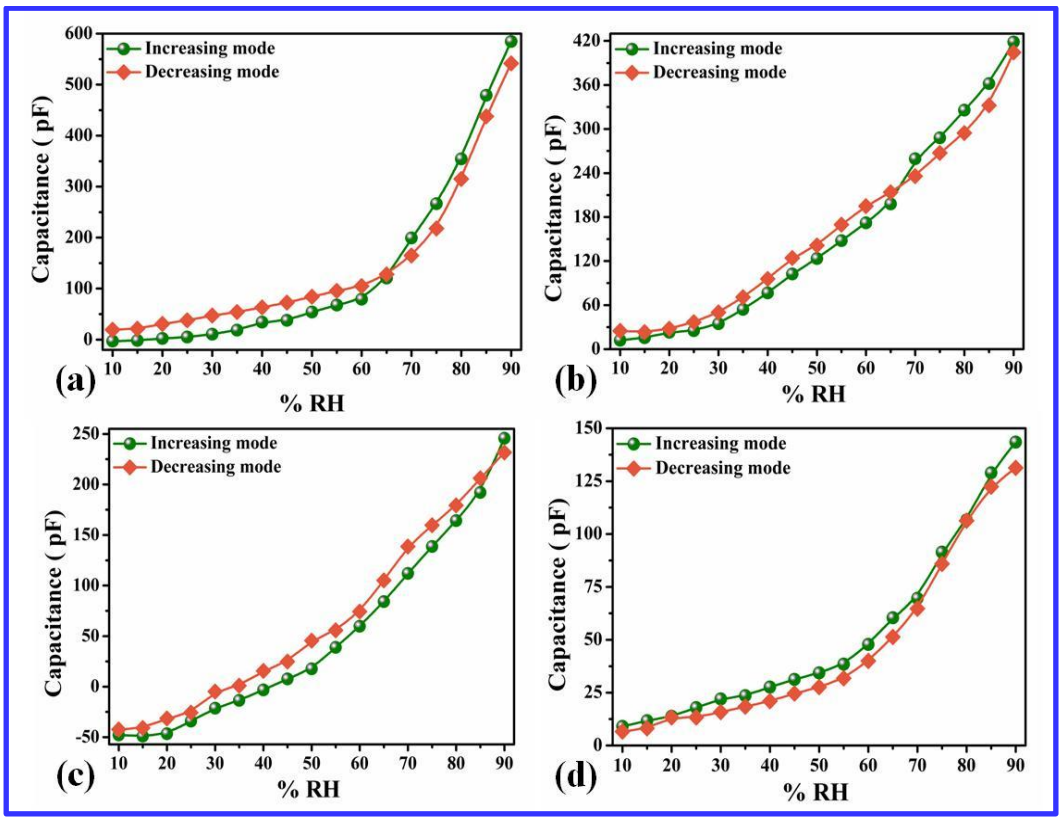

Figure 5.10: Relationship between %RH and capacitance for (a) one-, (b) two-, (c) three- and (d) four-layered films of nanostructured La_2O_3-Cr_2O_3-SrO in the range of 10-90 %RH showing the sensitivity of 7.345, 5.081, 3.667 and 1.680 pF/%RH respectively.

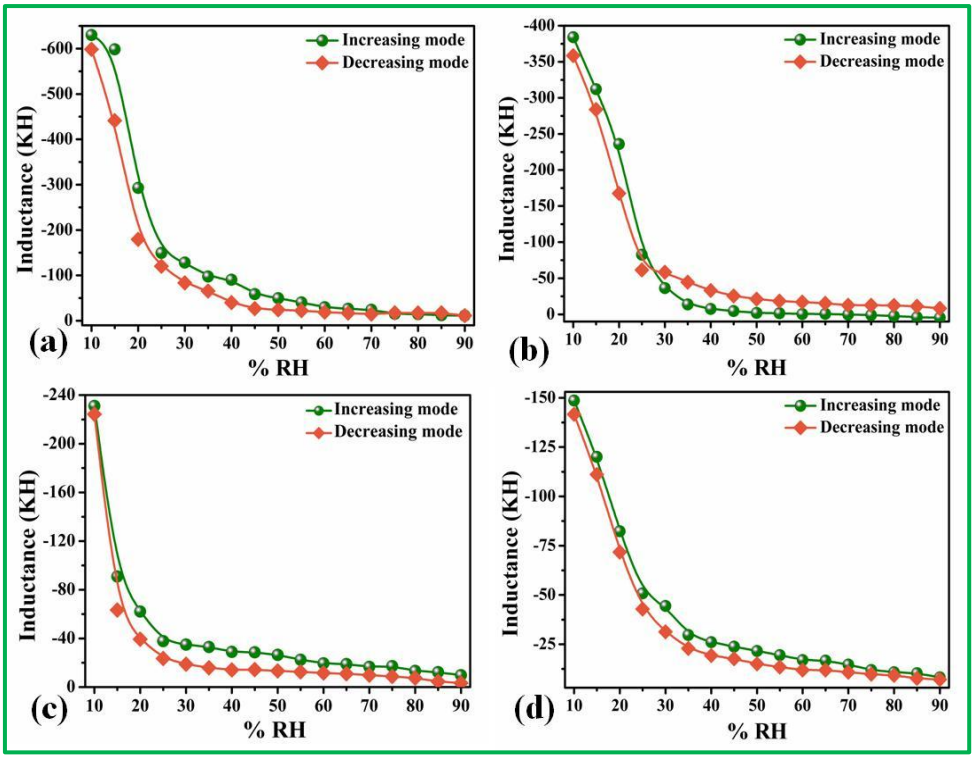

Figure 5.11: Relationship between %RH and inductance for (a) one-, (b) two-, (c) three- and (d) four-layered films of nanostructured La_2O_3-Cr_2O_3-SrO in the range of 10-90 %RH showing the sensitivity of 7.734, 4.861, 2.767 and 1.755 KH/%RH respectively.

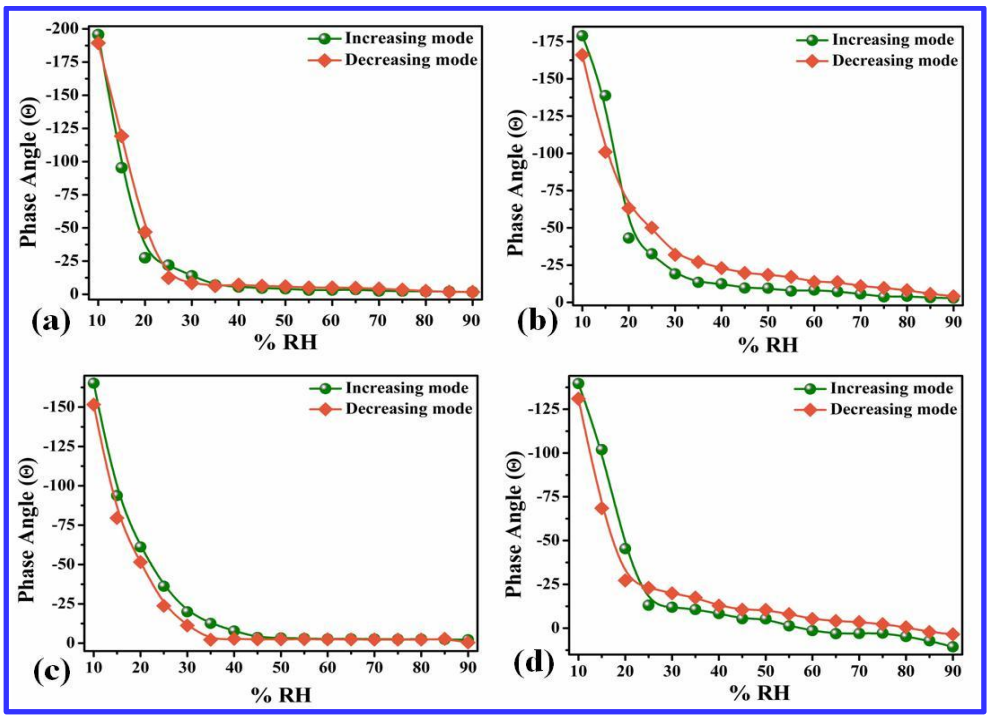

Figure 5.12: Relationship between %RH and phase angle for (a) one-, (b) two-, (c) three- and (d) four-layered films of nanostructured La_2O_3-Cr_2O_3-SrO in the range of 10-90 %RH showing the sensitivity of 2.429, 2.201, 2.039 and 1.878°/%RH respectively.

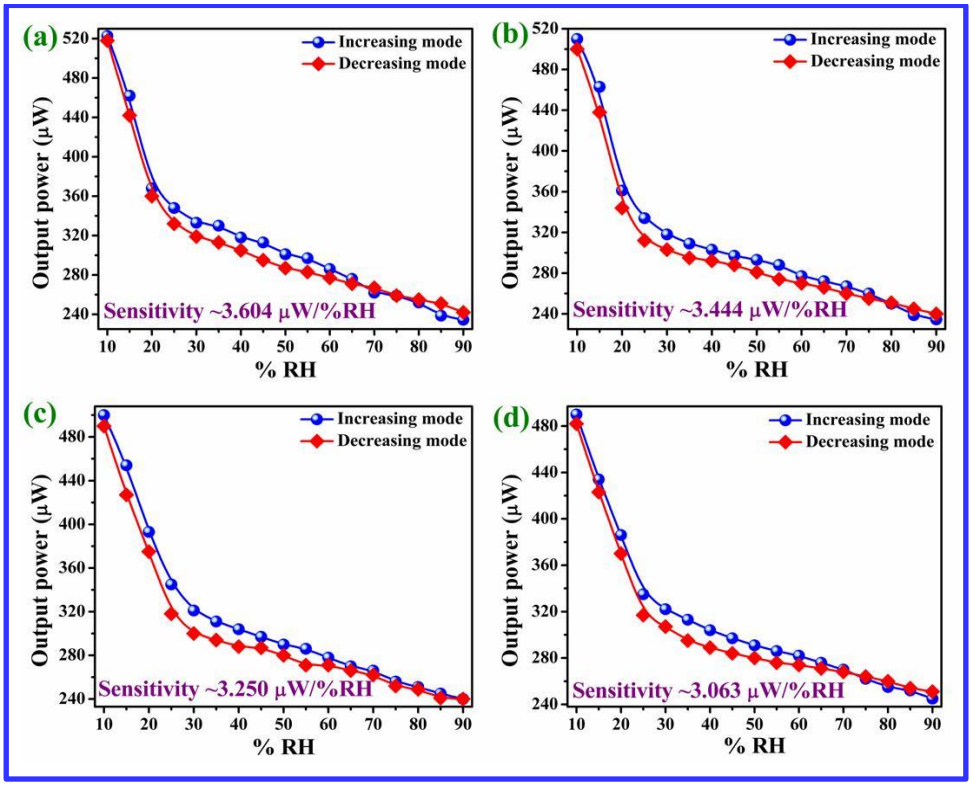

Figure 5.13: Humidity sensing characteristics of (a) one-, (b) two-, (c) three- and (d) four-layered films of the nanostructured La_2O_3-Cr_2O_3-SrO film in the range of 10-90 %RH showing the sensitivity of 3.604, 3.444, 3.250 and 3.063 μW/%RH.

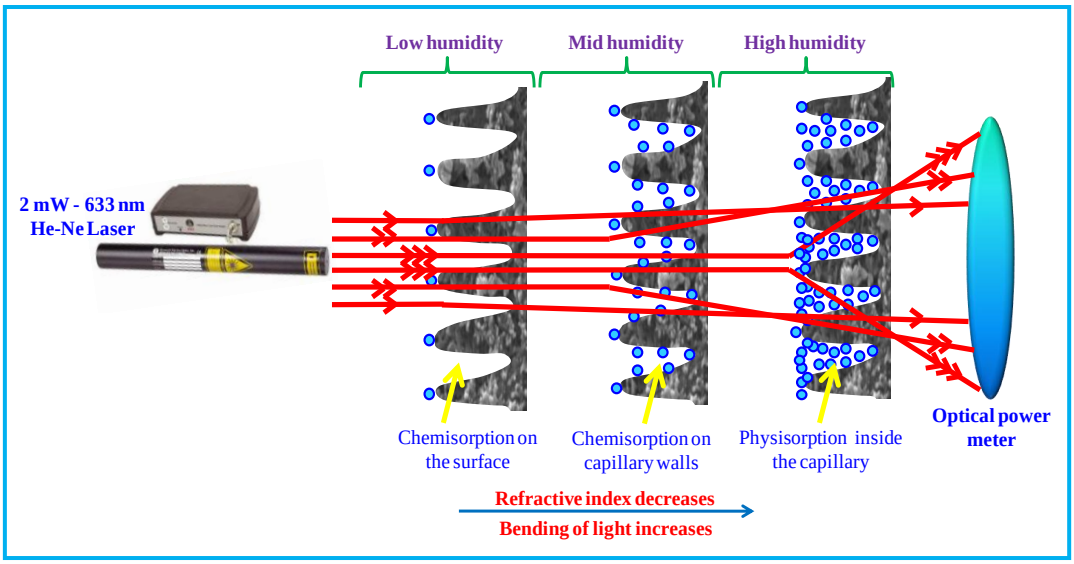

Figure 5.14: Mechanism of change in output power with exposure of humidity at different ranges of humidity.

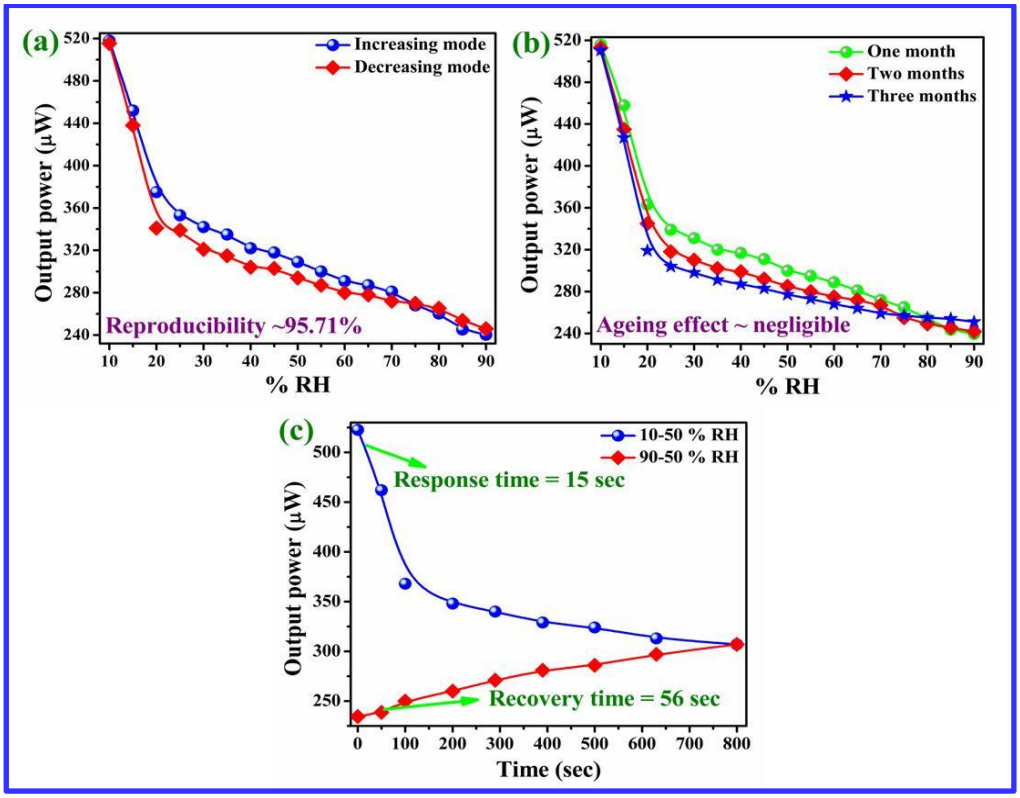

Figure 5.15: Variation of output power with %RH for one layered film to check (a) the reproducibility of the film and (b) the ageing effect after one month, three months and six months and (c) response and recovery times.

CHAPTER 6

Concluding Remarks and Scope of Further Research

A study of synthesis, characterization and humidity sensing properties of bimetallic and multimetallic oxide nanocomposites is summarized in the present chapter. This chapter also gives the guidelines for further research work in the field of nanodimensional metal oxide composites as a humidity sensor.

6.1 Conclusion

Nanoscience and nanotechnology are the most emerging fields in science and engineering. Nanomaterials exhibit unique and excellent mechanical, electrical, optical and magnetic properties. In the field of sensors, they have played a much efficient role by providing an enhanced surface area or higher aspect ratio. Also, the sensing capability is increased by alterations of the space charge layers for each grain and enhancing other electronic properties of the material in case of gases. The porous morphology and defect sites contribute much to the sensing ability of the nanomaterial by further enhancing the surface to volume ratio. Besides, metal oxide nanomaterials symbolize an increasing asset in numerous productions, particularly due to their sharp chemical, physical, and electronic properties and have versatile applications like environmental monitoring, health and personal care, energy, water treatment. Also, as the crystallite size of these materials reduces, an abundant boost in their properties is observed. This diverted the research community towards the low dimensional metal oxides while ensuring that their properties remain stable even at high operating temperature. Specifically, transition metal oxides are of great interest because of their vacant d-orbital. They can be easily oxidized as well as reduced and hence has potential application in gas/humidity sensing. A more interesting group of elements called rare earth metals have attracted the scientists more due to their vacant f-orbitals. Their exclusive 4f electron configuration has conveyed them with excellent magnetic, electrical, optical, and catalytic properties. Nanostructured rare-earth compounds are of much importance due to the occurrence of quantum confinement effects. Chapter 1 includes the introduction of recent development in metal oxides based humidity sensor using different physical principles. The drawbacks of electrical and mechanical phenomenon based principles have also been discussed and excellence of opto-electronic mode over their counterparts has been summarized. Different working set-ups and their working principles for the development of humidity sensor has been discussed and a wide literature review of the past decade has been tabulated. The versatile applications of humidity sensors have also been elaborated in this chapter. Also, the orientation of work, aims and objectives of the present research are well described at the end of the Chapter. Chapter 2 describes the synthesis of nanostructured

Y_2O_3-ZrO_2 and fabrication of their multilayered films for opto-electronic humidity sensing application working at room ambient. Humidity is one of the elementary biotic factors that fix the habitat of a particular living being. Therefore in order to monitor the humidity, reliable and cost-effective humidity sensors are needed. In the Chapter 3 an effort has been made to synthesize the nanocomposite CeO_2-Gd_2O_3-CoO using chemical extraction route. Further, its thin film was fabricated using spin coating technique for the quick detection of humidity at room temperature. A study of synthesis, characterization and humidity sensing properties of MnO_2-CoO is summarized in Chapter 4. Chapter 5 describes the synthesis, characterization and humidity sensing properties of nanocomposite La_2O_3-Cr_2O_3-SrO. Chapter 6 deals with a summary of the work done and the concluding remarks drawn from the present research work. Future scope for further research work in the field of bimetallic and multimetallic oxide nanocomposite films as efficient humidity sensor has been depicted at the end of this thesis. A study of synthesis, characterization and sensing properties of bimetallic and multimetallic oxide nanocomposites is summarized as below:

6.2 Fabrication of Nanostructured Y_2O_3-ZrO_2 Multilayered Films and their Optical Humidity Sensing Capabilities based on Transmission

We have successfully synthesized YSZ (Y_2O_3-ZrO_2) using sol-gel extraction route and fabricated an opto-electronic humidity sensor which is based on the modulation in the output power of light transmitted through the sensing element. Single and multilayered sensing films were fabricated using spin coating technique at 3000 rpm. The films were then annealed at 400°C. XRD of the film revealed the crystallinity, phase formation and minimum crystallite size as 5 nm, which was further confirmed from TEM and Particle Size Analyzer. A study of the optical band gaps of the sensing films demonstrates that as the number of layers or film thickness increase, their optical band gaps are found to be decreased. Energy band-gaps of one-, two-, three- and four-layered films were estimated as 3.927, 3.919, 3.873 and 3.830 eV respectively by UV-vis spectrophotometer. These results show that particle size increases with film thickness and hence absorption or band-gap decreases. Also, the sensitivity of the sensor decreases which is confirmed by the experimental results. The single-layered sensing element of YSZ was found most sensitive among the multilayered sensing elements. The maximum average sensitivity for the entire range of humidity (10-90 %RH) of opto-

electronic humidity sensor for one layered YSZ film was found 1.937 μW/%RH. Response and recovery times were found as 28 s and 30 s respectively. Experiments were repeated from time to time and found that ageing effect on the sensor was ~94%.

6.3 Synthesis and Characterization of CeO_2-Gd_2O_3-CoO Nanocomposite and its Application as Opto-electronic Humidity Sensor

Successful synthesis of CeO_2-Gd_2O_3-CoO nanocomposite using sol-gel extraction route and fabrication of its films on flat borosilicate glass substrates using spin coater at 3000 rpmwas done. The films were further annealed at 400°C. Refractive index of the film was found as 1.445538. XRD of the film revealed the crystalline nature of the material. Minimum crystallite size as calculated from the Debye Scherrer formula was 9 nm. Morphological investigation as obtained from SEM showed highly porous morphology. TEM analysis confirmed the formation of regular hexagonal crystals with diffused edges distributed uniformly. The minimum grain diameter as obtained from TEM image was ~6 nm which was further confirmed from Particle Size Analyzer. A study of the UV-vis spectra of the nanocomposite film demonstrated that the absorption of the material occurred in the UV-region (~320 nm). The optical energy band-gap as estimated from the Tauc plot was 3.987eV. Further, the film was checked for humidity detection capability using opto-electronic mode. The sensitivity obtained herefor 10-90 %RH was ~2.006 μW/%RH. The experiment was repeated and the sensor gave ~98% reproducible results. The effect of ageing was also checked and it was found negligible after a long run. The response and recovery times were found as 71 s and 86 s respectively.

6.4 Synthesis and Characterization of Nanostructured MnO_2-CoO and its Relevance as Opto-electronic Humidity Sensing Device

Nanostructured MnO_2-CoO was successfully synthesized using metal carboxylates as precursors and thin films were fabricated via spin coating technique (at 3000 rpm) and annealed at 650°C. The refractive index of the film was found as 1.445930. TEM investigated the minimum grain diameter of ~5.7 nm and SAED confirmed the

polycrystalline nature. The minimum crystallite size as obtained from XRD was ~4 nm. The particle size was also confirmed from the Particle Size Analyzer. SEM micrographs exhibited the enhanced surface area of the film by the formation of pores on the surface of the film. The Tauc plot obtained from the UV-vis absorption spectrum estimated the optical energy band gap of 3.849 eV. The film was then employed efficaciously as opto-electronic humidity sensor and the average sensitivity was found as 2.225 μW/%RH along with the response and recovery times as 47 s and 59 s. Experiments were repeated from time to time and found that reproducibility of the result was~ 89%.

6.5 Synthesis of La_2O_3-Cr_2O_3-SrO Nanocomposite by Pyrolysis of Metal Carboxylates; its Characterization and humidity sensing

Nanostructured La_2O_3-Cr_2O_3-SrO composite using sol-gel extraction route was successfully prepared and its multilayered films for humidity detection based on the electrical and optical parameters were fabricated. Single and multilayered sensing films were fabricated using spin coating technique at 3000 rpm. The refractive index of the material was found as 1.442302. XRD of the film shows the crystallinity, phase formation and minimum crystallite size as 9 nm. TEM gave the minimum grain diameter of ~ 2.7 nm. Particle Size Analyzer reported that all the particles in the solution are in the range ~3-100 nm. A study of the UV-vis spectrum of the sensing films demonstrated that as the number of layers or film thickness increase, their optical band gaps were found to be decreased whereas the height of the humps increased. The estimated band-gap of the thin film was found to be 3.842, 3.837, 3.802 and 3.789 eV for one-, two-, three- and four-layered film respectively. Therefore sensitivity of the sensor decreases which confirmed by the experimental results. Single layered sensing element was found most sensitive towards humidity. The sensitivity of one-layered sensing element regarding electrical parameters of impedance, capacitance, inductance and phase angle were 9.369 MΩ/%RH,7.345 pF/%RH, 7.734 KH/%RH and 2.429°/%RH respectively; whereas for opto-electronic mode, it was ~3.367μW/%RH. The experiment was repeated and results were found ~98% reproducible. The effect of ageing was also checked and found the negligible variation of characteristic after a long run. The response and recovery times were found as 15 s and 56 s respectively.

A chapter wise sketch of the thesis including the materials, their crystallite size, optical energy band-gap, sensitivity, reproducibility and response and recovery time is depicted in Table 6.1. The main goal of our research work carried out was to design and fabricate a humidity sensor which would be robust, cost-effective and highly responsive than previously reported sensors. From this table, it can be inferred that nanostructured composite of La_2O_3-Cr_2O_3-SrO is an excellent material for humidity sensing application at room temperature and using this material a commercialized model of humidity sensor applicable for both indoor and outdoor detection may be designed.

The scope of Further Research Work

In future, research works for productive and efficient devices, the understanding about the role of nanodimensional metal oxides in low-temperature applications would be desirable. This includes incorporation of the recovery aspects onto the surface of sensing element.

- In the present work, a nanostructured composite of La_2O_3-Cr_2O_3-SrO has been optimized to improve the sensing parameters, while there is scope for integration of modifiers like of similar radius or some nanocomposite or CNT's for reducing the response and recovery times of humidity sensor.
- An effort may also be made for the synthesis of nanostructured composites of bimetallic and multimetallic oxides using other methods and their versatile sensing applications.
- The dielectric behaviour of these optical nanocomposites is an interesting area. So attention may be focused in this area.
- The effects of higher annealing temperature on the thin films, substrate, doping, substitution, magnetic field, etc. may be investigated in future.
- Detailed analysis of the evolution of the surface reactions with respect to temperature needs to be carried out, in order to exactly understand the reaction products from the surface interaction.

- Humidity sensing carried out with metal oxide nanocomposites using transmission technique discussed in the thesis should be further investigated using Prism and U-shaped configurations for different coating lengths and coating thicknesses.
- Spectroscopic evaluation of the sensing mechanism using simulations has been important in future research.

Table

Table 6.1: A chapter wise sketch of the Thesis

Chapter No.	**Sensing Material**	**Crystallite Size (nm)**	**Optical Energy Band-gap**	**Sensitivity (μW/%RH)**	**Reproducibility (%)**	**Response Time (s)**	**Recovery Time (s)**
Ch. 1	**Introduction**						
Ch. 2	Y_2O_3-ZrO_2	~5	3.927	1.937	94	28	56
Ch. 3	CeO_2-Gd_2O_3-CoO	~6	**3.987**	2.006	91	71	59
Ch. 4	MnO_2-CoO	~4	3.849	2.125	89	47	86
Ch. 5	La_2O_3-Cr_2O_3-SrO	**~2.7**	3.842	**3.604**	**96**	**15**	**30**
Ch. 6	**Conclusion**						

APPENDIX

Experimental Methods and Characterization Techniques

The experimental techniques used throughout the whole work for the preparation and characterization of the nanomaterials and sensor are over-viewed in this part. The synthesis of bimetallic and multimetallic oxide nanocomposites was performed by sol-gel technique. Thin film fabrication was done by spin coating method. For the identification, the prepared sample was characterized by Digital refractometer, X-ray Diffractometer, Scanning Electron Microscopy, Transmission Electron Microscopy, UV-visible spectroscopy and Particle Size Analysis. Further the variation in the intensity of laser light corresponding to %RH transmitted from the film was observed by Optical Power Meter.

A.1 Introduction

The methodology and various experimental techniques used in the synthesis and investigation of bimetallic and multimetallic oxide nanocomposite thin films have been described. Digital refractometer, X-ray deffractometer, Scanning electron microscope, Particle Size Analyzer and UV-vis spectrophotometer were used to characterize these films. A large number of techniques have been employed for getting the overall information about the properties, structure, shape and size, topology etc. of the specimen. Some of the techniques which have been used in this thesis work are described in detail in this chapter.

A.2 Methodology of Present Work

Following steps were carried out for the present investigation;

1. Synthesis of nanostructured composite of desired metal oxides.
2. Fabrication of the thin film.
3. Investigation of the material using different characterization techniques to know refractive index, phase, structure, size, morphology, band gap etc. of the film. The techniques used here are as follows:
   a. **Digital refractometer:** This instrument is used for the determination of refractive index of the material upto the 6^{th} place of decimal.
   b. **X-ray Diffraction (XRD):** XRD is used for the study of phase identification and structural properties. It is also used to find crystallite size.
   c. **Scanning Electron Microscopy (SEM):** SEM technique is used to know the surface morphology of the nanocomposite thin film.
   d. **Transmission Electron Microscopy (TEM):** TEM is used to obtain the topography of the sample which deals with the internal structure of the sample, and its grain distribution and grain diameter.
   e. **Particle Size Analyzer:** It is used to find out the particle size distribution in the sample.
   f. **UV-visible Spectroscopy:** This spectroscopy will provide information about the absorption spectra and the optical band gap of the sample.
   g. **Optical Power Meter:** It is used for measuring the optical power transmitted from the film.

A.3 Synthesis

A.3.1 So-gel Method

Nowadays sol-gel technique is widely used for the synthesis of metal oxide and metal nitride semiconductor based nanostructure. The term sol-gel is combination of two words ‘sol’ and ‘gel’, where the term sol referred to the colloidal solution and gel belongs to continuous integrated network. The sol is formed that then gradually evolves towards the formation of a gel-like diphasic system containing both a liquid phase and solid phase whose morphologies range from discrete particles to continuous polymer networks. This array should be zero, one, two and three-dimensional in the form of particle, fibres and plates. The main advantage of colloid is that it offers high volume to surface ratio and form at low temperature. Thus, the sol-gel is a process in which a 1D, 2D and 3D nano structures are synthesized by dissolving solute in appropriate solvent. This technique can be used for preparing both thin films and nanopowder.

If the particle density is very low relative to the solvent in the colloid, the excess amount of fluid is removed initially which involves sedimentation and centrifugation. For the removal of the remaining solvent, drying process is required which further leads to shrinkage and densification. The absolute microstructure of the final component will be strongly dependant on the environmental conditions during this phase of processing. Further, thermal treatment is done to promote polycondensation and enhance mechanical properties and structural stability via final sintering, densification, and grain growth. This method leads to densification at a much lower temperature. Also it is cost effective approach. Even small quantities of dopants, such as organic dyes and rare-earth elements, can be introduced in the sol and end up uniformly dispersed in the final product.

Sol-gel spin coated thin film has better homogeneity, purity from raw materials and effective control of particle size, shape, and properties. In the process of sol gel spin coating the properties of thin films can be controlled with parameters such as spin speed, drying and annealing process and molarity of precursor solution. The nanopowder was obtained from prepared solution by precipitation method by increasing pH of solutions. A schematic diagram of sol-gel process to obtaining different nanostructures is shown in Fig.A.1.

A.4 Fabrication Techniques for Thin Film

A.4.1 Spin coating method

Spin coating is a technique in which a thin layer is coated on a solid platform (substrate) using a machine called spin coater (Metrex RC100, India) which is shown in Fig. A.2. The spin coater, which is used for thin film deposition having many components but mainly a powerful motor, generally which can spin up to 6000 round per minute (rpm) and a vacuum pump for holding substrate. In spin coater spinning speed and time of spinning are responsible for the thickness of thin films, if time of spinning and rate of spinning is increased the thickness of thin film decreased. The coated thin films were dried at temperature 150-200°C to eliminate excess solvents from the resulting. The required thickness of thin film was obtained by the repeating the process of spinning and drying.

Dispense of the resin plays an important factor in the preparation of thin film. For this, the substrate must be cleaned in ultrasonic bath. Then after loading the substrate on spin coater, the main task starts. There are two ways to dispense the resin fluid on the substrate. They are as follows:

Static resin: Static dispense is the deposition of a small puddle of resin fluid on the center of the substrate. Highly viscous solution and large substrate is needed in this process with a higher spinning speed. It also requires a large amount of fluid to cover the whole substrate and due to high spinning rate much of the fluid is wasted.

Dynamic resin: In this process speed of the arm rotator is slow around 500-1000 rpm. This is more advantageous than static resins as the chances of void formation are low in this method. In this less amount of fluid is required and due to low speed, the wastage of fluid around the rotator is less.

A.5 Annealing

The heat treatment includes heating and cooling operations applied to any material in order to modify its metallurgical structure and alter its physical, mechanical and chemical properties. Annealing, normalizing, stress relieving, quenching, hardening and tempering are the six widely used heat treatment processes that affect the structure and properties of any material. Annealing is heating the sample, maintaining a temperature for a certain time, and cooling regularly after reaching the desired properties. Annealing is performed to reduce hardness, remove

residual stresses, improve toughness and restore ductility. Annealing enhance device stability and to alter various mechanical, electrical or magnetic properties of device through refinement of grains. Annealing treatment can be performed in different types of atmospheres: air, protective gas or vacuum. Annealing in air is usually an easy option, but the disadvantage is that the surface of the film oxidizes on annealing under protective gas or vacuum. In general, there are two types of annealing treatments viz. fast thermal annealing (FTA) and slow thermal annealing (STA). FTA was performed by placing the samples into a furnace pre-heated at the required annealing temperature whereas in STA process the sample was placed on the furnace plate at room temperature and heated gradually to the desired anneal temperature. Fig.A.3 shows STA of process of annealing plot between temperature and time.

A.6 Characterization Techniques

The bimetallic and multimetallic oxide nanocomposite films were characterized by various characterization techniques which are described as follows:

A.6.1 Digital Refractometer

Refractometer is an instrument for the measurement of refractive index and concentration of liquids, gels and solids. Most of the refractometers operate on principle of critical angle. The difference is that light from an LED light source is focused on the underside or a prism element. When a liquid sample is applied to the measuring surface of the prism, some of the light is transmitted through the solution and lost, while the remaining light is reflected onto a linear array of photodiodes creating a shadow line. The refractive index is directly related to the position of the shadow line on the photodiodes. Once the position of the shadow line has been automatically determined by the instrument, the internal software will correlate the position to refractive index, or to another unit of measure related to refractive index, and display a digital readout on an LCD or LED scale. The more elements there are in the photodiode array, the more precise the readings will be, and the easier it will be to obtain readings for emulsions and other difficult-to-read fluids that form fuzzy shadow lines. The working principle along with photograph of the digital refractometer is shown in Fig. A.4.

Most have a metal sample well around the prism, which makes it easier to clean sticky samples, and some instruments offer software to prevent extreme ambient

light from interfering with readings. Some instruments are available with multiple scales, or the ability to input a special scale using known conversion information. There are some digital handheld refractometers that are water-resistant, and thus washable under a running faucet.

A.6.2 X-ray Diffractometer

X-ray diffraction (XRD) is one of the most important non-destructive tools to analyze all kinds of matter ranging from fluids, to powders and crystals. From research to production and engineering, XRD is an indispensable method for materials characterization and quality control. X-ray diffraction experiment is performed by machine called X-ray diffractometer, the photograph of which is shown in Fig. A.5. Here crystalline structure causes a beam of incident X-rays to diffract into many specific directions. By measuring the angles and intensities of these diffracted beams, a crystallographer can produce a three-dimensional picture of the density of electrons within the crystal. From this electron density, the mean positions of the atoms in the crystal, chemical bonds, crystallographic disorder etc. can be determined. An X-ray striking an electron produces secondary spherical waves emanating from the electron. This phenomenon is known as elastic scattering, and the electron is known as the scatterer. A regular array of scatterers produces a regular array of spherical waves. Although these waves cancel one another out in most directions through destructive interference, they add constructively in a few specific directions, determined by Bragg's law given in Eqn. A.1:

$$\mathbf{2d\sin\theta = n\lambda} \qquad \ldots. (A.1)$$

Here d is the spacing between diffracting planes, θ is the incident angle, n is any integer, and λ is the wavelength of the beam. The schematic diagram for Bragg's law is shown in Fig. A.6. These specific directions appear as spots on the diffraction pattern called reflections. X-rays are used to produce the diffraction pattern because their wavelength λ is typically the same order of magnitude (1–100 Å) as the spacing d between planes in the crystal.

X-rays are generated in a cathode ray tube by heating a filament to produce electrons, accelerating the electrons toward a target by applying a voltage, and bombarding the target material with electrons. When electrons have sufficient energy to dislodge inner shell electrons of the target material, characteristic X-ray spectra are

produced. These spectra consist of several components, the most common being K_α and K_β. K_α consists, in part, of $K_{\alpha1}$ and $K_{\alpha2}$. $K_{\alpha1}$ has a slightly shorter wavelength and twice the intensity as $K_{\alpha2}$. The specific wavelengths are characteristic of the target material (Cu, Fe, Mo, Cr). Filtering, by foils or crystal monochrometers, is required to produce monochromatic X-rays needed for diffraction. $K_{\alpha1}$ and $K_{\alpha2}$ are sufficiently close in wavelength such that a weighted average of the two is used. Copper is the most common target material for single-crystal diffraction, with Cu K_α radiation = 1.5418Å. These X-rays are collimated and directed onto the sample. As the sample and detector are rotated, the intensity of the reflected X-rays is recorded. When the geometry of the incident X-rays impinging the sample satisfies the Bragg Equation, constructive interference occurs and a peak in intensity occurs.

The basic component of diffractometer is an X-rays coherent source (Cu K_α, 0.15418 nm) which provides a beam of X-ray directed towards the crystal (sample) and a detector which monitors diffracted beam intensity. Other components are several focusing optics, rotating stand sample holder and software. The X-rays diffraction software provides an intensity of diffractive X-rays as a function of d-spacing/2θ which contains peaks at certain positions. This XRD pattern is a signature of certain materials and these signature patterns are provided by International Centre for Diffraction Data (ICDD) and Joint Committee on Powder Diffraction Standards (JCPDS). The information obtained from this pattern includes types and nature of crystalline phases present, structural make-up of phases, degree of crystallinity, amount of amorphous content, micro strain & size and orientation of crystallites. The following formulae are used to calculate these parameters [2-4]. The crystalline size (D) of crystal was calculated by Debye-Scherrer's formula given in Eqn. A.2

$$\mathbf{D} = \frac{\mathbf{K\lambda}}{\mathbf{\beta cos\theta}} \quad \text{.... (A.2)}$$

where, constant factor K is nanostructure constant, β is the broadening of diffraction line measured at half of its maximum intensity (FWHM) and λ is the wavelength of the X-ray used (0.15418 nm).

A.6.3 Scanning Electron Microscope

A scanning electron microscope (SEM) is a type of electron microscope that produces images of a sample by scanning the surface with a focused beam of electrons. The electrons interact with atoms in the sample, producing various signals

that contain information about the surface topography and composition of the sample. The most common SEM mode is the detection of secondary electrons emitted by atoms excited by the electron beam. By scanning the sample and collecting the secondary electrons that are emitted using a special detector, an image displaying the topography of the surface is created. The photograph of scanning electron microscope used in the reported research is shown in Fig. A.7(a).

SEM consists of an electron gun of some kind such as Tungsten or Lanthanum Hexaborate (LaB_6) which acts as the source of electron beam. The filament inside the electron gun is heated until a stream of electron is produced. This stream of electron is then condensed by first condenser lens, this lens serves two purposes at a time. One, it eliminates the high-angled electron from the beam and second, it limits the amount of current in the beam. The second condenser lens makes the beam narrower and focused. Near the bottom of SEM a set of scanning coils is present that is used to focus the beam in the back and forth direction. When this beam hits the spot on the sample surface, it removes the secondary electrons and these electrons are detected by the detectors. The detectors role is to count the electrons and amplify the current and record it to visualize the image based on the number of electrons removed from the particular spot in pixels by a computerized system. The working of the SEM is shown in Fig. A.7(b).

Specimen interaction with the beam

Specimen interaction is the process that makes electron microscopy possible. The various interactions that occur at the surface of the specimen is shown in Fig. A.8 and listed in the following sub-heads:

Secondary electron emission: The emission of secondary electron is caused when the energized electrons strikes the surface of the sample. These electrons transfer some energy to the lower energy electrons (usually the K–shell) and this causes the ionization of the atoms present at the surface of sample. This electron removed from the surface is called as “secondary electron”. This is the most common mode used in the imaging with SEM. The brightness of the signals depends upon the number of secondary electrons reaching the detector.

Backscattered electrons: Backscattered electrons are reflected or backscattered out of the specimen interaction volume. This is caused by collision of incident electron to

an atom which is nearly normal to the incident path. The production of backscattered electrons varies directly with the atomic number of the specimen, that is, higher the atomic number, higher will the brightness. Backscattered electrons thus can be used to detect different chemical composition, by examining the contrast between the areas.

Cathodo luminescence: When the high energy electrons strike the surface they excite the atoms and when these atoms return to their ground state they emit light. This process is termed as Cathodo luminescence (CL). In SEM, CL detectors can be used to give image in real colour.

Auger electron: When the electron is removed from the core level of the atom, a vacancy is created which is filled by higher energy electron releasing energy which is transferred to another electron, which is then ejected as auger electron. Auger electron has a characteristic energy feature which is unique for each element. Thus these auger electrons are collected and provide useful compositional information of the sample surface.

A.6.4 Transmission Electron Microscope (TEM)

Transmission electron microscopy (TEM) is a microscopy technique in which a beam of electrons is transmitted through a specimen to form an image. The specimen is most often an ultra thin section less than 100 nm thick or a suspension on a grid. An image is formed from the interaction of the electrons with the sample as the beam is transmitted through the specimen. The image is then magnified and focused onto an imaging device, such as a fluorescent screen, a layer of photographic film, or a sensor such as a charge-coupled device. TEM provides the image in real time. The image of a TEM machine is shown in Fig. A.9 (a).

The TEM consists of an emission source, which may be a tungsten filament or needle, or a lanthanum hexaboride (LaB_6) single crystal source. The gun is connected to a high voltage source (typically ~100–300 kV) and, given sufficient current; the gun will begin to emit electrons either by thermionic or field electron emission into the vacuum. The electron source is typically mounted in a Wehnelt cylinder to provide preliminary focus of the emitted electrons into a beam. The upper lenses of the TEM then further focus the electron beam to the desired size and location. The schematic set-up depicting different parts is shown in Fig. A.9 (b).

Description of sample holder

TEM specimen stage includes airlocks which allow the insertion of the specimen holder into the vacuum with minimal loss of vacuum in other areas of the microscope. The specimen holders hold a standard size of sample grid or self-supporting specimen. Standard TEM grid sizes are 3.05 mm diameter, with a thickness and mesh size ranging from a few to 100 μm. The sample is placed onto the meshed area having a diameter of ~2.5 mm. Usual grid materials are copper, molybdenum, gold or platinum. This grid is placed into the sample holder, which is paired with the specimen stage. A wide variety of designs of stages and holders exist, depending upon the type of experiment being performed. Once inserted into the TEM, the sample has to be manipulated to locate the region of interest to the beam, such as in single grain diffraction, in a specific orientation. To accommodate this, the TEM stage allows movement of the sample in the XY plane, Z height adjustment, and commonly a single tilt direction parallel to the axis of side entry bolders. Sample rotation may be available on specialized diffraction holders and stages. The various steps involved in the working of TEM are:

- The electron beam produces a beam of electrons, which is then focused to a thin, coherent beam.
- This beam of electron is further restricted by the condenser lenses which knock out the high angled electron.
- This beam transmits through the specimen and is focused by the objective lenses to give an image.
- The image is then passed by the project lenses to enlarge the image, which then strikes the phosphor screen.
- The darker area represents the presence of few number of electrons transmitted through the sample (i.e. the sample must be thick there) whereas the brighter part will represent more transmitting electron area.

Detection of transmitted electrons

Following steps are involved in the detection of transmitted electrons and image formation:

Unscattered electrons: These are the incident electrons that are transmitted through the sample without any interaction. The image will appear darker if the unscattered

electrons are few as they vary inversely with the thickness and the image will appear brighter for large number of unscattered electrons.

Elastically scattered electron: There are incident electrons that get deflected from their path. The scattering of the electron follows Bragg's Law ($\lambda = 2d \sin\theta$). Since all the incident electrons have same energy and atomic spacing, so they will scatter with same angle. These scattered electrons can thus be collected by magnetic lenses to give pattern of spots which in turn are very useful in determining the orientation, atomic arrangement and phases present in the given sample.

Inelastically scattered electrons: There are many electrons that interact inelastically with the specimen transferring out all their energy to the atoms in the specimen. These electrons then transmit through the rest of the specimen. These unscattered electrons can be used to provide following information:

- The inelastic loss of energy is dependent on the element and is unique to the bonding state of the element, thus gives the information about composition and bonding.
- The alternate light and dark lines (Kakuchi bands) formed due to inelastic scattering; the width of these bands is inversely proportional to the atomic spacing.

A.6.5 UV-vis Spectrophotometer

Ultraviolet and visible (UV-vis) absorption spectroscopy is the measurement of the attenuation (weakening of strength) of a beam of light after it passes through a sample or after reflection from a sample surface. Ultraviolet and visible light are energetic enough to promote outer electrons to higher energy sublevels. The technique is usually applied to molecules or inorganic complexes in solution. Absorption measurements can be at a single wavelength or over an extended spectral range. UV-vis spectra have broad features that are of limited use for sample identification but are very useful for quantitative measurements. The concentration of an analyte in solution can be determined by measuring the absorbance at some wavelength and applying the Beer-Lambert Law. Since the UV-vis range spans the range of human visual acuity of ~400-750 nm, UV-vis spectroscopy is useful to characterize the absorption, transmission, and reflectivity of a variety of technologically important materials, such as pigments, coatings, windows, and filters. This more qualitative application usually requires recording at least a portion of the UV-vis spectrum for characterization of the

optical or electronic properties of materials. Electronic orbital of atoms and molecules have characteristic energies, giving rise to a set of discrete energy levels. An electron is able to change from an occupied orbital to another orbital, gaining or losing energy only in amounts exactly corresponding to the difference between two levels. The spectrophotometer used here for the determination of optical properties is shown in Fig. A.10(a).

The promotion of an electron from the ground state (lowest possible energy) at energy E_1 to higher energy state at E_2 is possible if the molecule absorbs electromagnetic radiation of the corresponding wavelength $\lambda = hc/(E_2-E_1)$ (where, c = speed of light, h = Planck's constant). The electron at a higher energy is then said to be in an excited state. Excited states usually exist only for very short periods of time (femto seconds to microseconds), because the higher energy state is unstable and the extra energy is lost through relaxation processes such as emission of light. The typical energy difference between the ground and the first excited levels of many molecules corresponds to electromagnetic waves of the ultra-violet (UV) and visible regions of the electromagnetic spectrum.

The UV-visible range is only a small part of the total electromagnetic spectrum, and is generally defined from wavelengths of 190 nm at the high energy UV end to about 800 nm at the low energy red end of the spectrum. Light of other regions of the spectrum gives rise to different types of transitions and hence different types of spectroscopy. For example, IR radiation is usually not energetic enough to cause electronic transitions but can excite vibrations of molecules.

UV-visible spectrophotometers usually measure absorbance, which is the log-ratio of transmitted (sample in beam) over incident (no sample in beam) intensities. The UV-vis photo spectrum of solution is recorded with respect to water placed in the reference beam using single beam spectrophotometer. The spectrum is analyzed by plotting $(\alpha h\nu)^2$ vs $h\nu$, based on eqn A.3:

$$\alpha h\nu = A(h\nu - E_g)^n \quad \ldots. (A.3)$$

where, α is absorption coefficient, A is a constant and n is the exponent that depends upon the quantum selection rules for the particular material. The value of n characterizes the nature of band transition (n = 1/2 and 3/2 corresponds to direct allowed and direct forbidden transitions while n = 2 and 3 corresponds to indirect

allowed and indirect forbidden transitions, respectively). A straight line is obtained when $(\alpha h\nu)^2$ is plotted against photon energy ($h\nu$), which indicates that the absorption edge is due to direct allowed transition. The intercept of the straight line on $h\nu$ axis corresponds to the optical energy band-gap (E_g).

In a standard UV-vis spectrophotometer, a beam of light is split; one-half of the beam (the sample beam) is directed through a transparent cell containing a solution of the compound being analyzed, and one-half (the reference beam) is directed through an identical cell that does not contain the compound but contains the solvent. The instrument is designed so that it can make a comparison of the intensities of the two beams as it scans over the desired region of the wavelengths. If the compound absorbs light at a particular wavelength, the intensity of the sample beam will be less than that of the reference beam. Absorption of radiation by a sample is measured at various wavelengths and plotted by a recorder to give the spectrum which is a plot of the wavelength of the entire region versus the absorption of light at each wavelength**.** And the band gap of the sample can be obtained by plotting the graph between ($\alpha h\nu$ vs $h\nu$) and extrapolating it along the x-axis**.** Ultraviolet and visible spectrometry are almost entirely used for quantitative analysis; that is, the estimation of the amount of a compound known to be present in the sample. The sample is usually examined in solution form. The working is shown in Fig. A.10(b).

A.6.6 Particle Size Analyzer

As the name suggests, Particle Size Analyser is a technique used to measure the size of the particles present in the solution. The idea behind this size measurement is called Dynamic Light Scattering (also known as PCS-Photon Correlation Spectroscopy) which measures the Brownian motion and relates this to the particle size. It does this by illuminating the laser and analyzing the intensity fluctuations in the scattered light. The photograph of the instrument is shown in Fig. A.11(a).

If a small particle is illuminated by a light source such as a laser, the particle will scatter the light in all directions. If a screen is held close to the particle, the screen will be illuminated by the scattered light. Fig. A.11(b) shows the propagated waves from the light scattered by the particles. The bright areas of light are where the light scattered by the particles arrive at the screen with the same phase and interferes

constructively to form a bright patch. The dark areas are where the phase additions are mutually destructive and cancel out each other.

Particles suspended in a liquid are never stationary. The particles are constantly moving due to Brownian motion. Brownian motion is the movement of particles due to the random collision with the molecules of the liquid that surrounds the particle. An important feature of Brownian motion for DLS is that small particles move quickly than large particles. As the particles move around, the constructive and destructive phase addition of the scattered light will cause the bright and dark areas to grow and diminish in intensity or to put it another way, the intensity appears to fluctuate.

A.6.7 Optical Power Meter

An optical power meter (OPM) is a device used measure the power in an optical signal. The photograph of the optical power meter used in the reported work is shown in Fig. A.12. The light power measuring devices are usually called radiometers, photometers, laser power meters, light meters or lux meters. A typical optical power meter consists of a calibrated sensor, measuring amplifier and display. The sensor primarily consists of a photodiode selected for the appropriate range of wavelengths and power levels. On the display unit, the measured optical power and set wavelength is displayed. Power meters are calibrated using a traceable calibration standard such as a NIST standard. A traditional optical power meter responds to a broad spectrum of light; however the calibration is wavelength dependent.

Sometimes optical power meters are combined with a different test function such as an Optical Light Source (OLS) or Visual Fault Locator (VFL), or may be a sub-system in a much larger instrument. When combined with a light source, the instrument is usually called an Optical Loss Test Set (OLTS). OLTS are available in hand-held instruments and platform-based modules to suit various network architectures and test requirements. They are used to measure optical power and power loss, and reflectance and reflected power loss. The products may also be used as optical sources or optical power meters, or to measure optical return loss or event reflectance.

Three types of equipment can be used to measure optical power loss:

Component equipment - Optical Power Meters (OPMs) and Stabilized Light Sources (SLSs) are packaged separately, but when used together they can provide a measurement of end-to-end optical attenuation over an optical path. Such component equipment can also be used for other measurements.

Integrated test set - When an SLS and OPM are packaged in one unit, it is called an integrated test set. Traditionally, an integrated test set is usually called an OLTS.

An Optical Time Domain Reflectometer (OTDR) can be used to measure optical link loss if its markers are set at the terminus points for which the fiber loss is desired. However a single-direction measurement may not be accurate if there are multiple fibers in a link, since the back-scatter coefficient is variable between fibers. The accuracy of such a measurement can be increased if the measurement is made as a bidirectional average of the fiber.

A.6.8 Vibration free table

The vibration free table is used to absorb the vibrations from the surroundings. Here Newport Model no. RS2000-48-8, as shown in Fig. A.13, was used in which the experimental set-up was kept. This 8 inch thick optical table has a 4 foot width, 8 foot length, and 1/4-20 holes on a 1 inch grid. The RS2000 series matches the top of the line performance from competitive models. The unmatched low frequency superiority of Newport vibration absorber tuned damping technology allows its larger sized tables to outperform all competitive models. Its supreme stability has meant the difference between success and failure in countless leading edge applications. The photograph of the above described vibration free table is shown in Fig. A.13.

References

[1] S.M. Attia, J. Wang, G. Wu, J. Shen, J. Ma, Review on sol–gel derived coatings: process, techniques and optical applications, J. Mater. Sci. Techno. 8 (2002) 211–217.

[2] D.W. Schubert, T. Dunkel, Spin coating from a molecular point of view: its concentration regimes, influence of molar mass and distribution; Mater. Res. Innovations 7 (2003) 314.

[3] J.D. Verhoeven, Fundamentals of Physical Metallurgy, Wiley, New York (1975) 326.

[4] D. Merkulovs, Cylindrical cell based refractometer and its applications methodology, Thesis: Riga Technical University (2015).

[5] W.H. Bragg, W.L. Bragg, The reflexion of X-rays by crystals, Proceedings of the Royal Society of London A 88 (1913) 428–438.

[6] A. Patterson, The Scherrer formula for X-ray particle size determination, Physical Review 56 (1939) 978–982.

[7] D.J. Stokes, Principles and Practice of Variable Pressure Environmental Scanning Electron Microscopy (VP-ESEM). Chichester: John Wiley & Sons. (2008) ISBN 978-0470758748.

[8] J. Frank, Electron tomography: methods for three-dimensional visualization of structures in the cell, Springer (2006) ISBN 978-0-387-31234-7.

[9] L. Sooväli, E.I. Rõõm, A. Kütt et al. Uncertainty sources in UV–Vis spectrophotometric measurement. Accreditation and Quality Assurance 11 (2006) 246–255.

[10] Zetasizer Nano Series User Manual Zetasizer: Malvern

[11] Hand-held Optical Power Meter: Model 1916-C/-R User's Manual: Newport

[12] Vibration free table: Newport Model no. RS2000-48-8 User's Manual: Newport

Figures

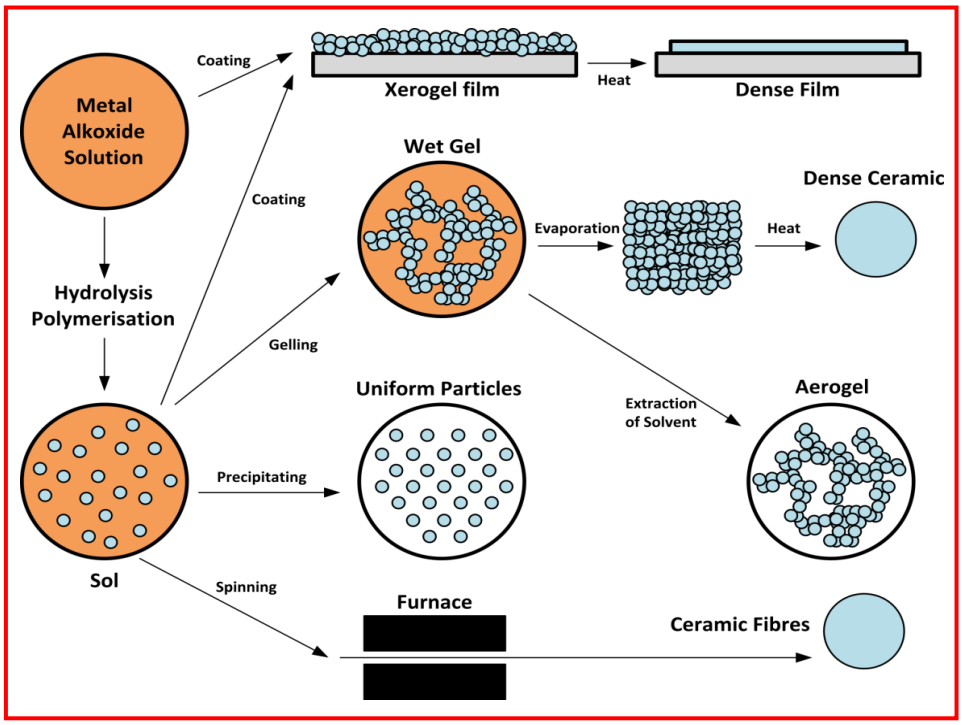

Figure A.1: Schematic representation showing different steps of Sol-gel process

Figure A.2: Photograph of spin coater (Metrex) used in the preparation of thin film

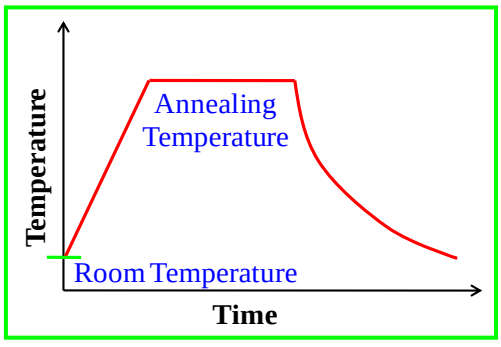

Figure A.3: Slow thermal annealing process diagram for annealing of samples.

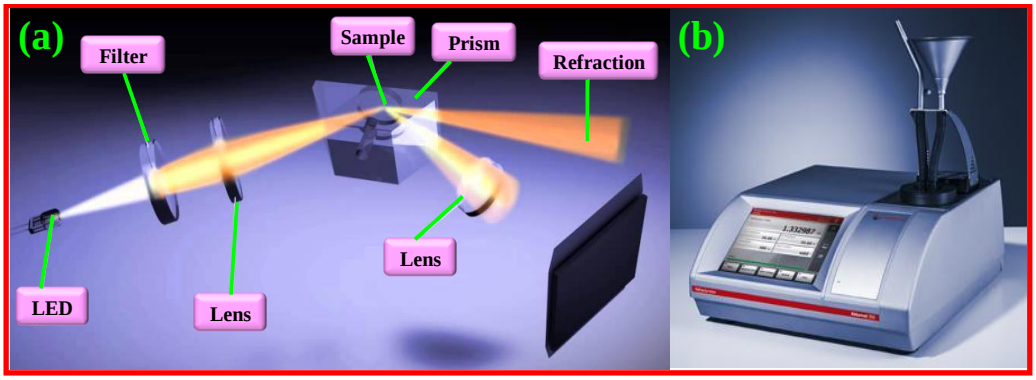

Figure A.4: a) Working principle of Digital Refractometer, (b) Photograph of Digital Refractometer (Anton Paar Abbemat) for the determination of refractive index

Figure A.5: Photograph of X-ray diffraction setup (X' Pert PRO PANalytical Ltd., Netherlands).

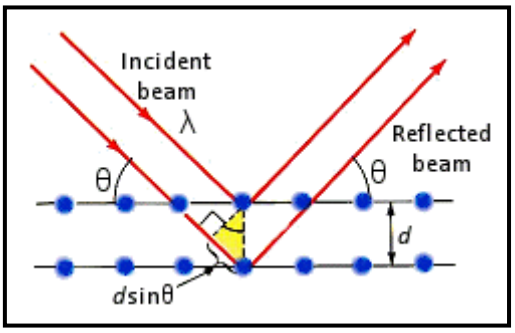

Figure A.6: Schematic diagram showing the phenomena of Bragg's law

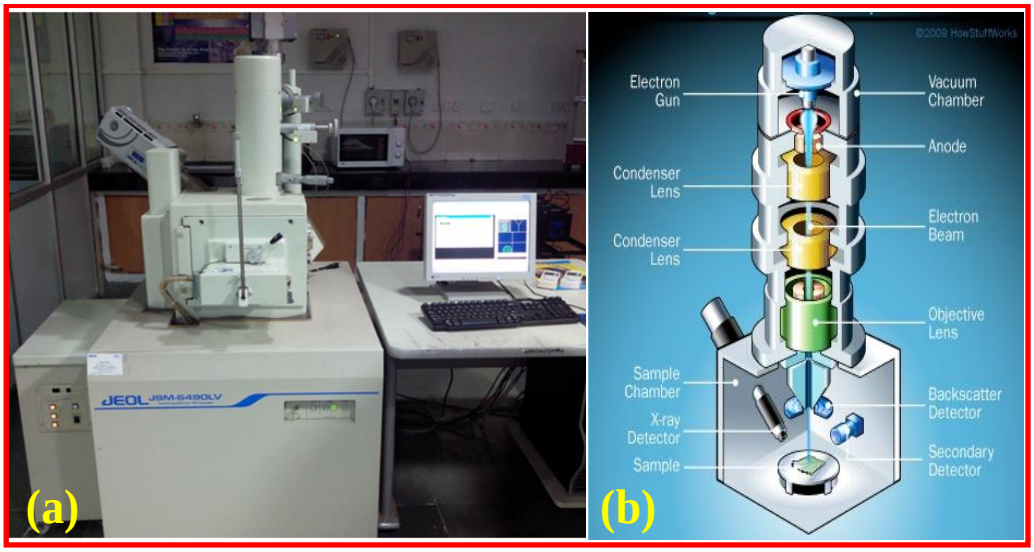

Figure A.7 (a) Photograph of Scanning Electron Microscopes (JEOL, JSM-6490LV) and its (b) working mechanism

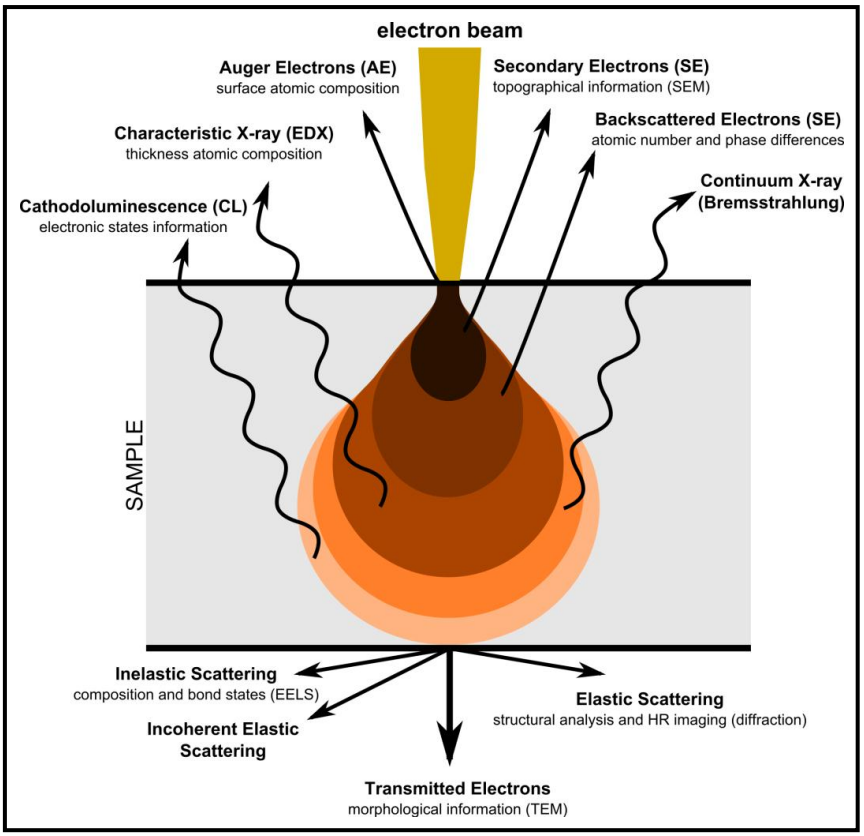

Figure A.8: Representation of various types of interactions of electron beam with the sample surface

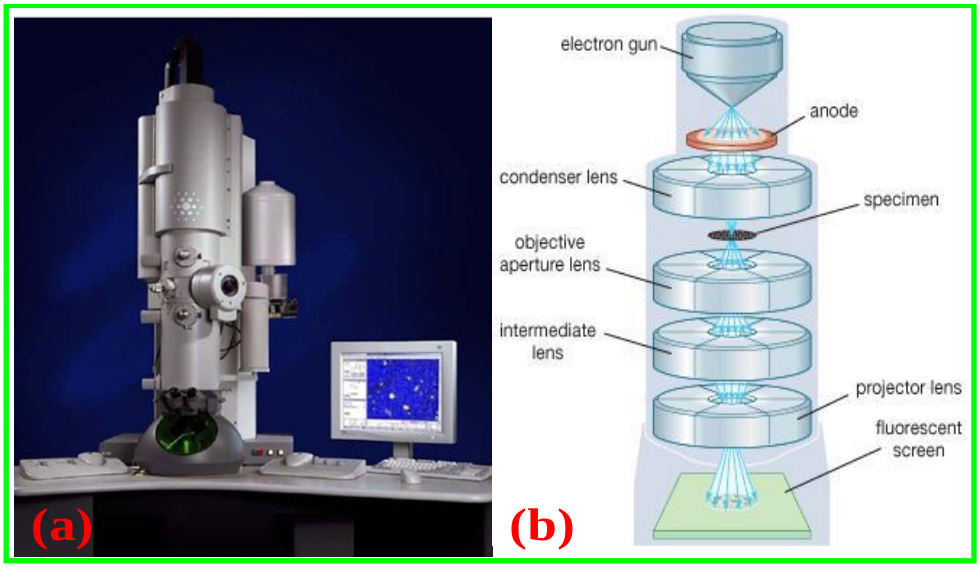

Figure A.9: (a) Photograph of High-Resolution Transmission Electron Microscope (Philips T20ST) and its (b) working mechanism

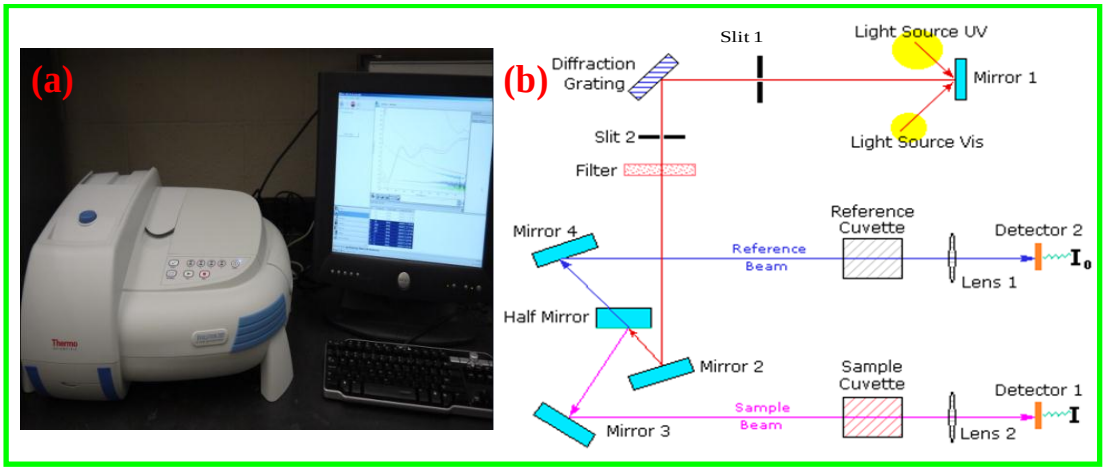

Figure A.10: Photograph of UV-Visible spectrophotometer (Evolution 201) and its (b) working mechanism

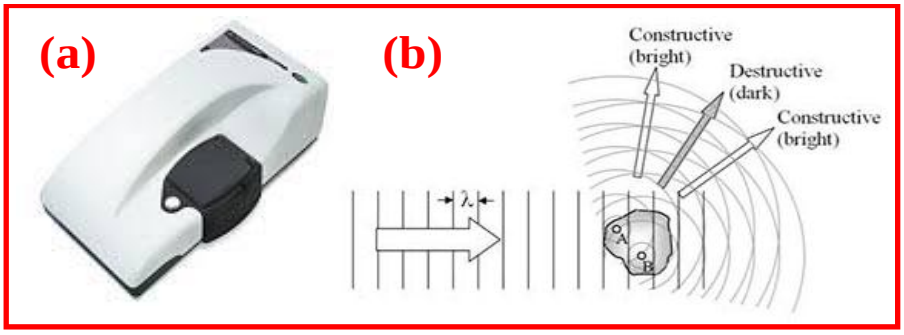

Figure A.11: (a) Photograph of Particle Size Analyzer (Nano-ZS90) (b) Scattering of light beam through a particle

Figure A.12: Photograph of the optical power meter (Newport 1916-R)

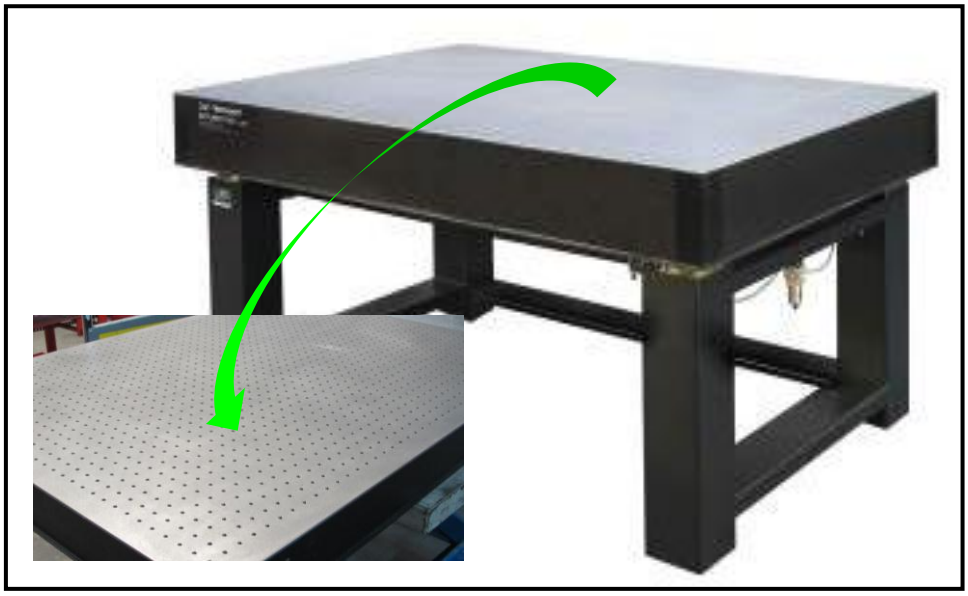

Figure A.13: Photograph of the Vibration free table (Newport RS2000-48-8)

Sensors and Actuators A 233 (2015) 54–70

Contents lists available at ScienceDirect

Sensors and Actuators A: Physical

journal homepage: www.elsevier.com/locate/sna

Review

Opto-electronic humidity sensor: A review

S. Sikarwar, B.C. Yadav*

Nanomaterials and Sensor Research Laboratory, Department of Applied Physics, School for Physical Sciences, Babasaheb Bhimrao Ambedkar University, Lucknow 226025, U.P., India

ARTICLE INFO

Article history:
Received 20 November 2014
Received in revised form 7 May 2015
Accepted 8 May 2015
Available online 19 May 2015

Keywords:
Humidity sensor
Sol–gel
Dip process
Spin coating
Opto-electronic
Fibre

ABSTRACT

The present paper reports the detailed study of various metal oxide nanomaterials as opto-electronic humidity sensor. The sensor elements were fabricated and characterized as thin or thick film based on the semi-conducting metal oxide. As semi-conducting metal oxides are known for their n-type conduction because of the presence of oxygen vacancies and change in refractive indices with the exposure of moisture therefore they were proven to be very good sensors for humidity. Depending upon the need, the sensing materials were deposited either on the base of the prism or on the U-shaped borosilicate glass rods or on some other transparent substrates for opto-electronic sensing. Light from LED or He–Ne laser was launched into the sensing element from one side and collected into the other side by optical power meter. The mode of propagation of light was transmission, reflection or partially refraction. Modulations in the intensity of light with changes in humidity were recorded. Being optical in nature, such types of sensors are very useful for detection of moisture level at remote places or unmanned stations. The primary purpose of this paper is to focus on the techniques used in these sensors.

Contents

* Corresponding author.
E-mail address: balchandra_yadav@rediffmail.com (B.C. Yadav).

http://dx.doi.org/10.1016/j.sna.2015.05.007
0924-4247/

Sensors and Actuators B 232 (2016) 283–291

Contents lists available at ScienceDirect

Sensors and Actuators B: Chemical

journal homepage: www.elsevier.com/locate/snb

Fabrication of nanostructured yttria stabilized zirconia multilayered films and their optical humidity sensing capabilities based on transmission

Samiksha Sikarwar[a], B.C. Yadav[a,*], Satyendra Singh[b], G.I. Dzhardimalieva[c], S.I. Pomogailo[c], Nina D. Golubeva[c], A.D. Pomogailo[c]

[a] Nanomaterials and Sensors Research Laboratory, Department of Applied Physics, Babasaheb Bhimrao Ambedkar University, Lucknow 226025, U.P., India
[b] Department of Physics, University of Allahabad, Allahabad 211002, U.P., India
[c] Laboratory of Metallopolymers, Institute of Problems of Chemical Physics, Russian Academy of Sciences, Chernogolovka, Moscow Region 142432, Russia

ARTICLE INFO

Article history:
Received 1 December 2015
Received in revised form 17 March 2016
Accepted 18 March 2016
Available online 25 March 2016

Keywords:
Nanostructure
Opto-electronic humidity sensor
Sol-gel spin coating
YSZ

ABSTRACT

The present paper reports the study of modulation in intensity of light transmitted through the thin films of nanostructured yttria stabilized zirconia (YSZ) with the exposure of moisture at room temperature. For this purpose the precursor of YSZ was prepared and used for the deposition of multilayered thin films on borosilicate substrates. The film was then investigated using SEM, XRD and UV–vis absorption techniques. The refractive index of the sensing material was found as 1.448829. SEM showed the macroporous nature of the film and XRD revealed the minimum crystallite size as 5 nm which was further confirmed using TEM and Zeta nanosizer. Energy band-gaps of one-, two-, three- and four- layered films were estimated as 3.927, 3.919, 3.873 and 3.830 eV respectively by UV–vis spectrophotometer. These films were employed as transmission based opto-electronic humidity sensor. Maximum sensitivity was found as ~ 1.937, 1.642, 1.393 and 1.143 μW/%RH for one, two, three and four- layered films, respectively. Response and recovery times of the sensor were found as 28 s and 30 s respectively. Experiments were repeated time to time and found that the sensor was ~94% stable after long run. Thus the investigated opto-electronic sensor has excellent potential to replace an electrical humidity sensor.

1. Introduction

In recent years, humidity/gas sensing is becoming more important, mainly in control systems for industrial processes and human comfort [1]. An extensive diversity of metal oxides and their nanocomposites, ceramics and polymers have been investigated as humidity sensors. These sensors are mainly based on the modulation in electrical signals such as impedance, resistance and capacitance [2–6]. Moreover, another category of the sensors is also available whose principle is based on modulation in optical parameters such as refractive index (r.i.), intensity modulation, frequency shift and wavelength modulation; these are frequently called as optical/opto-electronic sensors [7]. With the growth of industrialization, there is an urgent need of electrical-circuit-free sensor system. Optical sensors have tremendous advantages over their electrical counterpart as they can operate without any interference from nearby electric or magnetic fields and hence, optical humidity sensing is more effective compared to electrical humidity sensing [8].

Various morphologies of nanostructured metal oxides such as ZnO [9], TiO_2 [10], CuO [11], MoO_3 [12], SnO_2 [13], Fe_2O_3 [14] etc. were considered to be the promising candidates for the investigation because of their inherent chemical and physical stability. In this sequence nanostructured zirconia is also an important functional material known for its advanced applications such as biomaterial and orthopedic ceramic [15,16]. Nano zirconia ceramics are of more importance for their high improvement in strength and toughness which play an important role for its excellent mechanical, electrical, thermal, magnetic and optical properties [17,18]. Pure zirconia has three polymorphic phases (stable at various temperatures): cubic, tetragonal and monoclinic. The zirconia material commonly used by most manufacturers is a tetragonal polycrystalline zirconia, partially stabilized with yttrium oxide [19–21] which can be implicit by schematic shown in Fig. 1 [22]. The addition of yttria to pure zirconia replaces some of the Zr^{4+} ions in the zirconia lattice with

* Corresponding author.
E-mail addresses: balchandra_yadav@rediffmail.com, nano.lu71@gmail.com (B.C. Yadav).

http://dx.doi.org/10.1016/j.snb.2016.03.080
0925-4005/

RSC Advances

PAPER

Cite this: *RSC Adv.*, 2018, **8**, 20534

Synthesis and characterization of nanostructured MnO_2–CoO and its relevance as an opto-electronic humidity sensing device†

Samiksha Sikarwar,[a] B. C. Yadav,*[a] G. I. Dzhardimalieva,[b] N. D. Golubeva[b] and Pankaj Srivastava[a]

Metal carboxylates are widely used in science and technology and have been the subject of intense studies due to the practical importance of their products. The present paper reports the synthesis of MnO_2–CoO using metal carboxylates as precursors and the effect of humidity on the transmitted power through its thin film at room temperature. The refractive index of the material was found to be 1.445930 and the peak obtained from the photoluminescence spectra lies in the visible region. TEM reported a minimum grain size of ~5.7 nm and SAED confirmed the crystalline nature of the material, which was further confirmed by XRD. Fluorescence characteristics also confirmed the low dimensionality of the material. The film was then investigated using SEM which exhibited the porous morphology. Through UV-Vis spectroscopy, it was found that the absorption of the film takes place in the UV region and the optical band-gap was observed to be 3.849 eV from the Tauc plot. The film was employed as a transmission based opto-electronic humidity sensor. Average sensitivity was found to be ~2.225 μW/% RH with response and recovery times of 47 s and 59 s respectively. Experiments were repeated and the reproducibility of result was found to be ~89%.

Received 6th March 2018
Accepted 15th May 2018

DOI: 10.1039/c8ra01975d

rsc.li/rsc-advances

Introduction

Unique surface properties and high catalytic activity of metal oxides make them very attractive for various sensor applications.[1,2] Titanium, cerium, copper, iron, and manganese oxides have been widely used as catalysts, photocatalysts and electrocatalysts in a variety of reactions in organic synthesis.[3–6] Transition metal oxides, such as Mn_2O_3, Co_3O_4, NiO, *etc.*, are of interest for optical waveguide gas sensors.[7] V_2O_5 nanobelts ($V_2O_5 \cdot xH_2O$, V_2O_5·CTAB and V_2O_5 nanorods annealed at 400 °C) revealed the properties of an ethanol sensor with high selectivity and stability.[8] The Cu–CuO nanocomposite was successfully used to modify a glassy carbon electrode to detect H_2O_2 and glucose.[9]

Metal carboxylates are widely used in science and technology. They have been the subject of intense studies due to the practical importance of their products.[10] In particular, the controlled thermolysis of metal carboxylates can be considered as an effective way for the synthesis of nanocomposite materials.[11] Owing to the formation of ferromagnetic Fe_3O_4 and $CoFe_2O_4$ nanoparticles, the thermolysis products of metal acrylates and their co-crystallizates behave as solid magnets with a coercive force of 0.18 T and the residual magnetization of 15.5 mT at room temperature.[12] The spinel ferrites $Zn_{0.5}Mn_{0.5}$-Fe_2O_4,[13] $CoFe_2O_4$,[14] and $MnFe_2O_4$ [15] synthesized by pyrolysis of the corresponding polyacrylate salts exhibit superparamagnetic properties at room temperature.

Humidity measurement is one of the most required parameters for various applications not only for improving the quality of life but also for enhancing the industrial process.[16,17] Advancements in sensor manufacturing technologies lead the researchers to know the degree of efficiency with predictions based on simulation techniques and design aids to improve sensitivity and sensor quality along with time-saving.[18] The humidity plays very important role and has acquired such incredible significance due to the fact that these vapours consist of highly reactive dipolar molecules which get condensed on or evaporate from the surface even with small variations in temperature of the environment. Optical humidity sensors are better than their electronic counterparts due to their small size, low weight, immune towards electromagnetic disturbances, possibility of multiplexing information and working on high pressure and flammable environments.[19] Complex oxides containing cobalt and manganese show different oxidation states (Co^{2+}, Co^{3+}, Mn^{2+}, Mn^{3+}, and Mn^{4+})[20] and hence attractive distinct properties like enhanced tunable surface, specific

[a]*Nanomaterials and Sensors Research Laboratory, Department of Physics, Babasaheb Bhimrao Ambedkar University, Lucknow-226025, U.P., India. E-mail: balchandra_yadav@rediffmail.com; Tel: +919450094590*

[b]*Laboratory of Metallopolymers, Institute of Problems of Chemical Physics, Russian Academy of Sciences, Chernogolovka, Moscow Region, 142432, Russia*

† Electronic supplementary information (ESI) available. See DOI: 10.1039/c8ra01975d

Nanostructured spherical-shaped Sc(III) Polyacrylate for monitoring the moisture level

Samiksha Sikarwar, *INSPIRE Fellow,* Arun Kumar, *Ex-P.G. Student,* B.C. Yadav, *Professor*, G.I. Dzhardimalieva, *Professor* and Nina D. Golubeva, *Senior Researcher*

***Abstract*—The present paper reports the investigation of transmitted power through the nanostructured scandium polyacrylate (Sc(III) PAcr) deposited on flat borosilicate substrates to examine the adsorption/desorption of humidity at room temperature. For this purpose, the precursor of $Sc(CH_2=CH-COO)_3$ was prepared and used for film deposition. The film was then investigated using SEM and UV–Vis absorption techniques. Scanning Electron Microscope showed the spherical shaped clusters of the material. Energy band-gap of the film was estimated as 3.887 eV by UV–Vis spectrophotometer. Transmission Electron Microscope revealed the minimum grain diameter of ~21 nm and SAED showed its polycrystalline nature. From Zeta nanosizer, minimum particle size was found as 18 nm. FTIR confirmed the bond formation in the material. The surface area analysis shows that the pore volume of Sc(III) PAcr is 0.15 cm^3/g which is quite small whereas the surface area and mean pore radius of the spherical structure are 60.1 m^2/g and 41.2 Å respectively. The film was employed as transmission based opto-electronic humidity sensor. Maximum sensitivity was found as 2.1 µW/%RH with 89% reproducibility. Response and recovery times of the sensor were found as 25 s and 155 s respectively.**

Index Terms— **humidity, metallopolymer, polyacrylate, scandium, sensor**.

I. INTRODUCTION

Humidity is the amount of water vapour in the air which indicates the probability of precipitation. Also, humid air being less dense is one of the fundamental biotic factors that decide the habitat of a particular plant or animal [1]. There are three main measurements of humidity: absolute, relative and specific. Absolute humidity is the content of water vapour in air, regardless of temperature; relative humidity (RH) is the ratio of the current absolute humidity to the

Authors gratefully acknowledge the Department of Science and Technology (DST), Government of India, for financial support in the form of Indo-Russian project (Ref no. INT/RUS/RFBR/P-148) and S. Sikarwar is thankful to DST for INSPIRE AORC fellowship grant no. DST/INSPIRE Fellowship/2014/IF140317, India.

S. Sikarwar (email: samiksha9.2009@gmail.com), Arun Kumar (email: bhu331028@gmail.com) and Prof. B.C. Yadav (email: balchandra_yadav@rediffmail.com) are working in Nanomaterials and Sensors Research Laboratory, Department of Physics, Babasaheb Bhimrao Ambedkar University, Lucknow-226025, U.P., India

Dr. G.I. Dzhardimalieva and Dr. Nina D. Golubeva are working in Laboratory of Metallopolymers, Institute of Problems of Chemical Physics, Russian Academy of Sciences, Chernogolovka, Moscow Region 142432, Russia

Journal of Materials Science: Materials in Electronics
https://doi.org/10.1007/s10854-018-9415-3

Synthesis and investigation of cubical shaped barium titanate and its application as opto-electronic humidity sensor

Samiksha Sikarwar[1] · Rakesh K. Sonker[2] · Anuj Shukla[3] · B. C. Yadav[1]

Received: 23 March 2018 / Accepted: 1 June 2018

Abstract
In the current scenario, nanoscience and nanotechnology are playing a vital role in the upliftment of the quality of human life. The quantum confinement effect that arises at the nano-dimensional particles, changes the properties of the material in a drastic way. The present paper reports the successful synthesis of $BaTiO_3$ using rotary evaporator and fabrication of sensing elements by deposition of films on flat borosilicate glass substrates using 2-methoxy ethanol and homogeneous precursor in the ratio of 1:4, 2:4, 3:4 and 4:4. These films were then annealed at 650 °C and characterized through various techniques. Morphological investigation as obtained from SEM reported the cubical clusters and the dimensionality of these clusters, decreases with increase in the concentration of 2-methoxy ethanol. An optical investigation done through UV–Vis spectrum showed the absorbance in the UV range and Tauc plot estimated the optical band gaps of 3.842, 3.854, 3.864 and 3.872 eV for the respective films. Structural information as obtained from XRD of the film having 2-methoxy ethanol and homogeneous precursor in the ratio of 4:4 gave minimum crystallite size of ~ 18 nm. Further, these films were employed as opto-electronic humidity sensor where the maximum sensitivity of the sensing elements was found as 2.15, 2.79, 3.28 and 3.67 μW/%RH respectively. Thus as the concentration of 2-methoxy ethanol in the solution increases, the properties of the material increases and hence the humidity sensing potency also increases.

1 Introduction

Barium titanate with the general formula ABO_3 called perovskites, is a primitive cubic, with larger cation-A in the corner, smaller cation-B in the middle and the anion, commonly oxygen, in the centre of the face edges. Here 'A' is monovalent, divalent or trivalent metal and 'B' is pentavalent, tetravalent or trivalent element [1]. Barium titanate can be prepared by different methods depending upon the desired characteristics. It is a versatile electroceramic that adopts a prominent ferroelectric characteristic, high dielectric permittivity with a high level of inherent piezoelectric properties and photorefractive effect [2]. It is chemically and mechanically very stable [3]. Also, it is transparent in the visible and infrared region with strong electro-optic coefficients. In its purest form, it is highly resistive at room temperature but this resistivity decreases by the addition of dopants and increasing oxygen deficiency at high temperatures in reducing gas environment. It transforms to the cubic, paraelectric state at the Curie temperature of ~ 130 °C. Barium titanate can exist in five phases (in a wide range of temperature): hexagonal, cubic, tetragonal, orthorhombic, and rhombohedral crystal structure, among which all exhibit the ferroelectric properties except the cubic phase [4]. When $BaTiO_3$ cools down to Curie point of 120 °C, the crystal undergoes a ferroelectric transition from cubic to tetragonal phase and becomes spontaneously polarized due to the unidirectional intermittent displacement of Ti^{4+} ions to neighbouring O^{2-} ions. This process is accompanied by altering of unit cell parameters caused by the destabilization of tetragonal phase of $BaTiO_3$ nanoscale crystals below 120 °C due to mechanical defects.

Ferroelectric materials have drawn the great attention of researchers for the development of base-metal-electrode capacitors, piezoelectric actuators, thermistors, and electro-optic devices. Combination of nanotechnology with different

✉ B. C. Yadav
balchandra_yadav@rediffmail.com

[1] Nanomaterials and Sensors Research Laboratory, Department of Physics, Babasaheb Bhimrao Ambedkar University, Lucknow, U.P. 226025, India

[2] Department of Physics and Astrophysics, University of Delhi, Delhi, India

[3] Defence Laboratory, Rattan Palace, Jodhpur, Rajasthan 342011, India

Published online: 05 June 2018

Sensors and Actuators A 263 (2017) 415–422

Contents lists available at ScienceDirect

Sensors and Actuators A: Physical

journal homepage: www.elsevier.com/locate/sna

Synthesis and characterization of copper (II) nitrate polyacrylamide & its application as opto-electronic humidity sensor

Priyanka Chaudhary[a], Samiksha Sikarwar[a], B.C. Yadav[a,*], G.I. Dzhardimalieva[b], Nina D. Golubeva[b], Igor E. Uflyand[c]

[a] Nanomaterials and Sensors Research Laboratory, Department of Applied Physics, Babasaheb Bhimrao Ambedkar University, Lucknow, 226025, U.P., India
[b] Laboratory of Metallopolymers, Institute of Problems of Chemical Physics, Russian Academy of Sciences, Chernogolovka, Moscow Region, 142432, Russian Federation
[c] Department of Chemistry, Southern Federal University, B. Sadovaya Str. 105/42, Rostov-on-Don 344006, Russian Federation

ARTICLE INFO

Article history:
Received 19 April 2017
Accepted 3 July 2017
Available online 6 July 2017

Keywords:
Opto-electronic humidity sensor
Transmission
Polyacrylamide
Copper nitrate

ABSTRACT

The present paper reports the effect of humidity on the transmitted power through the nanostructured copper (II) nitrate polyacrylamide (AAm) complex film at room temperature. For this purpose, the precursor of Cu(II) nitrate polyAAm was prepared and used for the deposition of a film on the substrates of borosilicate. The film was then investigated using SEM which revealed the uniform leaf-like structured morphology. By UV–vis spectrophotometer, it was found that the absorption of light took place in UV-region and the corresponding optical energy band-gap was observed as 4.02 eV. The diffraction pattern obtained from TEM showed the crystalline nature of the material. Powder XRD revealed the minimum crystallite size as 9 nm and average size as 13 nm which was further confirmed by the Zeta Nano-sizer. The film was employed as transmission based opto-electronic humidity sensor. Maximum sensitivity was found as ~ 0.838 μW/%RH. Response and recovery times were found as 31 s and 76 s respectively. Experiments were repeated time to time and reproducibility was found ~96% with negligible ageing effect. The investigated sensor being optical in nature has the capability of multiplexing the information with the signal.

1. Introduction

The current focus of the nanotechnology is to synthesize different nanostructures in such a way that they can be easily used for different applications in different field such as physics, chemistry and biology like as electronic device, energy storage, medical field, engineering, nano fibers, solar system, sensors etc. Nanoscale dimension composition of semiconducting oxide nano-crystals have fascinated a great devotion due to their enhanced properties as gas sensors with a definite sensing mechanism [1].

Water is an essential compound for human on the Earth and can exist in two different forms. The term moisture refers to the water in liquid (condensed) form and humidity refers to the water in gaseous phase [2]. Water vapours consist of highly reactive dipolar molecules which get condensed on or evaporate from the surface even with slight variation in temperature of the environment. Therefore, humidity controls many environmental phenomena. In recent years, a lot of metal oxides including polymeric materials have been employed as humidity sensors by the researchers but up to our knowledge, no polyacrylamide complex has been yet used as a humidity sensor. So here our aim is to employ the Cu(II) nitrate polyacrylamide complex as opto-electronic humidity sensor [3].

Organic polymers have played an innovative role in terms of the materials available to society. Although the initial advances were biggest in the area of products like thermoplastics and elastomers, towards the end of the 20th century the importance shifted to special materials with advanced properties. The development of new, easily processed materials via the combination of metal centres into synthetic polymer chains have motivated scientists since the 1950s until recently the metallopolymer area was back by synthetic difficulties. In general, the polymerization procedures that work so well for organic polymers normally lead to undesirable side reactions giving low molecular weight metallopolymers that are often insoluble and poorly characterized. Since in 1990s, many of the complications to the preparation of high molecular weight and soluble materials have been overcome by a number of groups, which led the path for the development of new synthetic approaches that are well-matched with the presence of metal centres. There is a

* Corresponding author.
E-mail address: balchandra_yadav@rediffmail.com (B.C. Yadav).

http://dx.doi.org/10.1016/j.sna.2017.07.006
0924-4247/

Sensors and Actuators A 272 (2018) 267–273

Contents lists available at ScienceDirect

Sensors and Actuators A: Physical

journal homepage: www.elsevier.com/locate/sna

Fabrication of tin substituted nickel ferrite (Sn-$NiFe_2O_4$) thin film and its application as opto-electronic humidity sensor

V. Manikandan[a,*], Samiksha Sikarwar[b], B.C. Yadav[b], R.S. Mane[c]

[a] Department of Physics, RVS Technical Campus, Coimbatore, Tamil Nadu, 641021, India
[b] Nanomaterials and Sensors Research Laboratory, Department of Applied Physics, Babasaheb Bhimrao University, Lucknow, UP, 226025, India
[c] Center for Nanomaterial & Energy Devices, Swami Ramanand Teerth Marathwada University, Dnyanteerth, Vishnupuri, Nanded, 431606, India

ARTICLE INFO

Article history:
Received 11 November 2017
Received in revised form 11 January 2018
Accepted 29 January 2018
Available online 2 February 2018

Keywords:
Nanostructured ferrites
Humidity sensor
Thin film
Surface morphology

ABSTRACT

A well nanocrystalline structured tin substituted nickel ferrite thin film was prepared by chemical co-precipitation method. XRD analysis reveals the average crystallite size as 51 nm and most preferential peak (311) affirms the formation of tin substituted nickel ferrite. The SEM morphology shows the large number of active sites. FT-IR analysis reveals the general nature of ferrite materials. TEM analysis shows the inhomogeneous distribution of particles. Also, the SAED pattern exhibits the polycrystalline nature. From UV analysis, it was observed that material has absorption in visible region at ~201 nm. Humidity sensing analysis reveals that material has average sensitivity is 2.08 MΩ/%RH and excellent reproducibility with response and recovery times of 44 and 180 s respectively.

1. Introduction

In recent years, there is an increasing need for low cost, highly reliable and functional humidity sensors. In humidity sensors, there are three main problems such as sensitivity, selectivity and stability. Humidity sensors are usually exposed to atmospheres and it contains various other components. They tend to lose their inherent sensitivity during usage as result of several complicated physical and chemical processes [1,2]. These difficulties were reduced in ferrite materials. Nickel ferrite has huge potential in electronic device applications and its electrical and magnetic properties are based on their distribution among tetrahedral and octahedral sites [3]. Nickel ferrite exhibits ferromagnetic nature which originates from anti-parallel spins between Ni^{2+} ions at octahedral sites and Fe^{3+} ions at tetrahedral sites respectively [4–7]. Tin oxide is an essential N-type metal oxide semiconductor with huge band gap, superb electrical and optical properties. These characteristics make tin an efficient material for large applications such as opto-electronic devices, gas sensing, photo catalyst, transparent conducting electrodes and solar cells [8–12]. Besides, the tin element has the capacity to increase the porosity, specific surface area and pore size distribution. A large surface area implies a much more active sites towards water vapor. Hence, the sensitivity of humidity sensor would be increased. The ferrite material can be prepared by various methods such as chemical co-precipitation method [13], hydro thermal method [14], auto combustion method [15], sol-gel method [16] and micro oven method [17]. Among them, chemical co-precipitation method is cost effective and therefore, adopted here. So, tin substituted nickel ferrite can be synthesized by chemical co-precipitation method. In our knowledge, there is no report on tin substituted nickel ferrite humidity sensor in open literature.

Rich Srivastava et al. have reported the synthesis and characterization of nickel ferrite prepared by chemical co-precipitation method and employed its thin film as humidity sensor. The results indicate that nickel ferrite has good sensing properties [18]. Fatih Bayansal et al. have reported the sensing properties of manganese doped nickel ferrite prepared by chemical co-precipitation method. From the results, the sensor was notably sensitive to humidity but weakly sensitive towards acetone, ethanol, methanol and benzene [19]. Iulian et al. has reported the effective humidity sensing and electrical properties of Ni-Zn-Dy ferrite and it showed significant effect on frequency range 20 Hz–20 MHz for humidity sensing applications [20]. A.R. Iordan et al. has reported the nickel ferrite as possible sensing material for humidity applications [21]. In recent years, humidity sensor was very important in the field of material science. Table 3 indicates a short literature evaluation of some materials as optical humidity sensors in latest years.

In this paper, the humidity sensing properties of tin substituted nickel ferrite has been reported. The prepared material is characterized by XRD, SEM, FTIR, TEM and UV–Vis Spectrophotometer.

* Corresponding author.
E-mail address: manikandan570@gmail.com (V. Manikandan).

https://doi.org/10.1016/j.sna.2018.01.059
0924-4247/

Journal of Materials Science: Materials in Electronics
https://doi.org/10.1007/s10854-018-8774-0

Preparation of zinc (II) nitrate poly acryl amide (PAAm) and its optoelectronic application for humidity sensing

B. C. Yadav[1] · S. Sikarwar[1] · R. Yadav[1] · P. Chaudhary[1] · G. I. Dzhardimalieva[2] · N. D. Golubeva[2]

Received: 30 September 2017 / Accepted: 14 February 2018

Abstract
The present paper reports the investigation of transmitted power through the nanostructured zinc (II) nitrate polyacrylamide deposited substrate to investigate the adsorption/desorption of humidity at room temperature. For this purpose, the precursor of $Zn(NO_3)_2{\cdot}(AAm)_4{\cdot}2H_2O$ was prepared and used for the deposition of films on borosilicate flat substrates. The film was then investigated using SEM, XRD and UV–Vis absorption techniques. Scanning Electron Microscope showed the macroporous nature of the film with multiple pores in situ. XRD revealed the nature of monomer and polymer. Energy band-gap of the film was estimated as 3.865 eV by UV–Vis spectrophotometer. SAED confirmed the crystalline nature of the material. From Zeta nanosizer, the minimum range of particles was found as 5–20 nm. The film was employed as transmission based opto-electronic humidity sensor. Maximum sensitivity was found as 1.831 µW/%RH. Response and recovery times of the sensor were found as 250 and 37 s respectively. Experiments were repeated time to time and found that the sensor was ~96% stable after a long run. Thus the investigated opto-electronic sensor being polymeric is flexible in nature.

1 Introduction

Nanoscale structures have attracted the researchers across the globe due to their unique properties, whether they are metal oxide framework, organic framework or metal-organic framework [1, 2]. The polymer matrix attracts a significant scientific and technological interest in the field of nanotechnology [3]. The synthesis of nanoparticles in a polymer matrix involves a lot of methods for confirming the conservation and stabilisation. The conversion of monomer to a polymer matrix can be done by the Frontal polymerization technique. This technique utilises the kinetic and dynamic properties of the polymeric materials including polyacrylamide [4, 5]. Polyacrylamide is a chemical compound that has the interesting property of being soluble in water. It is useful for the treatment of industrial wastewater. Polyacrylamide is a combination of polymers and acrylamide (C_3H_5NO). Acrylamide due to its toxic nature adversely affects the nervous system so it must be handled by various protecting techniques [6]. Acrylamide is a highly water-soluble compound made from the hydration of acrylonitrile. It can be easily shown by titration, colorimetry and high-performance gas chromatography in the air, water, biological fluids [7].

There is a wide variety of polymers that contain metals in the chain. These polymers are hence called "Metallopolymers". These new materials have the properties of polymers as well as some functionality of metals; hence these materials have a wide range of application in solar cells, memory devices, sensors and light emitting devices etc [8–11]. These polymeric ligands were synthesised in order to remove certain metal ions or groups from aqueous media [12, 13]. The solid-state chemistry of acrylamide complexes with a variety of divalent transition metals such as Mn^{+2}, Fe^{+2}, Co^{+2}, Ni^{+2}, Cu^{+2}, Zn^{+2} and Cd^{+2} can be studied. Chlorides, nitrates, perchlorates and tetrafluoroborates can also be studied for the investigation of acrylamide complexes [14, 15]. The molecular structure of octahedral $[Zn(AAm)_4(H_2O)_2]^{+2}$ including nitrate and the oxygen has four acrylamide compound and two water molecules. The bond length of Zn-O (amide) and Zn-O (water) are 2.133 Å and 2.073 Å respectively [16]. Some researchers have also synthesised the complexes of

✉ B. C. Yadav
balchandra_yadav@rediffmail.com

[1] Nanomaterials and Sensors Research Laboratory, Department of Physics, Babasaheb Bhimrao Ambedkar University, Lucknow, UP 226025, India

[2] Laboratory of Metallopolymers, Institute of Problems of Chemical Physics, Russian Academy of Sciences, Chernogolovka, Moscow Region, Russia 142432

Published online: 19 February 2018

Optical Materials 83 (2018) 342–347

Contents lists available at ScienceDirect

Optical Materials

journal homepage: www.elsevier.com/locate/optmat

Spherical growth of nanostructures ZnO based optical sensing and photovoltaic application

Rakesh K. Sonker[a,*], S. Sikarwar[b], S.R. Sabhajeet[b], Rahul[c], B.C. Yadav[b]

[a] Department of Physics and Astrophysics, University of Delhi, Delhi, 110007, India
[b] Nanomaterials and Sensors Research Laboratory, Department of Physics, School of Physical and Decision Sciences, Babasaheb Bhimrao Ambedkar University, Lucknow, 226025, U.P., India
[c] Department of Applied Sciences and Humanities, Jamia Millia Islamia, New Delhi, 110025, India

ARTICLE INFO

Keywords:
Spherical nanostructures
Solar cells
Optical sensor
Sol-gel spin coating
Zinc oxide film

ABSTRACT

The present paper reports deviation in the intensity of light transmitted through the film of ZnO spherical nanostructure (SNSs) with the exposure of humidity at room temperature. For this purpose, the precursor of ZnO SNSs was prepared and used for coating thin film on borosilicate substrates. The efficient dye-sensitized solar cells (DSSCs) are promisingly low-cost molecular solar cell devices. ZnO SNSs are promising materials used to use to create photoanodes for DSSCs. The film was then investigated using SEM, HR-TEM, XRD and UV–visible transmittance techniques. Further, it was employed as transmission based optical humidity sensor, the maximum sensitivity of which was found a ~ 1.81 μW/%RH with response and recovery time of 36 s and 124 s respectively. The sensor showed ~97% reproducible results. The fabricated ZnO SPSs based DSSC shows a short circuit current density (J_{sc}) of 3 mA/cm^2, open circuit voltage (V_{oc}) of 0.62 V and efficiency (η) of 1.3% at one sun condition.

1. Introduction

The humidity/gas sensing is becoming much significant, essentially in industries and human comfort [1,2]. The consumption of non-renewable fossil fuel resources, such as oil, natural gas, coal, and the subsequent damages to the environment and human health caused by their combustion in the twentieth and twenty-first centuries have forced the nations of the world to think about exploring alternative, renewable energy sources [3]. Water vapour being an important atmospheric greenhouse gas plays a vital role in various environmental phenomena. A wide variety of metal frameworks and polymers have been examined as humidity sensors, generally based on the intonation in electrical parameters [4–7]. Bulk zinc oxide is an n-type semiconductor material having a wide band gap and large exciton binding energy [8,9] with the properties of ruggedness, chemical inertness, visible luminescence, wide range of resistivity, high transparency, high electron mobility, good chemical and thermal stability [10–13]. Among the renewable energy resources, solar energy is one of the promising candidate for alternative energy sources, to either replace or reduce the dependence of world energy needs on fossil fuels. ZnO nanostructures can be controlled by the precursor concentration, rate of evaporation and reaction time to produce a variety of nanostructures ranging over ZnO nanoparticles, nanorods and nanospheres. The employed synthesis method is simple and reproducible for a variety of nanostructures on a potentially large synthetic scale. For slow evaporation of a nanoparticulate colloidal system, the nanoparticles are driven to be arranged and aligned in a linear fashion to form one-dimensional nanorods. On the other hand, fast evaporation of the solvent promotes a point-initiated vectorial growth of nanospheres. The photovoltaic device based on the nanorod structure with ruthenium dye shows a power conversion efficiency ~1.5 times greater than that for a similar device based on nanoparticles. It is believed that improved photovoltaic performance can be expected through optimizing the dimensions of the ZnO nanostructures [14–16]. Synthesized ZnO nanostructures can be used for the fabrication of white light emitting diodes, display devices, biological labelling and detector etc [17]. ZnO SNSs possess significantly different properties from their bulk counterpart hence suitable for various applications such as light emitting diodes [18], polariton laser [19], field effect transistor [20], photo-catalyst [21], UV sensor [22] and gas sensor [23–27]. Yang et al. studied interesting optical properties of different types of ZnO nanostructures ranging from nanodots to tetrapods [28]. The indivisible studies of ZnO structure by Kim et al. [29], Woo et al. [30], Sonker et al. [31] and Dutta et al. [32] have shown that ZnO SPSs materials depend on the structural which further depend on

* Corresponding author.
E-mail address: rakesh.sonker81@gmail.com (R.K. Sonker).

https://doi.org/10.1016/j.optmat.2018.06.046
Received 4 May 2018; Received in revised form 9 June 2018; Accepted 19 June 2018

J Mater Sci: Mater Electron
DOI 10.1007/s10854-016-6184-8

Growth and characterization of sol–gel processed rectangular shaped nanostructured ferric oxide thin film followed by humidity and gas sensing

B. C. Yadav[1] · K. S. Chauhan[1] · S. Singh[2] · R. K. Sonker[1] · S. Sikarwar[1] · R. Kumar[1]

Received: 4 September 2016 / Accepted: 5 December 2016

Abstract In the present work nanostructured ferric oxide has been synthesized using sol–gel method. Thin films of ferric oxide were fabricated via spin coating process. The surface of the thin film was scanned by scanning electron microscope that exhibited the surface morphology of ferric oxide nanostructures. The material was also characterized by XRD, Acoustic particle sizer and FTIR. All the particles distributed on the surface have some spaces among them known as pores. These pores serve as adsorption sites for moisture and other gases. EDX confirmed the elements forming the ferric oxide in pure form. The particle size of the ferric oxide was estimated as ~12.2 nm. The pore size of the film was ~50 nm i.e., nature is mesoporous. Annealing effect on the surface morphology was also observed. Humidity sensing, electrical as well as optical of the prepared film was carried out. The results showed the suitability of material for the development of humidity sensors. Variations in resistance with the exposure of LPG were recorded and found that resistance of film increases with the increasing exposure time and concentration of gas. The maximum sensing response of the sensor was recorded as 3.26 for 1000 ppm at room temperature. The response and recovery times of the sensor were found to be ~12 and 9 min, respectively.

✉ B. C. Yadav
balchandra_yadav@rediffmail.com

[1] Department of Applied Physics, Babasaheb Bhimrao Ambedkar University, Vidya Vihar, Raebareli Road, Lucknow, UP 226025, India

[2] Department of Physics, University of Allahabad, Allahabad, UP 211002, India

1 Introduction

Amongst the various metal oxides, iron oxide (III) has been one of the extensively investigated transition metal oxides. Besides amorphous phase, Fe_2O_3 has four polymorphs: (1) α-Fe_2O_3; (2) β-Fe_2O_3; (3) γ-Fe_2O_3; and (4) ε-Fe_2O_3, while the highly crystalline α-Fe_2O_3 and γ-Fe_2O_3 occur in nature, β-Fe_2O_3 and ε-Fe_2O_3 are generally synthesized in the laboratory [1, 2]. Ferric oxide has a wide range of applications as magnetic material but in recent years it has produced a large interest as a gas sensitive material [3–9] because it does not require a costly noble metal catalyst to perform as a good sensor [10–17]. Also due to the temperature dependent surface morphology and photo catalytic activity, it is considered to be the most promising sensing material. Various shapes of iron oxide or hydroxide with controlled grain size are available and have been of great research interest [18–22]. For gas sensing applications, the materials having lower density and higher active surface area are challenging for the fabrication of sensors. With this intention, several methods of preparation of ferric oxides are known. Co-precipitation, micro emulsion, pulsed wire discharge and hydrothermal processes are employed in order to obtain nanostructured powder [23–27].

The mechanism of sensing for the reducing/oxidizing gases is based on the change in electrical resistance or capacitance resulting from the interaction between the gas molecule and adsorbed oxygen species on the surface of the metal oxide [28, 29]. The states of the amount of the oxygen adsorbed on the surface of the materials are strongly dependent on the microstructure of the materials, namely specific surface area, particle size as well as surface morphology. As the sensing phenomenon mainly occurs on the surface of the sensing element, the surface morphology has an essential role on the sensitivity of the sensor [30].

ISSN (Online) 2393-8021
ISSN (Print) 2394-1588

International Advanced Research Journal in Science, Engineering and Technology
Vol. 2, Issue 11, November 2015

Synthesis, Characterization and Development of Opto-Electronic Humidity Sensor using Copper Oxide Thin Film

B. C. Yadav[1], Samiksha Sikarwar[2], Abhisikta Bhaduri[3] and Praveen Kumar[4]

Nanomaterials and Sensors Research Laboratory, Department of Applied Physics, Babasaheb Bhimrao Ambedkar University, Lucknow, U.P., India[1, 2, 3, 4]

Abstract: The present paper reports the study of modulation in light transmitted through nanostructured cupric oxide thin films with the exposure of moisture at room temperature. For this purpose the precursor of CuO was prepared and was then investigated using SEM and UV-visible absorption techniques. SEM showed the porous nature of the material and energy band-gaps were estimated as 2.8-3.2 eV for different concentrations by UV-Vis spectrophotometer. The precursor of CuO in the form of gel was prepared and later used for the deposition of thin film on borosilicate substrates with dimensions 1.5×1.5 cm^2 using sol-gel spin coating technique. The film was employed as transmission based opto-electronic humidity sensor. Maximum sensitivity was found 0.85 µW/%RH. As the investigated opto-electronic sensor has remote access capability, therefore, may be used to replace an electrical humidity sensor.

Keywords: Nanostructure, opto-electronic humidity sensor, sol-gel spin coating, cupric oxide.

I. INTRODUCTION

In recent years advancements in sensor manufacturing technologies have driven by post-process high-speed, low-power and low-cost microelectronic hybrid circuits [1-3], modern signal conditioning methods and progress in miniaturization technologies [4-5] product reliability. Furthermore, it is vital to know the degree of efficiency of each sensor related to its calibration circumstances and sensing mechanism [6-7]. Today, simulation techniques and design aids are adequately used to predict and improve output data prior to implementation of mass production processes to save time and enhance quality [10-11]. Miniaturization of sensor devices offers numerous advantages such as low hysteresis [5], batch fabrication [12], and ease of packaging/integration along with the corresponding cost reductions [13-16].

It is well documented that humidity plays a significant role in every part of the Earth including biology and automated industrial processes. To have a desirable surrounding atmosphere, it is essential to monitor, detect and control the ambient humidity under different conditions ranging from low temperature to high or in mixtures with other gases by precise and provident sensors [17-18]. Utilization in intelligent systems and networks as monitoring sensors to determine the soil moisture during irrigation in agriculture, or for diagnosis of corrosion and erosion in infrastructures and civil engineering are among the major applications of humidity sensors [19]. In fact, the need for protection of environmental conditions has been leading to extensions in various humidity sensor developments based on the use of physical and chemical methods in presence of organic, inorganic or hybrid materials since long back [20-21]. Advancement of humidity sensor systems encompasses enhanced efforts in betterment of transducer performance such as sensing elements [22], structure design [23-24], principle of mechanism [25-26], and fabrication technologies [27]. In this milieu, the transducer materials are the key features, followed by the availability of suitable manufacturing technologies, free choice of device geometrical properties to attain the required dimensional efficiencies, optimization of surface for the occurrence of conductance, ease of production flow and investment expenses.

Copper (II) oxide or cupric oxide (CuO) is the higher oxide of copper. As a mineral, it is known as tenorite. It is a black solid with an ionic structure which melts above 1200°C with some loss of oxygen. Copper (II) oxide belongs to the monoclinic crystal system, with a crystallographic point group of 2/m or C2h. The space group of its unit cell is C2/c, and its lattice parameters are a = 4.6837(5), b = 3.4226(5), c = 5.1288(6), α = 90°, β = 99.54(1)°, γ = 90°. The copper atom is coordinated by 4 oxygen atoms in an approximately square planar configuration [28].

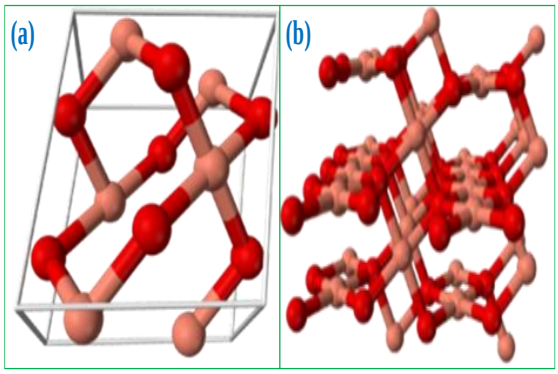

Fig. 1 CuO (a) Unit cell (b) Crystal structure

CuO has molar mass 79.545 g/mol and density 6.315 g/cm^3. Its melting point and boiling points are 1326 °C and